Multi-scale Observations and 3D Modelling of Inkjet Printing Modified Carbon Fibre Composite

A thesis submitted for the degree of
Doctor of Philosophy

Qingchuan Lu
Department of Materials
Linacre College

University of Oxford
Michaelmas Term 2024

‘There is a crack in everything, that is how the light gets in.’

- Leonard Cohen

Abstract

Multi-scale Observations and 3D Modelling of Inkjet Printing Modified Carbon Fibre Composite

Qingchuan Lu

Linacre College, Michaelmas Term, 2024

Carbon fibre reinforced polymer (CFRP) composite is in high demand in industries such as wind turbine, automobile, and aerospace due to its exceptional strength and stiffness with low weight. However, its internal defects can lead to catastrophic failure by delamination. Therefore, enhancing interfacial resistance is critically important. Inkjet printing of polymethyl methacrylate (PMMA) or polyethylene glycol (PEG) between prepregs has shown promise in increasing fracture toughness with minor weight penalty and negligible compromise of other mechanical properties. To obtain the insight into the toughening mechanism, a series of characterizations as well as 3D finite element models were applied in this thesis.

This project began with a description of manufacturing process for inkjet printing modified CFRP. The mechanical performance was then evaluated using Double Cantilever Beam (DCB) test, which verified the reported toughening effect. A series of in situ observations were conducted on the laminates to study the Mode I fracture propagation behaviour: Dual X-ray imaging and diffraction analyses were employed with the aim of monitoring the lattice strain in carbon fibres via X-ray diffraction (XRD), while tracking crack tip position through radiographs processed with Digital Image Correlation (DIC). In-situ synchrotron X ray computed tomography was used to image the 3D evolution of damage propagation. Post processing using Digital Volume Correlation (DVC), the displacement fields were resolved, and larger critical crack openings were observed for the printed specimens. The displacement field was imported into a finite element model as boundary conditions to evaluate J-integral and quantify the different modes of stress intensity factor (K), confirming the enhancement in fracture energy post printing. The fracture surface of laminates was observed by multiple characterization methods, and larger surface unevenness was observed to correspond with higher fracture toughness. Confocal microscopy revealed that PEG diffused into the epoxy matrix during curing, whereas PMMA remained separate. Fractography observed micropores and fractured particles in the PMMA-printed sample. It was deduced that the PMMA deposits facilitated crack deflection and cavitation formation, while PEG improved the matrix adhesion. Both printed laminates exhibited increased active functional groups on the fracture surfaces, suggesting enhanced bonding activity. A finite-element microstructure meshfree (FEMME) model was then applied to simulate DCB experiments with varying interfacial strength. The model replicated the wider crack opening in printed samples, consistent with XCT observations.

Acknowledgements

Firstly, I want to express my sincere gratitude to my supervisor, Professor (Thomas) James Marrow, for his teaching, guidance and support during my D.Phil study. He is always rigorous to research work, and his knowledge, work ethic and motivation to science have encouraged me a lot. I cannot expect more to be supervised by such a role model. Thank you so much for your patience and always willing to discuss and support my ideas throughout this work.

Besides my supervisor, I also wish to thank Dr Patrick Smith and his team for the help and insightful comments during the sample manufacturing. I would like to thank Dr Luis Saucedo Mora for his help in the model and simulation work. This work could not be achieved without the help from synchrotron beam scientists. I thank Dr Sharif Ahmed, Dr Andrew James, Dr Christoph Rau and Dr Kaz Wanelik in the UK Diamond Light Source, as well as Dr Goran Lovric in the Paul Scherrer Institute, Swiss Light Source. Thank you for all the help from experiment design, implementation, equipment training towards data transferring and processing. Your overnight helps are also greatly appreciated.

I also wish to thank all the support from the Department of Materials: I thank Dr Phani Karamched for his help on SEM; Dr Andrew Lui and Dr Phil Holdway's assistance on XPS. Special thanks to all the TJM group members Yang, Shraddha, Talha, Ziyang, Phil, Abdo, Thomas, Marcus, Marin, Rory, Bingkun and Xiao to give me such great working experience. The nights we spent together in Synchrotron light source are memorable.

I would also like to thank all the lovely friends in Oxford: Yalun, Yingrui, Yuzhe, Anlin, Ruining, Tongshan and Kai Ling, the mutual supports gave me the power to get through the difficulties. Thank you, my flatmate Nikki (Lan), the happy memory and festival we celebrated together could always heal me. The time in Phoenox dance society also leaves me with many valuable memories.

Last but not least, I wish to give the deepest thanks to my dear family. I am grateful for all the mental and financial support from my parents Meihua Lu and Qian Tan, your love brings me to where I am. Thank you to my husband Peng Sun, who always encourages me to pursue my passion. You bring happiness and power to my life, I would not make it without you.

Acronyms

carbon fibre reinforced polymer (CFRP)
poly(methyl methacrylate) (PMMA)
polyethylene glycol (PEG)
double cantilever beam (DCB)
digital image correlation (DIC)
digital volume correlation (DVC)
crack opening displacement (COD)
X-ray computed tomography (XCT)
X-ray diffraction (XRD)
scanning electron microscopy (SEM)
X-ray photoelectron spectroscopy (XPS)
phase congruency (PC)
finite element (FE)
stress intensity factor (SIF)
field of view (FOV)
region of interest (ROI)
Finite Element Microstructure Meshfree (FEMME) model
microstructure-based meshfree (MAM) model
cellular automata (CA)

Table of Content

Chapter 1

1. Introduction

1.1 Project Background

Carbon fibre reinforced polymer (CFRP) composite is a material in high demand due to its high specific strength, modulus, resistance to fatigue and lightweight. It was first invented in 1950s and began to be widely applied in industries in the 1970s. As shown in Figure 1.1, by the 1990s, CFRP prepregs began to be adopted by aircrafts such as Boeing 777 and Airbus 320. Replacing certain metal alloys with CFRP allowed to produce light weight components with improved aerodynamic performance. Aircraft weight reduction is critical: a 20% weight reduction can result in up to 12% fuel savings [1], significantly lower the energy cost. Consequently, the demand for CFRP in aerospace industry has steadily risen. A notable example is the Airbus 350 XWB, where CFRP accounts for 53 wt.% of the aircraft structure. [1]

CFRP has also found extensive applications in other industries: in wind turbines, its high modulus enables the design of longer and slender blades to achieve superior aerodynamic performance. In automobile, the reduced weight and high strength makes CFRP attractive. For instance, BMW established a joint venture to produce carbon fibre for its lightweight vehicles. As a result, the global demand of CFRP is projected to reach 285 Kilo-ton by 2025 (Figure 1.2).

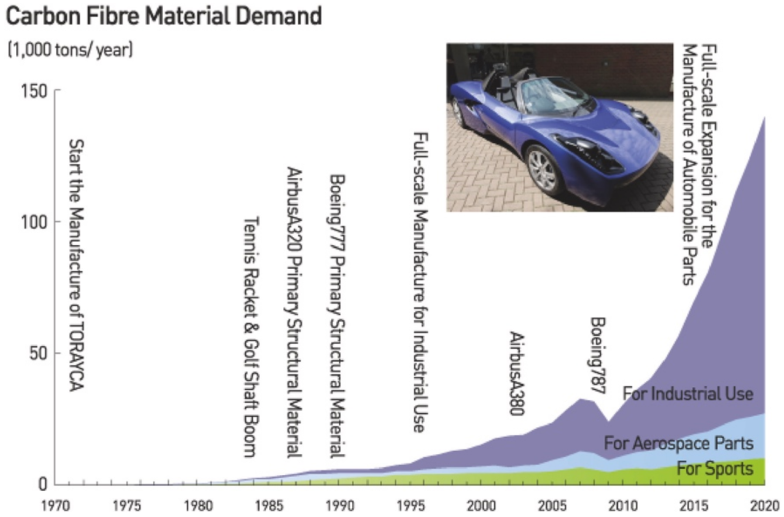

Figure 1.1. The development history of carbon fibre materials [1]

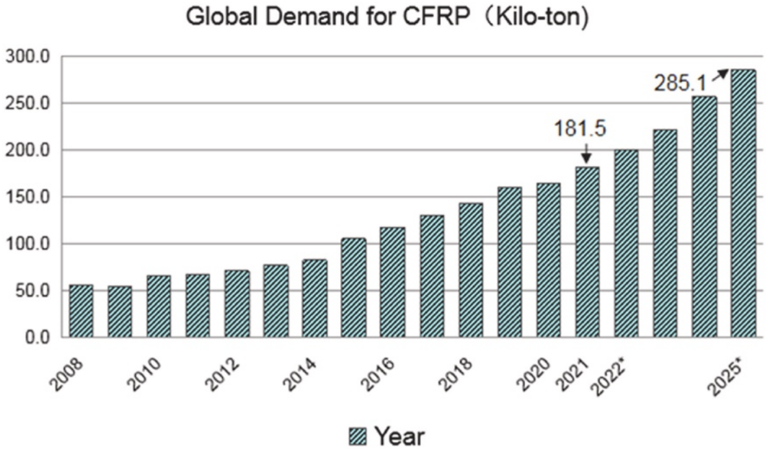

Figure 1.2. Global demand of CFRP from 2008 to 2025 [1]

However, due to the weak bonding between prepreg interfaces, CFRP is prone to delamination, which could lead to catastrophic failure. Delamination initiates from internal microcracking, which is hidden from the surface and is hard to monitor. Enhancing the interfacial delamination resistance thus becomes essential to broaden the CFRP's applications. Inkjet-printing technique has recently been demonstrated could improve the interfacial fracture resistance. Unlike other toughening methods, inkjet printing achieves this enhancement with minimal impact on other mechanical properties and a negligible weight penalty. This work aims to investigate the toughening mechanism behind inkjet printing methodology, which would advance the present understanding of the materials and potentially aid the future design to modify the properties of the composite.

1.2 Thesis structure

To study the damage behaviour and effect of inkjet printing, this thesis is structured as below: A theoretical background of the project is firstly described, where details of CFRP materials, ink-jet printing technique, composite failure as well as in-situ characterization methodologies are included. In Chapter 3, the sample manufacturing process is present, followed by the mechanical test to demonstrate the enhancement of fracture energy in printed specimens with scale-down size. The in-situ characterizations are displayed in Chapter 4, where an in-situ dual diffraction-radiation characterization has been explored, which aims to assess the elastic behaviour as well as the correlation with crack propagation. Additionally, a series of XCT were conducted to optimize the image quality, and the 3D volumetric results are analysed qualitatively and quantitively. Following the in-situ test, samples were then characterized with ex-situ analysis to study the surface morphology and chemical properties in Chapter 5. With the experimental observation, in Chapter 6, a finite element microstructure meshfree fracture model (FEMME) is generated to simulate the fracture behaviour. The thesis concludes in Chapter 7, together with a discussion on potential direction of the future research.

Chapter 2

2 Literature review

2.1 Carbon fibre reinforced polymer (CFRP) composite

Carbon fibre reinforcement polymer have gained escalating demanded in industries such as aerospace, automobile and wind turbine owing to its superior strength to weight ratio as well as stiffness. This section will give an introduction about composite materials, mechanical failure of composite and existing methods for toughness enhancement.

2.1.1 Introduction of composite materials

2.1.1.1 Composite

'Composite' denotes a class of materials that consists of two or more discrete components to synthesize an enhanced substance. It enables designers and engineers to tailor materials for specific needs. Constituents of composite materials typically encompass a matrix and a reinforcement element. The reinforcement could be particulates, short fibres or long fibres which as an example could be a sand toughened cement concrete, glass-fibre/epoxy and unidirectional carbon fibre reinforced composite respectively [2]. Depending on the matrix constituent, composites are generally classified into three primary categories: polymer matrix composite, ceramic matrix composite and metal matrix composite. Polymer matrix composites have garnered significant attention due to their optimal strength and stiffness coupled with low weight [3]. This work concentrates on carbon fibre reinforced polymer matrix composite, with more expansive details in the subsequent sections.

Composite materials are distinguished from other structural substances by their customizable properties that can yield exceptional stiffness and strength with low weight.

Additionally, their superior corrosion and fatigue resistance contribute to extended lifespans. The toughness could also be modified by designing toughening mechanisms through different multiple crack paths [4]. Despite the above benefits, composites typically have a higher cost than traditional materials and exhibit anisotropy, which results in diminished strength and toughness along certain orientations. Another significant limitation of composites with polymer matrix is their susceptibility to thermal degradation, leading to unsuitability for high-temperature applications. Moreover, temperature variation, especially during cooling post-curing, could impact the structural integrity by inducing residual stress between reinforcement and matrix, resulting from the different thermal expansion coefficients, which may potentially lead to damage. [5]

Due to the light weight and customizable properties, composites have a board range of applications from aerospace to marine industries. CFRP, for instance has been increasing used in aircraft component such as wings, fuselages, and rear pressure bulkheads. The Boeing 787 Dreamliner has increased the amount of CFRP to 50 wt.%, yielding enhanced fuel efficiency and payload capacity [6]. Additionally, the adaptability of CFRPs to be moulded into complex structures in a single piece could optimize manufacturing efficacy while obviating joint failure concerns. The laminated composite however suffers from interfacial debonding, which can cause delamination. Internal delamination is hard to detect but might lead to catastrophic failure that limits the applications of CFRP.

2.1.1.2 Fibre

Reinforcements are categorized into continuous and discontinuous types, with the former showing better mechanical properties with high cost. In a composite, continuous reinforcement such as long fibres acts as the load carrier, which provides stiffness and strength that dominate the mechanical property of final component [7].

Continuous fibres could be arranged unidirectionally or woven to create fabrics. When arranged unidirectionally, the fibres lie parallel, optimizing stiffness and strength along the fibre orientation while compromising the properties perpendicular to this direction [8]. Woven fibres generate isotropic mechanical property in both directions within the fabric plane and are also more flexible so they can be moulded easily into complex shapes. The stiffness of a woven fibre composite however is not as high as that of the unidirectional fibre composite [9].

When the composite is subjected to external load, the force transfers from matrix to fibre, therefore, the interface between fibre and matrix becomes essential. Surface treatments such as coating of silane coupling agents are commonly employed to fibres that promotes the bonding. A strong fibre matrix interface is instrumental in imparting superior mechanical properties to the final component, including stiffness, strength, and fatigue resistance. [10, 11]

The most common fibre materials used in commercial applications are aramid, glass and carbon. A summary of comparisons between these fibres is provided in Table 2.1. Aramid fibres are distinguished by high Youngs modulus and strength. Attributed to their highly crystallized molecular structure, aramid fibres confer excellent chemical resistance and damage tolerance [12]. The high cost and low compressive strength are the primary drawbacks that limit aramid fibre usage [13]. Glass fibre has the longest history among the three categories, it is also the most commonly used fibre and is made by drawing filaments of molten glass [14]. Typical types such as E-glass, C-glass and S-glass represent electrical usage, high chemical resistance and high modulus and strength respectively. Glass fibres are commonly used in areas where lower cost is required. Their application in environment where high mechanical required, however, is limited by the relatively low tensile modulus and fatigue resistance. [15]

Carbon fibre was initially developed in the early 1960s to improve on the low stiffness of glass fibre. With a diameter of 5-10 micrometre, carbon fibre could bear a stress of up to 3.5 GPa [16]. Unlike the amorphous structure of glass fibres, carbon fibres exhibit a crystalline form, with carbon atoms covalently bonded and arranged in hexagonal lattice (graphite) along the basal plane. These planes are stacked parallel and aligned along the fibre axis, resembling a rolled architecture of graphite sheets as depicted in Figure 2.1 [17]. The alignment of carbon atoms' plane in radial direction could be circumferential, radial, random or a combination as illustrated in Figure 2.2.

The graphite planes are bonded by weak van der Waal bonds (~ 10 kJ/mol) in the radial direction [18] while the covalent bond between carbon atoms along the fibre axis are considerably stronger (~ 525 kJ/mol) [19], culminating in anisotropic performance of carbon fibre.

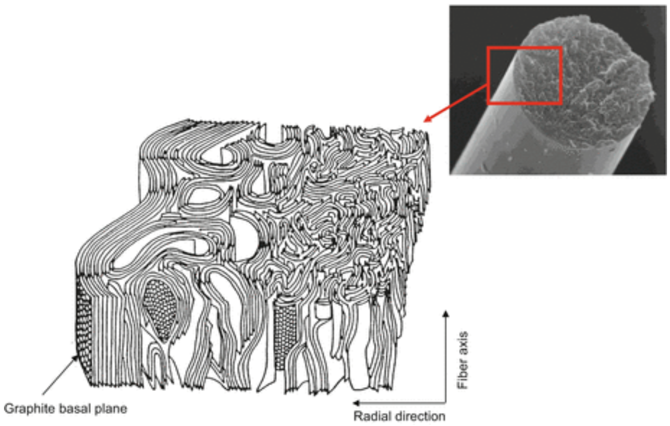

Figure 2.1. Structure of carbon fibre [17]

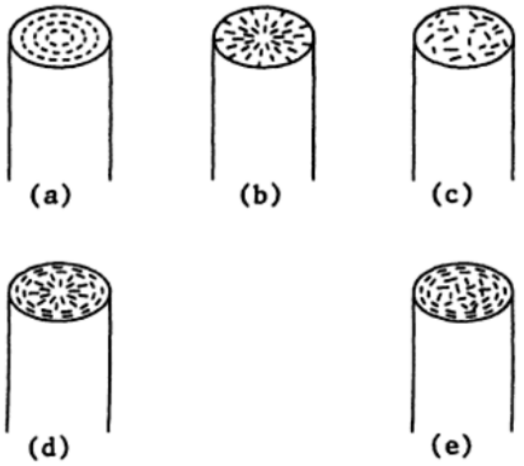

Figure 2.2. Alignment of graphite sheet in radial direction of (a) circumferential, (b) radial, (c) random (d) & (e) mixed arrangement [13]

Approximately 90% of carbon fibres are fabricated from PolyAcryloNitrile (PAN). Although alternatives such as pitch and cellulose can reduce costs, this often results in a compromise on quality. The manufacturing process of carbon fibres begin with the drawing of PAN precursors into elongated strands, which are subsequently subjected to a heat treatment at 300°C to achieve stabilization. This is followed by carbonization, where the fibres are heated in an oxygen-free environment to remove non-carbon atoms and that facilitate the alignment of carbon crystals along the fibre's longitudinal axis. After that, the surface of the fibres undergoes a controlled oxidation to enhance bonding capacity and to affect the mechanical properties by modifying the surface roughness. Finally, the fibres are coated to afford protection during subsequent manufacturing processes. [13]

As shown in Table 2.1, carbon fibre exhibits exceptional mechanical properties especially in terms of high specific strength and modulus with low weight. Making a comparison with a conventional structural metallic material such as aluminium alloys, carbon fibres demonstrate a tensile strength that is more than sevenfold greater, while their density is approximately 35% lower [20].

Table 2.1. Summary of typical properties for the three main types of fibre [19, 21]

Fibre	Density (g/cm^3)	Tensile modulus (GPa)	Tensile strength (GPa)
Aramid	1.4	83	3.6
Glass (E-type)	2.5	73.5	3.5
Carbon (PAN-based)	1.8-2.0	240-300	4.3-7.1

2.1.1.3 Matrix

The matrix transfers load between fibres, provides toughness for the composite and protects fibres against wear and buckling [22]. The interfacial bonding between fibre and matrix is crucial: weak bonding results in insufficient strength and stiffness, while if the interfacial connection is too strong, composite might be unacceptably brittle as it invalidates the toughening mechanism such as fibre pull out [23]. Depending on the application requirement, the matrix could be metal, ceramic, polymer, or a hybrid.

Polymer matrices are commonly used in applications where weight reduction is essential. It also has some advantageous properties such as substantial chemical resistance and electrical insulation capabilities. Polymer matrices are typically categorized into thermoset and thermoplastic groups [24]. A schematic of molecular chains for these two types is shown in Figure 2.3. Thermoplastic polymer maintain mobility and independence among molecular chains, which translates to high fracture toughness and impact strength [25]. However, they are limited by lower thermal stability and creep resistance. In contrast, thermoset polymers feature molecular chains that are interconnected through covalent bonds, forming a rigid three-dimensional network that constrains chain mobility. As a matrix material, thermoset polymers exhibit elevated strength and modulus; however, they are also associated with inherent brittleness and reduced fracture toughness.[26, 27]

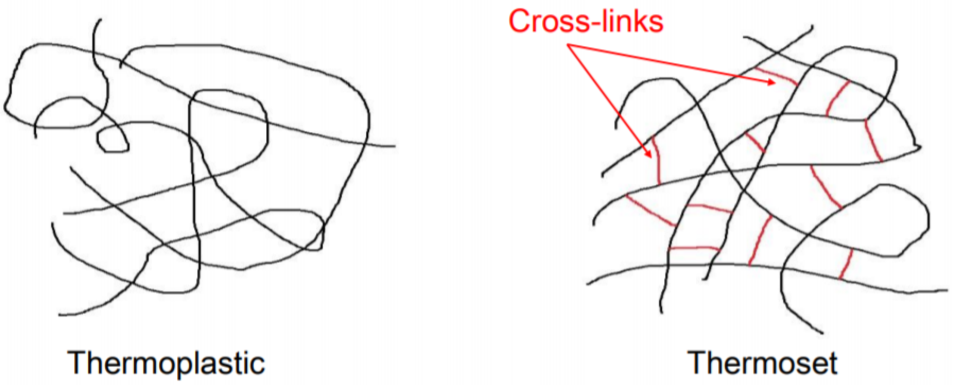

Figure 2.3. Schematic of molecular chains for thermoplastic and thermoset polymers [20]

Epoxy is a predominant class of thermoset polymer matrix material commonly used combining with carbon fibre to fabricate high performance composites. It bonds with the carbon fibres to improve the load carrying capacity while its durability and chemical resistance protects the fibres from the environment. Specifically, the relatively high glass transition temperature (Tg) also guarantees the composite performance in high ambient temperature. Besides, epoxy possess low shrinkage during curing, which mitigates the induction of residual stress. Moreover, the water resistance also makes it suitable in application such as offshore wind turbines. The polymerization of epoxy contains three stages: In stage A, epoxy is still in low viscosity state allowing the combination with reinforcement. Cross-linking will be largely formed in stage B, and the viscosity increases to a high level. In stage C, external heating is applied, and the curing continues until being fully cured to form the cross-linked 3D-structure. A curing agent is always applied to aid the progress. [22]

2.1.1.4 Prepreg and laminate

Prepreg or pre-impregnated refers to the sheet prepared for immediate use that embeds fibres with pre-defined orientations and volume fractions in a partially cured matrix. The resin in the prepreg has undergone an initial cure to reach the ‘B stage’. The utilization of prepregs offers several advantages over wet lay-up methods: (1) the partially cured resin reduces the risk of hazard of handling liquid resin of the stage A; (2) as the resin is carefully pre-mixed, the strength and stiffness could be optimised; (3) the fibre volume fraction could be controlled, typical ranging between 50 – 70%. Since the epoxy in prepreg has been partially cured, prepregs must be stored in low temperature environment (~ -20℃) and prolonged storage leads to material degradation. Another limitation of prepregs is that their composites are sensitive to delamination, the interlaminar region is more resin-rich and is prone to contaminations and void formation, which might initiate microcracks that can escalate to delamination and structural failure.

Prepreg could be fabricated using unidirectional or woven fibre fabrics. An individual sheet of prepreg is called a lamina and stacking of laminas is known as a laminate. Unidirectional laminates exhibit the highest tensile strength and tensile modulus along the fibre direction. However, the transverse mechanical properties in direction are much weaker. To balance the properties in different orientations, laminas could be laid up in different angels, as shown in Figure 2.4. During the manufacturing, consistent process should be followed using the same prepreg to ensure the materials reproducibility.

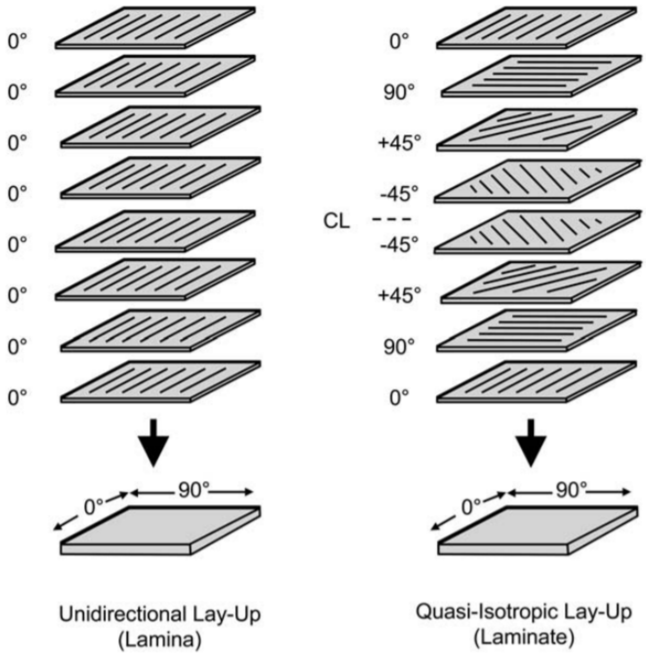

Figure 2.4. Unidirectional and quasi-isotropic stacking of laminates [28]

2.1.2 Composite Failure

The failure of fibre-reinforced composite materials is complex, involving different mechanisms and is largely influenced by both materials' intrinsic properties, such as stiffness, laminates lay out direction and the external loading conditions. The primary damage mechanisms include fibre-matrix debonding, matrix cracking, fibre fracture and delamination:

Fibre-matrix debonding typically happens when the external load is applied perpendicular to the fibre direction. Since the fibre possesses a higher Young's modulus than the matrix, strain magnification would occur between the two phases which leads to debonding. A fractography illustrating debonding is presented in Figure 2.5. Debonding has also been observed in fibres parallel to the loading (mostly under fatigue loading), which initiate from a broken fibre and grows from fracture end, driven by the shear stress [29]. Since the load can only be transferred in bonded materials, debonding results in an increased load on the remaining fibres and reduce the component's stiffness.

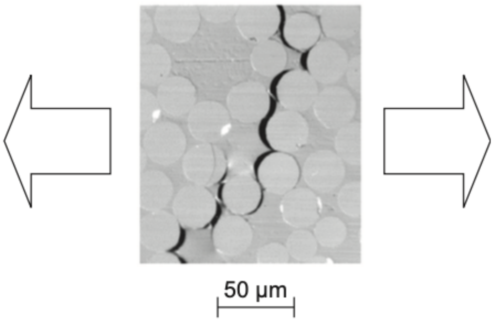

Figure 2.5. Example of fibre-matrix debonding [30]

The matrix fracture in an epoxy typically occurs when the strain reaches about 0.6% under a quasi-static loading condition transverse to the fibres [30]. Following the fibre-matrix debonding, matrix cracking could occur and propagate perpendicular to the loading direction, which further reduce the mechanical properties of materials. The reduction of stiffness is proportional to the matrix crack density [31]. With the degradation of stiffness, the onset of matrix cracking could be characterized in stress-strain curve by nonlinearity. Besides affecting the mechanical properties, matrix fracture also leads to a reduction in the thermal expansion coefficient [32]. Matrix cracks could also propagate parallel to the applied load through splitting, which arises from the mismatch of Poisson ratio between adjacent plies [33]. In addition to reduction of materials properties, matrix cracking also lead to fibre fractures and delamination.

Fibre fracture could be initiated in two ways. Firstly, following the matrix cracking, the stress concentration can lead to local fibre fracture [34]. For instance, in Figure 2.6, accumulation of fibre fractures was observed adjacent to a matrix crack. Secondly, due to the differences in fibre diameter and defects induced during manufacturing, fibres will fail at different applied strain. The isolated fractured fibre then induces a localized stress concentration, leading to accumulation of fibre fractures. Failure of the composite then occurs in two ways: (1) fibre fracture could propagate through the matrix (Figure 2.7), leading to the composite failure or (2) debonding of fibre-matrix due to shear stress, resulting in reduced load transfer and subsequent component fracture [35]. Apart from the negative effects, fibre breaking followed by fibre pull out dissipates energy, which acts as a main toughening mechanism in composite.

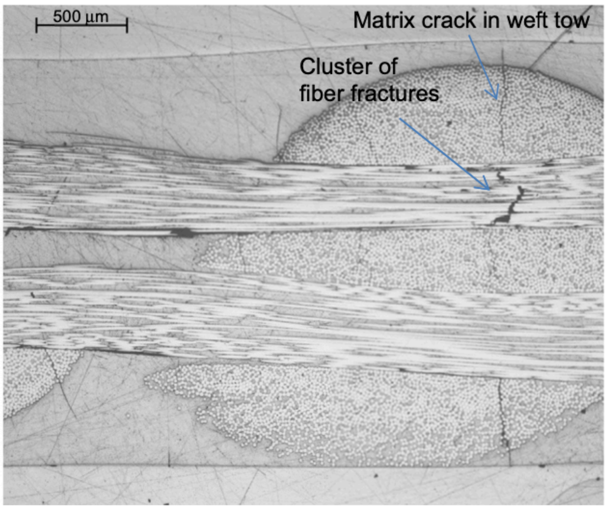

Figure 2.6. Image of fibre fracture following matrix cracking [36]

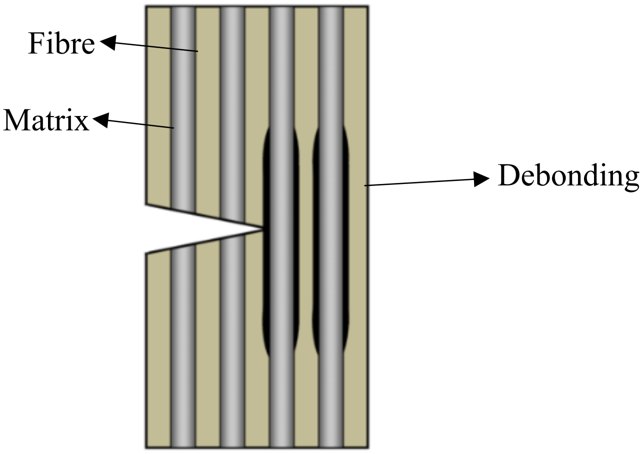

Figure 2.7. Schematic of fibre fracture propagate through matrix [37]

Delamination represents peeling apart of the adjacent plies (Figure 2.8), which can significantly reduce the stiffness and strength of the component. In multidirectional CFRP, delamination initiates from shear stress due to the difference of Poisson's ratio and strength between plies [35]. For CFRP made from prepregs, the existence of resin rich region between plies contribute to delamination propagation. The resin rich region contains little or no reinforcement, creating an energy favourable path for crack growth. The thickness of the resin-rich region also affects the delamination propagation: if the fracture process zone is thicker than the resin-rich area, the neighbouring fibres are constrained, inducing a higher maximum principal stress around the crack tip and producing a longer fracture process zone that advance the delamination rapidly [38]. Delamination begins with microcracks or contamination that is hard to detect, which might develop into separation of component and subsequential catastrophic failure. Debris, contaminations and micropores are easily induced during manufacturing of laminates from prepregs; therefore, delamination is the most critical failure mechanism for composites.

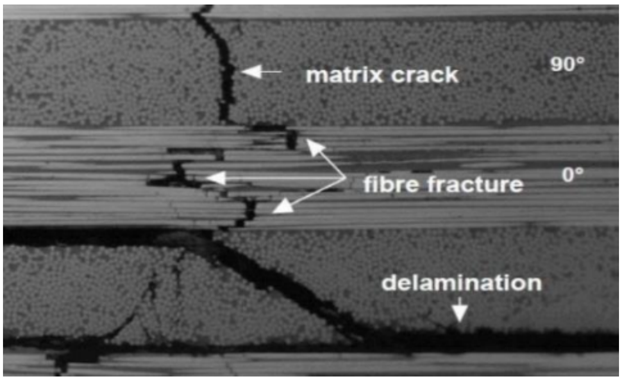

Figure 2.8. Failure mechanism in CFRP [39]

The resistance to delamination in a composite is quantified using the interlaminar fracture toughness. Whether a crack can propagate or not depends on the materials' energy balance. Griffith proposed that, in linear elastic materials, there is an equilibrium between surface energy and elastic energy generated from external load and internal strain. When the material's global energy exceeds the energy that required to create new surface, crack propagation would continue [40]. Griffith's damage criteria was successfully applied in perfectly brittle materials, however, for materials such as alloys that exhibit plasticity, his approach significantly underestimates the fracture strength.

Irwin and Orowan extended Griffith's theory to account for plasticity. Irwin concluded that under plastic deformation, a plastic zone would develop in the vicinity of crack tip, dissipating energy so the total fracture energy is the sum of surface energy and the dissipated energy [41]. The strain energy release rate (G) was then proposed as the total energy available for crack propagation per unit area [41]. For elastic-plastic materials, the energy release rate represents the energy released with increment of crack plus energy absorbed by plastic deformation. The critical strain energy release rate (Gc) could be defined as the energy required for crack extension, which is a quantification of material's fracture toughness regardless of geometry and loading conditions.

In linear elastic materials, the stress field near the crack tip is proportional to $1/\sqrt{r}$, where r is the distance from the crack tip. Its magnitude is quantified by the stress intensity factor (SIF), K, which considers the sample geometry, size and location of crack as well as the external load [42, 43]. The critical value of stress intensity factor is Kc. As shown in Figure 2.9, for a crack subjected to any arbitrary loading, the load type could be resolved into three categories of mode: Mode I is opening mode where crack is perpendicular to the crack plane and opens the crack with tensile stress, Mode II is the in-plane shear where the crack planes slide over each other and Mode III is out-of-plane shear mode where the crack surfaces move opposite to one another parallel to edge of the crack [44]. Each loading mode has a corresponding K value: K_I, K_{II} and K_{III}. In linear elastic materials, SIF K is directly linked with strain energy release rate as:

$$G = \frac{{K_I}^2}{E'} + \frac{{K_{II}}^2}{E'} + \frac{{K_I}^2}{2\mu} \quad (2.1) \ [45]$$

where $E' = E$ for plane stress and $E' = E / (1-\nu^2)$ for plane strain, μ is the shear modulus and ν stands for the Poisson ratio. Both Gc and Kc could describe the fracture toughness.

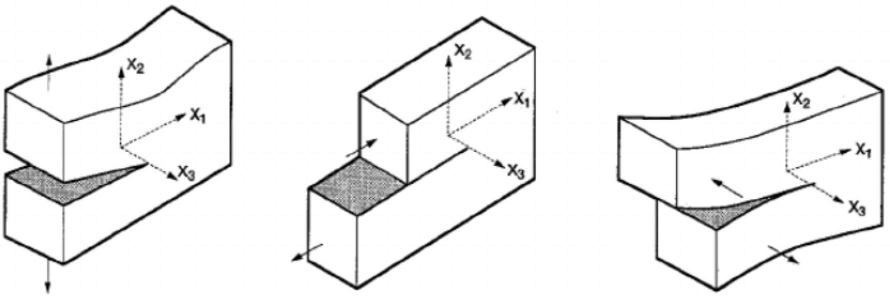

Figure 2.9. Three modes of loading: mode I, mode II and mode III respectively [46]

The J-integral is utilized to quantify the strain energy release rate for both linear elastic and elastic-plastic materials. It was independently developed by Rice and Cherenkov [40, 47]. As shown in Figure 2.10, the J-integral is a path-independent contour integral encircling the crack tip, with its value equating to the strain energy release rate. For a close contour that encompasses no crack, the J-integral value is zero [48]. The standard formulation of J, excluding the body force and kinetic energy is expressed in equation 2.2:

$$J = \int_{\Gamma} (W dy - T_i \frac{\partial u_i}{\partial x} ds) \quad (2.2)$$

where Γ is the contour, W represents the strain energy density, T is the traction vector defined as $T_i = \sigma_{ij} n_i$, σ_{ij} is the stress tensor, n_i is normal to the contour path, and u_i is the displacement vector components.

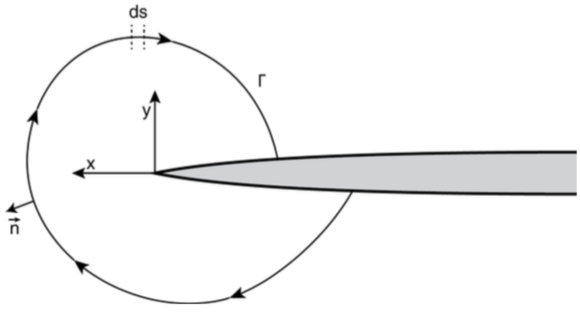

Figure 2.10. Example of J-integral enclose the crack tip [49]

Compared with strain energy release rate, J-integral stands out for its versatility that accounts for a broader range of materials behaviour, including yielding and plastic deformation [50]. And in linear elastic materials, J is equal to G, the critical value of J represents the fracture toughness. The contour independence of J makes it robust to crack tip position uncertainty and this feature is particularly advantageous in numerical methods like finite element (FEM) analysis where the path can be selected in a way that avoids mesh irregularities and distortion. The intrinsic properties of the J-integral make it suitable for finite element analysis [51]. FEM is a numerical method that address mathematical engineering problem by discretizing the domains, imposing boundary conditions, and implementing physical laws to elements interconnected by the boundary nodes within the complex geometry. Essentially, FEM solves partial differential equation by reducing it to linear algebra to find the approximate solutions to boundary value problems [52]. The adaptability allows the J-integral to be segmented into different modes of stress intensity factors for either 2D or 3D configurations. The J-integral is a widely used approach for crack quantification. Becker et al. developed the JMAN framework to compute the J-integral using full field displacement data obtained from DIC [53, 54]. Barhli refined the methodology and achieved a more precise calculation of J-integral with an error below 7% [49]. The approach for determining the strain energy release rate by J-integral in finite element analysis using the strain/displacement field has expanded to measurements from DIC, DVC and diffraction techniques [55-57].

2.1.3 Toughening

Given that delamination represents the principal failure mechanism constraining the applications of CFRP, it is of great significant to enhance the resistance to crack propagation within the interlaminar region. Delamination resistance could be enhanced by improving the matrix toughness or deflecting crack paths to increase the work of fracture. The predominant toughening strategies could be classified into three groups: particle toughening, interleaving and stitching.

Particle toughening typically involves mixing matrix with polymer particles or inorganic nanoparticles such as silica to increase the fracture toughness of matrix. For example, Chikhi et al. have demonstrated that by adding 11 wt.% amine-terminated butadiene acrylonitrile (ATBN) into the epoxy can elevate fracture toughness by 50% [58]. The addition of rubber particles however diminishes the modulus of epoxy [58], and the toughening is predominately restricted to epoxy with a low degree of cross-linking [59]. Other researchers also found integration of thermoplastic particles or inorganic nanoparticles could also enhance the fracture toughness of epoxy. For instance, Pearson and Yee reported a 63% increase in work of fracture with the addition of 17 wt.% poly(phenylene oxide) (PPO) as a toughening agent [60]. The major mechanisms of particle toughening have been discussed are: (1) plastic deformation of particles; (2) plastic deformation of matrix in the vicinity of particles; (3) crack deflection by particles; (4) reducing of matrix cross-link density that decrease the brittleness and (5) pinning of crack by the particles [61, 62]. The applications of particle toughening however, always accompanies with compromises in other mechanical properties such as reduction of modulus or shear strength [63]. Furthermore, the addition of thermoplastic particles in epoxy increases the viscosity of blends that complicate the manufacturing process.

As the crack tends to propagate along the interface of plies in CFRP fabricated from prepregs, the toughening method by inserting interlayers between the laminate plies was investigated (Figure 2.11). Arai et al. introduced carbon nanofibers interleaves into CFRP laminates, achieving a 50% increase in Mode I interlaminar fracture toughness [64]. Interleave materials, which typically exhibit high shear strength and toughness, serve to arrest crack between the laminates. Typical materials for interleaves include Nylon 6,6, epoxy and carbon nanofibers [65]. The primary drawback of incorporating interleaves is the associated increment of weight and thickness of composite, which would change the component structure. Additionally, a potential reduction in interlaminar shear strength and stiffness is a significant factor that must be carefully evaluated [20, 66].

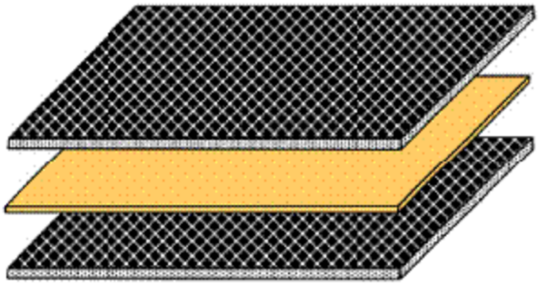

Figure 2.11. interleaving toughening in CFRP [67]

Stitching stands out as the method providing the most significant enhancement to interfacial fracture toughness in CFRP. This technique involves sewing the laminates using high stiffness and strength materials. A schematic illustration of stitching in CFRP is presented in Figure 2.12. Dransfield et al. reported that the fracture toughness of CFRP could be 15 times higher with stitching [68]. The most discussed toughening mechanism attributed by stitching include: (1) failure and subsequent pull out of stitching materials; (2) stitching debonding and (3) suppression of crack propagation by elastic deformation of stitching materials [68]. However, the efficacy of stitching as a toughening method is contingent upon various parameters, including the choice of stitching materials, the stitching density, and the type of loading applied, which complicates its adoption in commercial manufacturing practices [69]. Moreover, the introduction of stitching can lead to stress concentrations at the stitching point, which may adversely impact the in-plane properties of the composite.[70]

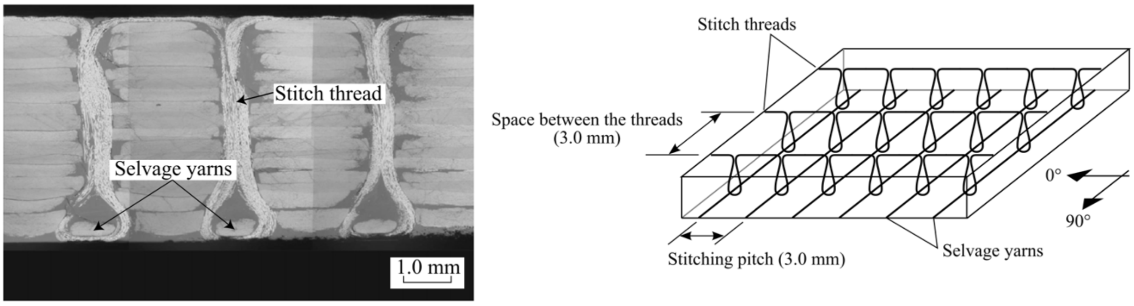

(a) Cross section of the laminate along a stitch thread

(b) Scehmatic of stitch pattern

Figure 2.12. Toughening by stitching in CFRP [71]

2.2 Inkjet printing on CFRP

2.2.1 Inkjet printing technique

Inkjet printing is a non-contact additive manufacturing technology that directly deposit the desired amount of liquid phase materials (ink) and boasts broad applicability across various domains [72]. It enables the selective printing of picolitre volume deposits, as predetermined by computer to construct 2D or 3D structures on diverse substrates. Inkjet printing possesses some distinct advantages which makes it an attractive technique: (1) Inkjet printing eliminates the need of masks, simplifying the manufacturing process and cutting the cost; (2) being a non-contact manufacturing technique, inkjet printing significantly reduces the risk of contaminations in the final product; (3) its flexibility allows for operation with both single and multiple ink systems and imposes no limitations regarding substrate types. [20]

Inkjet printing can be categorized into two groups: continuous inkjet printing (CIJ) and drop on demand inkjet printing (DOD) [73]. As shown in Figure 2.13, in CIJ, a continuous stream of electrically charged inks are expelled. Under an electrostatic or magnetic field, the droplets are directed to print the predefined pattern, while the unwanted droplets are received by the recycling gutter [74]. This method is favoured commercially due to its rapid deposition rate, although its use is somewhat limited by the potential contamination of recycled inks and the electrical conductivity requirements of the printing materials. DOD inkjet printing produces ink deposits only as needed, which minimizes the materials wastage and prevent the ink contamination from recycling [75]. A schematic of the DOD working principle is presented in Figure 2.14. The most commonly used DOD inkjet printing methods are thermal DOD inkjet printing and piezoelectric DOD inkjet printing [73]. The former ejects droplets by heating a resistive element in the ink chamber to evaporate the ink and create a bubble to force the ink out. This limits the use of fluids as the ink needs to endure ultra-high temperature while also be vaporizable. Piezoelectric printing generates deposits by piezo-ceramic distortion manipulated by an applied electric field. As shown in Figure 2.15, the process encompasses five stages: rise, dwell, fall, echo and final rise, the voltage and duration will affect the size of droplets, which need to be carefully tuned.

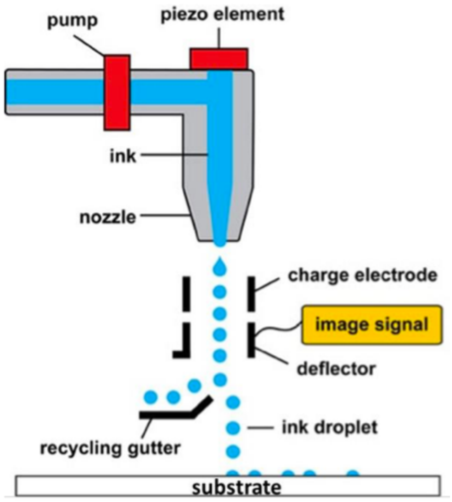

Figure 2.13. Continuous inkjet printing [20]

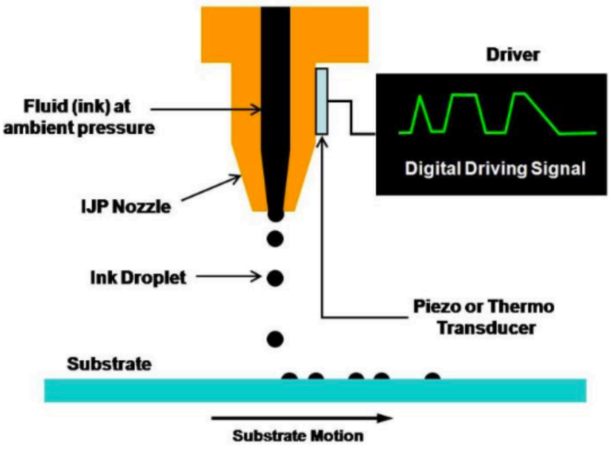

Figure 2.14. Drop on demand inkjet printing [76]

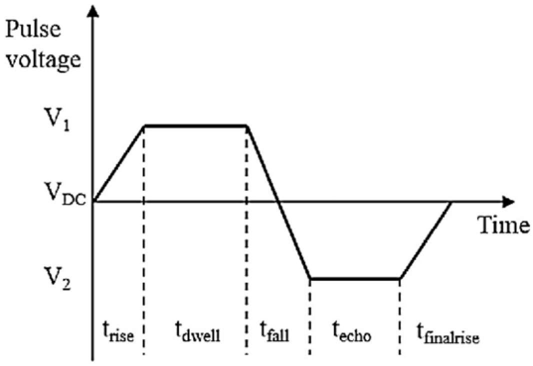

Figure 2.15. Typical pulse waveform to generate deposit in DOD printer [77]

Surface tension and viscosity are the major factors to determine the solution's suitability for inkjet printing [78, 79]. The surface tension controls the morphology of droplets, and it has been reported that inks with surface tension in the range of 28 mN m^{-1} to 350 mN m^{-1} are suitable for printing [80], where the ink tend to form a stable spherical shape to minimize the surface energy. Inks with high viscosity would hinder the printing, with 20 mPa·m identified as the upper viscosity limit for inkjet printing [81]. The Ohnesorge number (Oh), measures the ratio of viscosity to surface tension and is commonly employed to evaluate the printability [82, 83]:

$$\mathrm{Oh} = \frac{\eta}{\sqrt{\rho d \sigma}} \qquad (2.3)$$

In the above equation, η represents the solution viscosity, ρ is the ink density, d stands for the diameter of orifice and σ is the surface tension of the ink. The reciprocal of Oh, denoted as Z is also popular used for printability assessment [82]. Some studies suggest ink within $1 < Z < 10$ is suitable for printing [84], while others demonstrated inks with Z outside this region are still viable for printing [85]. This is mainly because the measured Z is not the same as the Z of ink while printing: when the ink is printed from the nozzle, its Z value can differ due to the shear forces acting on the polymer chains, leading to the chains rearrangement and altering the ink's viscosity. The printability has been proved by our partner in University of Sheffield [20].

Inkjet printing's versatility and cost-efficiency have spurred its widespread adoption across various sectors. Inkjet printing has been increasing applied in scaffolds manufacturing owning the ability to print 3d structure in a single procedure and deposit cells and scaffold at the same time [86]. For example, Cui used thermal DOD to print fibrin scaffolds, and the porous structure is conductive to cell attachment and proliferation [87]. Inkjet printing's application also extends to bio-ceramics that emulate natural bone, utilizing materials that are non-toxic, biocompatible, and exhibit osteoconductive properties [88]. In electronic domain, inkjet printing of polymers is widely used to make polymer light-emitting diode (PLED) displays. For instance, Yang used a semiconducting aqueous polymer poly(3,4-ethylenedioxythiophene) (PEDOT) to fabricate PLED [89]. Moreover, inkjet printing has also been adapted to deposit nanoparticles or nanotubes, with piezoelectric DOD inkjet printing being utilized to place silver nanoparticles, achieving conductivity levels up to 23% of bulk silver, indicating its potential in integrated electronic components [90].

Despite the advantages that inkjet printing brings, it is also necessary to consider its limitation. The necessity for inks to meet specific viscosity and surface tension criteria restricts the range of suitable materials, while the printing resolution, influenced by factors like the post-printing drying process, typically spans several tens of microns, presenting a challenge for applications requiring finer detail. [91]

2.2.2 Inkjet printing modified CFRP

Previous studies have demonstrated that thermoplastic polymers can enhance the toughness of Carbon Fibre Reinforced Polymers by integrating thermoplastic particles within the matrix as a particle toughening or by inserting polymer interleaves between laminates [92]. However, these methods often result in compromised mechanical properties, such as reduced interlaminar shear strength. The propensity for delamination at the laminate interfaces suggests that using inkjet printing to deposit toughening droplets on the target situation could optimize the toughening efficiency, minimizing weight increase and mechanical property degradation.

Previous research from Sheffield University has demonstrated the toughening effect of PMMA in multi-layer CFRP, and the main reasons for choosing PMMA as the printing material are as follows: (1) PMMA tends to form discrete particles in the hardened epoxy after curing, which might be able to act as the filter to toughen the resin [93]; (2) PMMA exhibits similar melting point with the CYCOM® 977-2 resin, enabling the toughing effect of PMMA in CFRP at relatively high temperature; (3) the low water absorption property of PMMA is crucial for the practical application. [20]

A wide range of molecular weight of PEG is available commercially and the degree of crystallization increase as the raise of molecular chain length. PEG shows good miscibility with epoxy, and it has been found that the additional of small amount of PEG would increase the toughness of epoxy resin by plasticisation [94]. Therefore, PEG was selected as another dropping material in this work. Comparing with Carfagna et al., who mixed the PEG with epoxy to enhance the fracture resistance, by printing the toughening material on the specimen, the region being enhanced is more targeted, which result in much less weight penalty and eliminating the negative effect on other mechanical properties with the added polymer.

Using inkjet printing to deposit thermoplastic particles purposefully to enhance the work of fracture was initially proposed by Smith and Zhang [20]. Zhang experimented with various concentrations, printing patterns, pulse settings of PMMA and PEG, and achieved up to 40% increment of G_{Ic} in 12-ply CFRP, Figure 2.16 shows the dots on the prepreg with fluorescein to aid the visualization. Under SEM characterization, separated particles were observed in the PMMA-printed fracture plane (Figure 2.17). Cartledge reported that inkjet printing PMMA and PEG also enhanced the tensile strength of CFRP [35]. Chechik and Zhang conducted the first in-situ observation for the printed specimens under x-ray computed tomography (XCT) and validated the use of digital volume correlation (DVC) to study the crack propagation for the two-ply laminates [95, 96]. Lim demonstrated a stable enhancement of fracture toughness with different printing patterns and found the choice of pattern however does not make any difference to the enhancement. It has also been observed that the PMMA printed specimen possesses a rougher fracture surface, however there is no pattern in the toughness that corresponding to the printing design. Under in-situ XCT, it has also been observed that PMMA influence the crack growth ductility: cracks propagated by simple cleavage post printing while voids and necking were observed in the pristine specimen (Figure 2.18) [97]. The toughening mechanism of inkjet printing however remains unsure. This project aims to conduct advanced in-situ characterizations for crack propagation observation, optimizing the image quality by removing fringe artifacts and obtaining better resolution to get more information of the internal structure, which would contribute to better understanding in the role of inkjet printing droplets in CFRP.

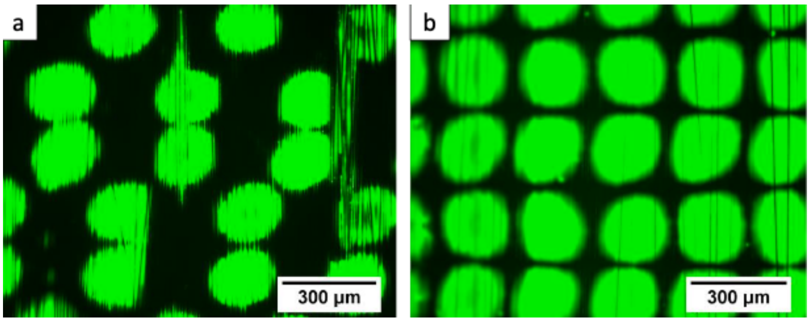

Figure 2.16. Inkjet printing deposits with fluorescein on CFRP in **(a)** hexagonal and **(b)** square pattern [20]

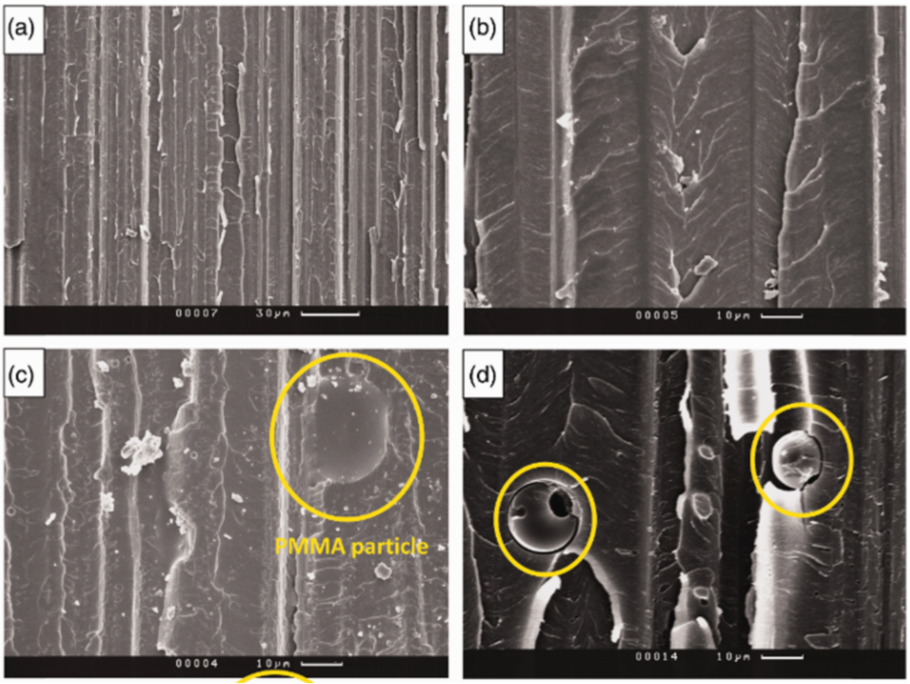

Figure 2.17. Fracture surface of DCB tested laminates **(a)** and **(b)** without printing; **(c)** and **(d)** with PMMA printing [98]

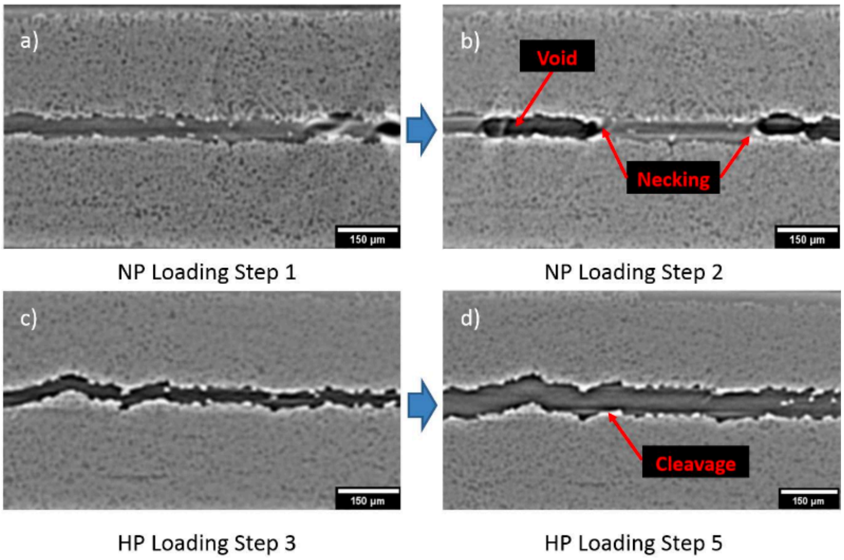

Figure 2.18. Cross section X-ray image of fractured specimen showing a more ductile crack growth in **(a,b)** non-printed specimen compared to **(c,d)** PMMA printed CFRP [97]

2.3 In-situ characterization for crack propagation

2.3.1 X ray computed tomography

X-ray was initially discovered by Wilhelm in 1895, and the first X-ray computed tomography (XCT), which revolutionized clinical diagnostics, was invented by Godfrey in clinical diagnosis. Since its inception, XCT has been successfully developed and applied in the medical field. Thanks to the rapid development of high-performance computer and software tools for reconstruction, visualization of 3d dataset and date processing, XCT's application has been expand to diverse sectors such as energy, aerospace, and automotive industries [99].

XCT is a non-destructive technique that allows the 3d visualization of an object without restriction on materials properties. The core components of an XCT system includes a radiation source, a sample holder, and a signal detection system. In a lab based standard XCT, X-rays are produced in a vacuum tube where electrons are accelerated from a cathode to an anode under a typical acceleration voltage of up to 450 kV [99]. The acceleration results in collisions at the anode, generating an X-ray spectrum. Ideal anode materials, such as tungsten, molybdenum, or copper, have high melting points and produce a convenient X-ray energy spectrum.

The interaction of X-ray photons with materials includes absorption and scattering, quantitatively described by Lambert-Beer's law [100]:

$$I = I_0 e^{-\int \mu(s)ds} \quad (2.4)$$

Here, I_0 and I denote the incident and transmitted intensities of X ray respectively, $\mu(s)$ represents the liner absorption coefficient at specific position. The X-ray mass attenuation coefficients (μ/ρ) for various elements are well-documented by NIST [101]. The attenuation increases significantly with decreasing applied energy, as X-rays with low energy are easier to be absorbed and attenuated by the component. Figure 2.19 shows the variation of attenuation coefficient of carbon element at different voltages. Components with higher attenuation coefficient result in lower outgoing X-ray intensity, appearing as brighter region in the image [102].

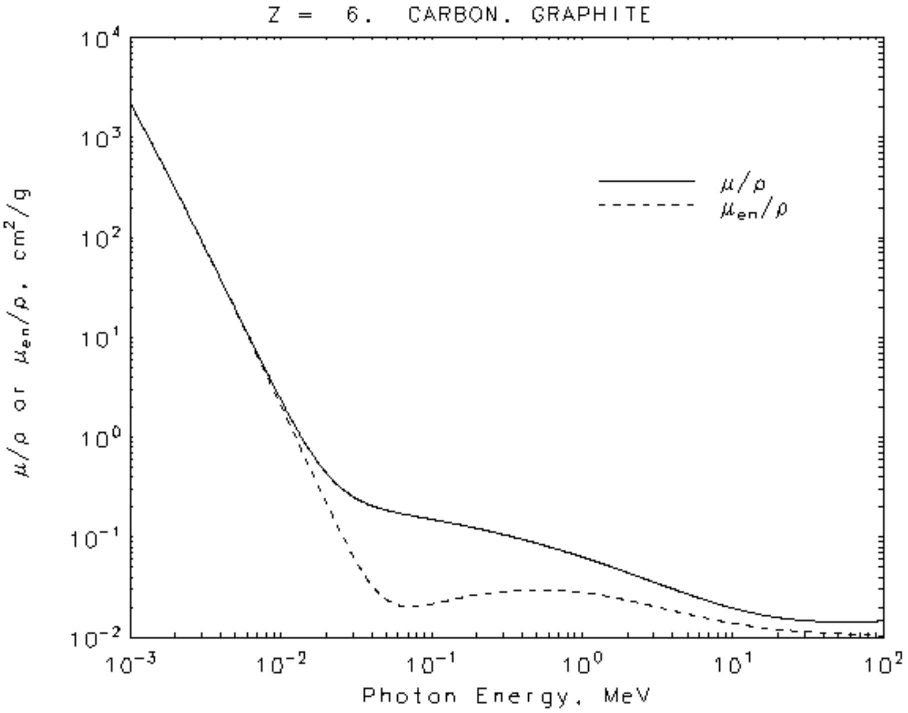

Figure 2.19. X-ray mass attenuation coefficients for carbon [101]

The detector captures the emergent X-rays, converting the photon flux into electrical signals to produce 2D radiographs. The object undergoes a step-by-step scan, encompassing a full rotation of 180° or 360°. Reconstruction algorithms then process the projected sinograms to create 3D volumetric data. In laboratory XCT, the Feldkamp-Davis-Kress (FDK) algorithm is commonly employed [103]. This algorithm filters the weighted projection data on X-ray and back projections into the reconstruction space. In the resulting 3D dataset, each volumetric element, or voxel, has a grey scale value that correlates to the specific attenuation at that position.

Laboratory-based XCT typically employs cone beam geometry, as demonstrated in Figure 2.20. In this setup, a cone-shaped beam of X-rays is emitted from the source, passing through the specimen, and then been captured by the detector. A magnification is introduced in the cone beam geometry, that is quantified by the ratio of source-detector distance (SDD) to source-object distance (SOD):

$$m = \frac{\mathrm{SDD}}{\mathrm{SOD}} \quad (2.5)$$

Reducing the SOD could improve the resolution and magnification, but the field of view will be narrowed also.

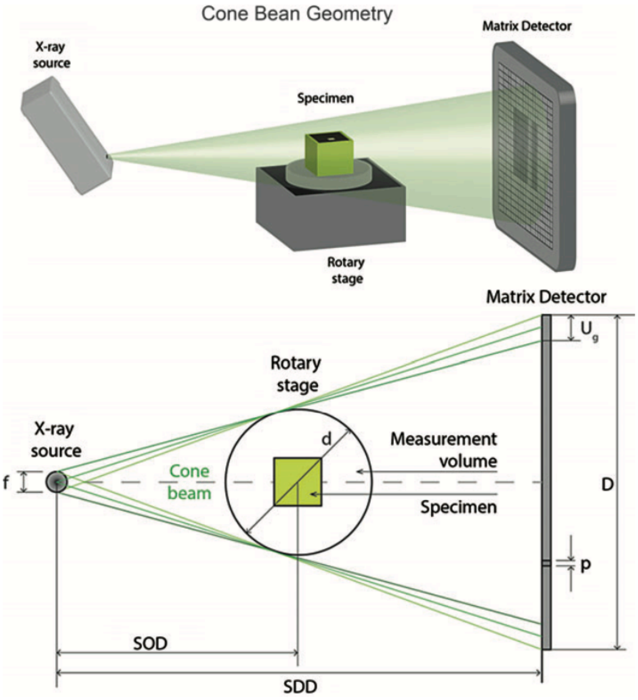

Figure 2.20. Schematic of cone beam geometry [99]

The incident X-ray could also be generated in a synchrotron light source, which typically employ parallel beam geometry as shown in Figure 2.21. Compared with laboratory X-ray source, synchrotron radiation offers several significant advantages: (1) Synchrotron radiation generate high flux X-ray which is at least 1000 times brighter than the lab-based sources. This enables fast, time-resolved studies which contributes to in-situ and in-operando characterization; [104, 105] (2) The X-ray generated in a synchrotron could be highly coherent, allowing for the use of phase contrast imaging. This method significantly improves the visualization of phase interfaces, achieving a level of resolution unattainable with standard attenuation contrast in materials of similar attenuation (discussed further below). The availability of monochromatic radiation also mitigates the problem of beam hardening, enhancing the quality of the resultant images; (3) Synchrotron XCT can be integrated with diffraction techniques on specific beamlines, enabling a comprehensive analysis that links the 3d structural information of materials with their crystallographic characteristics. This integration offers a unique opportunity to simultaneously investigate the materials' elastic and overall deformation, providing a multifaceted view of the object under study. [99]

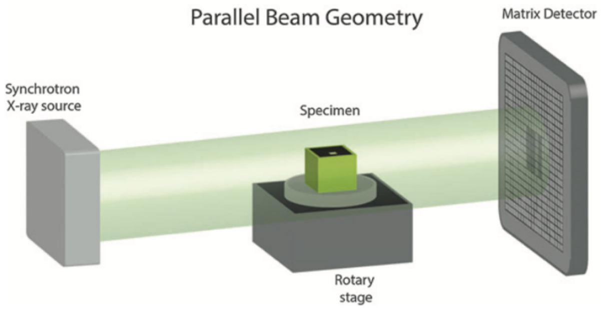

Figure 2.21. Parallel beam geometry in synchrotron sources [99]

In conventional XCT, contrast is primarily derived from the X-ray absorption by the specimen. However, variations in the specimen's density and thickness not only affect the intensity of the transmitted X-rays but also alter their phase where phase contrast could be introduced. This is quantified as equation 2.6 [99]:

$$n = 1 - \delta + i\beta \quad (2.6)$$

Here, n is the complex X-ray refractive index, which is determined by refraction index (δ) and absorption index (β) together. Both δ and β depend on the object composition and the X-ray energy. For lightweight material where the density is around or below than 1 g/cm^3, δ/β becomes significant making propagational-based phase contrast pronounced. The phase shift leads to a change in the X-ray trajectory, which is shown as upward and downward overshooting of grey values on the edge of specimen to enhance the image contrast. Phase contrast is normally applied with monochromatic beam by increasing the sample to detector distance to enlarge the edge effect. It has also been reported that phase contrast could be achieved in polychromatic radiation source when the focal spot size is below 1μm and the distance between object and detector is large enough [106]. As shown in Figure 2.22, this propagation-based phase contrast is significantly useful to increase the visibility for low-absorption materials. There are also other phase contrast enhancement methodologies such as Talbot-Lau grating interferometer XCT, crystal interferometer XCT, analyser-based imaging and edge illumination [107, 108].

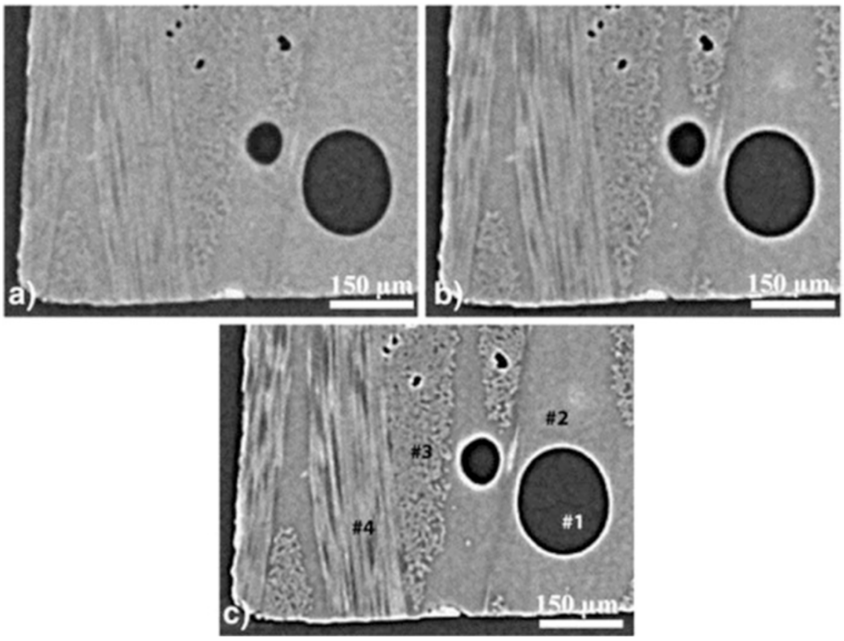

Figure 2.22. Cross section XCT on CFRP showing phase contrast enhancement as the sample-detector distance increase from **(a)** 189mm, **(b)** 283.5 mm to **(c)** 486.25 mm [106]

A major challenge of XCT is the artifacts. Artifacts are artificial features in the XCT image that do not represent the real structure of object or arise from noise and these can affect the interpretation and dimensional accuracy. In cone beam geometry, beam hardening (also known as cupping effect) is a typical artifact. Under a board-band energy spectrum X-ray, the soft beams are easier to be absorbed than the high energy rays, resulting in hardening of the radiation as it penetrates through the specimens [109]. Beam hardening can be mitigated by using an attenuation filter to remove the low energy rays or could be completely avoid with monochromatic X-ray in synchrotron light source [110]. The commonly observed ring artifact is introduced because of the irregularities of neighbouring pixels on the detector. It appears as concentric ring on the images and one effective correction way is applying a random horizontal movement on the detector [111]. In phase contrast XCT, the refracted X-ray might alter the wavefront and produce features such as bright fringes on the edges that does not present in the object. This is so called phase contrast artifact and could be mitigated by reducing the sample detector distance or employing sophisticated phase retrieval algorithms [112].

As a non-destructive characterization method, XCT presents a superior capability to detect micro-features inside the object such as microcracks, pores and material structure. This is suitable for fracture study in composite materials, where defects that initiate from internal with micro scale are hard to detect but can lead to catastrophic failure. Therefore, it has been widely applied for mechanical damage studies, microstructure observation and image-based modelling [113]. Ex-situ XCT is more accessible and has been successfully used for capturing of complex internal structure as well as studying the fatigue damage development in composite. However, crack closure and observation on dynamic mechanical behaviour are the major issues. Using intense X-rays, in-situ XCT offers time-lapse imaging, providing a powerful way for dynamic analysis of damage propagation in composites such as impact [114] and fibre kinking [115]. In this study, various XCT techniques were employed to refine image quality for CFRP. The 3D datasets were then analysed qualitatively and quantitatively to elucidate the effects of inkjet printing on damage propagation within both printed and non-printed laminates, offering a deeper understanding of the mechanism involved.

2.3.2 Digital volume correlation

Following in-situ XCT characterization, 3d volumetric images are obtained and digital volume correlation (DVC) is employed as an effective solution for quantification analysis that map the full-field displacement and strain field.

Figure 2.23 illustrates the operation principle of local DVC, which includes three main stages: Initially, the 3D image is divided into defined smaller subvolumes so called ‘correlation. Subsequently, the cross correlation algorithm computes the translation, rotation and deformation that best matches these subvolumes in their reference (undeformed) and subsequent deformed states. For each subvolume, a displacement vector is determined by determining the shift in position between the images, effectively tracking the movement of each subvoxel. Finally, the strain field is derived using a differentiation approach to the displacement field. [116, 117]

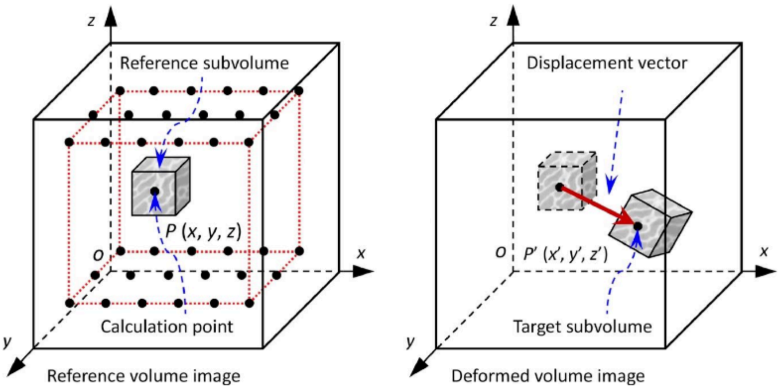

Figure 2.23. Working principle of local DVC showing displacement vector for sub volume P in the reference and deformed stage [118]

Image volume pattern is usually an array of voxel intensities, and to find the correct shift vector, the pattern in the undeformed stage would be moved around until the best matches is achieved in the deformed image. Correlation coefficient (C) mathematically quantifies the quality of the match. In real images, there is always an intensity difference between deformed and reference image, which is so called illumination difference. In local DVC, for example DaVis, normalized correlation (C_{norm}) is applied to describe the degree of match that is robust to the illumination changes which resolves the issue:

$$C_{norm}(dx, dy, dz) = \sum_{(i,j,k)} \frac{(A_{i,j,k} - <A>)(B_{i+dx,j+dy,k+dz} - <B_{dx,dy,dz}>)}{\sqrt{|A'|^2}\sqrt{|B'_{dx,dy,dz}|^2}} \quad (2.7)$$

Here, A and B represent the reference and deformed images respectively. $< A >$ and $< B >$ are images' arithmetic means. dx, dy and dz are the current shift in the three directions [119]. The correlation coefficient defines the level of matching for subvolumes in the deformed stage, with value of 1 signifying perfect correlation. The shift of a subset is represented by the displacement vector at the centre of the element (red arrow).

The choice of subvolume size determines the DVC calculation precision. Smaller subvolumes can theoretically enhance spatial resolution, yet they may also increase noise due to the reduced amount of information they contain. Conversely, excessively large subvolumes might diminish resolution without significantly reducing noise. Therefore, selecting an optimal subvolume size is crucial for effective DVC analysis. [120]

Enhancing spatial resolution of the displacement field can be achieved through strategies such as overlapping subvolumes to increase the density of the displacement vectors. For example, with a 75% overlap, the number of vectors along one axis is quadrupled [121]. Another strategy to optimize the resolution is adopting multi-pass analysis. This involves using the displacement field from a larger initial subset size to inform the subsequent pass with smaller subset. It repeats for several passes to reach the final pass, with displacement field being refined every step to provide a good spatial resolution while also minimize the noise [122].

The discontinuity of displacement showing as high localized strain from the presence of damage is difficult to compute in DVC. This usually been observed near the crack surface or shear bond, showing poor correlation in areas near these features. An effective strategy to solve it is by applying a mask to exclude the region from DVC calculation [123].

2.4 Summary and thesis objective

Carbon fibre reinforced polymer composites are increasingly demanded in industry such as aerospace, wind energy and automotive owning to its exceptional strength to weight ratio and corrosion resistance. A critical challenge in CFRP applications is interlaminar delamination, often initiated by hard-to-detect internal microcracks, which can lead to catastrophic failure. The resistance to delamination is described by fracture toughness, which could be quantified by strain energy release rate (G) or J-integral. Efforts to improve fracture toughness have included various methods like particle toughening, the insertion of interleaves, and stitching, but these often come with trade-offs such as increased weight or diminished other mechanical properties. Inkjet printing with thermoplastic polymers such as PMMA and PEG has been proved could improve the fracture toughness with little compromising of other properties. The mechanism behind it however remains uncertain.

This project aims to conduct a series of in-situ and ex-situ characterizations to examine the fracture behaviour in both printed and non-printed specimens, which will help with the interpretation of the inkjet droplets' behaviour in CFRP. Toughening of CFRP using inkjet printing shows some significant advantages over other strategies, which offering benefits such as low weight penalty and minimal impact on other mechanical properties. However, the primary limitation lies in the extent of the toughening effect. Understanding the mechanism behind the toughening would help with the choice of optimum printing materials and settings to maximize the fracture energy enhancement, making this research highly significant.

2.5 References

[1.] Zhang J, Lin G, Vaidya U, Wang H. Past, present and future prospective of global carbon fibre composite developments and applications. Composites Part B: Engineering. 2023;250:110463.

[2.] Matthews FL, editor. Composite Materials: Composites Science and Engineering. F.L. Matthews1999.

[3.] Kangishwar S, Radhika N, Sheik AA, Chavali A, Hariharan S. A comprehensive review on polymer matrix composites: material selection, fabrication, and application. Polymer Bulletin. 2023;80(1):47-87.

[4.] Karandikar HM MF. Tailoring Composite Materials Through Optimal Selection of Their Constituents. Journal of Mechanical Design. 1992.

[5.] Sicot O GX, Cherouat A, Lu J. Determination of Residual Stress in Composite Laminates Using the Incremental Hole-drilling Method. Journal of Composite Materials. 2003;37(9):831-44.

[6.] Glover B. History of development of commercial aircraft and 7E7 dreamliner. Aviat eng. 2004;592:16-21.

[7.] Michno LPaM. High Performance Fibers," in Advanced Composite Materials. Heidelberg SB, editor1994.

[8.] Kamarudin KA, Abdul Hamid I. Effect of High Velocity Ballistic Impact on Pretensioned Carbon Fibre Reinforced Plastic (CFRP) Plates. IOP Conference Series: Materials Science and Engineering. 2017;165(1):012005.

[9.] Zhao L, Gong Y, Qin T, Mehmood S, Zhang J. Failure prediction of out-of-plane woven composite joints using cohesive element. Composite Structures. 2013;106:407-16.

[10.] Thomason JL. The interface region in glass fibre-reinforced epoxy resin composites: 1. Sample preparation, void content and interfacial strength. Composites. 1995;26(7):467-75.

[11.] George J, Sreekala MS, Thomas S. A review on interface modification and characterization of natural fiber reinforced plastic composites. Polymer Engineering & Science. 2001;41(9):1471-85.

[12.] Dorey G, Sidey GR, Hutchings J. Impact properties of carbon fibre/Kevlar 49 fibre hydrid composites. Composites. 1978;9(1):25-32.

[13.] Mallick PK. Fibre-Reinforced Composites: Materials, Manufacturing, and Design: CRC Press; 2007.

[14.] Loos M. Chapter 2 - Composites. In: Loos M, editor. Carbon Nanotube Reinforced Composites. Oxford: William Andrew Publishing; 2015. p. 37-72.

[15.] Mouritz AP, Baini C, Herszberg I. Mode I interlaminar fracture toughness properties of advanced textile fibreglass composites. Composites Part A: Applied Science and Manufacturing. 1999;30(7):859-70.

[16.] Yeung CM, Bhashyam AR, Patel SS, Ortiz-Cruz E, Lozano-Calderón SA. Carbon Fiber Implants in Orthopaedic Oncology. J Clin Med. 2022;11(17).

[17.] Endo M. High-Performance and Specialty Fibers2016.

[18.] D.Hull, T.W.Clyne. An introduction to composite materials. Cambridge University Press, editor 1996.

[19.] Soutis C. Fibre reinforced composites in aircraft construction. Progress in Aerospace Sciences. 2005;41(2):143-51.

[20.] Zhang Y. The effect of inkjet printed polymer on the mechanical properties of carbon fibre reinforced plastic: University of Sheffield; 2015.

[21.] Bledzki AK, Gassan J. Composites reinforced with cellulose based fibres. Progress in Polymer Science. 1999;24(2):221-74.

[22.] Strong AB. Fundamentals of composites manufacturing : materials, methods and applications. Dearborn, Mich.: Society of Manufacturing Engineers Dearborn, Mich.; 2008. Available from: https://search.ebscohost.com/login.aspx?direct=true&scope=site&db=nlebk&db=nlabk&AN=882330.

[23.] Ian Smith EL MG. Fracture and Fatigue in Wood. WILEY, editor2003.

[24.] Islam MS, Shahruzzaman M, Khan MN, Islam MM, Kabir SF, Mallik AK, et al. 1 - Composite materials: Concept, recent advancements, and applications. In: Haider S, Haider A, editors. Renewable Polymers and Polymer-Metal Oxide Composites: Elsevier; 2022. p. 1-43.

[25.] Van den Oever M, Peijs T. Continuous-glass-fibre-reinforced polypropylene composites II. Influence of maleic-anhydride modified polypropylene on fatigue behaviour. Composites Part A: Applied Science and Manufacturing. 1998;29(3):227-39.

[26.] Mallick PK. 5 - Thermoplastics and thermoplastic–matrix composites for lightweight automotive structures. In: Mallick PK, editor. Materials, Design and Manufacturing for Lightweight Vehicles: Woodhead Publishing; 2010. p. 174-207.

[27.] Matthews FL, Rawlings RD. 5 - Polymer matrix composites. In: Matthews FL, Rawlings RD, editors. Composite Materials: Woodhead Publishing; 1999. p. 168-205.

[28.] FC C. Structural Composite Materials. International A, editor2010.

[29.] Pupurs A, Goutianos S, Brondsted P, Varna J. Interface debond crack growth in tension–tension cyclic loading of single fiber polymer composites. Composites Part A: Applied Science and Manufacturing. 2013;44:86-94.

[30.] Ogin SL, Brøndsted P, Zangenberg J. 1 - Composite materials: constituents, architecture, and generic damage. In: Talreja R, Varna J, editors. Modeling Damage, Fatigue and Failure of Composite Materials: Woodhead Publishing; 2016. p. 3-23.

[31.] Ogin S, P. Smith and P. Beaumont. Matrix cracking and stiffness reduction during the fatigue of a (0/90)s GFRP laminate. Composite science and technology. 1985;1985.22(1):p.23-31.

[32.] Boniface L, Ogin S, Smith P, Stinchcomb W, Ashbaugh N. The Change in Thermal Expansion Coefficient as a Damage Parameter During Thermal Cycling of Crossply Laminates. Composite Materials: Fatigue and Fracture, Fourth Volume. STP1156-EB: ASTM International; 1993. p. 0.

[33.] Boniface L. Damage development in fibre-reinforced plastics' laminates: University of Surrey (United Kingdom); 1989.

[34.] Jamison R, Thomas Hahn H. On the Interrelationship Between Fiber Fracture and Ply Cracking in Graphite/Epoxy Laminates. Composite Materials: Fatigue and Fracture. STP907-EB: ASTM International; 1986. p. 0.

[35.] Cartledge AL. The fatigue of carbon fibre composites containing interlaminar inkjet printing polymer droplets: University of Sheffield; 2017.

[36.] Topal S, Baiocchi L, Crocombe AD, Ogin SL, Potluri P, Withers PJ, et al. Late-stage fatigue damage in a 3D orthogonal non-crimp woven composite: An experimental and numerical study. Composites Part A: Applied Science and Manufacturing. 2015;79:155-63.

[37.] Fazal A. Polymer fibre composites: investigation into performance enhancement through viscoelasticity generated pre-stress 2014.

[38.] Sue HJ, Jones RE, Garcia-Meitin EI. Fracture behaviour of model toughened composites under Mode I and Mode II delaminations. Journal of Materials Science. 1993;28(23):6381-91.

[39.] Xie J, editor Analytical and Numerical Modeling of Delamination Evolution in Fiber Reinforced Laminated Composites Subject to Flexural Loading2016.

[40.] Griffith AA, Taylor GI. VI. The phenomena of rupture and flow in solids. Philosophical Transactions of the Royal Society of London Series A, Containing Papers of a Mathematical or Physical Character. 1921;221(582-593):163-98.

[41.] Irwin GR. Onset of fast crack propagation in high strength steel and aluminim alloys.1956. Contract No.: NRL-4763; PB-121224 2008-02-05.

[42.] Irwin GR. Analysis of Stresses and Strains Near the End of a Crack Traversing a Plate. Journal of Applied Mechanics. 2021;24(3):361-4.

[43.] Sneddon IN. The Distribution of Stress in the Neighbourhood of a Crack in an Elastic Solid. Proceedings of the Royal Society of London Series A. 1946;187:229-60.

[44.] Dou L, Zuo X, Qu L, Xiao Y, Bi G, Wang R, Zhang M. A New Method of Quantitatively Evaluating Fracability of Tight Sandstone Reservoirs Using Geomechanics Characteristics and In Situ Stress Field. Processes. 2022;10(5):1040.

[45.] Energy release rate (fracture mechanics) 2024 [Available from: https://en.wikipedia.org/wiki/Energy_release_rate_(fracture_mechanics).

[46.] Lewicki D, Ballarini R. Rim Thickness Effects on Gear Crack Propagation Life. International Journal of Fracture. 1997;87:59-86.

[47.] C.E.Inglis. Stresses in a Plate due to presence of Cracks and Sharp Corners. Transactions of the Royal Institute of Naval Architectes. 1913;60 (1913), pp. 219–241.

[48.] Rice JR. A Path Independent Integral and the Approximate Analysis of Strain Concentration by Notches and Cracks. Journal of Applied Mechanics. 1968;35(2):379-86.

[49.] Barhli SM. Advanced quantitative analysis of crack fields, observed by 2D and 3D image correlation, volume correlation and diffraction mapping: University of Oxford; 2017.

[50.] Kuang JH, Chen YC. The values of J-integral within the plastic zone. Engineering Fracture Mechanics. 1996;55(6):869-81.

[51.] Molteno MR, Becker TH. Mode I–III Decomposition of the J-integral from DIC Displacement Data. Strain. 2015;51(6):492-503.

[52.] Dhatt G LE, Touzot G. The finite element method. Finite Element Method: Wiley-ISTE; 2012.

[53.] Becker TH, Marrow T, Tait R. Damage, crack growth and fracture characteristics of nuclear grade graphite using the Double Torsion technique. Journal of Nuclear Materials. 2011;414:32-43.

[54.] Becker TH, Mostafaci M, Tait RB, Marrow TJ. An approach to calculate the J-integral by digital image correlation displacement field measurement. Fatigue & Fracture of Engineering Materials & Structures. 2012;35(10):971-84.

[55.] Koko A, Earp P, Wigger T, Tong J, Marrow TJ. J-integral analysis: An EDXD and DIC comparative study for a fatigue crack. International Journal of Fatigue. 2020;134:105474.

[56.] Koko A, Elmukashfi E, Dragnevski K, Wilkinson AJ, Marrow TJ. J-integral analysis of the elastic strain fields of ferrite deformation twins using electron backscatter diffraction. Acta Materialia. 2021;218:117203.

[57.] Jin X, Wade-Zhu J, Chen Y, Mummery PM, Fan X, Marrow TJ. Assessment of the fracture toughness of neutron-irradiated nuclear graphite by 3D analysis of the crack displacement field. Carbon. 2021;171:882-93.

[58.] Chikhi N, Fellahi S, Bakar M. Modification of epoxy resin using reactive liquid (ATBN) rubber. European Polymer Journal. 2002;38(2):251-64.

[59.] Shy TKCaHJ. Effects of matrix ductility on rubber/matrix interfacially modified epoxy resins. Polymer. 1992;vol. 33, pp. 1656-1663.

[60.] Pearson RA, Yee AF. Toughening mechanisms in thermoplastic-modified epoxies: 1. Modification using poly(phenylene oxide). Polymer. 1993;34(17):3658-70.

[61.] Garg AC, Mai Y-W. Failure mechanisms in toughened epoxy resins—A review. Composites Science and Technology. 1988;31(3):179-223.

[62.] Cardwell BJ, Yee AF. Toughening of epoxies through thermoplastic crack bridging. Journal of Materials Science. 1998;33(22):5473-84.

[63.] Bagheri R, Marouf B, Pearson R. Rubber-Toughened Epoxies: A Critical Review. Journal of Macromolecular Science®. 2009;Part C: Polymer Reviews:201-25.

[64.] Arai M, Noro Y, Sugimoto K-i, Endo M. Mode I and mode II interlaminar fracture toughness of CFRP laminates toughened by carbon nanofiber interlayer. Composites Science and Technology. 2008;68:516-25.

[65.] Hamer S, Leibovich H, Green A, Intrater R, Avrahami R, Zussman E, et al. Mode I interlaminar fracture toughness of Nylon 66 nanofibrilmat interleaved carbon/epoxy laminates. Polymer Composites. 2011;32(11):1781-9.

[66.] Shivakumar K, Lingaiah S, Chen H, Akangah P, Swaminathan G, Russell L. Polymer Nanofabric Interleaved Composite Laminates. Aiaa Journal - AIAA J. 2009;47:1723-9.

[67.] Paipetis A, Katerelos D. Post-Impact-Fatigue behaviour of composite laminates: Current and novel technologies for enhanced damage tolerance. Composite Laminates: Properties, Performance and Applications. 2010:1-82.

[68.] Dransfield KA, Jain LK, Mai Y-W. On the effects of stitching in CFRPs—I. mode I delamination toughness. Composites Science and Technology. 1998;58(6):815-27.

[69.] Mouritz AP, Leong KH, Herszberg I. A review of the effect of stitching on the in-plane mechanical properties of fibre-reinforced polymer composites. Composites Part A: Applied Science and Manufacturing. 1997;28(12):979-91.

[70.] Dransfield K, Baillie C, Mai Y-W. Improving the delamination resistance of CFRP by stitching—a review. Composites Science and Technology. 1994;50(3):305-17.

[71.] Yoshimura A, Nakao T, Yashiro S, Takeda N. Improvement on out-of-plane impact resistance of CFRP laminates due to through-the-thickness stitching. Composites Part A: Applied Science and Manufacturing. 2008;39(9):1370-9.

[72.] Tekin E, Smith PJ, Hoeppener S, van den Berg AMJ, Susha AS, Rogach AL, et al. Inkjet Printing of Luminescent CdTe Nanocrystal–Polymer Composites. Advanced Functional Materials. 2007;17(1):23-8.

[73.] Soleimani-Gorgani A. 14 - Inkjet Printing. In: Izdebska J, Thomas S, editors. Printing on Polymers: William Andrew Publishing; 2016. p. 231-46.

[74.] Derby B. Bioprinting: Inkjet Printing Proteins and Hybrid Cell-Containing Materials and Structures. Journal of Materials Chemistry. 2008;18:5717-21.

[75.] Zikulnig J, Kosel J. Fabrication Technologies for Flexible Printed Sensors. In: Narayan R, editor. Encyclopedia of Sensors and Biosensors (First Edition). Oxford: Elsevier; 2023. p. 33-50.

[76.] C. Z. Jun Xu aCF. Novel method for printing high-quality metal wires 2007 [

[77.] Wu C-H, Hwang W-S. The effect of the echo-time of a bipolar pulse waveform on molten metallic droplet formation by squeeze mode piezoelectric inkjet printing. Microelectron Reliab. 2015;55:630-6.

[78.] A. M. J. van den Berg PJS, J. Perelaer, W. Schrof, S. Koltzenburg, and U. S. Schubert. Inkjet printing of polyurethane colloidal suspensions. Soft Matter. 2007.

[79.] Mondrinos MJ, Dembzynski R, Lu L, Byrapogu VKC, Wootton DM, Lelkes PI, Zhou J. Porogen-based solid freeform fabrication of polycaprolactone–calcium phosphate scaffolds for tissue engineering. Biomaterials. 2006;27(25):4399-408.

[80.] de Gans B-J, Duineveld PC, Schubert US. Inkjet Printing of Polymers: State of the Art and Future Developments. Advanced Materials. 2004;16(3):203-13.

[81.] Calvert P. Inkjet Printing for Materials and Devices. Chemistry of Materials. 2001;13(10):3299-305.

[82.] Singh M, Haverinen HM, Dhagat P, Jabbour GE. Inkjet Printing—Process and Its Applications. Advanced Materials. 2010;22(6):673-85.

[83.] Perelaer J, Smith PJ, Wijnen MMP, van den Bosch E, Eckardt R, Ketelaars PHJM, Schubert US. Droplet Tailoring Using Evaporative Inkjet Printing. Macromolecular Chemistry and Physics. 2009;210(5):387-93.

[84.] Saunders RE, Gough JE, Derby B. Delivery of human fibroblast cells by piezoelectric drop-on-demand inkjet printing. Biomaterials. 2008;29(2):193-203.

[85.] Perelaer J, Smith PJ, van den Bosch E, van Grootel SSC, Ketelaars PHJM, Schubert US. The Spreading of Inkjet-Printed Droplets with Varying Polymer Molar Mass on a Dry Solid Substrate. Macromolecular Chemistry and Physics. 2009;210(6):495-502.

[86.] Zhang Y, Tse C, Rouholamin D, Smith P. Scaffolds for tissue engineering produced by inkjet printing. Central European Journal of Engineering. 2012;2.

[87.] Cui X, Boland T. Human microvasculature fabrication using thermal inkjet printing technology. Biomaterials. 2009;30(31):6221-7.

[88.] Dutta P, Rinki K, Dutta J. Chitosan: A Promising Biomaterial for Tissue Engineering Scaffolds. 2442011. p. 45-79.

[89.] Bharathan J, Yang Y. Polymer electroluminescent devices processed by inkjet printing: I. Polymer light-emitting logo. Applied Physics Letters. 1998;72(21):2660-2.

[90.] van Osch THJ, Perelaer J, de Laat AWM, Schubert US. Inkjet Printing of Narrow Conductive Tracks on Untreated Polymeric Substrates. Advanced Materials. 2008;20(2):343-5.

[91.] Hutchings IM, Martin G. Inkjet technology for digital fabrication. Chichester, West Sussex, United Kingdom: Wiley Chichester, West Sussex, United Kingdom; 2013. Available from: http://www.123library.org/book_details/?id=64295.

[92.] Quan D, Alderliesten R, Dransfeld C, Murphy N, Ivanković A, Benedictus R. Enhancing the fracture toughness of carbon fibre/epoxy composites by interleaving hybrid meltable/non-meltable thermoplastic veils. Composite Structures. 2020;252:112699.

[93.] Ritzenthaler S, Girard-Reydet E, Pascault JP. Influence of epoxy hardener on miscibility of blends of poly(methyl methacrylate) and epoxy networks. Polymer. 2000;41:6375-86.

[94.] Carfagna C, Nicolais L, Amendola E, Carfagna Jr. C, Filippov AG. Toughening epoxy resins by liquid crystalline polymers. Journal of Applied Polymer Science. 1992;44(8):1465-71.

[95.] Zhang Y. In situ 3D observation of delamination crack propagation in carbon-fibre/epoxy composites: University of Oxford; 2018.

[96.] Chechik L. In-Situ 3D observation of damage development and healing in a carbon fibre composite: University of Oxford; 2017.

[97.] Lim Y. In-Situ 3D observation of damage development and healing in a carbon-fibre/epoxy composite: University of Oxford; 2019.

[98.] Zhang Y, Stringer J, Hodzic A, Smith PJ. Toughening mechanism of carbon fibre-reinforced polymer laminates containing inkjet-printed poly(methyl methacrylate) microphases. Journal of Composite Materials. 2017;52(11):1567-76.

[99.] Kastner J, Heinzl C. X-Ray Tomography. In: Ida N, Meyendorf N, editors. Handbook of Advanced Non-Destructive Evaluation. Cham: Springer International Publishing; 2018. p. 1-72.

[100.] Lambert JH. J.H. Lambert ... Photometria Sive De Mensura Et Gradibus Luminis, Colorum Et Umbrae. Augustae Vindelicorum: Klett Augustae Vindelicorum; 1760.

[101.] NIST. X-Ray Mass Attenuation Coefficients. 2004.

[102.] Landis EN, Keane DT. X-ray microtomography. Materials Characterization. 2010;61(12):1305-16.

[103.] Feldkamp LA, Davis LC, Kress JW. Practical cone-beam algorithm. J Opt Soc Am A. 1984;1(6):612-9.

[104.] Requena G, Cloetens P, Altendorfer W, Poletti C, Tolnai D, Warchomicka F, Degischer HP. Sub-micrometer synchrotron tomography of multiphase metals using Kirkpatrick–Baez optics. Scripta Materialia. 2009;61(7):760-3.

[105.] Kastner J, Harrer B, Requena G, Brunke O. A comparative study of high resolution cone beam X-ray tomography and synchrotron tomography applied to Fe- and Al-alloys. NDT & E International. 2010;43(7):599-605.

[106.] Kastner J, Plank B, Requena G. Non-destructive characterisation of polymers and Al-alloys by polychromatic cone-beam phase contrast tomography. Materials Characterization. 2012;64:79-87.

[107.] Pfeiffer F, Weitkamp T, Bunk O, David C. Phase retrieval and differential phase-contrast imaging with low-brilliance X-ray sources. Nature Physics. 2006;2(4):258-61.

[108.] Yashiro W, Terui Y, Kawabata K, Momose A. On the origin of visibility contrast in x-ray Talbot interferometry. Opt Express. 2010;18(16):16890-901.

[109.] Kasperl S. Qualitätsverbesserungen durch referenzfreie Artefaktreduzierung und Oberflächennormierung in der industriellen 3D-Computertomographie: Friedrich-Alexander-Universität Erlangen-Nürnberg (FAU); 2005.

[110.] Wildenschild D, Vaz CMP, Rivers ML, Rikard D, Christensen BSB. Using X-ray computed tomography in hydrology: systems, resolutions, and limitations. Journal of Hydrology. 2002;267(3):285-97.

[111.] Barrett JF, Keat N. Artifacts in CT: recognition and avoidance. Radiographics. 2004;24(6):1679-91.

[112.] De Marco F, Marschner M, Birnbacher L, Noël P, Herzen J, Pfeiffer F. Analysis and correction of bias induced by phase stepping jitter in grating-based X-ray phase-contrast imaging. Opt Express. 2018;26:12707.

[113.] Gao Y, Hu W, Xin S, Sun L. A review of applications of CT imaging on fiber reinforced composites. Journal of Composite Materials. 2021;56(1):133-64.

[114.] Cao W, Zhang J, Sun B, Gu B. X-ray tomography and numerical study on low-velocity impact damages of three-dimensional angle-interlock woven composites. Composite Structures. 2019;230:111525.

[115.] Wang Y, Burnett TL, Chai Y, Soutis C, Hogg PJ, Withers PJ. X-ray computed tomography study of kink bands in unidirectional composites. Composite Structures. 2017;160:917-24.

[116.] Smith T, Bay B, Rashid M. Digital Volume Correlation Including Rotational Degrees of Freedom during Minimization. Experimental Mechanics. 2002;42:272-8.

[117.] Finegan D, Tudisco E, Scheel M, Robinson J, Taiwo O, Eastwood D, et al. Quantifying Bulk Electrode Strain and Material Displacement within Lithium Batteries via High-Speed Operando Tomography and Digital Volume Correlation. Advanced Science. 2015;3.

[118.] Wang B, Pan B. Incremental digital volume correlation method with nearest subvolume offset: An accurate and simple approach for large deformation measurement. Advances in Engineering Software. 2018;116:80-8.

[119.] Lavision. Product manual: Digital volume correlation for DaVis 8.4. 2017.

[120.] Roberts BC, Perilli E, Reynolds KJ. Application of the digital volume correlation technique for the measurement of displacement and strain fields in bone: A literature review. Journal of Biomechanics. 2014;47(5):923-34.

[121.] Mostafavi M, Collins D, Cai B, Bradley R, Atwood R, Reinhard C, et al. Yield behavior beneath hardness indentations in ductile metals, measured by three-dimensional computed X-ray tomography and digital volume correlation. Acta Materialia. 2014;82:468-82.

[122.] Palanca M, Tozzi G, Cristofolini L, Viceconti M, Dall'Ara E. Three-dimensional local measurements of bone strain and displacement: comparison of three digital volume correlation approaches. J Biomech Eng. 2015;137(7).

[123.] Poissant J, Barthelat F. A Novel “Subset Splitting” Procedure for Digital Image Correlation on Discontinuous Displacement Fields. Experimental Mechanics. 2010;50(3):353-64.

Chapter 3

3. Sample manufacturing and toughness measurement

3.1 Sample Preparation

This chapter provides the details of sample manufacturing, including the composite specimens for later characterization as well as the resin coated glass slides with printing droplets for observation of the deposit morphology in the matrix. The composite laminate specimens were then evaluated to measure the toughening effect in a two-ply specimen by the double cantilever beam (DCB) test using digital image correlation (DIC) to measure the load-line displacements.

3.1.1 Inkjet-printing of thermoplastic dots on composite

3.1.1.1 Prepreg

The CFRP specimens were fabricated from unidirectional carbon fibre/epoxy pre-impregnated prepreg tape from Cytec Engineered Materials Ltd (CYCOM® 977-2-35-12KHTS-268-300). This prepreg tape had been made by pre-impregnating the carbon fibres into the toughened epoxy resin and had a thickness of 0.25-0.27 mm thickness.

The continuous UD carbon fibre (Toho Tenax HTS40 12 K 800tex) was used in the prepreg and its properties are listed in Table 3.1. The matrix of this CYCOM® 977-2 prepreg is a toughened thermoplastic epoxy. The typical properties of this epoxy resin after curing are exhibited in Table 3.2.

Table 3.1. Summary of properties of carbon fibre used in this work [1]

Properties	**Data**
Elastic modulus	239 GPa
Tensile strength	4629 MPa
Density	1.76 g/cm^3
Average fibre diameter	6.96 µm

Table 3.2. Summary of typical properties of the CYCOM® 977-2 toughened epoxy resin (from Cytec Engineered Materials Ltd.)

Properties	**Data**
Tensile modulus	3.52 ± 0.14 GPa
Tensile strength	81.4 ± 11.0 MPa
G_{1C}	478 ± 84 J/m^2
Tg	212 °C
Density	1.31 g/cm^3

The prepreg was previously cut by Yi Zhang from Sheffield University into 150 x 150 mm sheets and stored in a freezer [2]. Before printing, the tape was defrosted at room temperature for 12 hours.

3.1.1.2 Droplet materials

Three types of solutions were prepared for droplet printing: PMMA (Poly-methyl methacrylate, Mw ~ 15,000), PEG (Polyethylene glycol) with Mn ~20,000 and Mn ~ 400 respectively. PMMA (Poly-methyl methacrylate, Mw ~ 15,000) is an amorphous linear thermoplastic polymer (

Figure **3.1**), which has high strength and modulus (Table 3.3). A suitable solvent is important for the solution used in inkjet printing: the solvent needs to easily dissolve the solute and volatility is required to evaporate after printing and before subsequent lay-up and curing. However, if the evaporation rate is too high, the solvent would evaporate before printing, resulting in solute accumulating at the print tip to cause print head clogging. DMF (N,N-Dimethylformamide) was chosen for the PMMA solution as it satisfies the above demand. The 5wt% PMMA solutions were prepared with an ultrasonic bath to help PMMA dissolve in DMF at room temperature to form a clear liquid. To investigate the droplet behaviour in the matrix before and after curing, 0.1 wt.% fluorescein (Sigma Aldrich, UK) was added for the solutions that were prepared for printing on the laminates and epoxy coated glass slide.

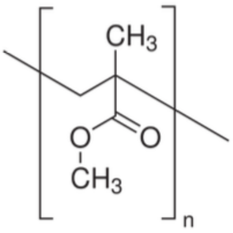

Figure 3.1. PMMA molecular structure

PEG (Polyethylene glycol) is a linear, crystalline polymer (

Figure **3.2**). PEGs, with Mn at ~20,000 and ~400 were dissolved separately in de-ionised water with the help of an ultrasonic bath to form a clear liquid solution at 5wt%. As with PMMA, 0.1 wt.% fluorescein was added in a solution for the later droplet movement study. Fluorescein is not miscible with water, so a 5wt% PEG/ethanol (PEG Mn~400) solution was prepared here, with a controllable hot plate to dissolve PEG in ethanol at 60°C.

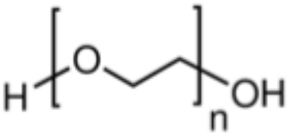

Figure 3.2. PEG molecular structure

Table 3.3. Typical physical properties of PMMA and PEG [2]

Properties	PMMA	PEG
Ultimate tensile strength (MPa)	47-79	1.5
Youngs modulus (GPa)	2.2-3.8	1.3
Density (g/cm^3)	1.15-1.19	1.19
Water absorption (wt%)	0.3-0.4	Soluble in water

3.1.1.3 Inkjet printing

The inkjet printing was achieved through a drop-on-demand (DoD) piezoelectric inkjet printer (MicroFab IV, MicroFab Inc., USA) as shown in Figure 3.3. A low temperature printhead with 50 µm orifice diameter, which is suitable to dispense aqueous droplets up to 50 °C, was used to print the thermoplastic solutions.

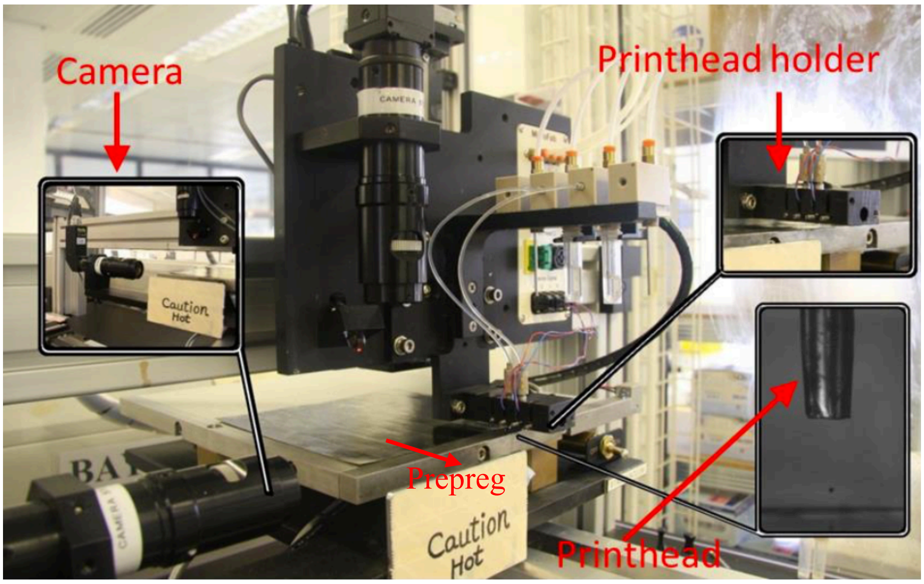

Figure 3.3. DoD piezoelectric inkjet printer used for sample preparation [2]

The printability of solutions is dominated by viscosity and surface tension. Ideal viscosity is supposed to be below < 20 mPa·s [3]. As described in chapter 1, the reciprocal of the Ohnesorge number: *Z* can be applied for the evaluation of printability. The *Z* value of solutions used in this work range from 11.85 to 35.36. During printing, shear force acts on the polymer chains which alter the actual viscosity and Z value. The printability has previously been proved by University of Sheffield [2]. Therefore, the inks were printable even though they did not fall into the perfect range.

A pneumatic controller (MicroFab CT-PT-4) was used to control the air pressure applied to the reservoirs that transfer ink to the printhead via a polytetrafluoroethylene (PTFE) tube (Figure 3.4). The printing speed is adjustable, and the printer used in this work had a maximum speed of up to 50 mm/s. Lower printing speed results in high-resolution features, but increases the printing time. A speed of 30 mm/s was chosen here, which gave a good printing quality. Each prepreg took ~ 45 minutes to be printed.

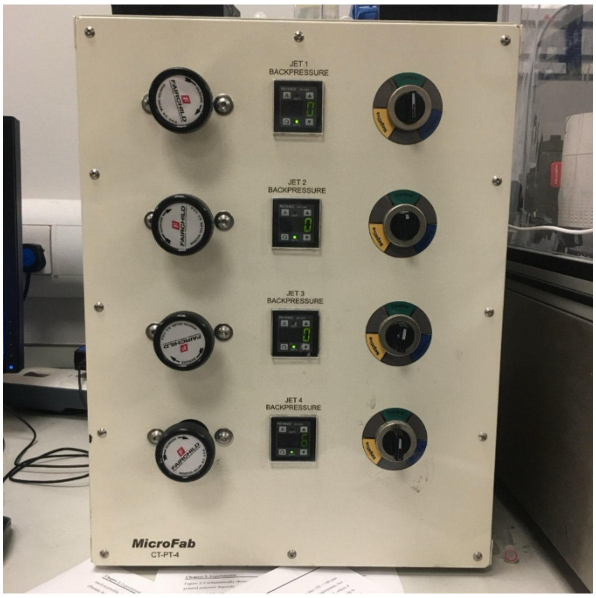

Figure 3.4. Pneumatics controller

An JetLab operation program is used to control the printer, with a stroboscopic camera (Figure 3.3) monitoring the droplets' morphology while printing. In ideal printing status, there would be a stable single droplet coming from the print head tip (Figure 3.5 (a)). Satellite droplets (Figure 3.5 (b)) should be avoided, as they interfere with the printing resolution. For different printing materials, Zhang conducted the initial printing on epoxy coated glass and characterized under optical microscopy to determine the repeatability, this worked followed the same printing settings as described in [2].

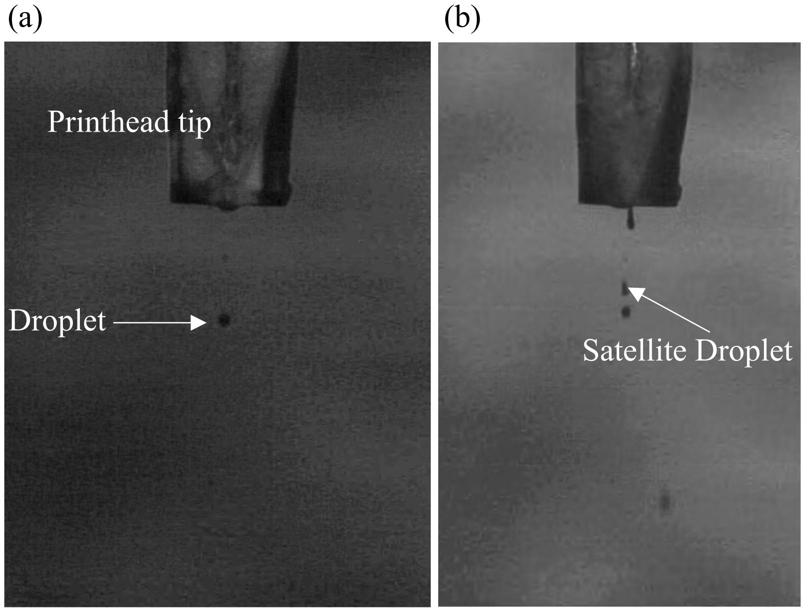

Figure 3.5. (a) Good printing set and **(b)** printing with satellite droplet

The pattern of the printing could be customized by scripting dx and dy: the distances between adjacent dot centres in the x and y axis respectively. In this work, three patterns were designed for composite laminate manufacturing, as shown in Figure 3.6. To investigate the toughening mechanism, PMMA (Mw ~ 15,000) and PEG (Mn ~ 400) were printed on the prepreg in a **line** pattern, from which in-situ observation could be conducted in FoV when crack propagated in printed and non-printed region for comparison. This was achieved by narrowing the distance between dots to be smaller than droplet diameter (according to Yi, the deposit diameter is ~150μm [2]) in the x axis, and the line was formed by the overlapped dots (dx = 0.05mm, dy = 0.25mm). The **hexagonal** pattern (dx = 0.2mm, dy=0.4mm) has been previously found to have a high toughening effect and was applied with the PMMA (Mn ~20,000) and PEG (Mn ~20,000) ink [2]. As displayed in Figure 3.7, the hexagonal pattern printing deposits initiated at 60mm from the top edge (perpendicular to the fibre direction) of prepreg sheet, covering a printing region of 90x150mm. The line printing profile was uniformly applied across the entire specimen. The **square**, as the simplest pattern, was applied to the inks with fluorescein addition on both prepreg and epoxy coated glass slide to study the droplets behaviour (further details are described in Chapter 5). As the specimens were printed with various materials, molecular weight and patterns in different time, the names of laminate specimens are summarized in Table 3.4. It is worth noticing that NP_0 and PMMA_Hex_15000 samples were manufactured and characterized by previous researchers working on the project before this DPhil project started, where the corresponding XCT data were analysed in this work which would be detailed in Chapter 4.

After printing on the prepreg, the sheets were separately stored in trays and sealed with plastic bag to protect the printing pattern for one day before the lay-up and curing.

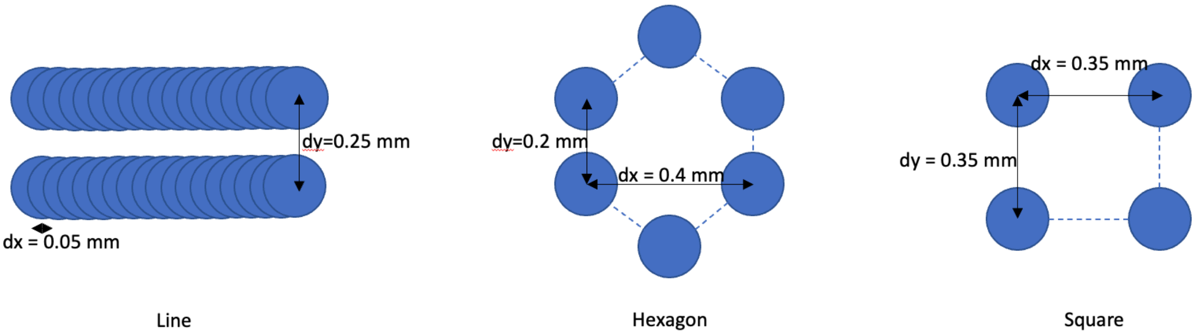

Figure 3.6. Printing patterns used in this work

Table 3.4. Summary of CFRP specimens used in this work

Sample name	**Ink**	**Pattern**	**Manufacturing Year**
NP_0	Non printed	N/A	2017
PMMA_Hex_15000	PMMA (Mn ~15,000)	Hexagonal	2017
NP_1	Non printed	N/A	2019
PEG_Hex_20000	PEG (Mn ~20,000)	Hexagonal	2019
NP_2	Non printed	N/A	2021
PMMA_Line_15000	PMMA (Mn ~15,000)	Line	2021
PEG_Line_400	PEG (Mn ~400)	Line	2021
PMMA_Flu	Fluorescein with PMMA (Mn ~15,000)	Square	2021
PEG_Flu	Fluorescein with PEG (Mn ~400)	Square	2021

3.1.1.4 Lay-up and curing

Two-ply of prepregs were manually laid up on a steel plate, positioning the printed layer at the bottom with the plane containing dots facing upward. The unprinted prepreg was aligned unidirectionally on the top of the bottom sheet. To facilitate the future mechanical tests, a rectangular PTFE film with 50mm width was inserted between the two plies to create a pre-crack, as illustrated in Figure 3.7. During the hand lay-up, a blunt plastic plate was used to eliminate the air between the two plies as much as possible.

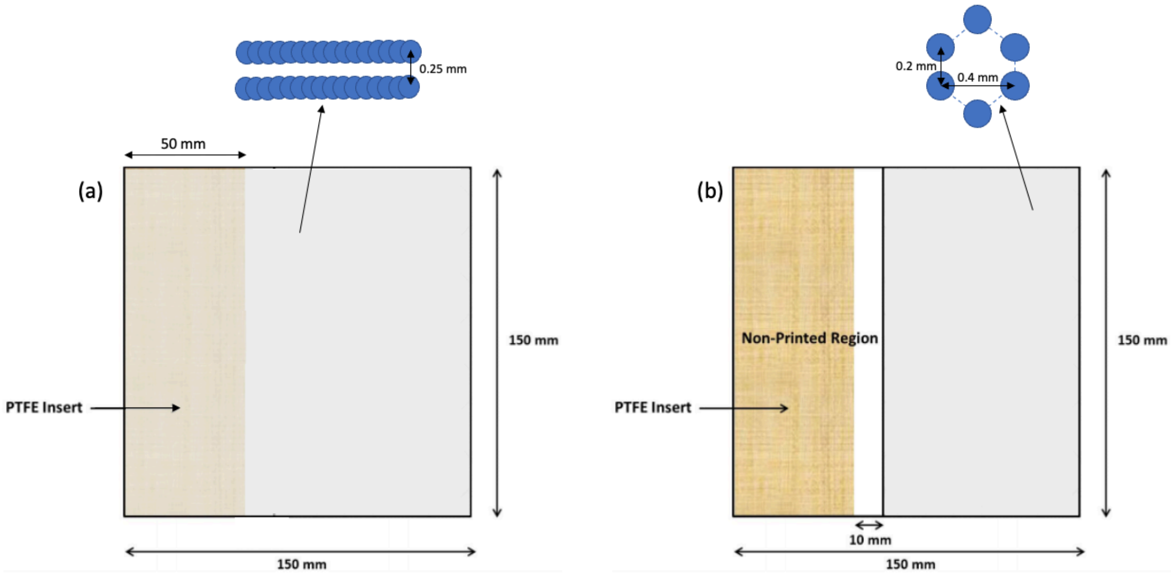

Figure 3.7. Schematic graph of the **(a)** line pattern and **(b)** hexagonal pattern printing sample with PTFE insertion, where grey areas represent the region with printing

Following the manual laying up process, the specimens were vacuum bagged, as shown in Figure 3.8. To ensure consistent curing conditions for all the specimens, the printed and non-printed laminates were placed together in the same vacuum bag and cured simultaneously in the autoclaves. The cross-linking of epoxy necessitates elevated temperature and pressure over a specific time, with curing conditions tailored to particular resin for the production of final composites. For the CYCOM 977-2 series, the cycle condition adhered to the steps outlined by Yi in the previous research [2], as detailed in Table 3.5. The final CFRP laminates all had a thickness of 0.5 mm.

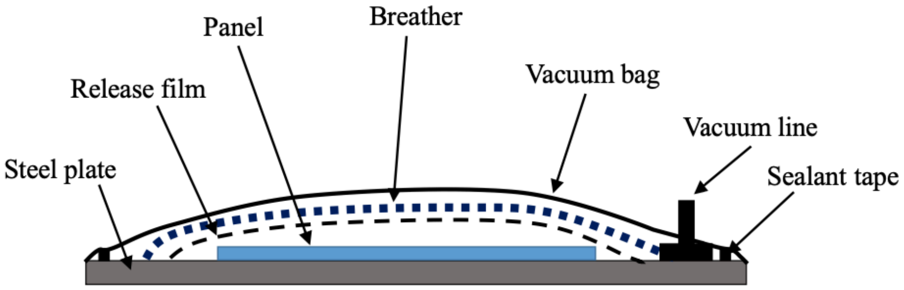

Figure 3.8. Schematic graph of the vacuum bag

Table 3.5. Curing condition for the CYCOM 977-2 prepreg

	Cycle 1: ramp	Cycle 2: dwell	Cycle 3: ramp
Temperature	177°C (2°C/min)	180 min	20°C (2°C/min)
Pressure	90 psi (5 psi/min)	300 min	0 psi (5 psi/min)

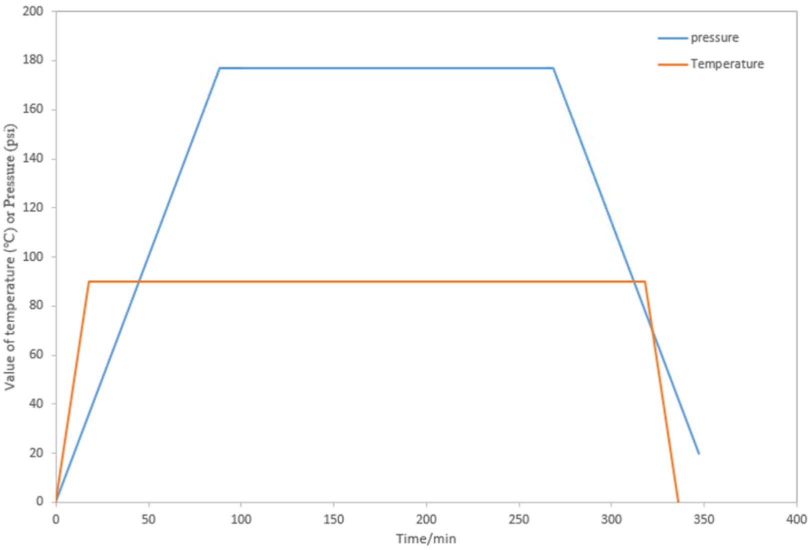

Figure 3.9. Curing condition applied for laminate manufacturing

3.1.2 Resin coated glass slides with printing droplets

To study the morphology of printing dots on the epoxy resin, printing was executed with a square pattern on resin coated glass slides and subsequently characterized under an optical microscope.

EL 160 high temperature epoxy laminating resin was initially mixed with the hardener in a 100:35 ratio. The hardened epoxy liquid was then manually coated on microscope glasses slides without any pre-treatment, achieving a thickness of ~50um. All the coated glass slides were then heated to 120°C (2°C/min) for 2 hours in the thermo scientific oven to partially cured the epoxy that simulate the B-stage of resin in CYCOM 977-2 resin. The surface of epoxy coated slides exhibited unevenness after heating, attributed to the contraction of liquid epoxy in elevated temperature (Figure 3.10). 0.1wt% of fluorescein (Sigma Aldrich 46955) was added in the 5wt% PMMA/DMF solutions. Given that the fluorescein is not dissoluble in water, 5wt% PEG (Mn ~400) solutions with ethanol was prepared, and 0.1wt% of fluorescein was incorporated. Subsequently, a square printing pattern with dx/dy at 0.35/0.35mm (Figure 3.6) was applied on the partially cured resin coated glass. CRFP 2-ply composites were manufactured using the same ink and print pattern (see Table 3.4).

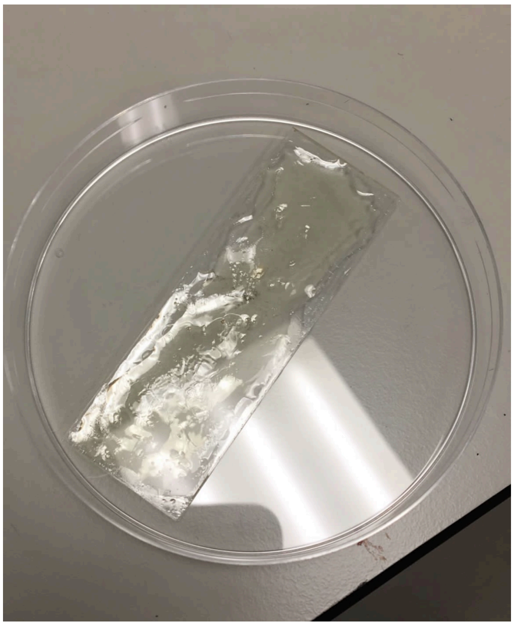

Figure 3.10. Uneven surface of epoxy coated glass slide post curing

3.2 Mechanical Test

After manufacturing the laminates, double cantilever beam (DCB) tests were conducted following ASTM 5528 standard, using digital image correlation (DIC) to measure the opening displacement to evaluate the model I interlaminar fracture toughness (G_{IC}). Note that mechanical tests were only conducted on samples that been printed without fluorescein.

3.2.1 Sample Preparation

The two-ply CFRP laminates were cut into samples with dimensions of 50x3x0.5 mm using a low-speed diamond saw, with a 10 mm pre-crack introduced by removal of the PTFE insert. It is worth mentioning that the specimen dimension is smaller than suggestion from ASTM 5528, which is due to the restriction of sample dimension during in-situ synchrotron characterization and that the mechanical test aims at measuring the fracture toughness from the same dimension of laminates. Within a thinner specimen, materials near the free surface experience a plane stress condition while the state inside the specimen towards plane strain. The plane stress leading to an overvalued fracture toughness whereas plain strain yields the lower bond. As the main propose of DCB here is for comparison of different printing pattern, with all the samples having the same dimension, the sacrifice thus become acceptable.

As illustrated in Figure 3.11, for the specimen with hexagonal printing pattern, there is a 10 mm gap between pre-crack front and boundary of the printed and non-printed region (dot line), while the line pattern was printed across the whole specimen.

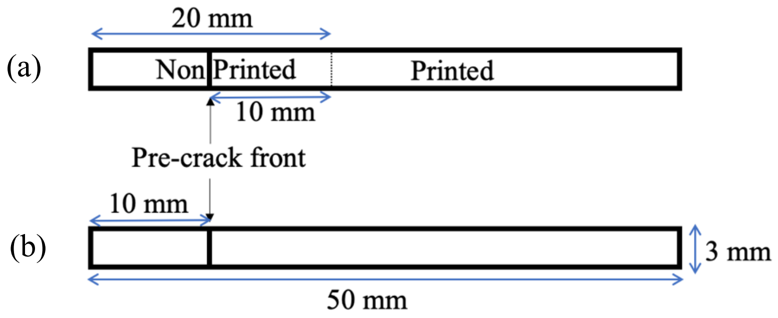

Figure 3.11. DCB specimen schematic of **(a)** hexagonal printed sample with dotted line marks the boundary between printing and non-printing region, **(b)** non- and line- printed specimens

M4 stainless steel nuts were glued to two sides of the specimens on the pre-crack end as the loading blocks. The bonding was achieved by 'super glue' (cyanoacrylate) and the specimens were put in a custom-made alignment block to obtain good alignment between sample and the axis of the nuts (Figure 3.12). The samples were left for at least 24 hours for glue drying before testing. White paint (Vallejo) was applied using a TimberTech airbrush on the edge of the specimens to aid crack tip visibility under the optical lenses in the GOM system. After painting, the specimens were left for another 24 hours before the mechanical test.

Figure 3.12. DCB specimen in alignment block for nuts bonding with scale bar

3.2.2 Experimental

The mechanical tests were conducted using an Instron 3366 with a 500N load cell. The specimens were mounted to the Instron via custom-made tensile jigs fitted with the load machine as shown in Figure 3.13 a. A GOM ARAMIS 5M 2-Camera system was placed in front of loaded specimen to capture the opening displacement of the cantilever arms and the correlating delamination length, with LED lights on for illumination. A speckle pattern of white paint on a uniform black substrate on the bolts was achieved using the airbrush. The speckle patterns should be random, isotropic and high contrast to reduce the measurement noise [4].

A black ink layer was painted on the jigs via the airbrush to mitigate reflections from the LEDs that could compromise the later image processing step (Figure 3.13 b). The crack mouth opening displacement (COD) was determined by employing DIC to measure the displacements of the bolts.

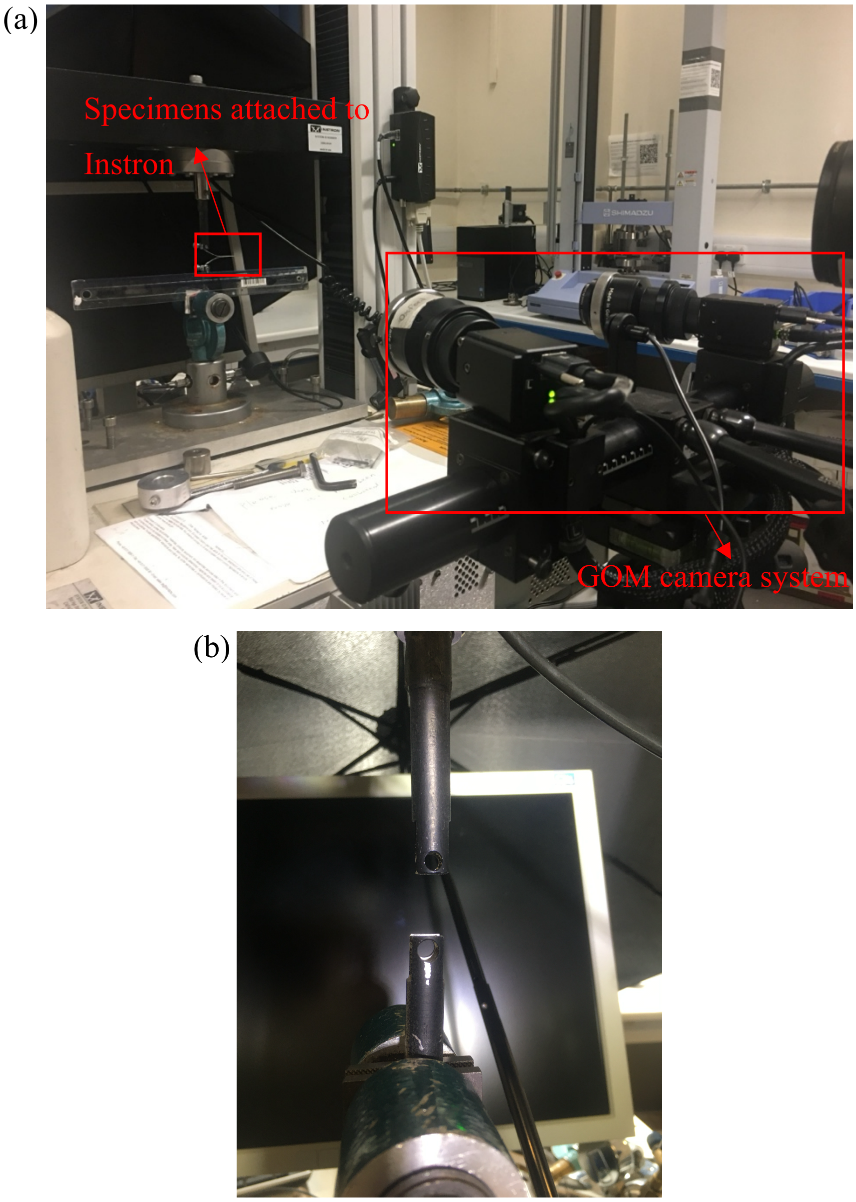

Figure 3.13. (a) experiment set up, **(b)** jigs with black paint

The GOM camera system was configured with 75 mm lenses, positioned 595 mm from the specimen centre. The system featured with 224 mm slider distance and 25° camera angle, which provides a 50 x 42 mm measuring volume. The cameras were calibrated using a calibration cube (55 x 44 / CQG1112), and an ideal calibration should have a deviation less than 0.04 pixels. Re-calibration was done whenever there was any physical movement of the camera system. A typical calibration result, with a deviation of 0.02 pixels (pixel size of 22 µm) is illustrated in Figure 3.14.

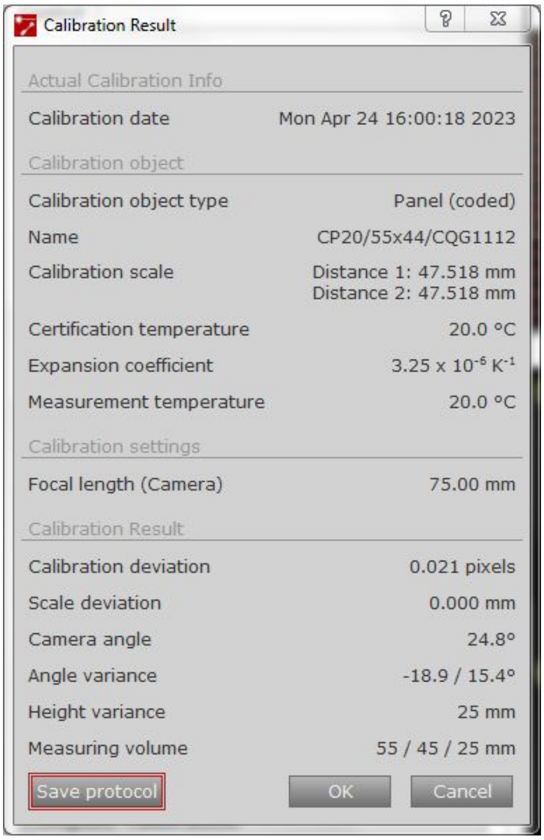

Actual Calibration Info

Calibration date	Mon Apr 24 16:00:18 2023

Calibration object

Calibration object type	Panel (coded)
Name	CP20/55x44/CQG1112
Calibration scale	Distance 1: 47.518 mm Distance 2: 47.518 mm
Certification temperature	20.0 °C
Expansion coefficient	3.25 x 10^{-6} K^{-1}
Measurement temperature	20.0 °C

Calibration settings

Focal length (Camera)	75.00 mm

Calibration Result

Calibration deviation	0.021 pixels
Scale deviation	0.000 mm
Camera angle	24.8°
Angle variance	-18.9 / 15.4°
Height variance	25 mm
Measuring volume	55 / 45 / 25 mm

Figure 3.14. Calibration result used in this work

The samples underwent mode I opening, and the load was recorded through Instron software. The loading was conducted under displacement control, with a crosshead displacement rate set at 2 mm/min, this is chosen as rapid delamination growth may introduce dynamic effect for the fracture while a lower strain rate resulted in more frequent unstable delamination. To avoid the non-printed region and eliminate the resin rich effect in the areas near the PTFE film, each specimen was firstly opened to extend the initial crack tip by 15 mm. The specimen was then unloaded completely and reloaded with the same loading rate. Because the specimen has been opened with 15 mm crack length propagation, measuring before that would underestimate the work of fracture. Therefore, image-capturing and load recording commenced simultaneously once the reloading reached the displacement point where the initial opening ceased. Images were captured at two second intervals and continued until the crack propagated for at least 12 mm, which took approximately 10 minutes for each specimen.

The DIC processing was performed using GOM ARAMIS 6.3.0-6 software to measure the opening of the cantilever beam. The analysis was conducted on the front surface of bolts with speckle pattern by applying circular masks on the captured stages (Figure 3.15). A suitable square facet size and step size were then configured for the displacement evaluation. A larger facet size, encompassing more speckle patterns will enhance the correlation between each stage and improve the measuring accuracy but requires longer computation time, whereas a smaller facet size has better resolution for local effects. In GOM, facet size is usually chosen between 15-30 pixels [5]. The facet step determines the measuring point density that a smaller facet step leads to an increase of measuring density. Stationary and rigid body tests were carried out to quantify the effect of facet size and step on the measuring uncertainty. As displayed in Figure 3.16, the deviation between stationary and rigid body tests decreases with increasing facet size, and after certain point the enhancement becomes less significant by further raising the facet size. A facet size of 30 pixel and step size of 15 pixels were selected in the work, yielding an error less than 1%. By combining random and isotropic speckle with suitable facet size, a high correlation between steps was achieved, which enhanced the DIC calculation accuracy. This is visually displayed as the masked region appearing in green colour after evaluation in the GOM software interface (Figure 3.15). Notably in Figure 3.15 & Figure 3.20, asymmetry of top and bottom ply was observed in several laminates during loading. This is due to the poor bonding of nuts on sample edges, they were not perfectly aligned where mix mode loading would be introduced.

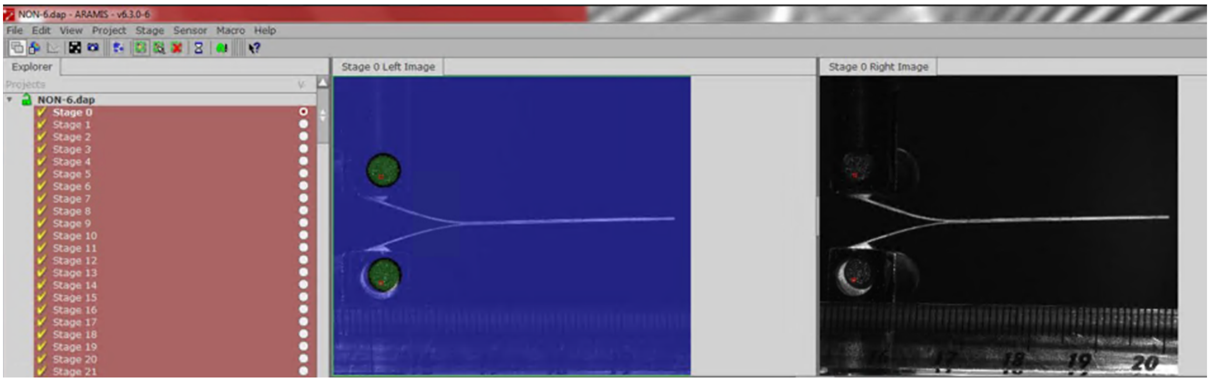

Figure 3.15. Tracking of displacement on bolts in ARAMIS with good correlation between image steps

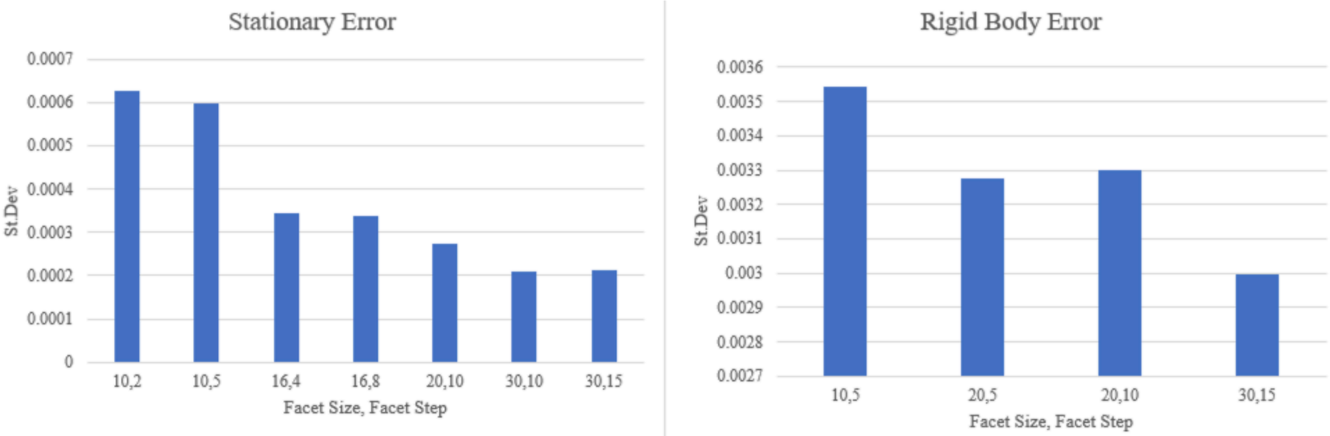

Figure 3.16. Stationary and rigid body error analysis for facet size and step chosen

Ideally, monitoring of COD on the nuts would yield a more accurate result than the crosshead displacement of the Instron, since the nuts were bonded with the arm and the displacement was in line with the cantilevers during opening. To evaluate the potential discrepancy between the displacement obtained from DIC and Instron machine, a calibration test was performed at an opening rate of 2 mm/min. As indicated in Figure 3.17, the COD and crosshead agreed with an error of 0.4%.

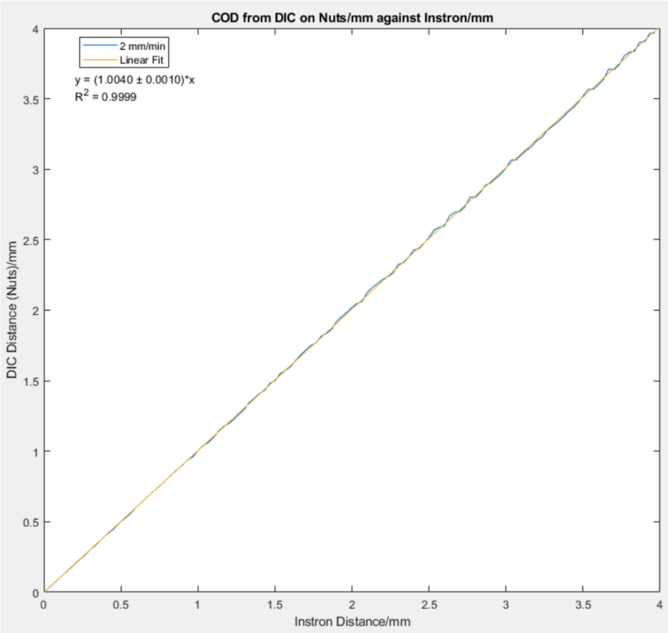

Figure 3.17. Comparison of COD measured from DIC (nuts) and Instron

3.2.3 Post-processing and Data Analysis

The fracture toughness G_{IC} was calculated following ASTM D5528 [6]. There are three data reduction methods for evaluating the interlaminar fracture toughness: modified beam theory (MBT), compliance calibration method (CC) and modified compliance calibration method (MCC). These three methods have been reported to provide a calculation of G_{IC} with less than 3.1% difference [7], therefore there is no priority among them. The MBT method yields the most conservative calculation for the work of fracture, and it was therefore chosen [8].

The MBT method (Equation 3.1) was applied to calculate the mode I fracture toughness, which is based on assumptions: 1. The beam behave linear elastically; 2. Both arms are identical in geometry and material properties, with symmetrical opening under applied load; 3. Negligible shear deformation occurs in the loading and crack growth in pure Mode I:

$$G_{IC} = \frac{3P\delta}{2b(a+|\Delta|)} * \frac{F}{N} \qquad (3.1)$$

Here, P is the load measured from Instron, δ represents the opening displacement, which was determined by DIC, b is the specimen width measured by a calliper and a stand for the delamination length.

A correction factor, Δ, was incorporated into the measured delamination length to account for the rotation of delamination front, which otherwise would result in overestimation of G_{IC}. As shown in Figure 3.18, Δ was determined by plotting the cube root of compliance (C) verses the delamination length, where the compliance, C is the ratio of load point displacement to the applied load.

The parameter F, is introduced for correction of large displacement effects that accounts for moment arm shorting and block tilting:

$$F = 1 - \frac{3}{10}\left(\frac{\delta}{a}\right)^2 - \frac{3}{2}\left(\frac{\delta t}{a^2}\right) \qquad (3.2)$$

where t is displayed in Figure 3.19.

The relatively small dimension of specimen makes the influence of loading block un-neglectable (otherwise the distance between load line and end of insertion should be at least 50 mm), and the second parameter, N, was used to account for the sample stiffening by the blocks:

$$N = 1 - \left(\frac{L'}{a}\right)^3 - \frac{9}{8}\left[1 - \left(\frac{L'}{a}\right)^2\right]\left(\frac{\delta t}{a^2}\right) - \frac{9}{35}\left(\frac{\delta}{a}\right)^2 \qquad (3.3)$$

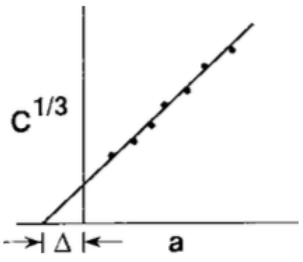

Figure 3.18. Calibration of modified beam theory for delamination length [6]

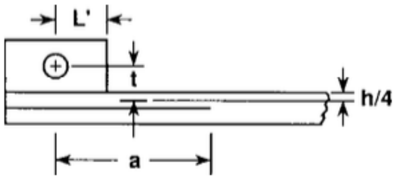

Figure 3.19. Schematic diagram showing the parameter used in F & N calibration [6]

The delamination length, a, is normally measured as the distance from load line to crack tip. Because of the large crack opening in this work, the high compliance of cantilever during the bending would underestimate the crack length. The method from Lahuerta et al. [9] was applied here to determine the delamination length:

$$a = (\text{specimen total length}) - (\text{undelaminated length}) \qquad (3.4)$$

The tiff files exported from GOM were imported to ImageJ for the delamination length measurement. Thresholding of images was applied to distinguish the specimen from the background, which was then outlined by the magic wand tool (Figure 3.20). The coordinates of the specimen edge were then exported. The crack tip and sample end were identified by MATLAB to determine the undelimitated length, the delamination length was subsequently determined by deducing the undelimitated portion from the total length of the specimen.

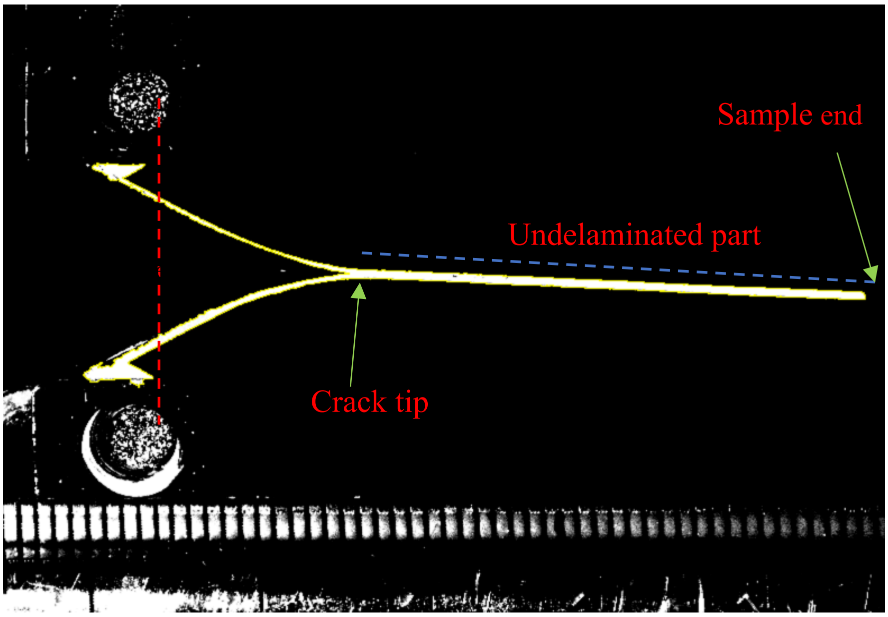

Figure 3.20. Determination of delamination length

The opening displacement, δ, was determined by subtracting the averaged Y displacement of bottom bolts from the top bolts. Because of the large number of images (steps) captured in each sample, a MATLAB script was written to process the data following the above workflow.

The details of processing from raw data to final G_{IC} using MBT method are demonstrated in the following using one of PMMA_Line_15000 specimens as an example:

The specimen total length was measured before the mechanical test using a vernier calliper. The non-delaminated length was determined by evaluating the distance between crack tip and sample end at each interval, using the coordinates obtained from ImageJ. Subsequently, the delamination length of each step was inferred by subtracting the non-delaminated segment from the specimen entire length. The opening force was exported from the Instron, with a time interval of 2s per record, which is synchronised with the GOM image capture rate. Figure 3.21a shows a typical force-delamination length curve from the DCB test.

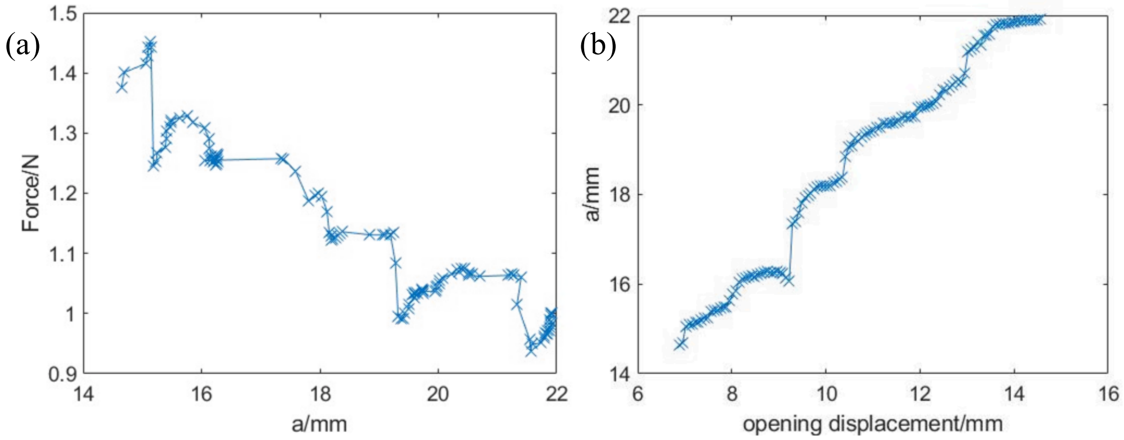

Figure 3.21. (a) Force-delamination length curve for a typical DCB test (PMMA_Line_15000) and (**b)** its corresponding delamination length versus opening displacement

The opening displacement was obtained from DIC. The displacement of the top and bottom plies was computed by taking the average displacement along the y-axis across each of the bolts. The opening displacement was the difference in displacement between two bolts. The compliance, *C,* for each step was calculated by dividing the force by the displacement. The rotation correction factor, Δ, was then determined by plotting $C^{1/3}$ against delamination length a and fitting a linear equation to the data. Extending the fitted line to intersect with the x-axis provided the value of Δ. In this instance, Δ is found to be 4.0061 mm with R-squared of 0.9921, indicating over 99% of variability could be explained by the fitting.

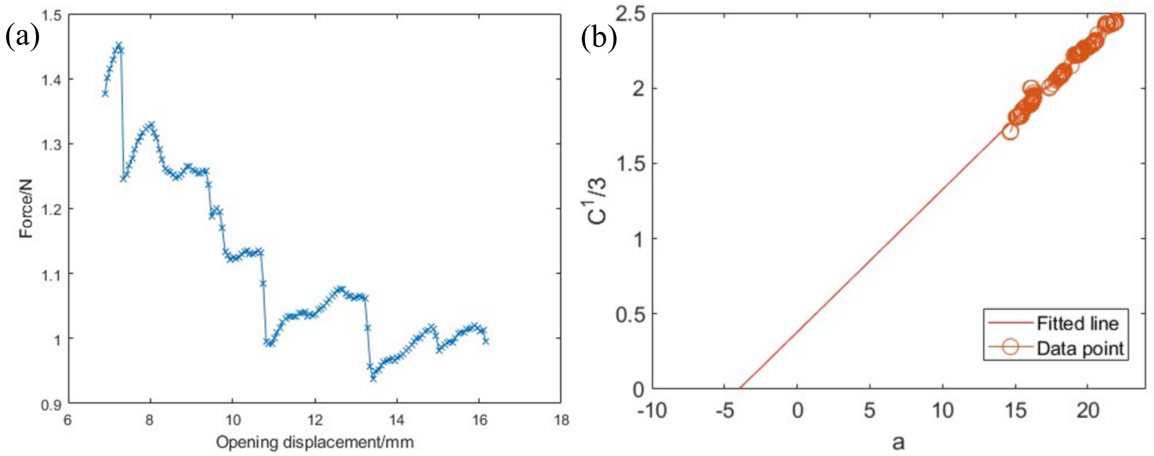

Figure 3.22. Example of **(b)** Determining of *Δ* for delamination length calibration (PMMA_Line_15000 specimen) from **(a)** Force-displacement curve

The correlation factors *F* and *N* were computed using equitation 3.2 and 3.3 respectively. Figure 3.23 illustrates the ratio of *F* to *N* as crack progress. Following the determination of these correlation factors for each specimen individually, they were then incorporated into equation 3.1 to determine the fracture toughness. The results of this calculation are presented and discussed in the subsequent section.

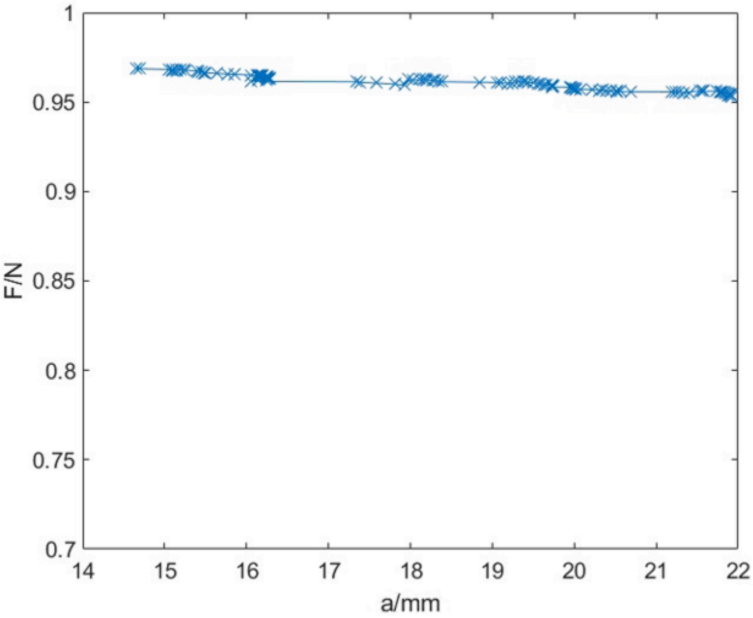

Figure 3.23. Correlation F/N with crack propagation (in PMMA_Line_15000 specimen)

3.2.4 Results and discussion

The details of G_{IC} evolution with crack propagation for the NP_1 and PEG_Hex_20000 specimens are given in Figure 3.24. Both were printed in 2019. Overall, there is no significant R-curve behaviour.

Standard deviation (σ) and standard error (ϵ) were calculated for each specimen group:

$$\sigma = \sqrt{\frac{1}{n-1}\sum_{i=1}^{n}(G_{ICi} - \overline{G_{IC}})^2} \qquad （3.5）$$

$$\epsilon = \frac{\sigma}{\sqrt{n}} \qquad （3.6）$$

where n is the number of specimens and $\overline{G_{IC}}$ was the arithmetic mean of the measured fracture toughness in the certain sample group). Standard deviation measures the amount of variability of a set of data, which quantifies how much the values in the dataset deviating from the average of the dataset. Whereas standard error counts the precision with which a sample mean represents the population mean, and it provides information about the accuracy of the mean of a dataset as an estimation of the population mean.

The average $\overline{G_{IC}}$ of the NP_1 specimen is 266 J/m^2 from 9 samples, with a standard deviation (σ) of 17 J/m^2 and standard error (ϵ) at 6 J/m^2. The scatter of G_{IC} is stronger for the PEG-printed specimen. According to un-paired, two tailed student's t-test analysis, the measured fracture toughness of PEG_Hex_20000 is statistically higher than the NP_1 specimens.

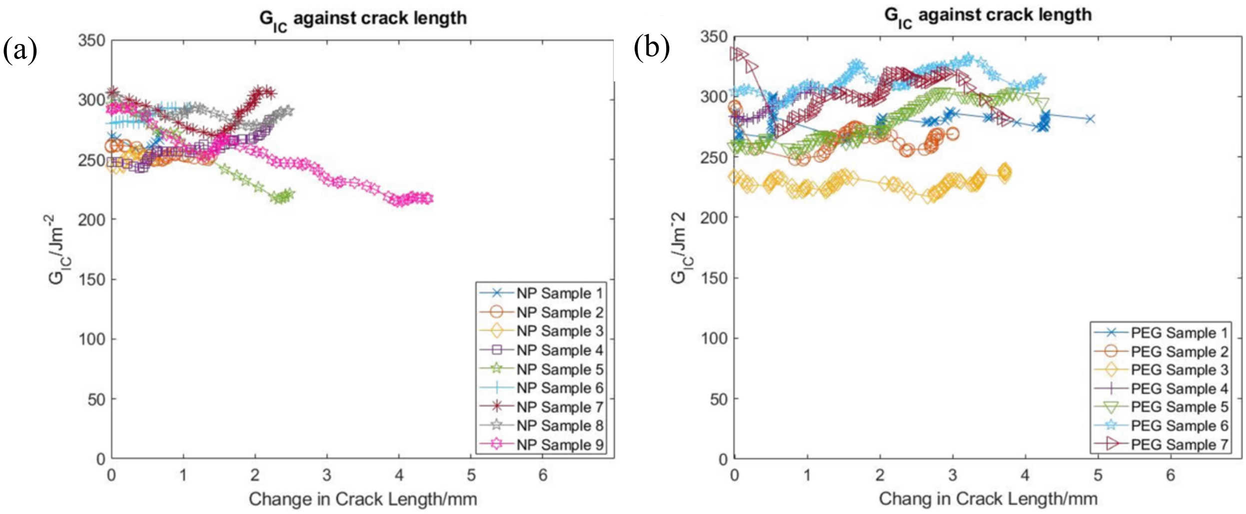

Figure 3.24. Comparison of fracture toughness evolution with crack propagation between **(a)** NP_1 [10] and **(b)** PEG_Hex_20000 specimens

The fracture toughness of line-printed PEG_Line_400 and PMMA_Line_15000 as well as the corresponding NP_2 laminates were summarized in Figure 3.25. These were all printed in 2021. The measured fracture toughness with standard error for the three specimens are: NP_2: 242 ± 8 J/m^2, PEG_Line_400: 304 ± 12 J/m^2 and PMMA_Line_15000: 275 ± 7 J/m^2 respectively.

The hexagonal and line pattern specimens were made separately with a 2.5-year gap (Owing to the lockdown during the pandemic). It has previously been reported by Yi that there would be a degradation of prepregs by storing in fridge over time, which results in a decline of composite fracture toughness post curing. Therefore, the PEG_Hex_20000 specimens were compared with Yijun's non-printed DCB measurement (NP_1) [10], where the prepregs were freshly cut. The PMMA_Line_15000 and PEG_Line_400 samples were analysed alongside the non-printed laminate (NP_2) that was stored for the same duration and cured together.

This shows 26% enhancement of the work of fracture with PEG droplets and 14% with PMMA deposits. Non-paired, two-tail student t test (significant level at P = 0.05) was conducted between the measured G_{IC} data within the three sample groups, as shown in Table 3.6, the result illustrates that all the printed specimens were statistically more tough than the specimens without printing.

Table 3.6. Student T-test for work of fracture

Sample compared		**P value**	**Result (Different: P<0.05)**
PMMA_Line_15000	NP_2	0.007	Different
PEG_Line_400	NP_2	0.001	Different

The PEG_Line_400 shows 20% higher toughness than the hexagonal pattern PEG_Hex_20000. Given that it has been reported that the printing pattern does not affect the toughening efficiency [10], this indicates printing dots with a smaller molecule might provide a better toughness enhancement. Moreover, by comparison with the previous group of non-printed (NP_1) specimens' measurement, the fracture toughness of laminate (NP_2) underwent a degradation of 9% over the 2.5 years.

The summary of fracture toughness for all the non- and printed- specimens is displayed in Figure 3.26. Note that specimen 'NP_1' and 'PEG_Hex_20000' were made together previously, while the 'NP-2' and line-printed samples (PMMA_Line_15000 and PEG_Line_400) were manufactured later using raw CFRP prepregs that had been stored in fridges for two and half years.

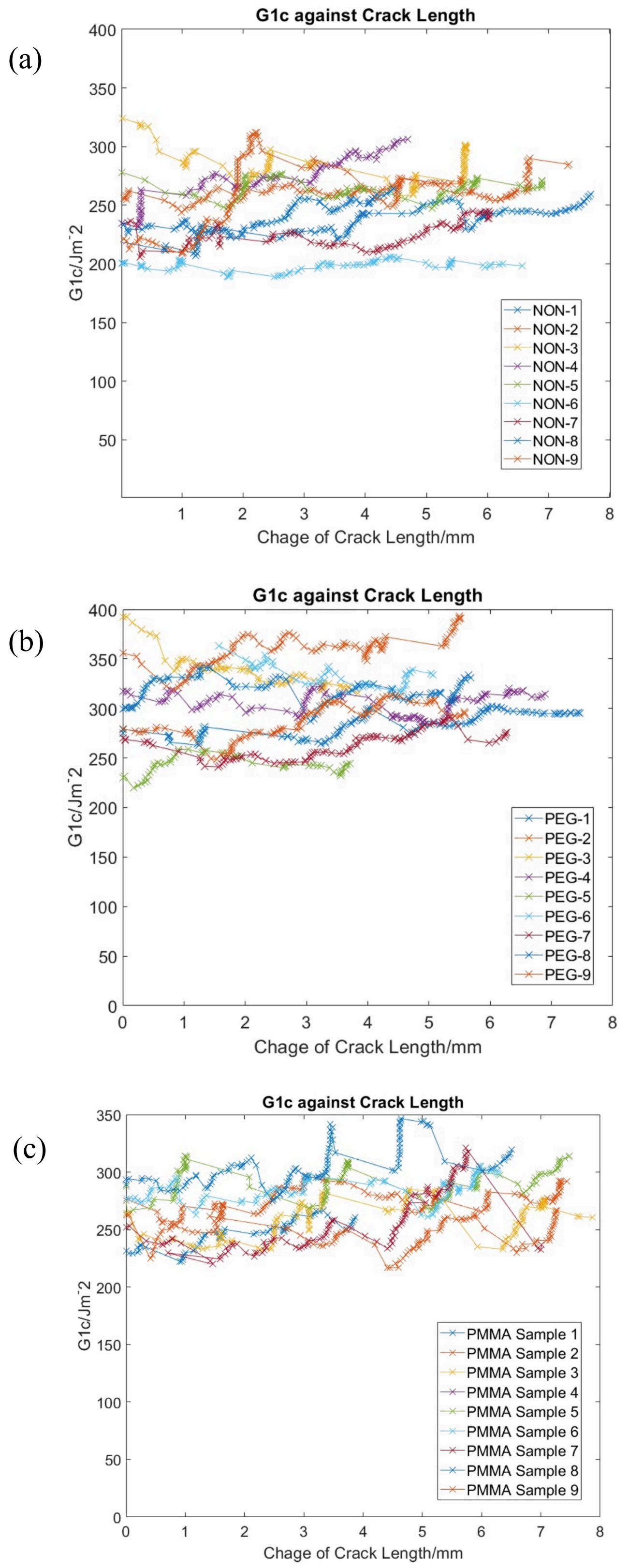

Figure 3.25. Comparison of fracture toughness evolution with crack propagation between **(a)** NP_2, **(b)** PEG_Line_400 printed specimens and **(c)** PMMA_Line_15000 printed specimens

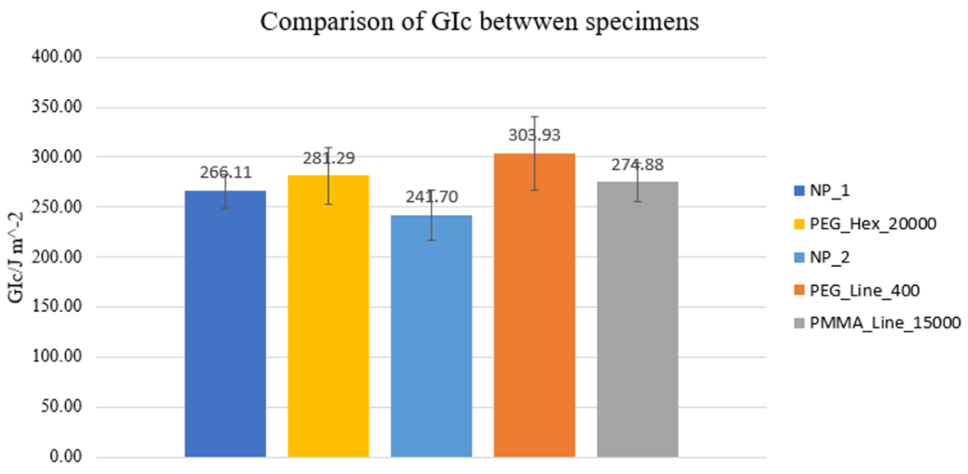

Figure 3.26. Comparison of G_{IC} between printed specimens and virgin laminates

3.2.5 Error Analysis

The errors associated with G_{IC} evaluation came from the uncertainty of determination of delamination length (a), sample dimension (b), opening displacement (δ) and the track of load (σ), which could be estimated for non-correlated errors using equation from:

$$\frac{\Delta G_{IC}}{G_{IC}} = \sqrt{(\frac{\Delta a}{a})^2 + (\frac{\Delta b}{b})^2 + (\frac{\Delta \delta}{\delta})^2 + (\frac{\Delta P}{P})^2} \qquad (3.7)$$

The major error resulted from the un-avoiding paint fibres (Figure 3.27) formation during the loading, which underestimated the crack length using the segmentation method mentioned above. An uncertainty test has been conducted to quantify the inaccuracy using the segmentation method, and on average the measured crack tip was 0.6 mm behind the visual crack tip. The delamination length error from torturous crack tip was neglectable compared with that from paint bridges, which according to observation under XCT that the crack front position varied by around 60 um across the width [11]. The other three errors of quantities were determined by the resolution of equipment, which was summarized in Table 3.7. Overall, the measuring uncertainty of G_{1c} was around 3%, which is less than the variability of the measurements.

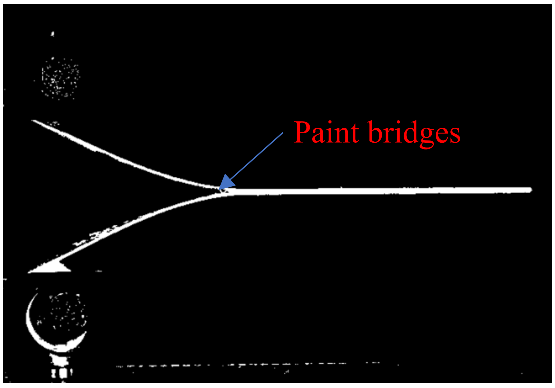

Figure 3.27. Example of paint bridge formation during the opening

Table 3.7. Sources of error for G_{IC} quantification

Factor	**Error (ΔX)**	**Fraction Error ($\frac{\Delta X}{X}$)**
Delamination Length a (mm)	-0.6	3×10^{-2}
Sample Width b (mm)	$\pm$ 0.01	3×10^{-3}
Opening displacement δ (mm)	$\pm$ 0.003	4×10^{-4}
Load P (N)	$\pm$ 0.00001	4×10^{-6}

3.3 Summary

PMMA (Mw ~15,000) and PEG (Mw ~ 400 and 20,000) were inkjet printed in line and hexagonal patterns onto carbon fibre resin matrix prepregs as interfacial tougheners. This was followed by hand lay-up and curing to create the final composite. For the purposes of observational dots behaviour in the resin, printing was also applied on epoxy-coated glasses with fluorescein added, which would then be characterized under fluorescein microscope. The detailed methodology and result available in the Chapter 5.

To assess the fracture toughness of the two-ply composite laminates, double cantilever beam tests were performed, utilizing digital image correlation (DIC) to monitor the opening displacement during loading. All the printed specimens demonstrated statistically significant higher toughness than the virgin composite, with PEG_Line_400 exhibiting the largest improvement in work of fracture that showing a 24% higher G_{IC}. A 9% of decline was noted on the non-printed laminate specimens over the two-years storge. Overall, the toughening effect of inkjet printing of thermoplastic droplets has been demonstrated in the scale-down specimens, which will be further employed in subsequent characterizations for observation and exploring the toughening mechanisms.

3.4 References

[1.] Jumahat A, Soutis C, Jones FR, Hodzic A. Fracture mechanisms and failure analysis of carbon fibre/toughened epoxy composites subjected to compressive loading. Composite Structures. 2010;92(2):295-305.

[2.] Zhang Y. The effect of inkjet printed polymer on the mechanical properties of carbon fibre reinforced plastic: University of Sheffield; 2015.

[3.] Calvert P. Inkjet Printing for Materials and Devices. Chemistry of Materials. 2001;13(10):3299-305.

[4.] Reu P. All about Speckles: Contrast. Experimental Techniques. 2015;39(1):1-2.

[5.] Baqersad J, Poozesh P, Niezrecki C, Avitabile P. Photogrammetry and optical methods in structural dynamics – A review. Mechanical Systems and Signal Processing. 2016;86.

[6.] International A. D5528-01 Standard Test Method for Mode I Interlaminar Fracture Toughness of Unidirectional Fiber Reinforced Polymer Matrix Composites1. 2009.

[7.] W. Johnson JM, T. O'Brien, and R. Martin. Round Robin Testing for Mode I Interlaminar Fracture Toughness of Composite Materials. J Compos Technol Res. 1993;vol. 15, no. 4, p. 269.

[8.] M. S. Sham Prasad CSV, and T. Jayaraju. Experimental Methods of Determining Fracture Toughness of Fiber Reinforced Polymer Composites under Various Loading Conditions. J Miner Mater Charact Eng. 2011;vol. 10, no. 13, p. 1263, 2011.

[9.] Lahuerta F, Westphal T, Nijssen RPL, van der Meer FP, Sluys LJ. Measuring the delamination length in static and fatigue mode I tests using video image processing. Composites Part B: Engineering. 2014;63:1-7.

[10.] Lim Y. In-Situ 3D observation of damage development and healing in a carbon-fibre/epoxy composite: University of Oxford; 2019.

[11.] Zhang Y. In situ 3D observation of delamination crack propagation in carbon-fibre/epoxy composites: University of Oxford; 2018.

Chapter 4

4. In-situ observation of crack propagation

The toughening effect due to inkjet printing was demonstrated in the scaled-down laminates with two plies in Chapter 3. To optimize the materials design, it is essential to examine crack propagation behaviour and subsequently understand the toughening mechanisms. Synchrotron X-ray technology offers a variety of advanced techniques for the in-situ observation of materials evolution. For example, by fast switching between image and diffraction mode, dual imaging and diffraction characterization could be achieved, which enables the capability to capture dynamic 2D or 3D images of complex structures while performing elastic strain mapping or phase identification with micro-diffraction. Moreover, the highly coherent and bright X-rays produced in a synchrotron light source enable high resolution, fast in-situ 3D tomographic images that are not achievable in lab based XCT.

In this chapter, Mode I opening behaviour induced by wedge insertion at the interface between plies was explored by dual radiography imaging/diffraction and in-situ phase contrast XCT. The dual beam approach marked a pioneering attempt to map the elastic strains in a unidirectional carbon fibre composite during delamination propagation, with digital image correlation (DIC) used to track the crack tip propagation. In-situ XCT studies were performed on different beamlines with both qualitative and quantitative analyses of crack behaviour to understand damage evolution in inkjet printing modified CFRP.

4.1 In-situ X-ray diffraction of strain mapping of damage development

To assess the mechanical effects of printing dots on the laminate, it is crucial to study the stress and strain evolution with crack propagation. Techniques such as in-situ X ray radiography or tomography imaging, subsequently analysed by DIC or DVC offer the capacity to map the total strain field in bulk materials and track the crack tip motion. Meanwhile, in-situ synchrotron X ray diffraction (SXRD) can be used to evaluate the elastic strains by measuring the crystal lattice deformation. A schematic of an in-situ XRD test set up is present in Figure 4.1: An incident X ray beam interacts with the target materials and undergoes Bragg diffraction in the periodic crystal structure. The emergent beam is collected by the detector where the Debye diffraction rings are observed. Following Bragg's law:

$$d = \frac{\lambda}{2sin\theta} \quad (4.1)$$

with the known monochromatic wavelength (λ) of incident X ray and calibration of the experimental set up geometry, the D spacing (d) can be measured [1]. A 1D diffraction spectrum is usually generated by integrating the Debye ring over specific azimuth angle ranges. The reciprocal of the D-spacing is sometimes used, where q is calculated as:

$$q = \frac{2\pi}{d} \quad (4.2)$$

With lattice deformation, the distances between crystal planes (D spacing) increase with tensile loading and reduce with compression, which results in a change of Debye ring diameter.

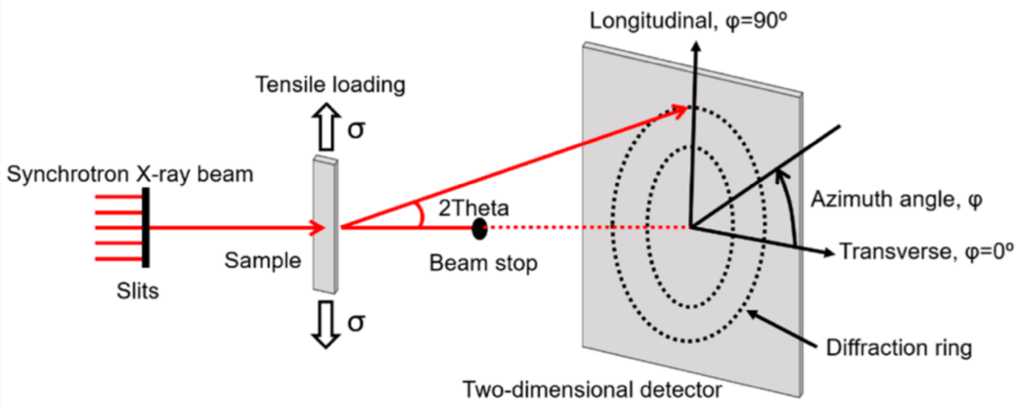

Figure 4.1. Schematic of in-situ synchrotron XRD experiment set up [2]

Strain evaluation using synchrotron X ray diffraction has been well developed in polycrystalline materials such as alloys and ceramics. Its application in carbon fibre composite has been limited due to the complex turbostratic crystal structure (Figure 2.1, Chapter 2). The feasibility of using SXRD for strain analysis in CF could be found in [3, 4]. For example, as shown in Figure 4.2, Srisuriyachot conducted an in-situ diffraction test to analyse strain in a 3-mm thick UD CFRP sample under buckling condition, characterized on the B16 beamline at the Diamond Light Source. The Debye ring with Miller index (002), whose lattice constant d(002) representing the spacing between the periodic graphene layers is highlighted in green. As the carbon fibre is partially crystallized and highly oriented, the (002) peak only exists over partial azimuth angles around the ring. This work introduces the application of SXRD to investigate strain evolution during damage development in CFRP, where delamination was achieved by wedge insertion, with the aims of understanding the impact of inkjet printing dots on crack propagation.

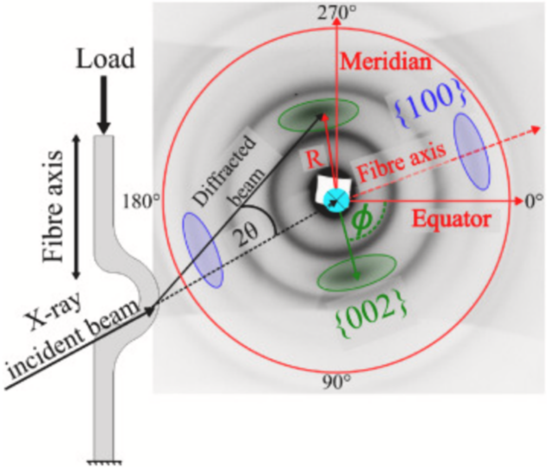

Figure 4.2. Buckling loading condition and the resulting diffraction pattern of CFRP [3]

The Dual Image and Diffraction (DIAD) beamline in Diamond Light source was utilized here to perform simultaneous X ray imaging and diffraction (Experiment Number 30723). Most synchrotron beamlines provide either imaging or diffraction, or only allow their combination by complicated and time-consuming changes of setup that limit the capacity to characterize the deformation through time. The DIAD beamline was opened in 2021, which provides X-rays in the medium energy range (7-38 keV) and a schematic of its optics and end station is presented in Figure 4.3: The imaging (red ray in the figure) and diffraction (blue ray) beams sharing one wiggler source were independently operated and converge at the same sample position. A beam selector is used to select the target beam while blocking the other. Between the beryllium window and exit window, a series of optics such as mirror and double crystal monochromators (DCM) was used to manipulate the beams. The outgoing beams are collected by the two detectors for either radiation or diffraction patterns. Typical diffraction beamlines with a fixed X-ray source often move the specimen to adjust the region of interest, which can be problematic in situations when the sample is not able to move rapidly such as large, heavy, or fragile specimens. DIAD's set up enables shifting of the diffraction beam within the imaging field of view to resolve the issue, enabling real-time monitoring of dynamic process by point the diffraction point to the region of interest in the specimen to collect data. However, a significant drawback of this moving beam in the dual set up is that the off-axis position of imaging detector can limit the capacity to collect the whole Debye ring with its centre on the detector. This can reduce the strain evaluation accuracy. As the relative position between the X ray source, sample and detector is not constant over the inclined 2D detector surface, the transformation from the collected data to reciprocal space is more complex. As a result, precise calibration of the moving beam and its energy are crucial on DIAD to determine the relative positions between sample/beam intersection point and detector [5].

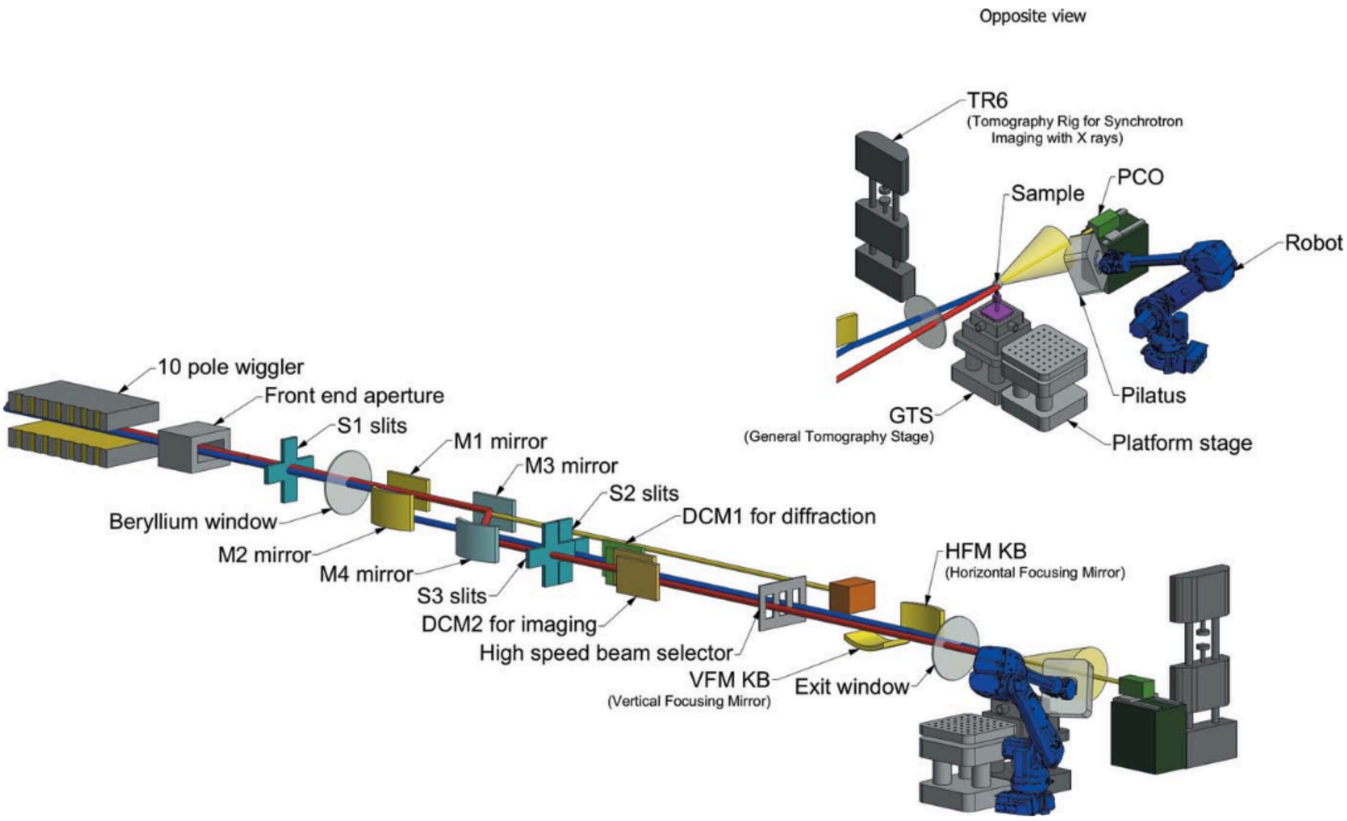

Figure 4.3. Schematic of DIAD beamline set up, with the red ray represents the imaging beam while blue ray the diffraction beam [5]

4.1.1 Experimental

In this experiment, samples of non-printed (NP_2), PMMA printed (PMMA_Line_15000) and PEG-printed (PEG_Line_400) were characterized. Each 0.5 mm thick laminate was cut by low-speed diamond saw to the final tested dimension of 0.5 x 3 x 50 mm with a 10 mm length pre-crack along the fibre direction that was generated by the PTFE film between the plies before curing (Chapter 3). A schematic of the customized experiment set up is shown in Figure 4.4: The sample loading was achieved by inserting a 1-mm thick aluminium plate into the pre-crack, using a PI ltd. M-229.25S linear actuator controlled by a C-663.12 stepper motor controller, operated with PIMikroMove 2.31.2.0 software. The other end of the sample was tightly clipped with a block. The actuator was supported by a 5 mm-thick aluminium tube. To avoid attenuation from aluminium, the tube was modified to have two opposing slots to transmit the incident and transmitted/diffracted X rays (4 x 30 mm and 8 x 30 mm respectively). The specimen was oriented at a fixed angle with the X ray beam of 45°.

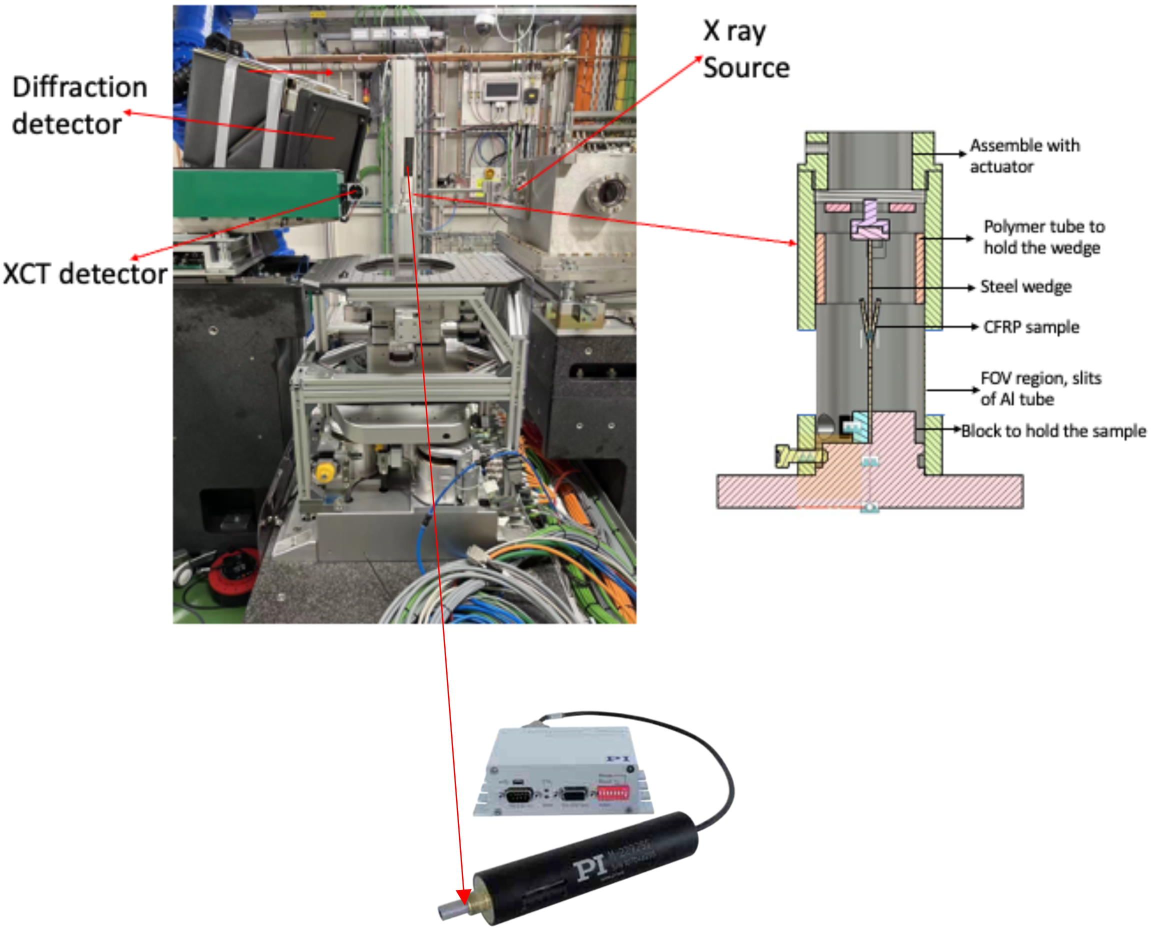

Figure 4.4. Experimental set up and detail of loading condition

The objective of the experiment was to measure the transverse strains in the carbon fibres ahead of the crack tip (i.e. strains perpendicular to the crack plane). Previous studies had shown that the crack front is not perfectly straight [6, 7], so measurements by diffraction with the transmitted beam parallel to the crack front would not be suitable to obtain measurements that were local to the crack tip. To address the problem, the diffraction measurement was conducted with beam 45° inclined to the sample, as schematic in Figure 4.5. The 45° orientation provided a compromise that was designed to obtain sufficiently local measurements of the transverse strains in the fibres, due to the crack tip opening, that could be used to study whether these are affected by printing. Tomography was not performed to reduce the risk of beam damage from prolonged exposure. The slits in the aluminium tube would also affect the background (flat) image. Analysis of radiographs was therefore used to identify the crack tip.

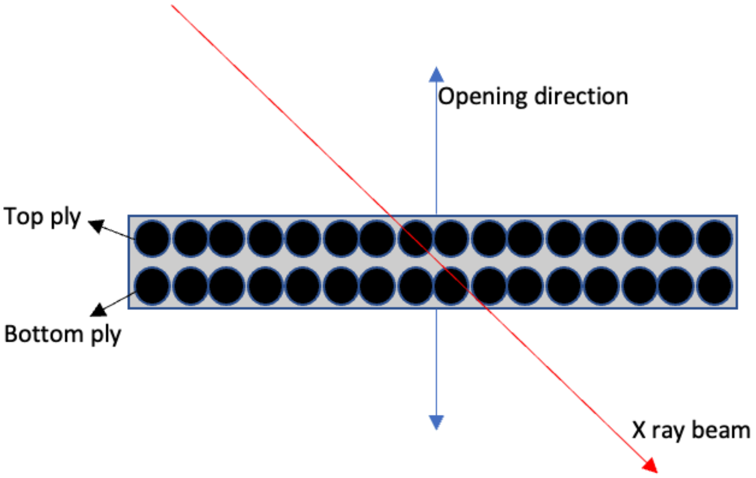

Figure 4.5. Schematic from top view (Figure 4.4) of relative position between laminate and X ray beam, black circles represent the cross-section of carbon fibres

Monochromatic X rays beam at 21 keV were used. Radiographs were captured by the PCO.edge 5.5 detector (2560 x 2160 pixel with 0.54 µm pixel size, with 1.9 s exposure time) with a field of view (FOV) of 1382 x 1166 µm. The diffraction measurements were obtained with the beam reduced by slits to 50 x 50 µm. Calibration of the photon energy and diffraction set-up were achieved using LaB_6 (SMR 600b) and CeO_2 (SMR 674b) standard samples.

Reference data were firstly taken before the crack was propagated into the field of view. The crack was then propagated by moving the wedge at 15 µm/s displacement rate. With this experimental set up, the crack was driven from the top of FOV to the bottom. The first observation step was taken once the crack had just propagated into the radiography FOV. At intervals of 30 µm wedge movement, the displacement was held constant while the radiography and then diffraction observations were recorded. All of the radiographs were taken through the slit in the tube, which captured the laminate at a 45° angle. As shown in Figure 4.6, each diffraction observation mapped a line profile along the fibre direction from the top to bottom in the middle of the radiography FOV with 50 µm distance between the centre of each diffraction point.

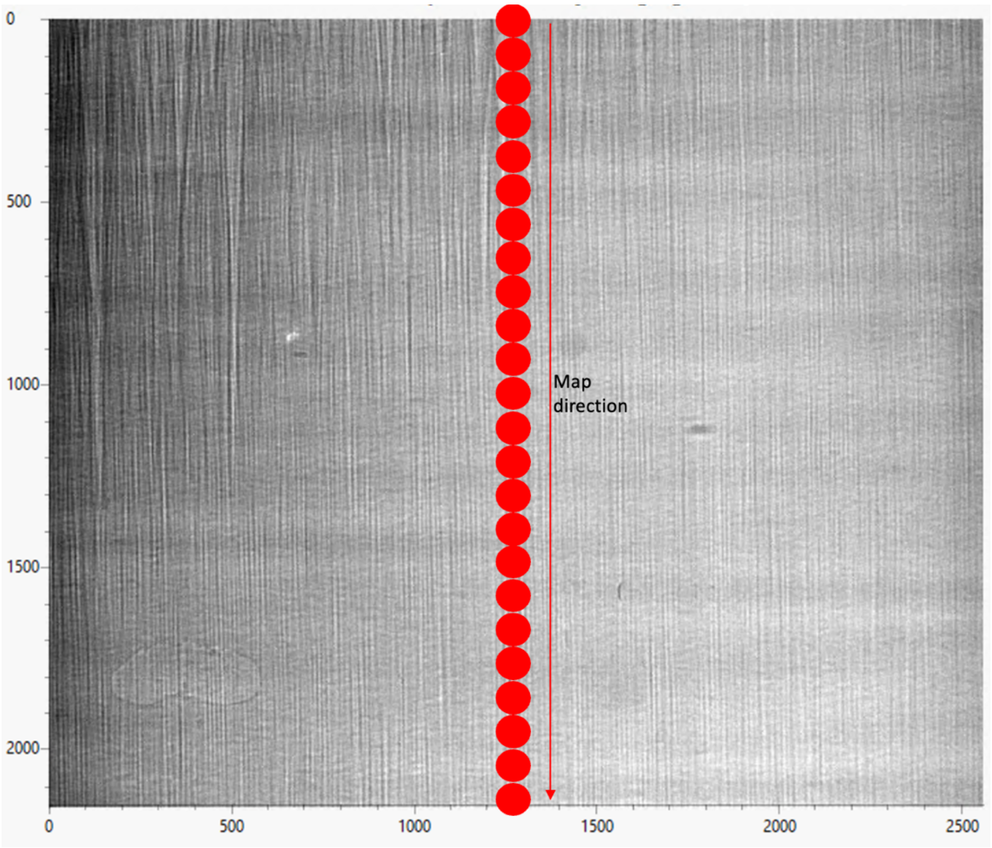

Figure 4.6. Schematic of diffraction points of line pattern (red circles) in the radiograph FOV

4.1.2 DIC detection of crack tip position

To monitor the crack tip propagation, radiography was performed at each step of advancement. These images were then analysed by digital image correlation (DIC) with reference to a radiograph of the intact region in its unstrained state. The reference radiograph was captured when the crack tip was several mm from the FOV. The subsequent in-situ radiographs were taken immediately after each step of crack propagation, prior to the collection of diffraction signal. In between the reference and the first in-situ image, the wedge was driven ~ 3.5 mm into the pre-crack, which resulted in a small horizontal movement of the specimen of ~ 150 µm. The vertical movement was negligible due to the fixing of the specimen base. This is illustrated by the motion of blue triangle and square in the radiographs in Figure 4.7 (a) & (c), which have not been corrected for scintillator artefacts (flat field correction). Images from reference and deformed states were registered in the horizontal direction based on the material features (marked in blue) using Fiji/ImageJ. Examples of registered images are presented in Figure 4.7 (b) & (d).

The red circles in Figure 4.7 (e) indicate detector defects (such as dust contamination of the scintillator), identified through a flat field image. To eliminate these artefacts and improve the DIC quality, both flat field and dark field corrections were applied to the radiographs. The dark field image was taken before any data acquisition by closing the X ray shutter and recording signal at the detector. The flat field image was obtained after the experiment by moving the sample and stage to acquire a direct image from the beam.

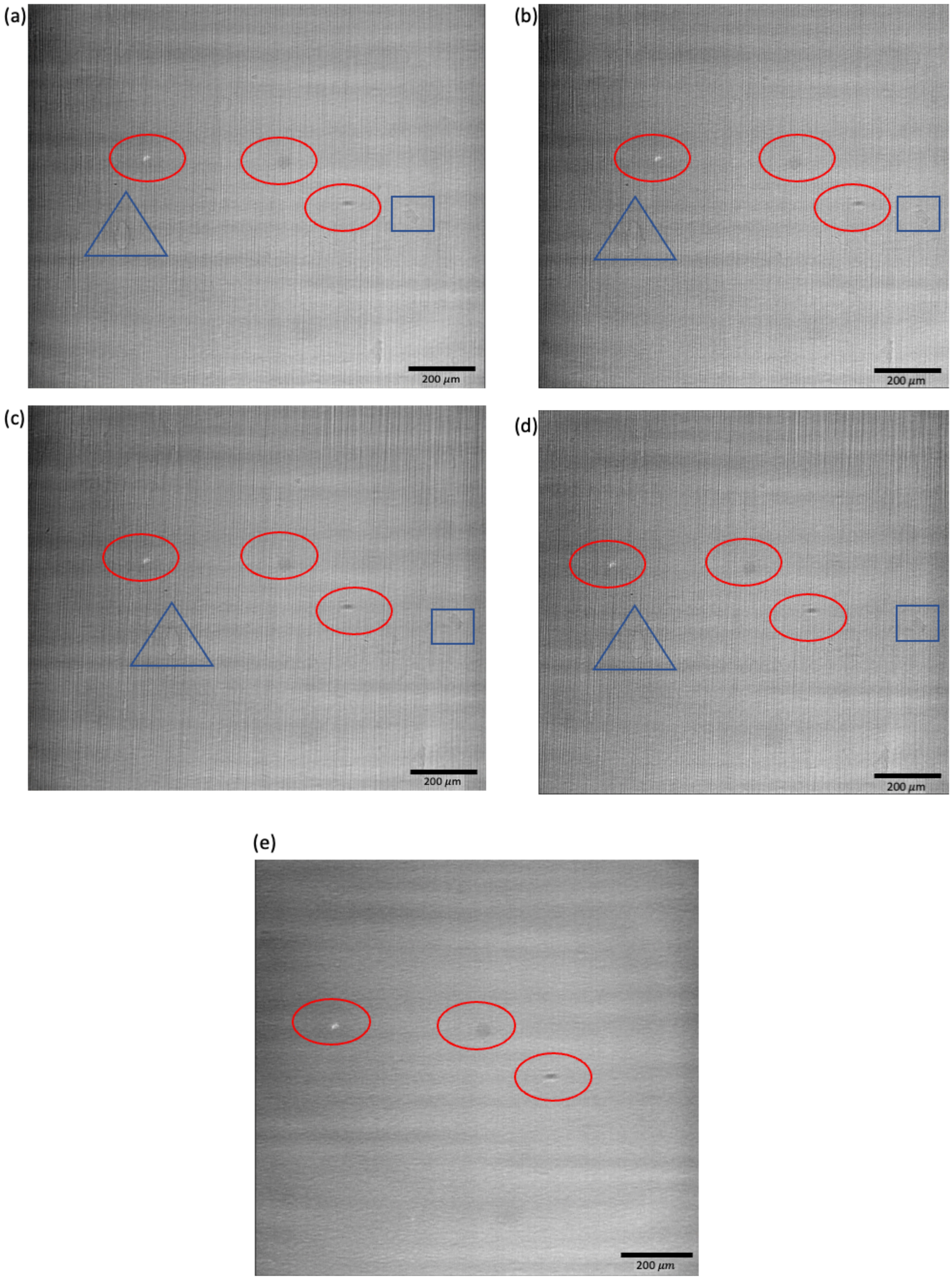

Figure 4.7. Radiographs (uncorrected) of reference **(a,b)** and deformed step **(c,d)** of PMMA printed specimen before and after location correlation respectively, where the blue triangle and square highlight the microstructure features on the specimen; **(e)** flat field image showing flaws on the detector marked by red circles.

The corrected image (C) is obtained using ImageJ following equation:

$$\mathrm{C} = \frac{(\mathrm{R}-\mathrm{D})\ \mathrm{x}\ \mathrm{m}}{(\mathrm{F}-\mathrm{D})} \qquad (4.3)$$

where R is the raw image, F and D represent the flat and dark field frame respectively and m stands for the image-averaged value of (F-D) scalar [8]. The corrected images in the same FOV as Figure 4.7 are shown in Figure 4.8, where defects from detector have been significantly removed and crack can be visualized at the top of the field of view in Figure 4.8 (b). The crack tip is quite difficult to see, so the corrected radiographs were analysed by digital image correlation (DIC) to detect the crack tip position. The DIC analysis was performed after registration to remove significant horizontal displacements by inspection of the position of microstructure features.

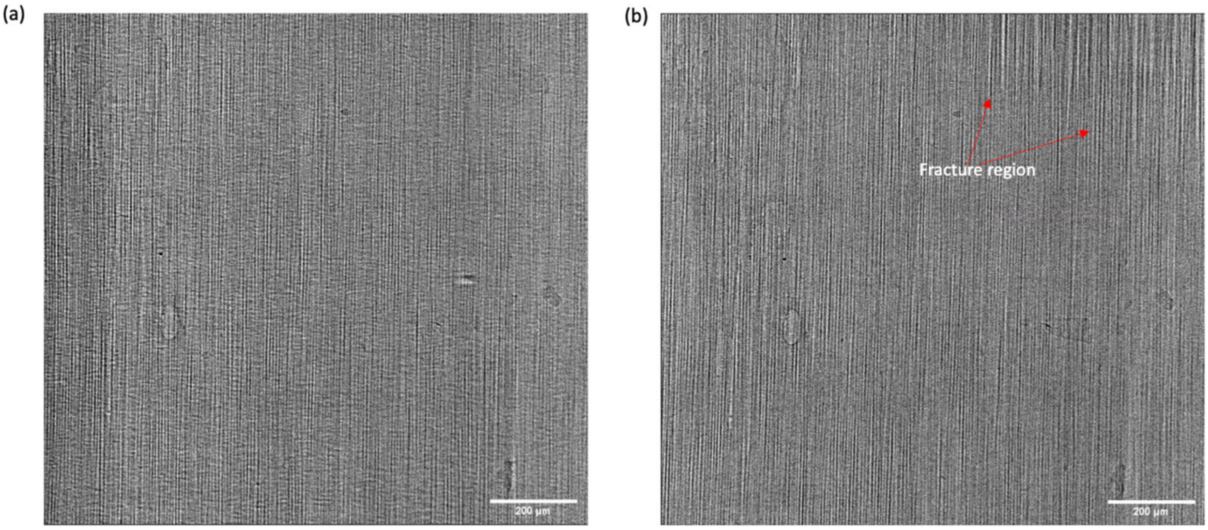

Figure 4.8. Example of radiography after flat field correction for **(a)** reference without crack and **(b)** step 12 of PMMA specimen

LaVision DaVis 8.4.0 software was used for Digital Image Correlation calculations. As the X ray image incident beam is inclined at an angle of 45° to the mode I fracture plane, conventional mapping of the displacement field is not possible. The opening of the crack alters the relative positions of fibres on either side of the open crack, which would lead to reduced correlation in the crack wake between the reference and loaded radiographs. High correlation is expected ahead of the crack tip in the undamaged region. This differentiation allows identification of the crack tip position.

In the DIC analysis, a 3x3 Gaussian filter was applied initially to smooth the images. The deformation calculation was achieved through the Least Square Matching (LSM) algorithm, where the radiograph was divided into multiple subsets, and within each subset, an interactive algorithm approximates the deformation through affine transformation. The subset size defines the area for displacement vector evaluation, which is related to the spatial resolution. A smaller subset size increases the resolution, while sacrificing the correlation accuracy. The maximum subset size available in DaVis 8.4.0 is 256 pixels [9]. To optimize the calculation parameters, DIC was first performed on a non-damaged observation of PMMA_Line_15000 where the image was expected to have high correlation with the reference. The subset size was sequentially reduced from 256 to 64 pixels. The maps of correlation value are presented in Figure 4.9: a higher correlation means better alignment between reference and strained images; position where correlation value is lower than certain point (will be defined in the next part) refers to where crack appear. To quantify the result, a 35 μm wide rectangular strip was selected in the middle of the map from the top to bottom of FOV (highlight in red). This represented the region of where the X ray diffraction line map would be done. The correlation values at each X position are the arithmetic mean across the strip, and are reported in Figure 4.9 (b), (d) & (f), where the error bar is standard error. Reducing the subset size from 256 to 128 pixels significantly improve the mapping resolution. A further reduction to 96 pixels offers marginal improvement and resulted in decreased correlation accuracy and increased computational cost. Therefore, a subset size of 128 pixels was selected in the work.

The step size was chosen through analysis of observations in the undamaged region (i.e. between step 1 and step 4, where the crack has not propagated into the field of view) that the bulk of material was expected to exhibit a uniform displacement. The DIC analysis was conducted on the raw images here instead of having a horizontal registration as shown in Figure 4.7. This is because between step 1 and step 4, with 90 µm movement of wedge insertion the shift of the laminate was minor compared with that between reference and first deformed image shown in Figure 4.7. By changing the DIC step size from 16, 32, 64 and 96 pixels respectively and averaging out the displacement of all the vectors, the apparent displacements U_X and U_Y with the corresponding standard deviation are displayed in Figure 4.10. The movement in the vertical direction was negligible because the sample was fixed to the bottom of the rig. While in the horizontal axis, the wedge insertion caused an apparent rigid body movement of ~ 4 pixels (2.16 µm). Measurements at 16-, 32- and 64-pixels step size yield consistent result of displacement, with the lowest deviation appeared at 64 pixels size. Besides, 64 pixels step size also gives the highest correlation value with smallest standard deviation at 0.84 ± 0.05. Therefore, 256 pixels subset size with 64 pixels step size was chosen for the following calculations.

Post correlation, an outlier filter and a 2nd order polynomial smoothing filter were applied over a 9x9 area to refine the calculated field of correlation values. A preliminary analysis tracked the first appearance of crack within the FOV, showing the earliest detection of crack from DIC in these specimens is in step 4. As shown in Figure 4.7, the ~3.5 mm wedge movement between reference and the first image leads to a significant rigid body movement of the ROI. As the crack developed further, the correlation between reference and deformed image becomes poorer. Therefore, for each specimen, the correlation was analysed using radiograph from step 2 as the reference for crack tip detection.

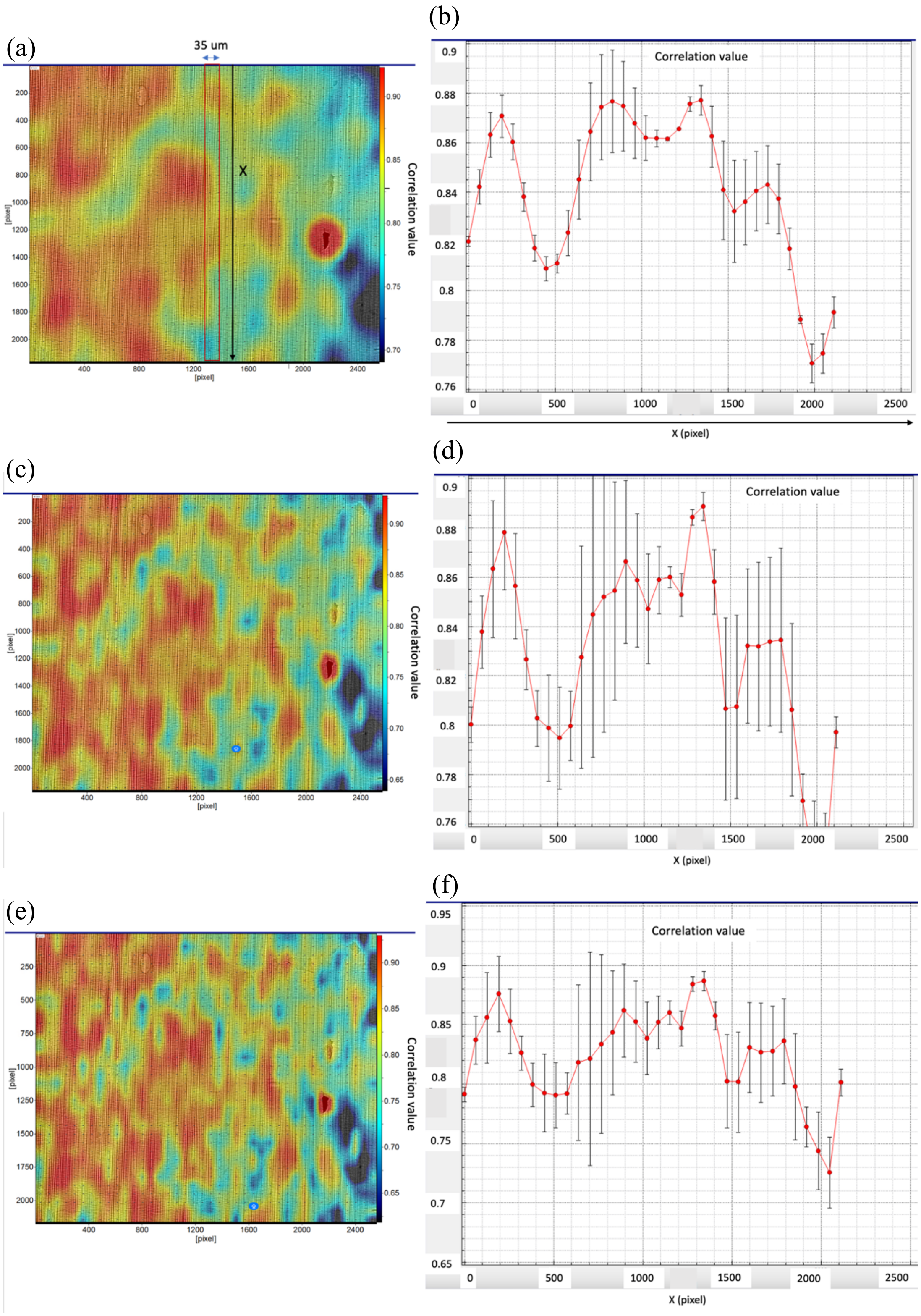

Figure 4.9. DIC correlation mapping and the averaged correlation value along the fibre direction in an undamaged region with subset size at **(a,b)** 256 **(c,d)** 128 **(e,f)** 96 pixels respectively in PMMA_Line_15000 specimen

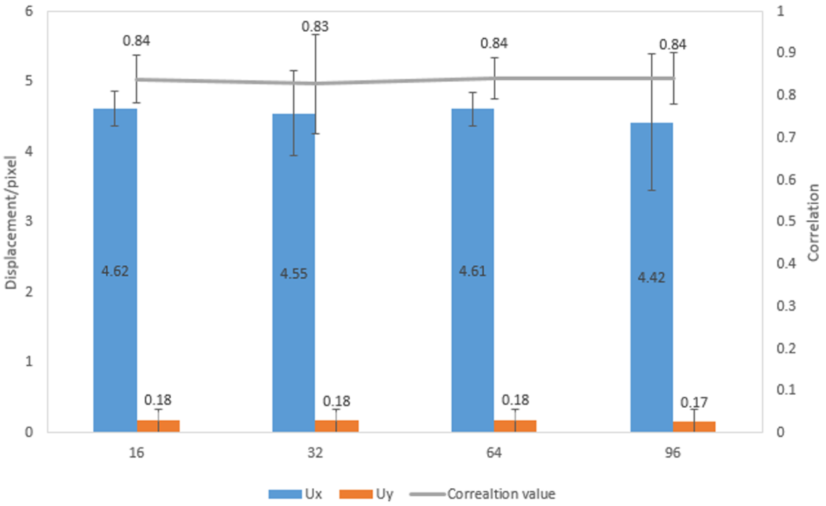

Figure 4.10. Rigid body test showing the horizontal (Ux) / vertical (Uy) displacement and the correlation values with the change of step size on PMMA_Line_15000 specimen

After determining the optimal calculation parameters, DIC analysis was conducted on all steps across the three specimens. Typical correlation maps for both the intermediate and final steps of the three groups are presented in Figure 4.11. It is clear that correlation is high ahead of the crack tip and low in the crack wake. An inclined crack front was observed in the NP_2 and PMMA_Line_15000 specimens, and less so in the PEG_Line_400 specimen. Similar to the undamaged analysis in the earlier description, an example of the averaged correlation values along the fibre axis is illustrated in Figure 4.12. To accurately determine the crack tip position in the field of the diffraction mapping, a criterion was established based on the average deviation of the data points in the clearly undamaged region (here, the last 10 points). The position of first inflection point within the above range of correlation was defined as the crack tip.

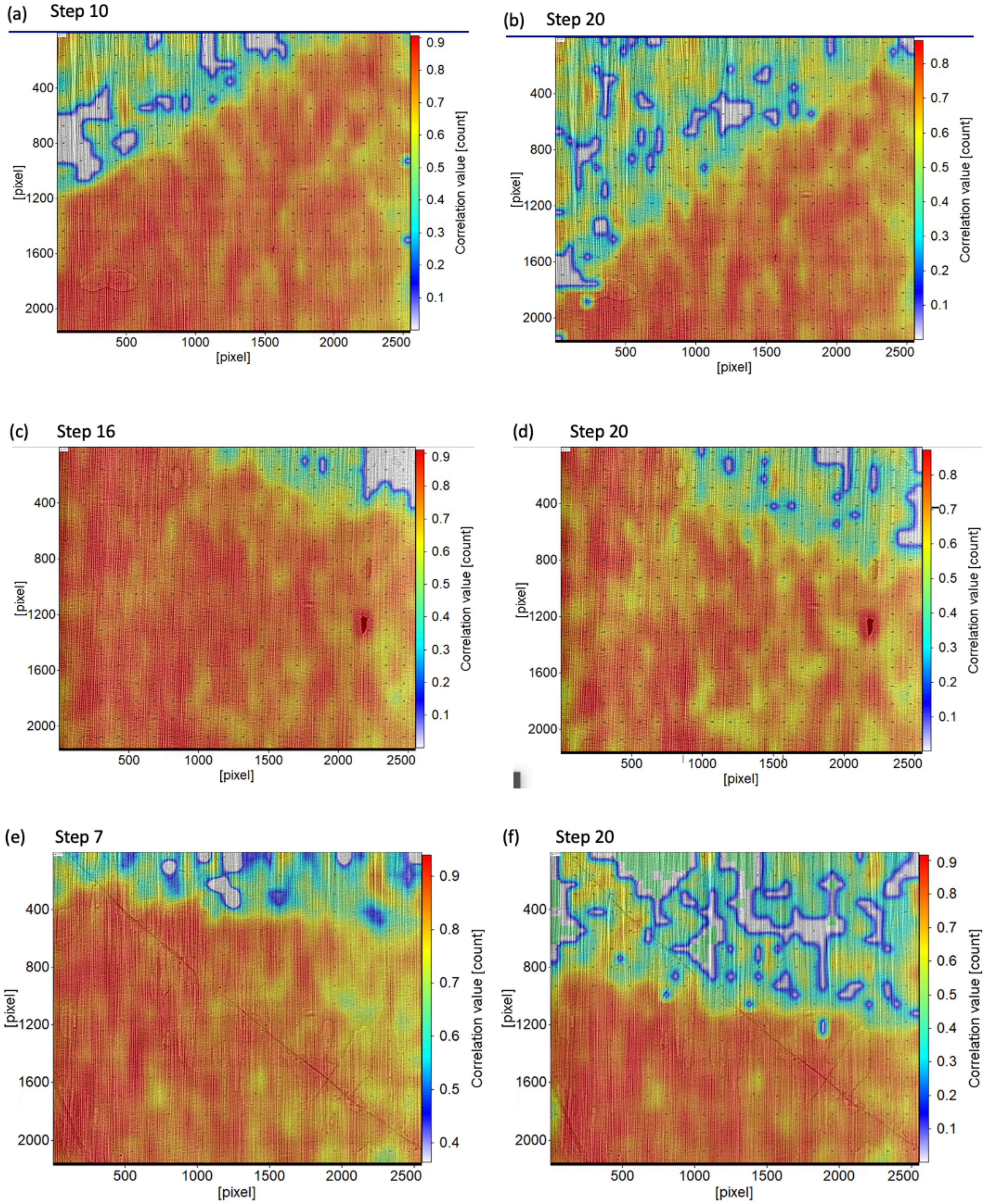

(a) Step 10

(b) Step 20

(c) Step 16

(d) Step 20

(e) Step 7

(f) Step 20

Figure 4.11. Correlation map of **(a,b)** NP_2, **(c,d)** PMMA_Line_15000, **(e,f)** PEG_Line_400 specimens at intermediate and final step of crack propagation

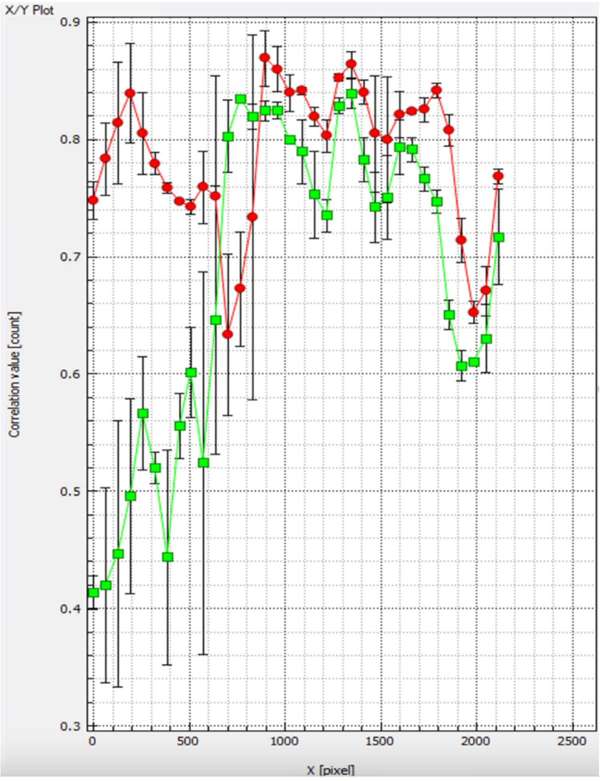

Figure 4.12. Variation of averaged correlation value along the direction parallel in step 5 (red) and step 20 (green) of PMMA_Line_15000

The determined crack tip positions within the region of the diffraction line with the insertion of wedge from first step of radiography are displayed in Figure 4.13. Error in the crack tip definition originates from two main sources: (1) The correlation of DIC: close to and ahead of the crack tip, the standard deviation of the correlation value is much reduced, even considering the fluctuation the value at the crack tip is still above the average level of undamaged area, therefore the correlation value is negligible; (2) Determination of crack tip following the standard as discussed earlier. The actual crack tip might be one point before or after the identified point, which leads to an error of 64 pixel size that equals to 34.56 µm. Due to the variations in the setup of the experiment which defined the start of characterization, the crack tip was first observed in the diffraction region of the FOV from step 6, 16 and 5 in NP_2, PMMA_Line_15000 and PEG_Line_400 samples respectively. To have a better comparison of crack propagation as wedge moved, Figure 4.13 (b) plots the variation of the change in the crack tip position from the first observation of damage in DIC. In the NP_2 and PMMA_Line_15000 laminates, the angle of crack tip changed as the wedge was inserted, therefore, the amount of crack growth at the position of diffraction line could be different. For PEG_Line_400 sample, with exhibited a flat crack front, a clear trend is observed with the progression of wedge insertion. A linear correlation with slope of 1.1 was fitted for PEG_Line_400, indicating the crack moves synchronously with the wedge, consistent with observation from previous in-situ XCT [6].

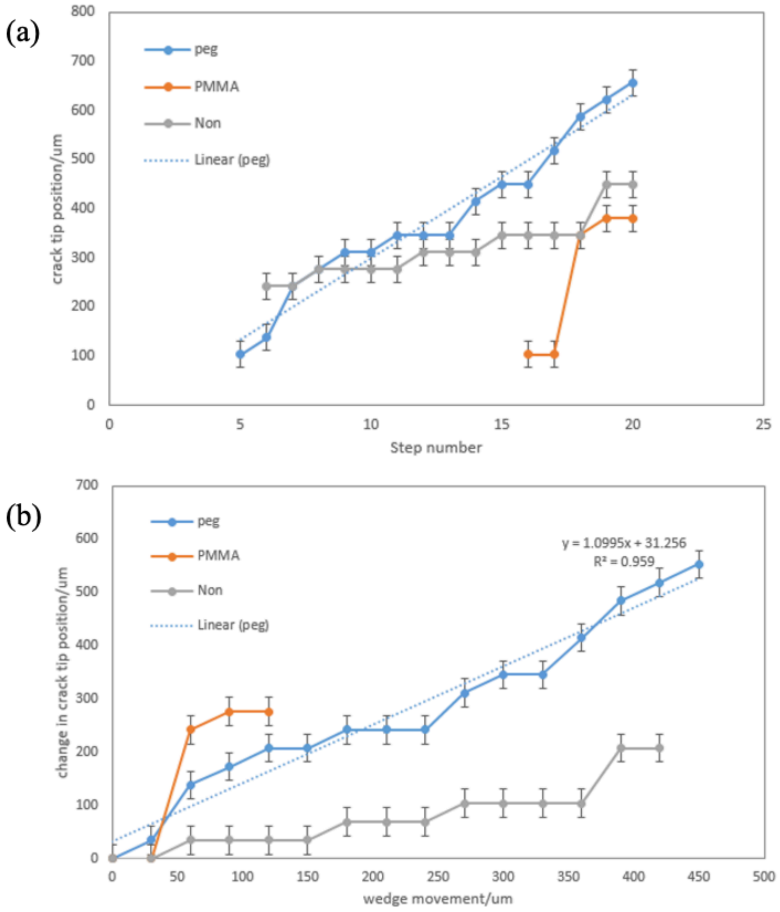

Figure 4.13. Tracking of crack tip positions verses **(a)** step number and **(b)** wedge movement by DIC among the three specimens

4.1.3 Elastic strain mapping

In-situ XRD was utilized to map the lattice strain variations in the same region monitored by radiography-informed DIC for crack tip detection. The diffraction data were recorded with 50 x 50 μm beam slits along the fibre direction, spaced 50 μm apart over a distance of 1200 μm length from the top to bottom of the radiograph.

The raw diffraction data were processed using DAWN [10, 11]. A representative diffraction pattern is displayed in Figure 4.14. Due to positioning constraints of the detector and the transmitting slots of the aluminium tube, only part of the Debye ring was captured. This is, however, sufficient to obtain data from the (0002) peak (q~1.8 A^{-1}) of the carbon fibres [3]. Following the beam calibration, a threshold mask was applied to exclude the spots with intensity counts lower than 0 or higher than 2000. Due to the highly oriented crystal structure of carbon fibre, the diffracted intensity does not appear uniformly with azimuthal angle. Caking over a limited azimuth angle range (-20° to 20°) was performed on the Debye ring to convert the two-dimensional images into 1D diffraction spectra. Pixel splitting was employed, which shared the intensity between bins to avoid step changes of peak and enhance the peak fitting accuracy. An example of resulting output spectrum, showing the q value versus intensity is displayed in Figure 4.15. The major peak, with q at ~ $1.81A^{-1}$ originates from the diffraction of carbon fibre; the peak from the partially crystalized fibres was board and of low intensity.

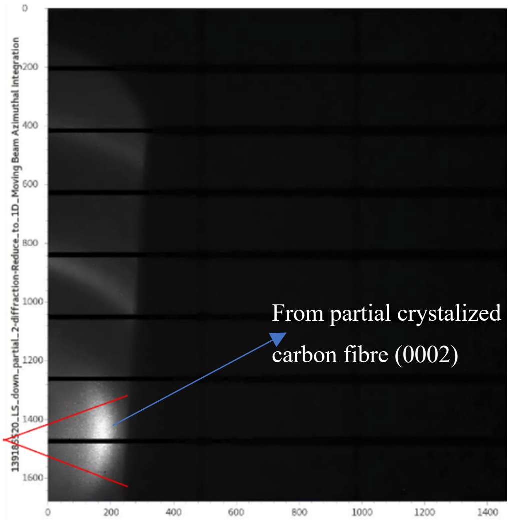

Figure 4.14. Diffraction pattern of CFRP captured in DIAD, with red lines showing the 40° (-20° to 20°) azimuth angle range for data integration

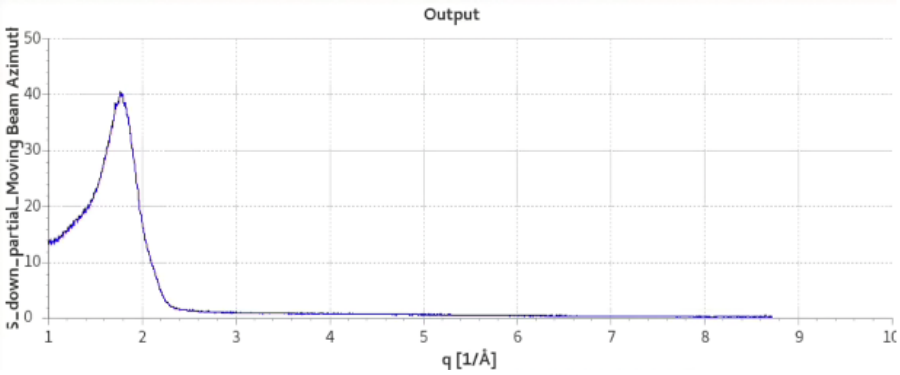

Figure 4.15. Diffraction spectrum after integration showing the distribution of q value

The lattice strain is evaluated as:

$$\varepsilon = \frac{D - D_0}{D_0} = \frac{q_0}{q} - 1 \quad (4.4)$$

where D_0 and q_0 represent the unstrained reference.

A pseudo-Voigt function [12] was used for peak fitting to find the q value of the carbon fibre peak at each diffraction point for strain evaluation. The Pseudo-Voigt function is a convolution of Gaussian and Lorentzian functions to describe a peak. It is defined as weight average of Gaussian peak $G(x)$ and Lorentzian peak $L(x)$, adjusted by a fourth parameter η

that ranges from 0 to 1, which shifts the profile more towards pure Gaussian or pure Lorentzian when approaching 1 or 0 respectively as:

$$pV(x) = \eta G(x) + (1-\eta)L(x) \quad (4.5)$$

The Gaussian and Lorentzian share three parameters: FWHM Γ (full width and half maximum of peak), Peak centre position x and peak intensity I. Therefore, the Pseudo Voigt function could be expressed as:

$$pV(x) = I \cdot (\eta \cdot G'(x,\Gamma) + (1-\eta) \cdot L'(x,\Gamma)) \quad (4.6)$$

In this work, a MatLab script was generated following the ‘pseudo-Voigt’ function, which is an approximation to Voigt function that is more convenient to program, and has been successfully used in analysing synchrotron X-ray data from Thompson et al. [13] :

$$pV(x) = I_0 \cdot \left\{\left(\frac{2\eta}{\pi\Gamma}\right)\left[1 + 4\left(\frac{x-x_0}{\Gamma}\right)\right]^{-1} + (1-\eta) \cdot \frac{2}{\Gamma} \cdot \left(\frac{\ln 2}{\pi}\right)^{0.5} \cdot \exp\left[-4 \cdot ln2 \cdot \left(\frac{x-x_0}{\Gamma}\right)^2\right]\right\}$$

(4.7)

the mixing parameter η related the FWHM of Gaussian (Γ_G) and Lorentzian (Γ_L) and was expressed as:

$$\eta = 1.36603\left(\frac{\Gamma_L}{\Gamma}\right) - 0.47719\left(\frac{\Gamma_L}{\Gamma}\right)^2 + 0.1116\left(\frac{\Gamma_L}{\Gamma}\right)^3 \quad (4.8)$$

and Γ was approximated by a series expansion derived from a group of convolutions:

$$\Gamma = ({\Gamma_G}^5 + 2.69269{\Gamma_G}^4\Gamma_L + 2.42843{\Gamma_G}^3{\Gamma_L}^2 + 4.47163{\Gamma_G}^2{\Gamma_L}^3 + 0.07842\Gamma_G{\Gamma_L}^4 + {\Gamma_L}^5)^{0.2}$$

(4.9)

therefore, the Pseudo Voigt function was determined by Γ_L, Γ_G, I_0 and x_0, where the x_0 represents the value of peak position in the reference. The non-linear least squares method was used for the function fitting, and an example of fitting result with 95% confidence bounds is shown in Figure 4.16.

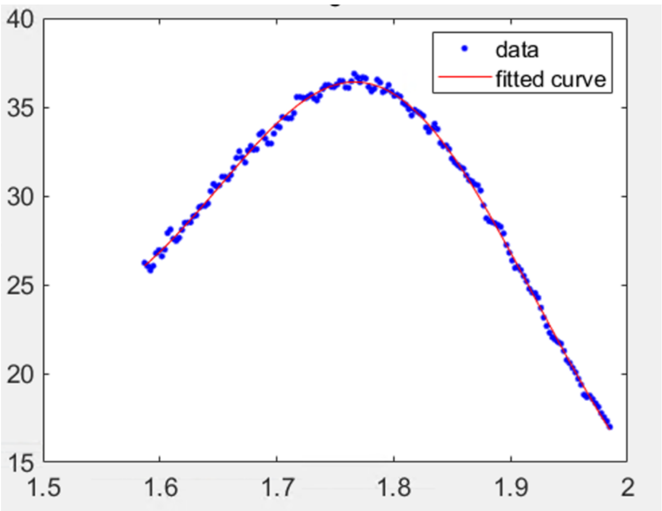

Figure 4.16. Pseudo Voigt fitting result of CF peak

The pseudo-Voigt fitting method was used to analyse the diffraction patterns as crack propagation, with the resulting colourmaps displayed in Figure 4.17. Near the crack tip, the fibres experienced tension perpendicular to the fibre axis, therefore an increase in the (0002) crystal plane (d spacing) and a corresponding decreased q value were expected. This appeared in Figure 4.17 as an inclined trace of low q value close to the crack tip position, which might have been observed for the PEG_Line_400 and NP_2 specimen. To determine the lattice parameter of undeformed carbon fibre, the q value of the last five columns (mark in a red rectangular in Figure 4.17 (a)) was averaged to determine a mean q value of undeformed carbon fibre, where the result is summarized in Table 4.1.

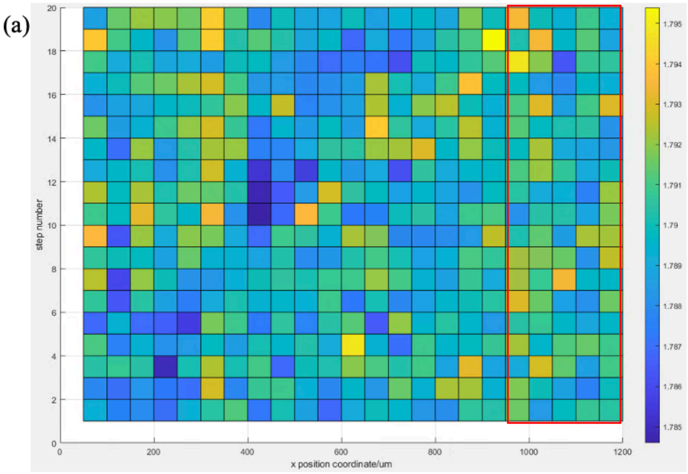

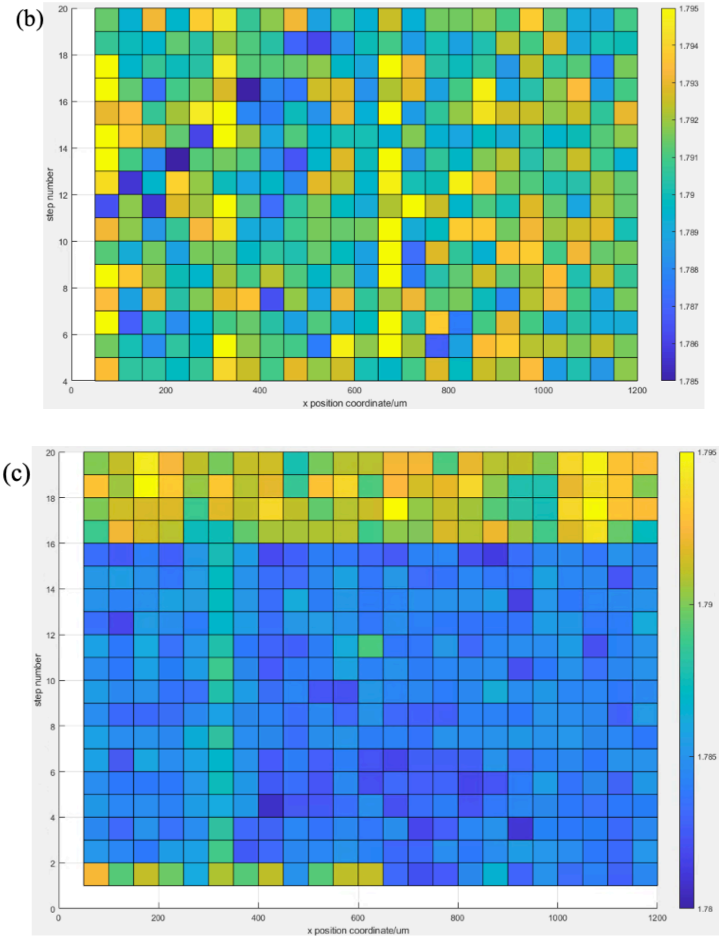

Figure 4.17. Colourmap showing the variation of q value along the diffraction line with increment of step size for **(a)** PEG_Line_400 **(b)** NP_2 and **(c)** PMMA_Line_15000; the blockiness in (c) suggests a fitting problem that q bias to ~ 1.786 in PMMA_Line_15000 specimen

Table 4.1. Q value and the corresponding standard deviation of undeformed carbon fibre for the three specimens

Sample name	**Undeformed q value ± standard deviation**
PEG_Line_400	1.790 ± 0.0015
NP_2	1.791 ± 0.0014
PMMA_Line_15000	1.786 ± 0.0036

For enhanced visualization, the relative q value map of PEG_Line_400, NP_2 and PMMA_Line_15000 respectively were generated by subtracting the mean q value (Table 4.1) of each specimen, as depicted in Figure 4.18 - 20 (a). Following equation 4.4, the lattice strain of each diffraction point was calculated relative to the remote undeformed q value, and mapping of strain for the three specimens are shown in Figure 4.18-20 (b). The linear relation of crack tip position with wedge movement from the Figure 4.13 was superposed as a red line. There is a tendency for lower q values, which would represent an elastic tensile strain of up to 0.3% close to this line. As shown in Figure 4.18, for PEG_Line_400 sample, it is observed that the most strongly tensile points were about 50 μm ahead of the crack tip detected through DIC. This is expected, as DIC analysis is sensitive to the relative movements of the material on either side of the open crack. These would be small close to the crack tip, which resulted in reporting a shorter crack than actually exists. In Figure 4.19, the tensile tendency was also observed in NP_2 specimen, where the mismatch of crack tip might result from the error in crack tip definition. The distribution of q value for PMMA_Line_15000 (Figure 4.20) was random, where blockiness of q value was observed (the boundary sit at wedge position of 500 μm). This suggested the position of PMMA_Line_15000 laminate might have shifted during wedge loading, resulting in a global changing of q value as the distance between sample and detector altered.

As the stress on the carbon fibre was transferred from the epoxy matrix, the highest stress on the fibre would not exceed the tensile strength of epoxy matrix, which is 81.4 MPa (CYCOM® 977-2 toughened epoxy resin). Given the elastic modulus of carbon fibre on (002) plane is ~ 25 GPa [14], following equation 4.10, the largest value expected to appear in the lattice strain was 0.32%. In Figure 4.18 & 19, the observed tensile strain near the crack tip was up to 0.3%, showing the magnitude of measured strain was reasonable.

$$\varepsilon = \frac{\sigma}{E} \quad (4.10)$$

During the fitting, an absolute error of 0.002 A^{-1} was accounted in determining the position of q from MATLAB. Considering the calculation in both reference (q_0) and deformed (q) stages following, the strain error is evaluated as:

$$\Delta\varepsilon = \varepsilon\sqrt{(\frac{\Delta q_0}{q_0})^2 + (\frac{\Delta \mathrm{q}}{\mathrm{q}})^2} \qquad (4.11)$$

with the elastic strain at ~ 0.3%, this gives a total of 0.0005% error for the strain evaluation by fitting.

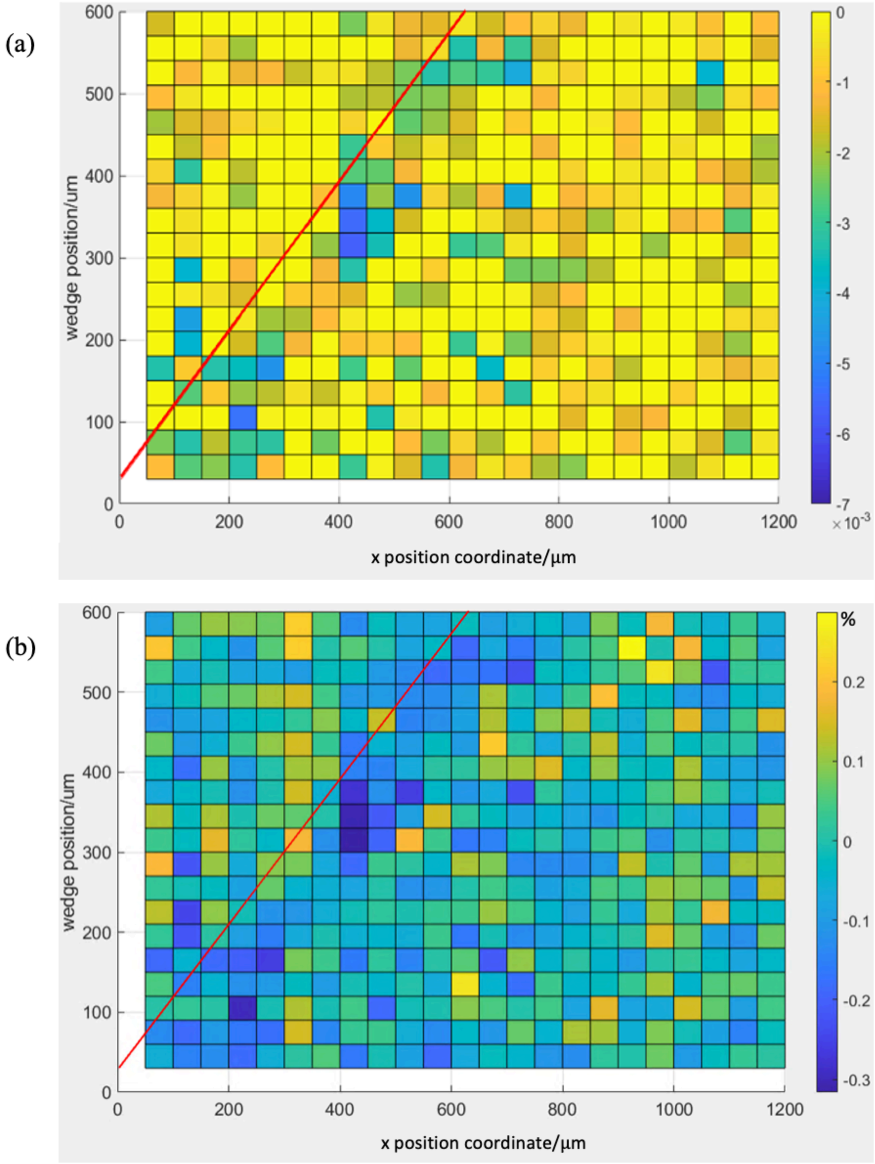

Figure 4.18. Diffraction mapping of **(a)** relative q value **(b)** lattice strain with superposition of crack tip position measured from DIC (red line) for PEG_Line_400

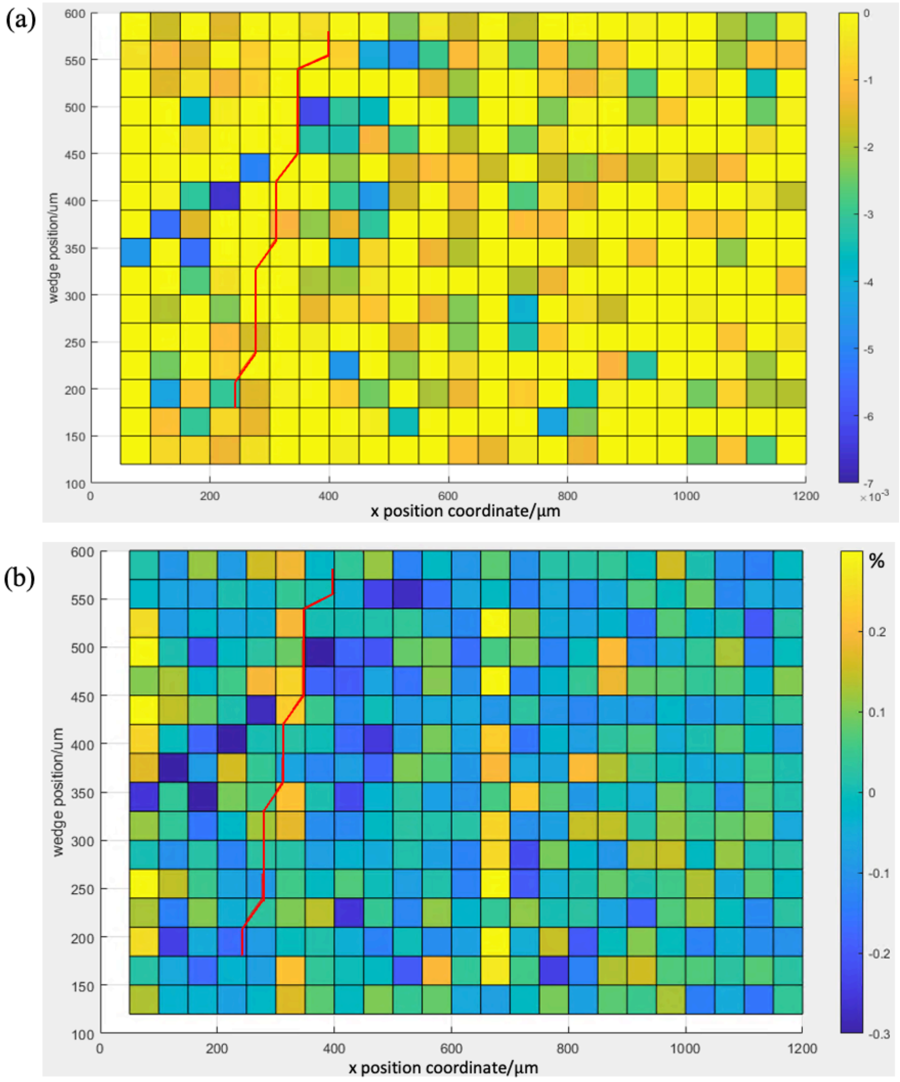

Figure 4.19. Diffraction mapping of **(a)** relative q value **(b)** lattice strain with superpose of crack tip position measured from DIC (red line) for NP_2

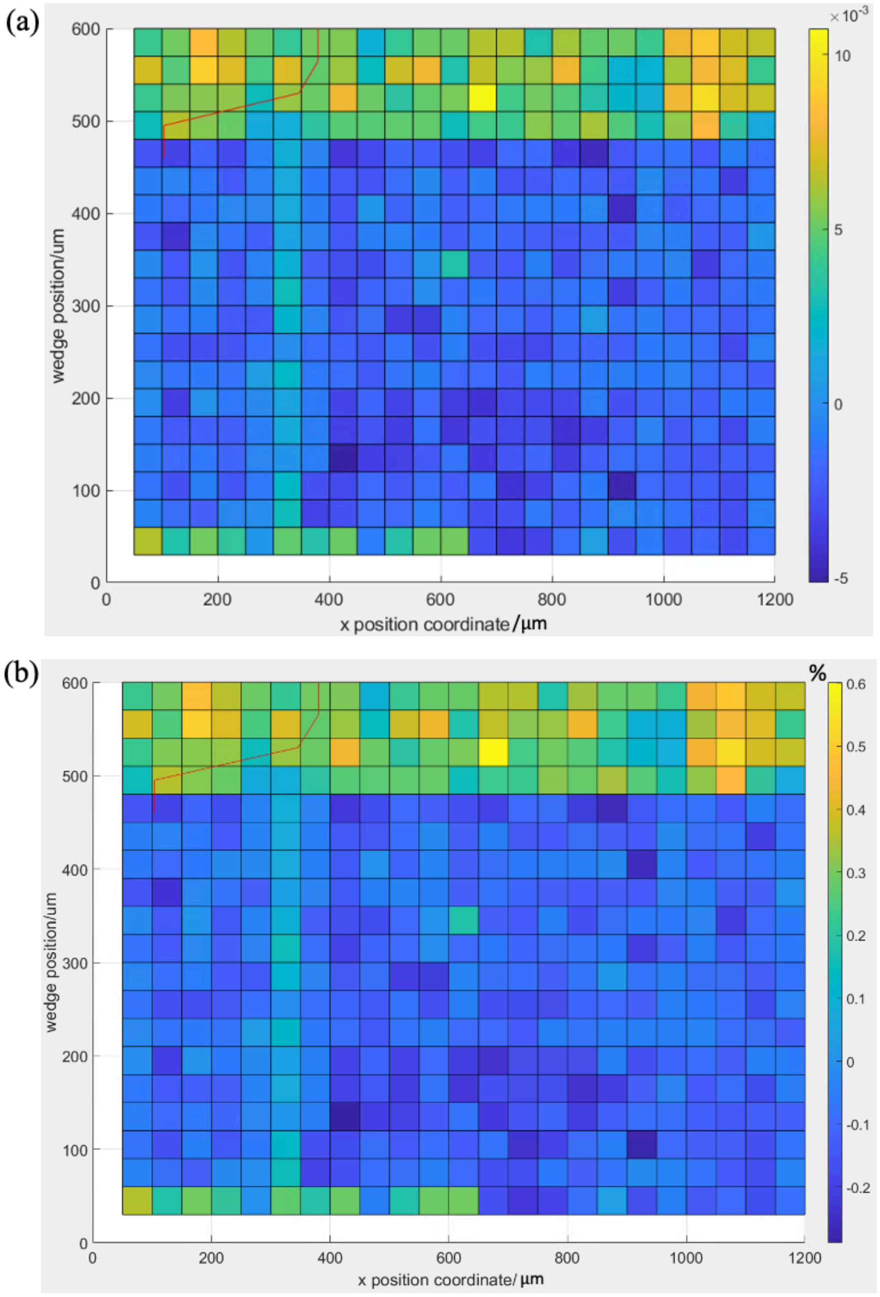

Figure 4.20. Diffraction mapping of **(a)** relative q value **(b)** lattice strain with superposion of crack tip position measured from DIC (red line) for PMMA_Line_15000

In PMMA_Line_15000 specimen, a peak with q value at ~1.71 A^{-1} sporadically appeared in the diffraction spectrum, as shown in Figure 4.21. This may originate from PMMA. The d spacing of PMMA is ~ 3.745 Ȧ [15] (q ~ 1.68 A^{-1}) and the actual q can vary in a range due to factors such as the level of crystallinity and deformation. In the captured Debye ring (Figure 4.14), the PMMA peak was only detected from -20° to -10°, which is highly overlapped with the diffused signal from carbon fibre, therefore the visual observation of PMMA ring was not obvious. As the PMMA crystalized phase is not highly oriented, the reasons why PMMA peak was only observed in certain angle of some diffraction points might be: (1) the crystallization of PMMA occurred under the exposure of X ray radiation, and the process was not completed; (2) there might be signal of PMMA in the area outside of capture region. The measured intensity of this sharp peak over the 20 steps at 24 points along the line map is summarised in Figure 4.22. Given that the horizontal distance between each point is 50 µm, and the gap of each printing line in the materials is 250 µm, a consistent periodicity over five points might be anticipated. However, this was not observed, suggesting the PMMA dots post curing might have redistributed or the peak detection was not reliable. The sharp peaks appeared more consistently in the later scanning steps, indicating that exposure to radiation may encourage the crystallization of PMMA. Besides the carbon fibre main peak and peak of PMMA, within the integration azimuth angle, no other signal was detected.

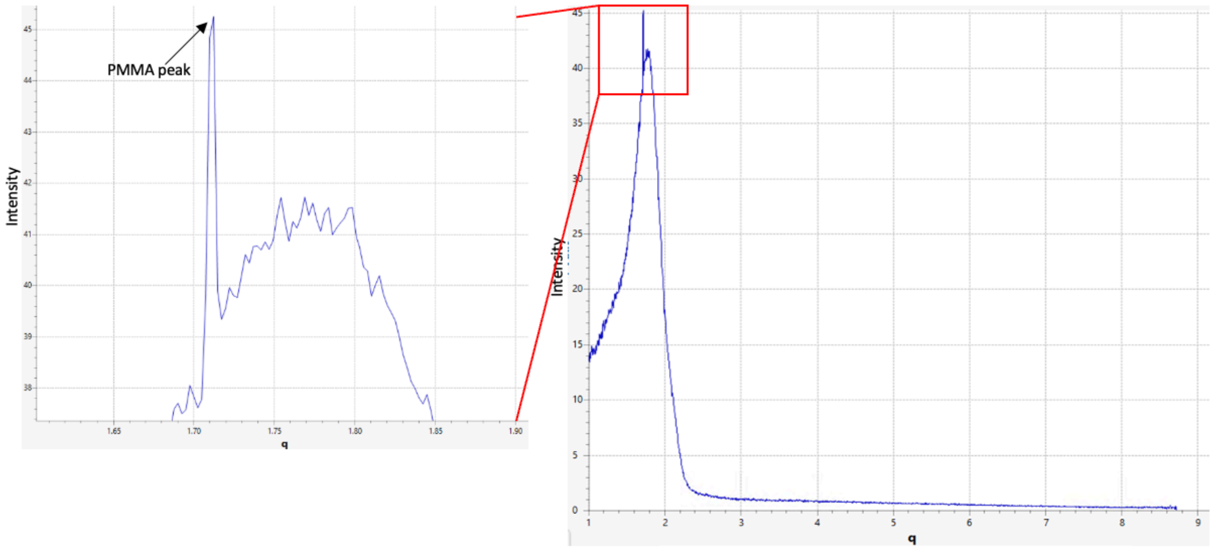

Figure 4.21. PMMA peak appearance in the diffraction spectrum; this was only observed in some position of diffraction spot (detailed in Figure 4.22), which would appear in all the position if PMMA crystallization is full

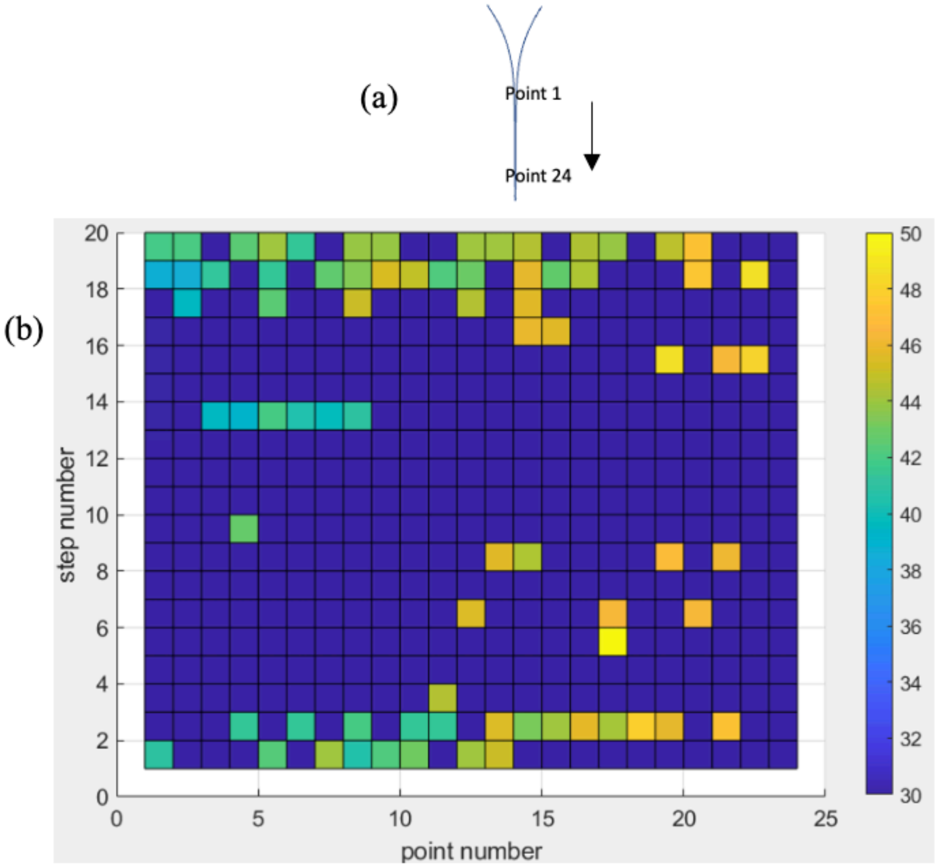

Figure 4.22. (b) Mapping of PMMA peak intensity, where the dark blue represents lack of PMMA signal at the certain position, with **(a)** showing the schematic of diffraction position relative to laminate and crack with the arrow showing the scanning direction

4.1.4 Conclusion

This section presents the first in-situ dual radiography-diffraction study on damage development in carbon fibre composites. A method to measure strains at crack front of CFRP was developed, although the strain in the fibres is small. Tracking of crack tip propagation has been achieved through digital image correlation applied to radiographs, using the loss of correlation in the crack wake to identify the crack front. The movement of the crack tip corresponded with the insertion of wedge. In-situ XRD was also employed to map the lattice strains in carbon fibres. The partially crystalized structure of the fibres results in a broad peak with strong texture, making the measurement notably noisy. PMMA peaks were detected in the diffraction spectrum, although the observed pattern of appearance was random.

4.2 In-situ 3D observation of delamination propagation

To study the damage development behaviour in CFRP, it is crucial to conduct three dimensional in-situ characterizations during crack propagation. X ray computed tomography (XCT) is a powerful non-destructive technique that offers the solution to capture high spatial resolution, 3D multiscale images of the internal structure of the object. Moreover, by repeating the image acquisition throughout the structural evolution, it opens the opportunity for in-situ study.

The contrast of XCT arises from two sources: absorption and phase contrast. In absorption mode, the contrast originates from difference of linear attenuation coefficient (μ) between material phases. The attenuation coefficient at a specific position is determined by [16, 17]:

$$\mu = K \cdot \rho \cdot \frac{Z^4}{E^3} \quad (4.12)$$

where K is a constant, ρ represents the density, Z stands for the atomic number and E is the energy of incident X ray. For the same specimen, a higher absorption is expected under lower energy beam. Moreover, materials with lower atomic number exhibit low degree of attenuation, which in CFRP means there is low contrast between the fibres and matrix. This could be improved by introducing phase enhancement. Following equation 2.5 in Chapter 2, for CFRP material under X-ray with energy at 10 - 60 keV, the refractive index (δ) is a thousand times higher than absorption index (β) [18, 19], which means a phase shift could significantly increase the feature detectability by increasing the image contrast. In this project, phase contrast XCT was conducted to better resolve the crack and potentially visualized the printing droplets. In synchrotron radiographs, phase contrast was achieved through using high coherent, low energy beam, with suitable sample-detector propagation distance for large phase shift generation to be collected by the detector. Post-acquisition, application of the Paganin filter [20] to process the sinogram could extract the phase shift. [21]

In this work, a series of in-situ XCT tests were conducted at different synchrotron light sources for the observation of mode I opening of laminates. The first in-situ XCT was conducted on beamline I12 JEEP at the DLS (experiment number EE17546) to test the feasibility. The 3D volume data was then processed to inform a finite element model that was used to calculate the J-integral at the crack tip. Artifacts were significant in these tomographic images. A second experiment was then performed at the TOMCAT beamline at the Swiss Light Source (SLS, proposal number 20211848). The 3D images were analysed qualitatively and quantitatively, which provided insights into the delamination development among the composite laminates.

4.2.1 In-situ 3D imaging and analysis

4.2.1.1 Experimental

The first in-situ synchrotron X-ray tomography and reconstruction were conducted by Zhang [6] at the I12 JEEP beamline of UK Diamond Light Source, where the mode I crack propagation behaviour of NP_0 and PMMA_Hex_15000 specimens were studied. The tested samples were firstly cut to have an initial length of 48 mm (with 5 mm of the PTFE film for pre-crack generation), and the width of NP_0 and PMMA_Hex_15000 samples were at 4.40 mm and 2.78 mm respectively. A fiducial marker was provided by a 2 mm-diameter stainless steel ball attached on the sample surface through cyanoacrylate adhesive at a position ~ 2 mm ahead of the printed boundary, which acted as an indicator of reference marker to locate the scanned region during the fracture test.

After removal of the PTFE insert, a 1-mm thick steel wedge was inserted using a Shimazdu AGS-X mechanical testing rig at a loading rate of 0.5 mm min^{-1}, with the specimen mounted vertically by clamping a short length at one end (~ 5 mm) between anvils, until the crack tip had propagated sufficiently (several mm that into the printed region for the PMMA_Hex_15000 specimen). Each specimen was then shortened to 42 mm length, by removing material in the pre-cracked region, to fit within the dimensional constraints of the 5 kN Deben CT5000 loading rig. Designed for in situ tomography, the CT5000 has an X-ray transparent glassy carbon extension tube; within this the specimen was again mounted vertically by clamping one end (~ 5 mm) between anvils and the 1 mm thick steel wedge was used to drive crack propagation as shown in Figure 4.23.

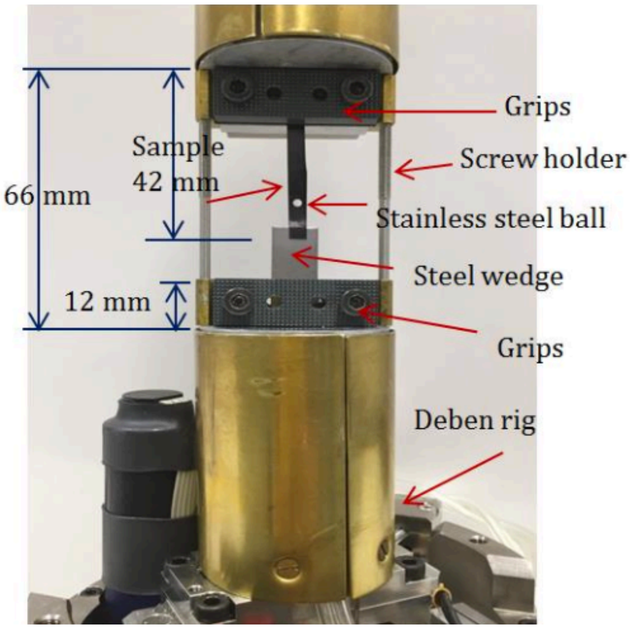

Figure 4.23. Loading setup for mode I crack propagation within the Deben rig [6]

The experimental set up is shown in Figure 4.24: Monochromatic X-rays of 53 keV energy were applied, with a sample to detector distance at ~ 1 m. Prior to the tomography observations, each specimen was characterized by radiography at 7.9 µm image pixel size (20 x 12 mm field of view, Module 2 at I12, exposure time 0.005 s) as the wedge was inserted at 1 mm min^{-1} to further propagate the pre-crack several mm into the region of interest. High resolution tomography was then conducted at 1.3 µm image pixel size (3.3 x 2.8 mm radiograph field of view, Module 4 at I12 1800 radiograph projections over 180° rotation at 1 s exposure per radiograph), as the crack was propagated by progressive insertion of the wedge in ~ 40 µm intervals. The insertion rates between observations were 0.1 mm min^{-1} and 0.2 mm min^{-1} for the PMMA_Hex_15000 and NP_0 specimens respectively, and the wedge was static during tomography capture. The long sample to detector distance provided some additional phase contrast. High resolution absorption contrast tomographs were then reconstructed, using the beamline software through 'gridrec' algorithm [22].

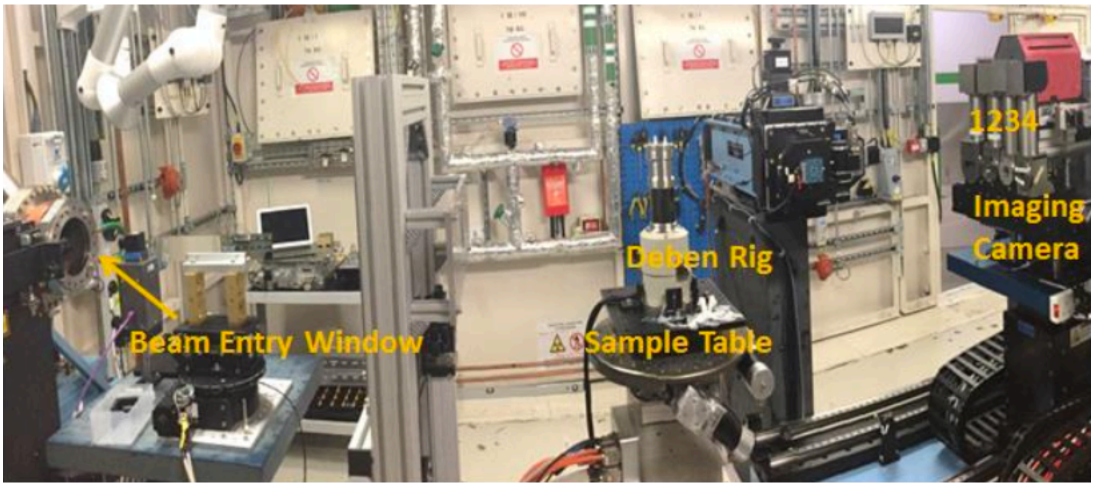

Figure 4.24. Experimental setup at I12-JEEP, hutch 1

4.2.1.2 Displacement field calculation

A typical example of visualization of the tomographic 3D volume is shown in Figure 4.25: Fibre bridging could be observed in both XY and YZ plane. The XZ cross section showed that the crack front does not move straight, a tortuous crack tip was observed. In Figure 4.25 (c), bright fringes severely hidden the identification of materials feature on the crack edge, which was causing by phase contrast artifact. Additionally, the fibres from YZ cross section were not well resolved. The s-XCT imaging in the next session conducted under TOMCAT would address these issues.

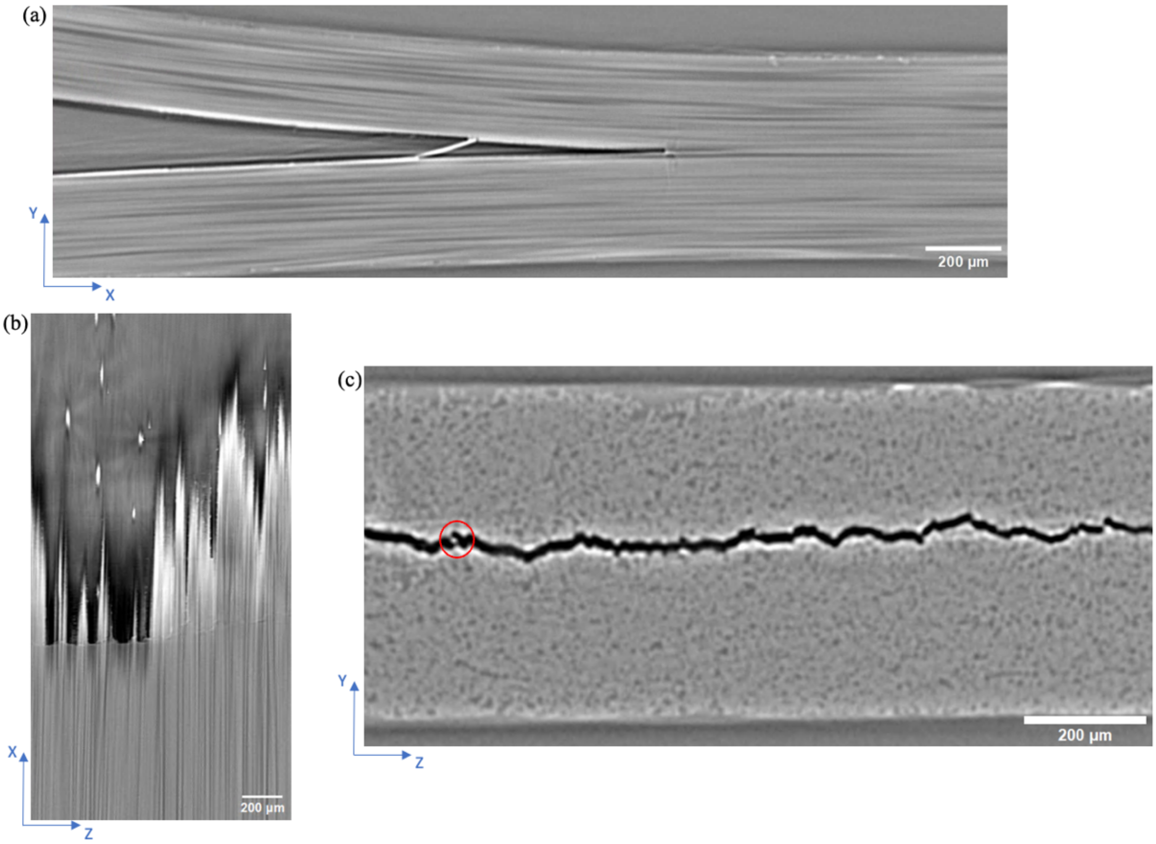

Figure 4.25. Cross section of PMMA_Hex_15000 XCT in **(a)** XY **(b)** XZ and **(c)** YZ plane, where an example of fibre bridging is highlighted in red

The reconstructed tomographs were post-processed firstly by ImageJ. The 32-bit images were resampled to 8-bit with the 0-256 greyscale range selected to maintain good contrast in the microstructure. A 3D Gaussian blur filter (1.1 voxel standard deviation) was then applied to reduce image noise. Zhang conducted the first DVC analysis which cropped the 3D volume to 2.1268 x 0.8138 x 2.6572 mm, where the opening displacements from which of the printed and non-printed sample was compared and would be displayed later. To save the calculation cost, this project then cut the images to 1.04 x 0.546 x 1.248 mm, for crack tip traction and full field evaluation for the later finite element analysis. The cropped 3D volume scans were input to digital volume correlation (DVC) to measure the displacement field of the deformed laminates, which was executed through Lavision DaVis 8.4.0 software. The image of the unloaded state was applied as the reference and displacement in X, Y and

Z directions were used to determine the Mode II, Mode I and Mode III crack opening respectively (Figure 4.26).

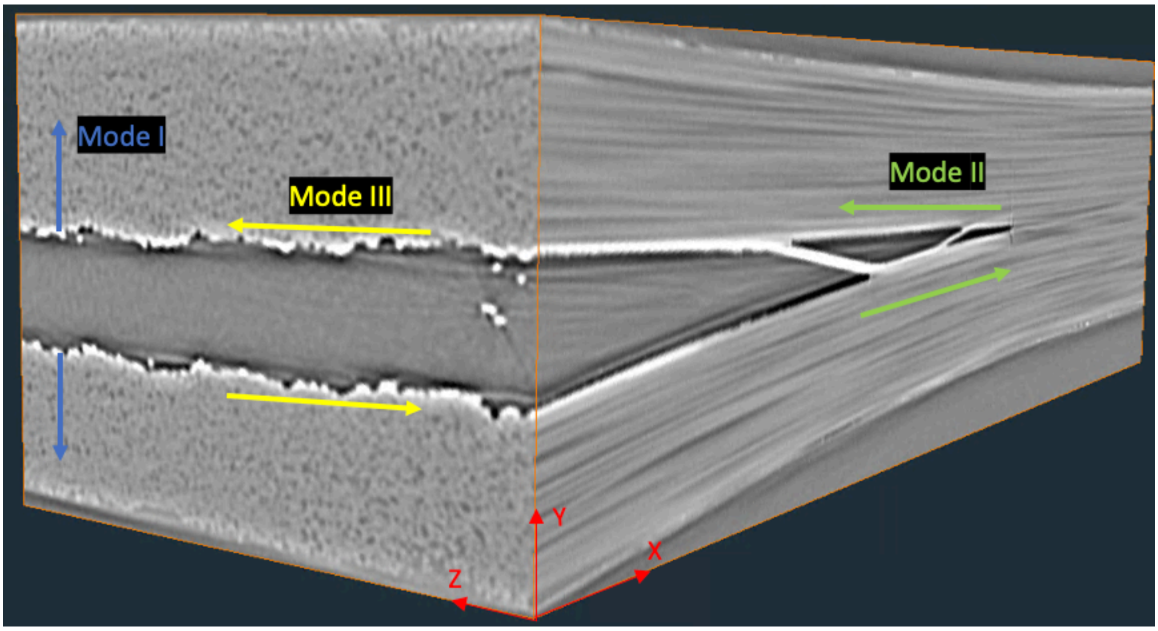

Figure 4.26. Schematic of Mode I, Mode II and Mode III opening with the corresponding axial directions

Fast Fourier Transform (FFT) DVC algorithm was employed between reference and each loaded steps. As detailed in Chapter 2, sub volume size shall be defined as the unit that the 3D image was cut into: a large subset size contains more information that improve the correlation quality, however this will sacrifice the special resolution. Therefore, multi steps were preformed, which initiated with large subset size and reducing gradually in the later steps. Two sets of measurement were conducted here: (1) subset size of 256 voxel, 128 voxel, 64 voxel and 32 voxel with 2 passes each step was used for the two size group; (2) the preliminary test has shown phase congruency (for tracking of crack tip position, will be detailed in the next session) performs the best with input subset size at 96 voxel. Therefore, another DVC calculation with subset size of 256 voxel, 128 voxel and 96 voxel, twice passes in each step was conducted on the 1.04 x 0.546 x 1.248 mm dataset. Both measurement groups applied 75% subset overlap between adjacent interrogation volumes, which leads to the spatial resolution at 10.4 μm (8 voxel) and 31.2 μm (24 voxel) respectively. Gaussian (round) shape was applied as the interrogation volumes and rigid body movement was removed from the vector result.

Post displacement calculation, vectors with coefficient less than 40% would be removed, which is lower than normal DVC setting (~ 90% in general) due to the lack of unique features among the unidirectional carbon fibres. Outliers were removed with threshold 2 following Westerweel and Scarano, 'Fill up all' was conducted to insert the missing vectors with the average number from their 7 x 7 neighbours. [23]

To evaluate the displacement error from the correlation algorithm, DVC was conducted on the same unstrained region in two adjacent steps, where the standard deviation of displacements was taken as the measured error. The results are shown in Table 4.2. Analysis with the final step of 32 voxels (for displacement field evaluation) possess lower correlation accuracy compared with 96 voxels group (for detecting crack tip position), which is expected as less information is included in the former that makes the correlation in a higher difficulty. The 96 voxels group would be applied for the full-field displacement informed FE analysis, where the largest displacement error is of one voxel size, showing the correlation accuracy is sufficient for the analysis.

Table 4.2. Displacement errors from correlation for the two DVC analysis group

Displacement error (μm)	**32 voxels**	**96 voxels**
$\mathbf{\Delta U_x}$	2.23	1.39
$\mathbf{\Delta U}_y$	0.97	0.97
$\mathbf{\Delta U_z}$	0.17	0.14

DVC is designed for situations involving uniform strain and smooth deformation gradient without any cracks. The rigid body motion is calculated as the average behaviour of the 3D volume, where the algorithm tries to find a displacement and rotation that minimize the differences between the vector fields. When there is a crack, different part of component moves in various directions, therefore the average result would not be correct. Here, we further implemented a computationally efficient method to the DVC data, based on Shoemake's [24] that consider the relative displacement field from reference tomography and a MATLAB script was written to achieve this. The region ahead of the crack tip was precisely aligned and registered by removal of the remaining small rigid body movement and rotations (typically less than 0.2 μm and 0.5°).

Following on that, mapping of the relative crack opening displacements (COD) in the XZ plane could be achieved, which is achieved through MATLAB: as shown in Figure 4.27, the displacement of top and bottom plies at each XZ position was averaged out along Y axis, where the difference values gave the opening displacement at each location. An example COD of the PMMA_Hex_15000 specimen (with wedge insertion of 726 μm in X axis) is shown in Figure 4.28: Mode I opening gradually decreased along the crack propagation direction, and its variation perpendicular to fibre (Z-axis) suggested the crack front does not move strictly vertical to the fibre direction, that said, the crack tip possesses a curved shape instead of a straight line (Figure 4.28 (a)). The CODs mapping of Mode II and mode III were much uniform with a few of extreme points were observed near the crack end. Similar observation has been reported in Zhang's analysis, which was considered as error raised from large curvature close to crack end [6]. Averaging the opening along Z-axis gives the variation of COD along the fibre direction (Figure 4.29): the crack opening is dominated by mode I, with minor mode II and negligible mode III. Significant COD in X direction (Mode II) appears even at the crack tip vicinity, suggesting mode II was caused by wedge insertion. The mode III displacements across the crack in comparison were negligible.

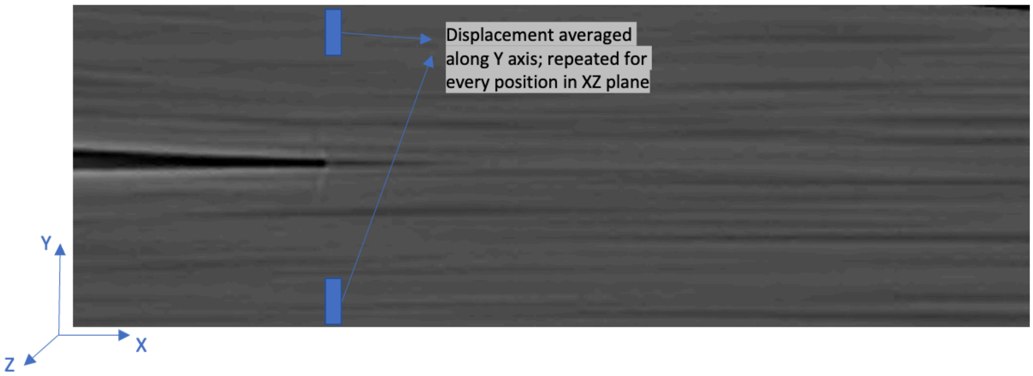

Figure 4.27. Schematic of displacement average calculation to get the opening displacement at each position in XZ plane

(a)

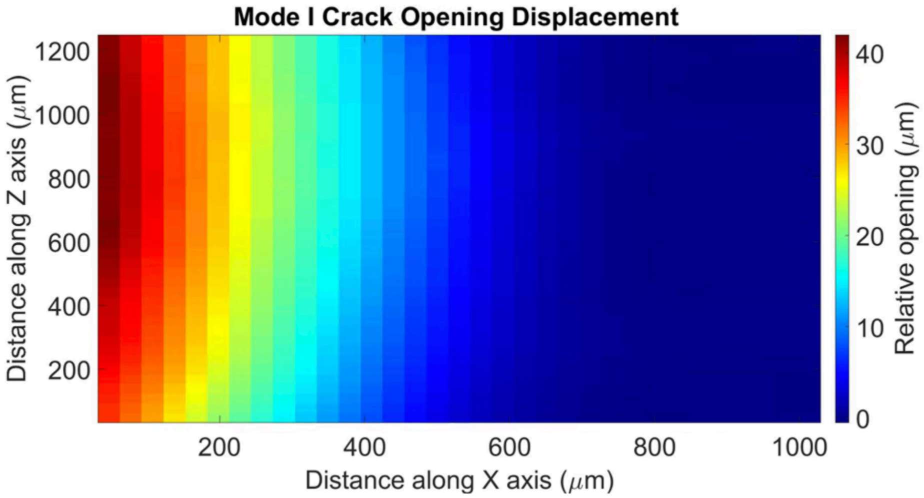

(b)

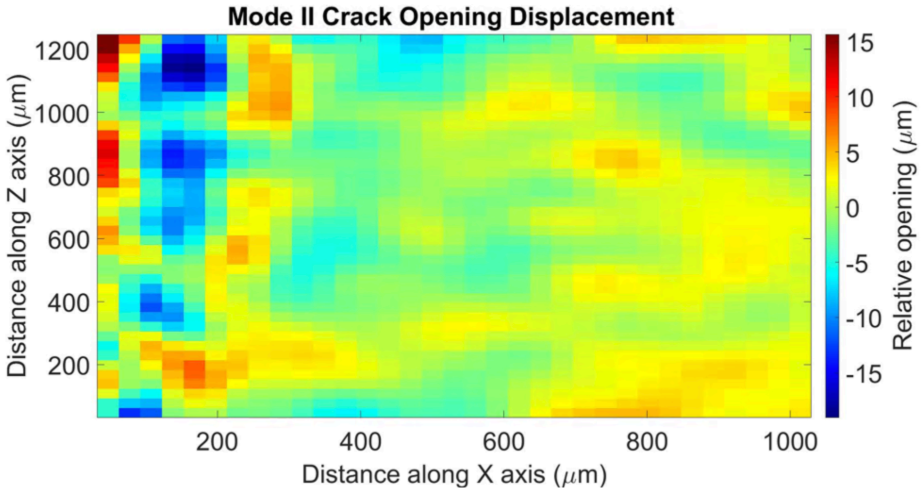

(c)

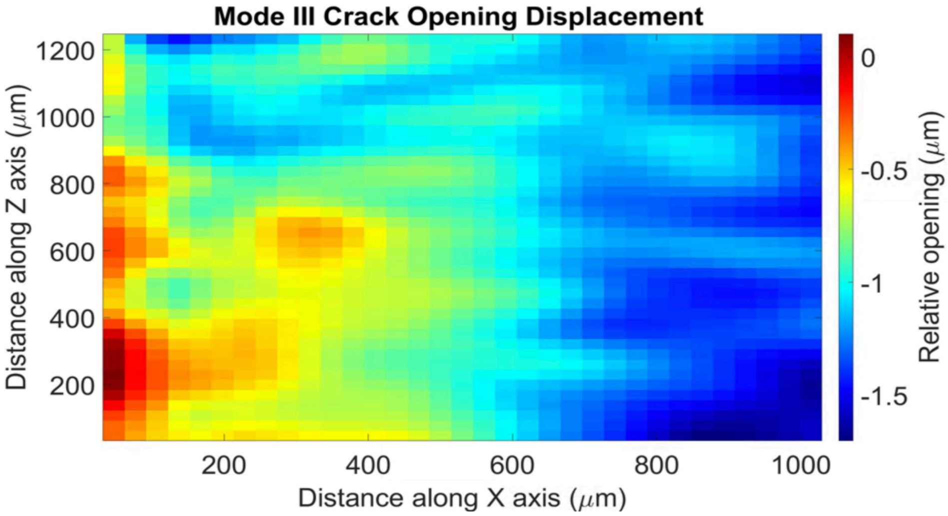

Figure 4.28. Crack opening displacement field of (a) Mode I, (b) Mode II and (c) Mode III of PMMA_Hex_15000 specimen with 726 μm wedge insertion

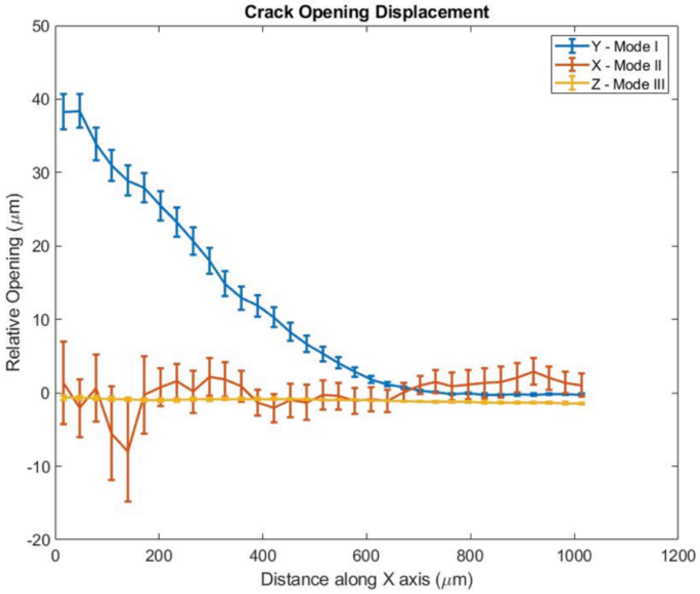

Figure 4.29. COD plot for PMMA_Hex_15000 specimen with 726 μm wedge insertion, where the opening is calculated as the average of data across Z direction

The same analysis was conducted on four steps of PMMA_Hex_15000 and NP_0 specimens for 2.1268 x 0.8138 x 2.6572 mm volume, which are shown in *Figure 4.30*. In *Figure 4.31* (a), the COD profiles were then shifted with the relative crack tip position, which allow comparison the Mode I opening of laminates with and without inkjet printing. *Figure 4.31*

(b) displayed the average COD of the two samples, which demonstrates the crack in the PMMA_Hex_15000 propagated with a larger COD (14.03 μm higher at 1 mm behind the crack tip) and thus wider crack opening angle than the NP_0 specimen.

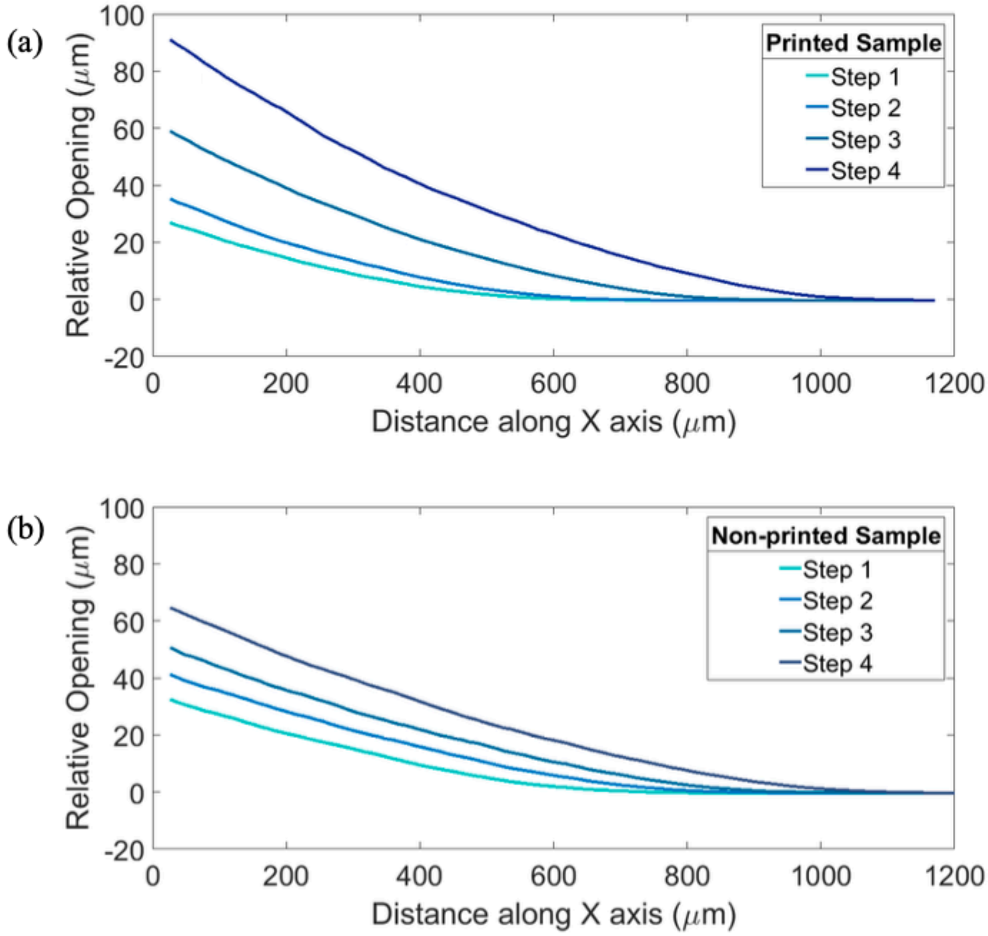

Figure 4.30. Mode I opening profile for **(a)** PMMA_Hex_15000 and **(b)** NP_0 specimens over four crack propagation steps

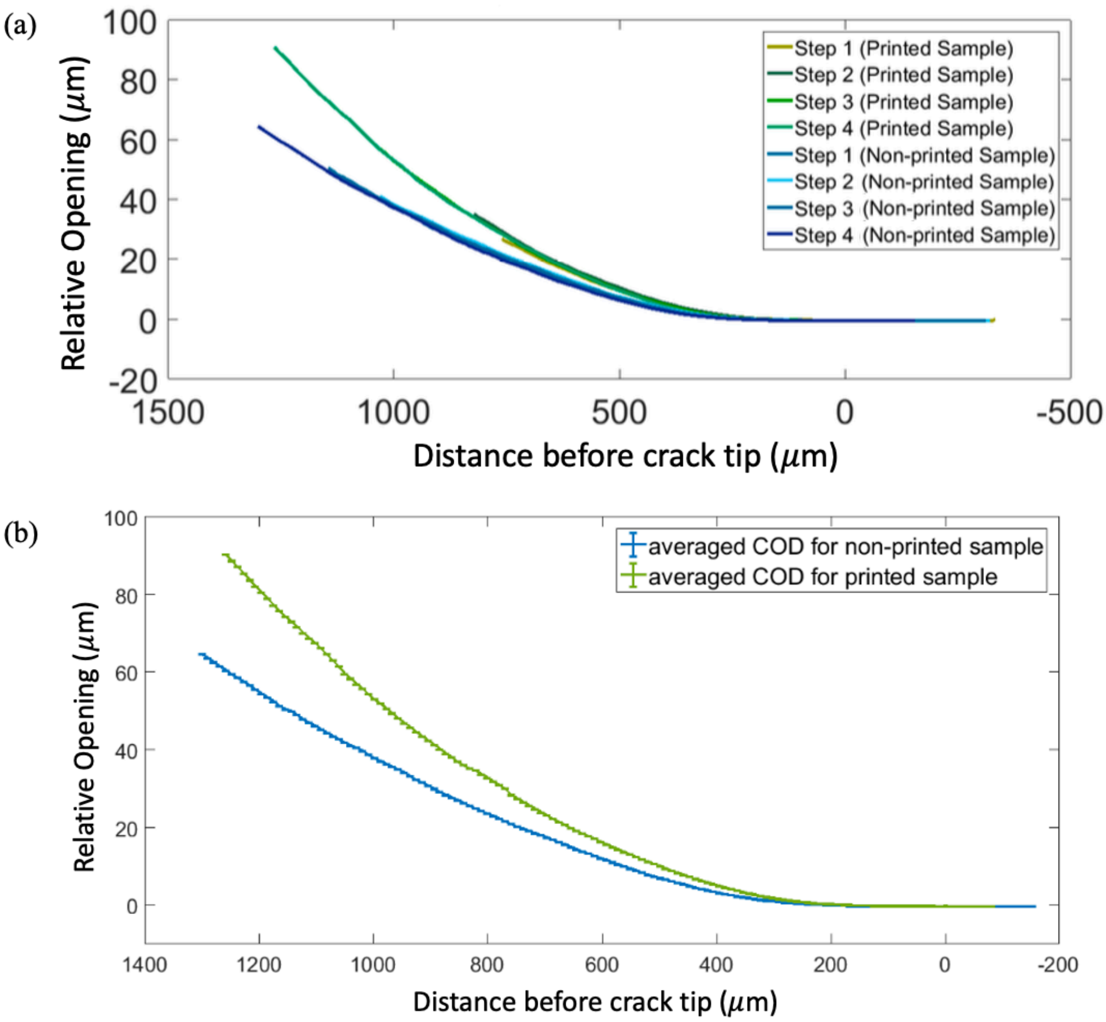

Figure 4.31. Comparison of Mode I COD between PMMA_Hex_15000 and NP_0 laminates in the form of **(a)** raw data plot and **(b)** averaged COD

4.2.1.3 Experiment informed J-integral evaluation

Post DVC analysis, the displacement field then informed a finite element model for strain energy evaluation. In short, phase congruency algorithm was conducted for the detection of crack tip position, which would aid the generating of finite element model that shared the same size with the tomographic data within the cropped ROI. The full field displacement from the previous section were then imported as boundary condition for the numerical analysis. J-integral and segregation of stress intensity factor in different modes could therefore been calculated, which enabled the comparison between laminates with and without printing as well as tracking the evolution of fracture energy as damage propagation. To locate the crack tip position, a phase congruency (PC) algorithm was applied on the full field displacement (in dat. format) exported from DVC in each step, achieved via a MATLAB code which was originally written by Cinar [25]. PC is an edge detection method based on the frequency signals of features in an image that highlight the data discontinuity as the cracked region. The algorithm is sensitive to the data resolution, thus, the DVC data was tested with different final step sizes, where data with the last subset size at 96 voxel poses the best accuracy with sufficient resolution thus was chosen here. As PC is relatively noise-sensitive, a median filter was initially applied to smooth the data. Phase deviation result was then been resolved, where a relative parameter needed to be fixed where a low value would make the result sensitive to fluctuation near the edge that led to fake crack generation (Figure 4.32 (a)), while a too large value would attenuate the magnitude and virtually close the crack (Figure 4.32 (b)); an optimal should be tested to balance between avoiding non-existent cracks and closing of the real one to select the correct damage area (Figure 4.32 (c)), amplification parameter at 2.3 was used in this case.

(a)

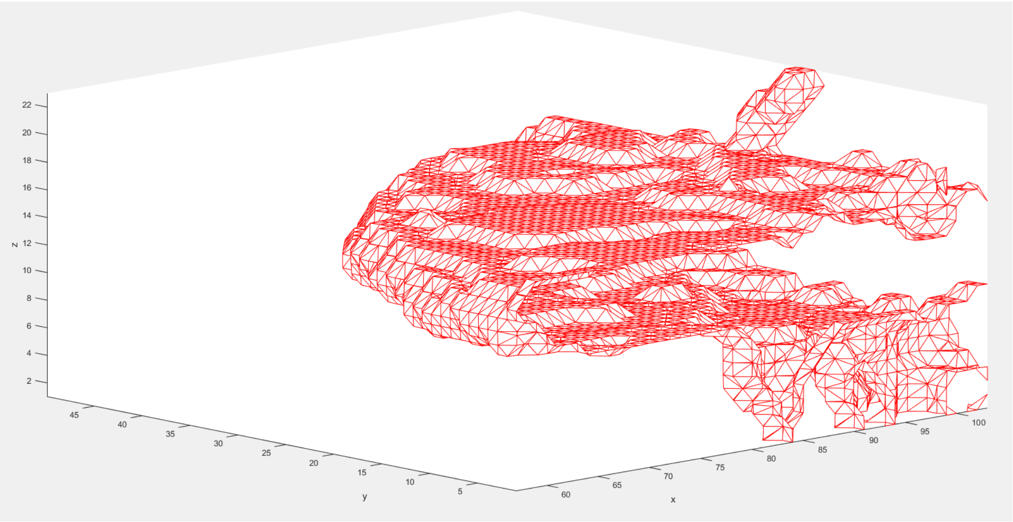

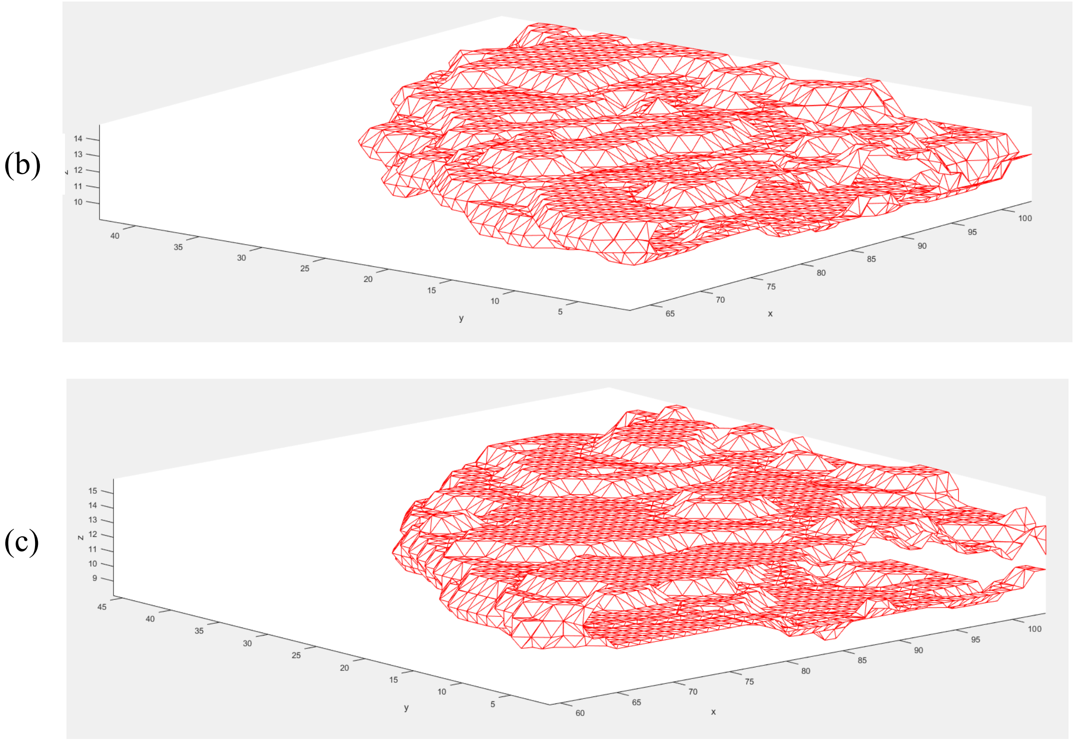

Figure 4.32. Crack visualization with phase deviation parameter at **(a)** too low, **(b)** too high and **(c)** optimum level

Following on from that, a snake algorithm was conducted to segment the crack region. As shown in Figure 4.33, a selected point (red point) shall be defined within the crack where the snake algorithm initiated from and grew a region to find the whole damage area (Figure 4.34). A fourth-degree polynomial function then fitted the tortuous crack tip into a smooth curve front, which would help avoiding mesh distortion and non-convergence in the later FE analysis.

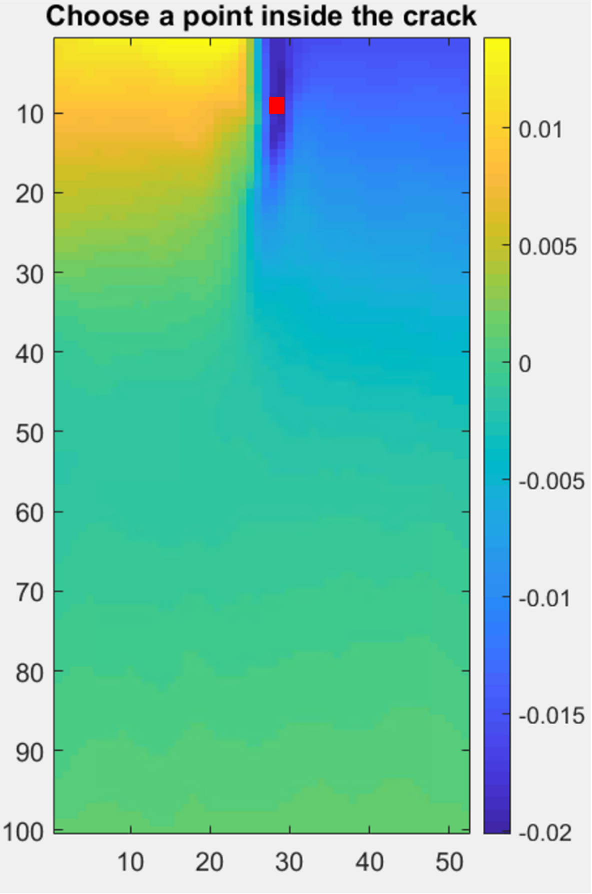

Figure 4.33. Selection of a point (red block) within the crack

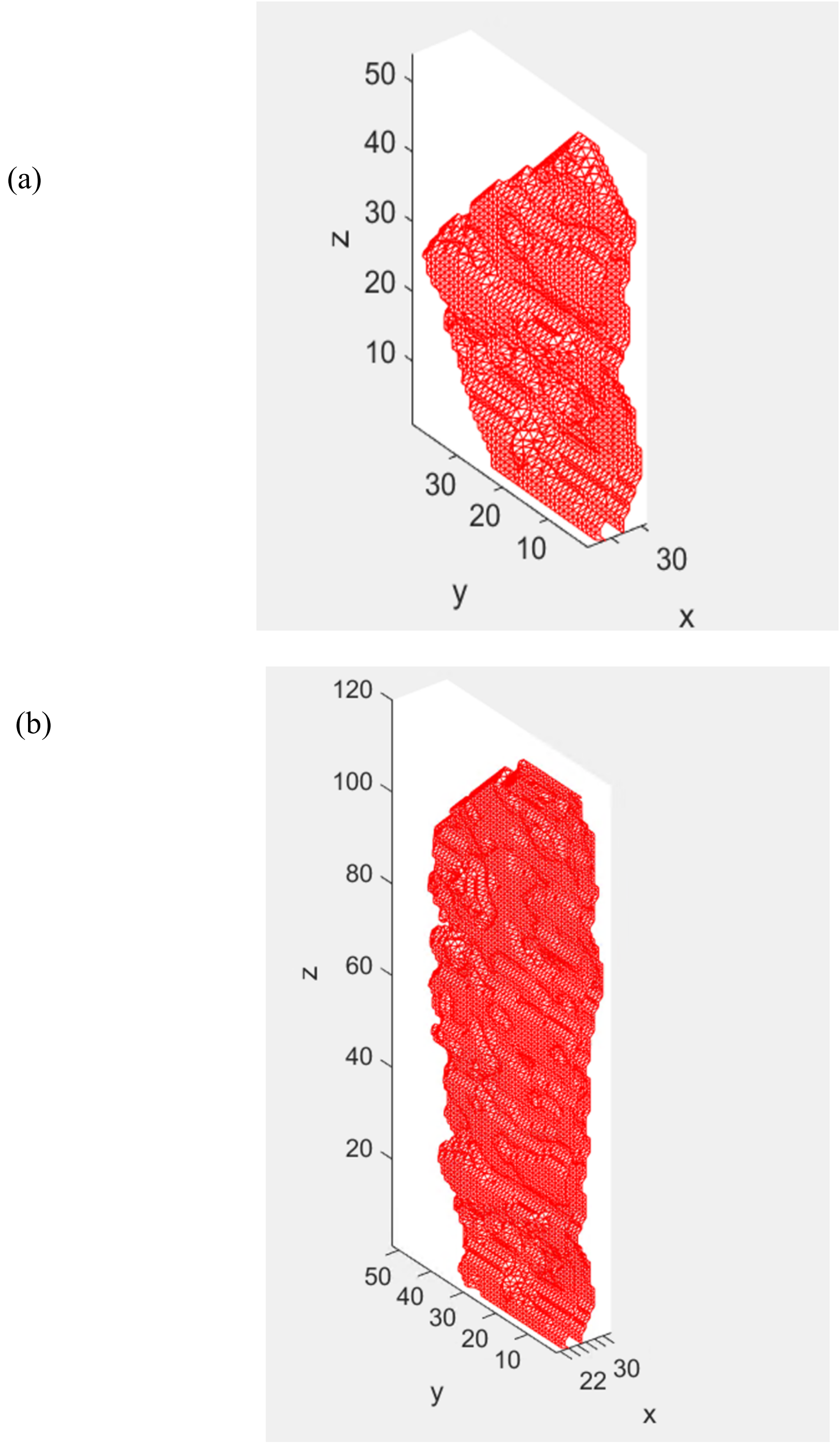

Figure 4.34. Snake algorithm to grow the detected crack region in the **(a)** early and **(b)** late stage

A finite element model was then generated to evaluate the variation of J-integral by injection of the crack displacement field into the numerical simulation. Compared to field fitting methods, this methodology has an advantage of being more robust to uncertainty in the vicinity of the crack, and it also enables analysis with non-isotropic materials [26]. The FE model with tomographic volume was generated in Abaqus CAE 6.14. A planar crack surface was then added as contour integral to define the crack path. As shown in Figure 4.35 (a), the curve crack front was measured from Phase Congruency, and q-vectors (blue arrows) were defined which were perpendicular to the crack tip that determined the damage growth direction. Following on, 3D hexahedron meshes were created, where mesh refinement in the crack vicinity was close to the grid-spacing of DVC analysis, whereas the mesh size in the bulk of the model was three times larger (Figure 4.35 (b)).

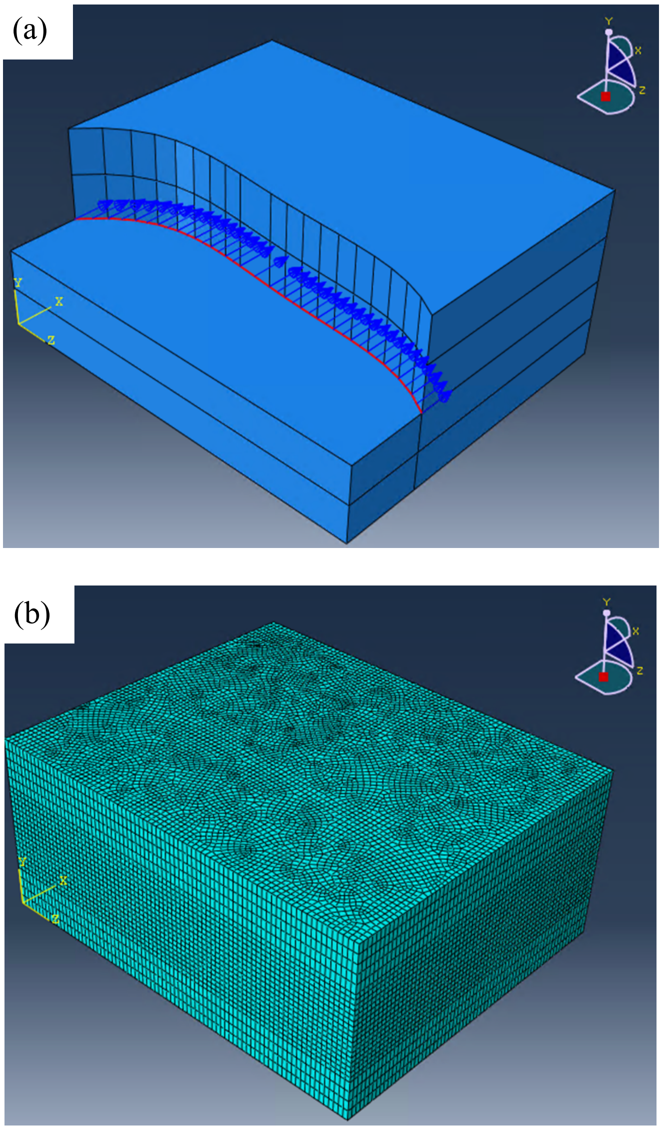

Figure 4.35. Schematic example of finite element model showing **(a)** the curved crack tip and **(b)** bulk component & mesh

The longitudinal elastic modulus of the unidirectional composite was estimated using the 'Vigot' rule of mixture: the isotropic tensile modulus of CYCOM 977-2 epoxy is 3.52 ± 0.14 GPa and carbon fibre has a tensile modulus of 239 GPa and transverse modulus of 23.8 GPa [27, 28]. The fibre volume fraction, estimated by segmentation of the tomographs, was 60.2% [6]. The transverse properties were estimated from similar materials, as the transverse elastic modulus of fibre was not known [28]. Transverse Poisson's ratio was defined with the hydrostatic assumption. The resulting material properties are summarized in Table 4.3.

Table 4.3. Orthotropic elastic material properties of composite applied in the FE analysis (E_{11} parallel to fibre direction)

Material Property	E_{11} (GPa)	E_{22} (GPa)	E_{33} (GPa)	G_{12} (GPa)	G_{13} (GPa)	G_{23} (GPa)	v_{12}	v_{13}	v_{23}
Value	145.3	7.115	7.115	4.7	4.7	3	0.256	0.256	0.48

The component model was exported as INP file (Input file) that contained parameters to completely define the Abaqus model (nodes, element position, connectivity & constitutive relationship). DVC displacement fields were then imported into the same position of FE model as boundary condition achieved through MATLAB. The value of discontinued points was interpolated as the value of the nearest point, using natural neighbour interpolation. Local outlier within the component where the displacement vector was more than ten times different from the neighbouring points were removed as the displacements are supposed to be continuous within the bulk material.

In the crack vicinity, a rectangular forbidden zone [29] was defined where nodes within this region were excluded because of the low DVC correlation coefficient that would affect the computation accuracy, displacement vectors calculated by DVC in this zone were removed. FE geometry with displacement vectors (red vectors) before and after removing the forbidden nodes are shown in Figure 4.36. It is noticeable that the chosen of forbidden zone size had a significant effect on the further finite element analysis. Figure 4.37 illustrates the effect of forbidden zone size on the following J-integral calculation. The fracture energy tended to decrease with the increase in forbidden zone width and converged at 0.46 mm scale. This was the same case for 0.85 mm in the length direction, which was 0.35 mm ahead of the crack tip. Therefore, the size of forbidden zone was chosen as 0.46 mm x (0.35 mm + crack front position) for all the steps. The displacement fields of forbidden nodes, as well as other nodes with no injected DVC displacement vectors, were calculated in Abaqus through the surrounding nodal displacements and crack surface as the boundary condition.

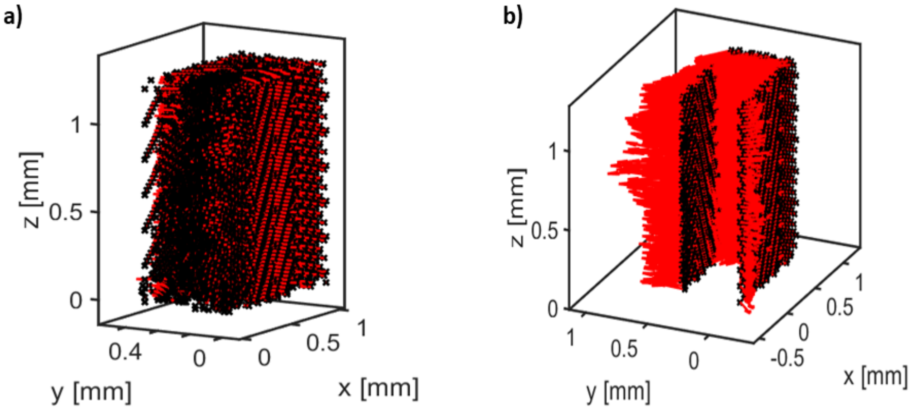

Figure 4.36. Displacement vectors (red arrow) injected as boundary condition in the FE nodes (black cross) **(a)** before and **(b)** after removal of forbidden points

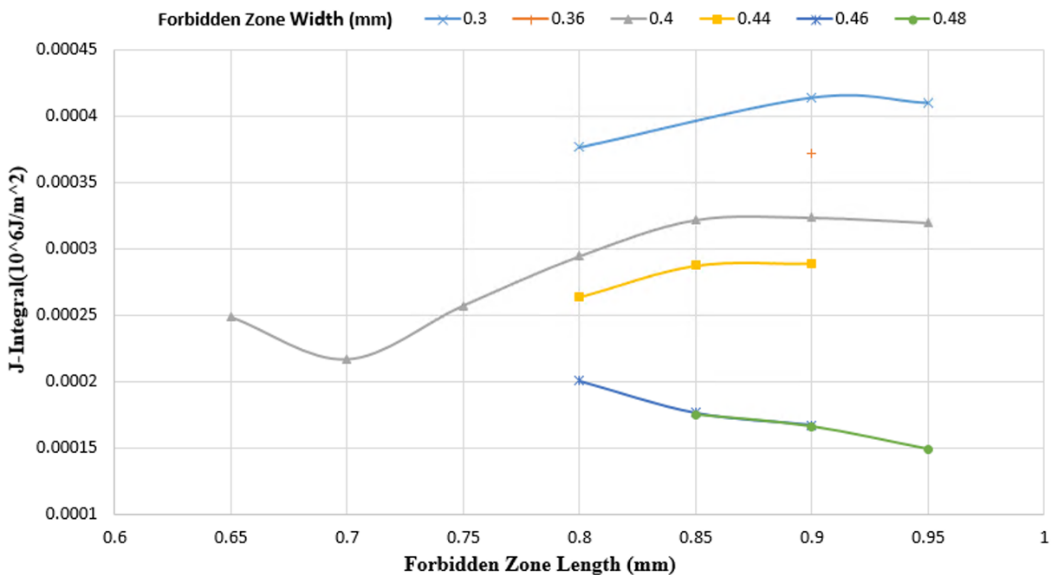

Figure 4.37. Effect of forbidden zone size on strain energy calculation, tested using data from printed sample and the 5th contour was chosen as the representative result

The J-integral was evaluated within Abaqus at all nodal positions along the crack front, using the virtual crack extension method, and the linear elastic SIFs (K_1 to K_3) were then retrieved using the interaction integral that is also implemented natively in Abaqus [30]. The bulk FE result with the mode I displacement field is shown in Figure 4.39. Contour two (red points series in Figure 4.39) was chosen as representative of result, where stable computational outcome initiate (Figure 4.38). The averaged value of J-integral, Mode I and II stress intensity factor over the crack front are presented as a function of the crack extension in Figure 4.40. The mode III SIF was negligible (Figure 4.29) compared with mode I & II thus it is not shown here. The Mode I SIF dominated, with a significant mode II SIF shear, resulting in the evolution of J displays similar trend with mode I. A significant jump of value in both J and K_1 was observed at step three of the non-printed specimen, which was considered as outlier as the value at this point appears around five times larger than the other steps, which was significantly beyond the confidential interval while no special crack behaviour was observed in qualitative analysis. A trend of R-curve behaviour could be seen in the printed specimen while this did not occur in the pristine sample. The averaged J integral excluding the outlier point demonstrated the improvement of fracture toughness, with 586 ± 169 $\mathrm{J/m^2}$ and 296 ± 95.81 $\mathrm{J/m^2}$ for hexagonal printed and non-printed sample respectively. A comparison of critical Mode I stress intensity factor measured from DCB test and the FE model is shown in Table 4.4, in both the printed sample shows a higher K_{1C}, demonstrating the toughening effect in the small scale. A larger K_{1C} was obtained in the FE model compared with from experiment, which was mainly due to the linear elastic model applied here, plasticity is not considered, therefore, a larger value of K was observed in FE analysis.

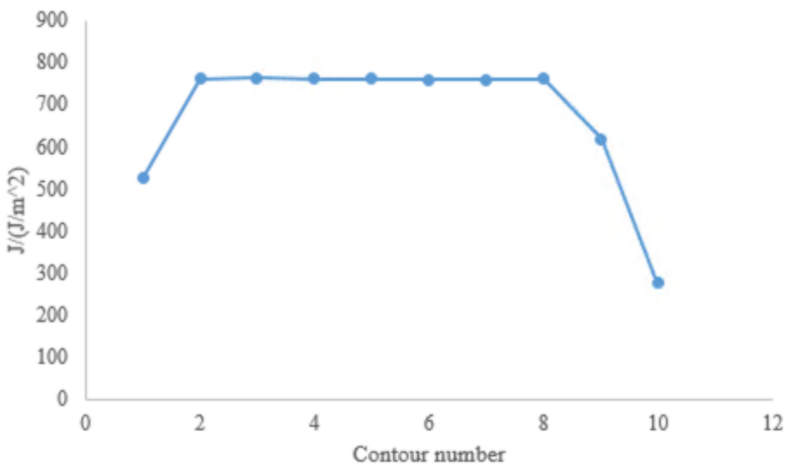

Figure 4.38. Example of J-integral variation with different contour in printed sample; where the calculation converged from the 2nd contour

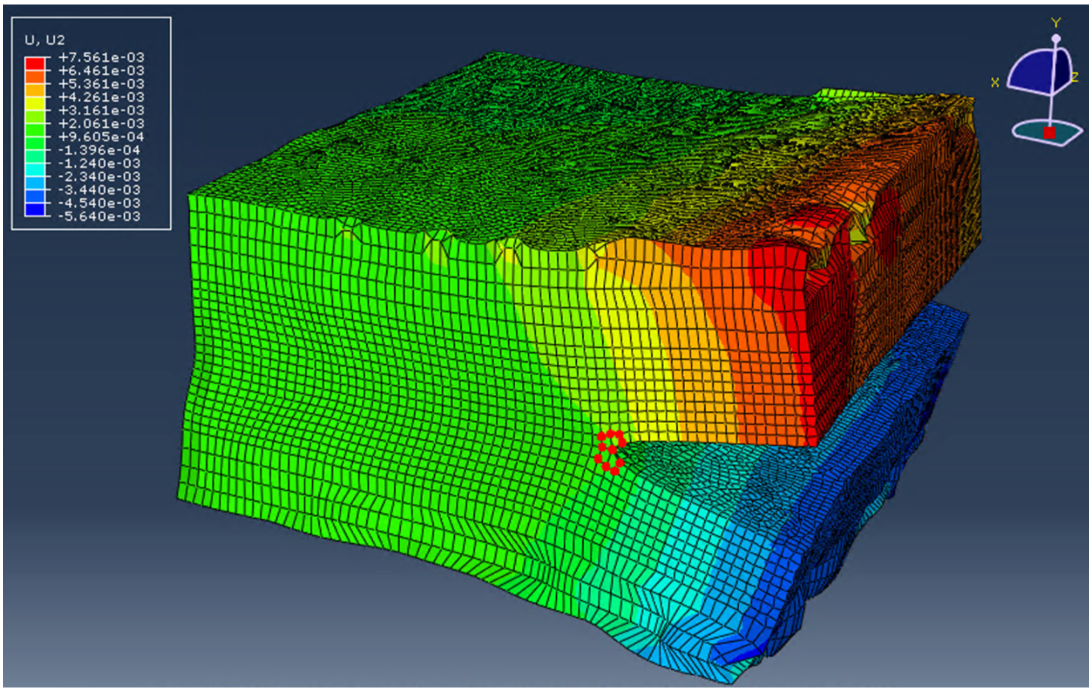

Figure 4.39. Typical example of FE result (wedge insertion at 214 µm for NP_0 sample) showing the deformation and mode I displacement field in the component

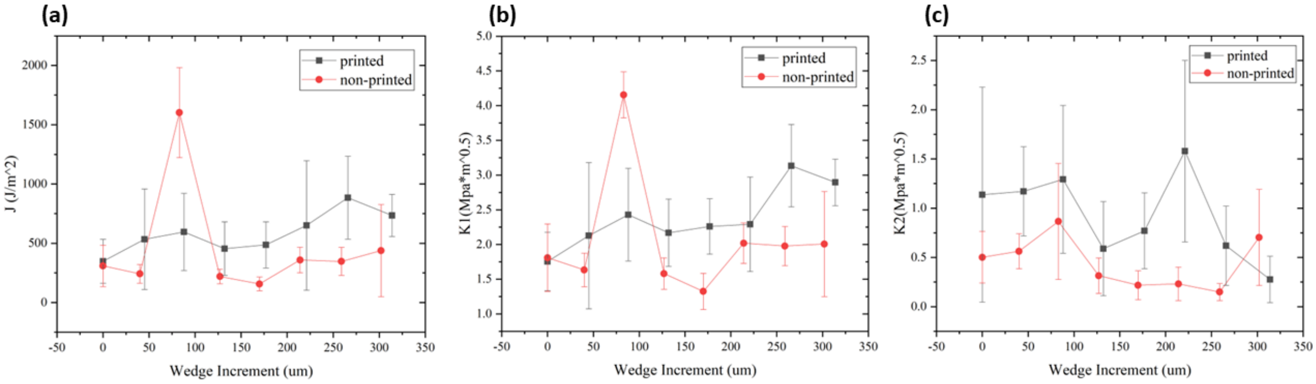

Figure 4.40. Evolution of **(a)** J-integral, **(b)** mode I SIF and **(c)** mode II SIF along Z-axis as wedge insert, averaging along the Z-axis

Table 4.4. Comparison of K_{1C} measured from experiment (DCB) and FE model

	DCB (K_{1C}/MPa*m$^{0.5}$)	**FE (K_{1C}/MPa*m$^{0.5}$)**
PMMA_Hex_15000	1.48 ± 0.04	2.38 ± 0.44
NP_0	1.38 ± 0.05	4.4 ± 0.26

4.2.2 In-situ monochromatic beam phase contrast XCT

To examine whether the toughening mechanism occurs locally or globally, line printed laminates (PMMA_Line_15000, PEG_Line_400 and NP_2 for comparison) were observed under in-situ s-XCT, following the characterization for hexagonal printing pattern CFRP. The experiment was conducted at the TOMCAT beamline at the Swiss Light Source, where the set-up is shown in Figure 4.41. Because of the limited sample stage load bearing capacity, a customized loading stage was designed: The sample opening was achieved by inserting a 1 mm thick aluminium plate into the pre-crack, using a PI ltd. M-229.25S linear actuator monitored by a C-663.12 stepper motor controller. The aluminium plate was locked in a polymer tube which moved together with the tube that fitted against the outside supporting aluminium tube to avoid tilt during the wedge movement. The other end of the sample was tightly gripped. The actuator was supported by the 2 mm-thick aluminium tube. To reduce the attenuation due to the aluminium, the tube thickness was reduced to 1 mm in the FOV region (80% of the X-ray intensity was absorbed by aluminium).

The diameter of the printing dots that makes the line is ~200 μm and the distance between centre of lines is 250 μm along the fibre direction with a dot spacing along the lines of 50 μm (Figure 2.6). The two-layer laminate was cut by low-speed diamond saw to the final dimension of 0.5 x 3 x 50 mm with a 10 mm length pre-crack along the fibre direction generated by a PTFE film inserted between the plies before curing. The monochromatic beam energy was optimized at 21 KeV, 2200 projections were taken over 180° with an exposure time of 120 ms per projection. The low energy monochromatic X ray at TOMCAT enabled propagational phase contrast, which was further enhanced by the Gridrec reconstruction algorithm [31]. The Gridrec was initiated by Dowd, which makes use of gridding method for resampling of the Fourier space from polar to Cartesian coordinates [32]. The Pco.edge 5.5 micro-image detector was applied to acquire the X-ray radiographs. In-situ tomography was conducted with the 20x magnification lens which provides 0.33 µm pixel size and 0.8 x 0.7 mm field of view.

The crack was propagated for at least 3.5 mm before the series of in-situ tomography observations were made. The region of interest was captured before the crack was propagated into it, in order to obtain a strain-free reference. The specimen was opened at 15 µm/s displacement rate of the wedge and tomographs were acquired at every 30-µm increment of the wedge, where the wedge movement stopped during the tomography acquisition. The sample-detector distance was 40 mm. The raw sinograms were reconstructed through the Gridrec algorithm with application of Paganin filter. The degree of Paganin filtering is proportional to the contribution of X-ray absorption (beta) and phase shift (delta) as detailed in Chapter 2, here, the two parameters were at 3.7e-8 and at 1.7e-10 respectively. [20, 33]

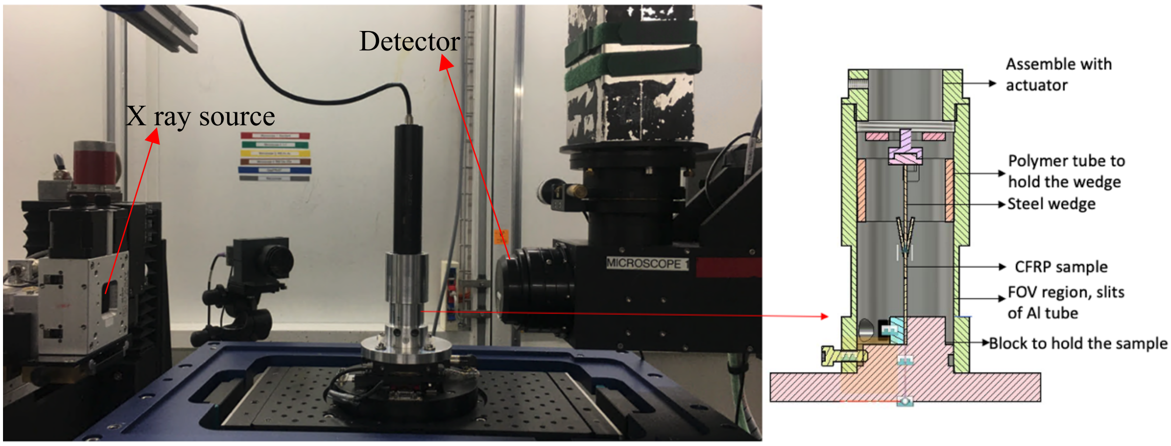

Figure 4.41. Experimental setup and the details of loading condition

The 32 bit volume image was resamples to 8 bit in ImageJ. Avizo was then applied for 3D visualization of the tomographic volume and phases segmentation (crack and laminate), where an example of PMMA_Line_15000 at step 7 (wedge insert movement at 210 μm) is shown in Figure 4.42 – 44, with the segmented crack shown in Figure 4.45. Due to the large calculation capacity required for processing in Avizo, the 3D volume was cut to along Z axis to save the computational cost, which was also sufficient to represent the component features. In Figure 4.42, fibre and matrix bridging were observed in the plane perpendicular to the fibres, where the resolution and fringe artifacts on the crack-material interface has been largely improved compared with tomographic characterization in I12-JEEP (Figure 4.25(c) & Figure 4.46). From the XY section, single, parallel, and broken carbon fibres were observed (Figure 4.47), while the three specimens demonstrated the similar level of bridging amount, which agreed with Lim's observation that the printing dots do not make a difference to fibre bridging [7]. As shown in Figure 4.49, the XZ section in the middle of the damage region revealed that the crack does not propagate with a straight front; instead, a serrated crack tip was observed, indicating the crack tended to grow along the fibre. With regards to the printing dots, no observations found evidence of the printing materials, which suggested either that the dots might diffuse into the matrix instead of existing as separated phase or the

XCT contrast was not sufficient to distinguish the polymer printed phase from the epoxy matrix.

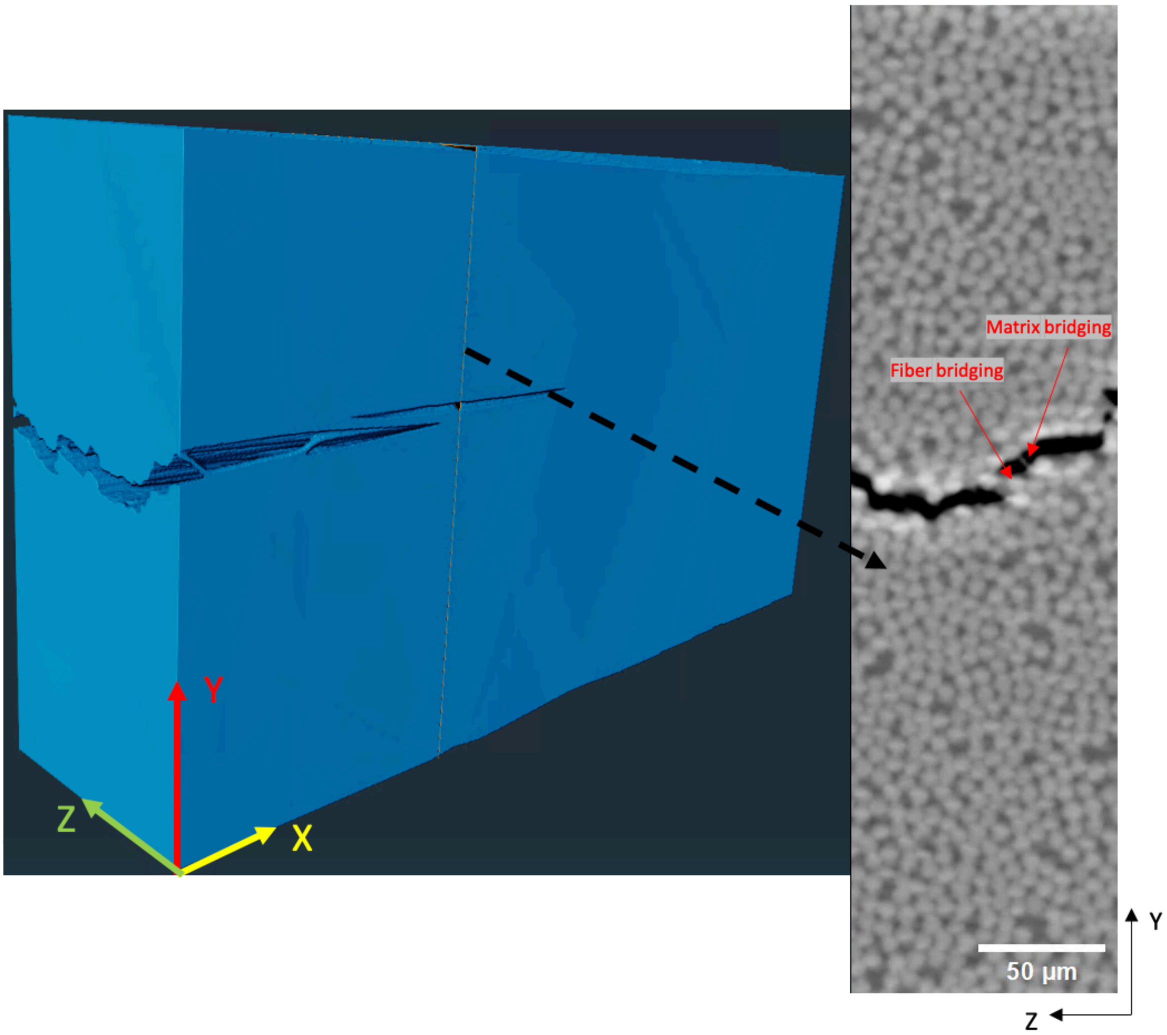

Figure 4.42. YZ cross section of PMMA_Line_15000 XCT in 3D visualization

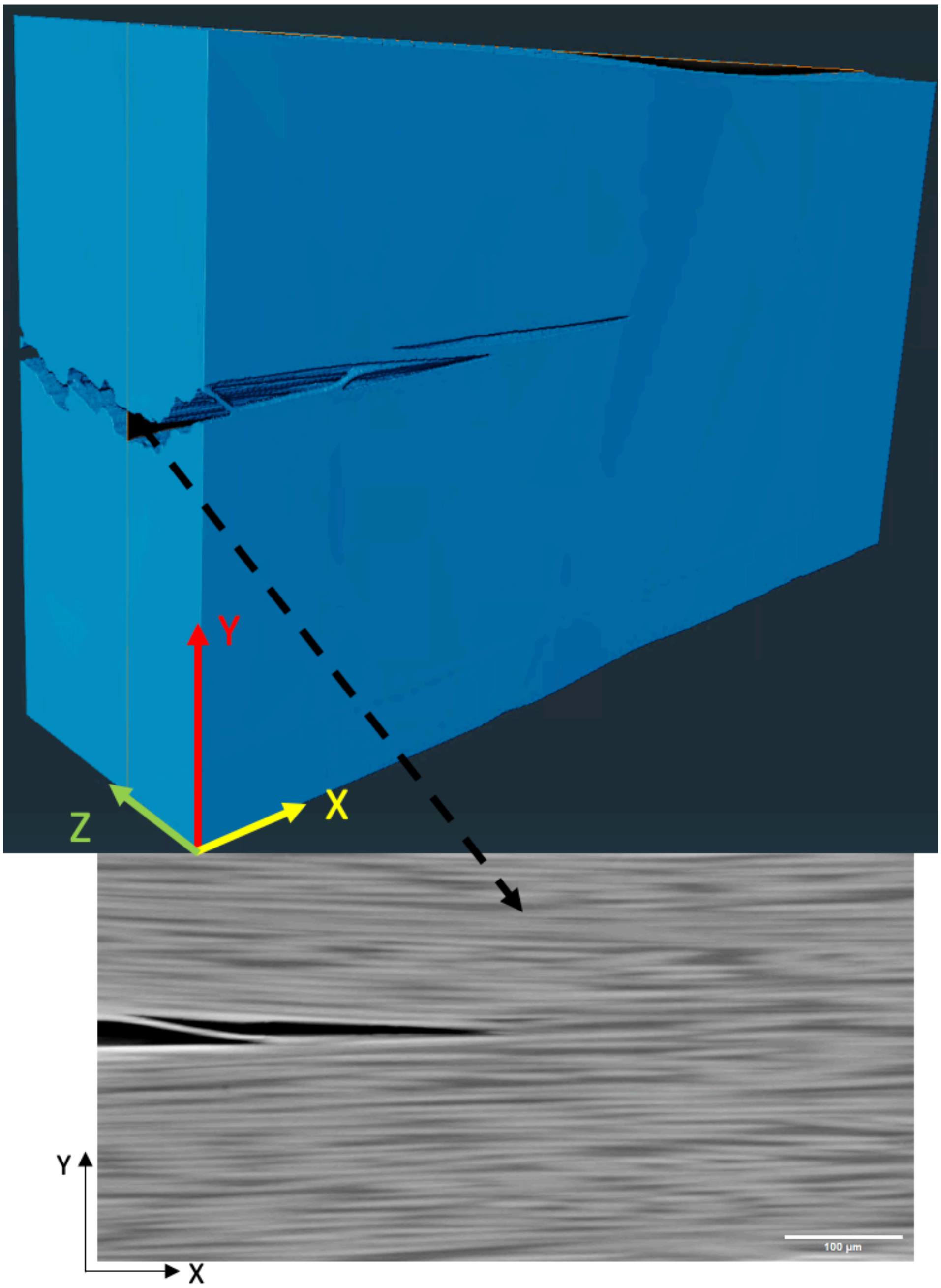

Figure 4.43. XY cross section of PMMA_Line_15000 XCT in 3D visualization

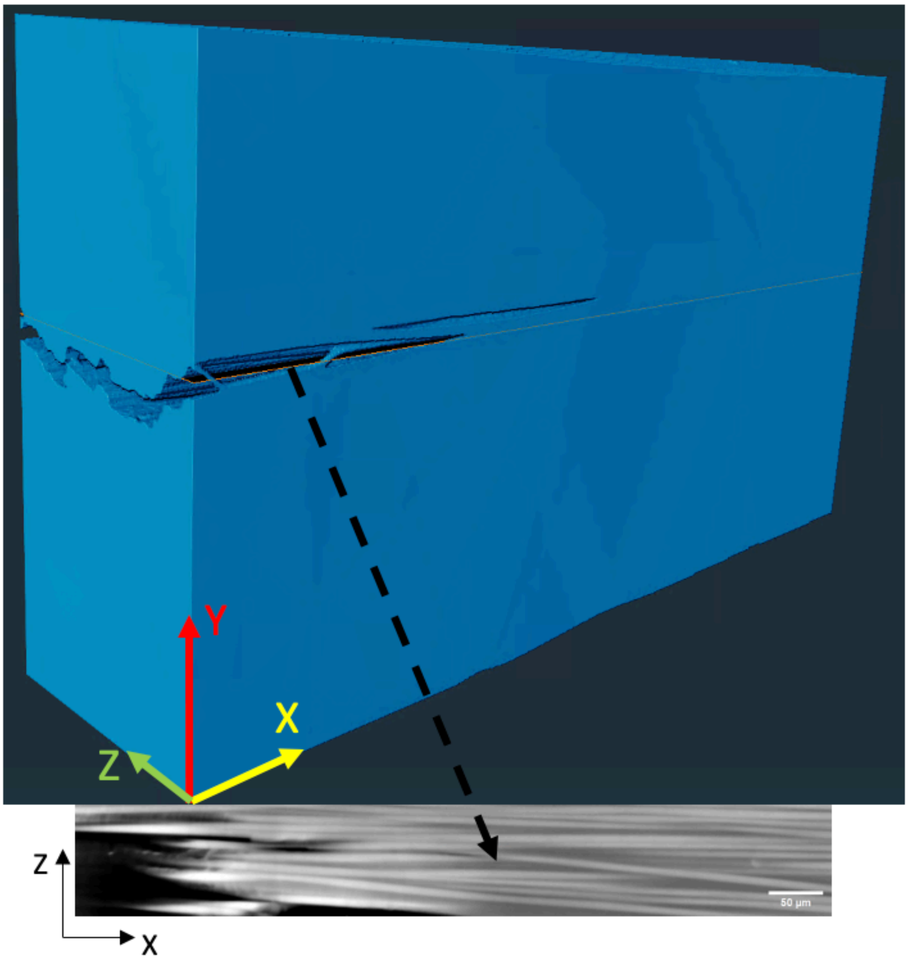

Figure 4.44. XZ cross section of PMMA_Line_15000 XCT in 3D visualization

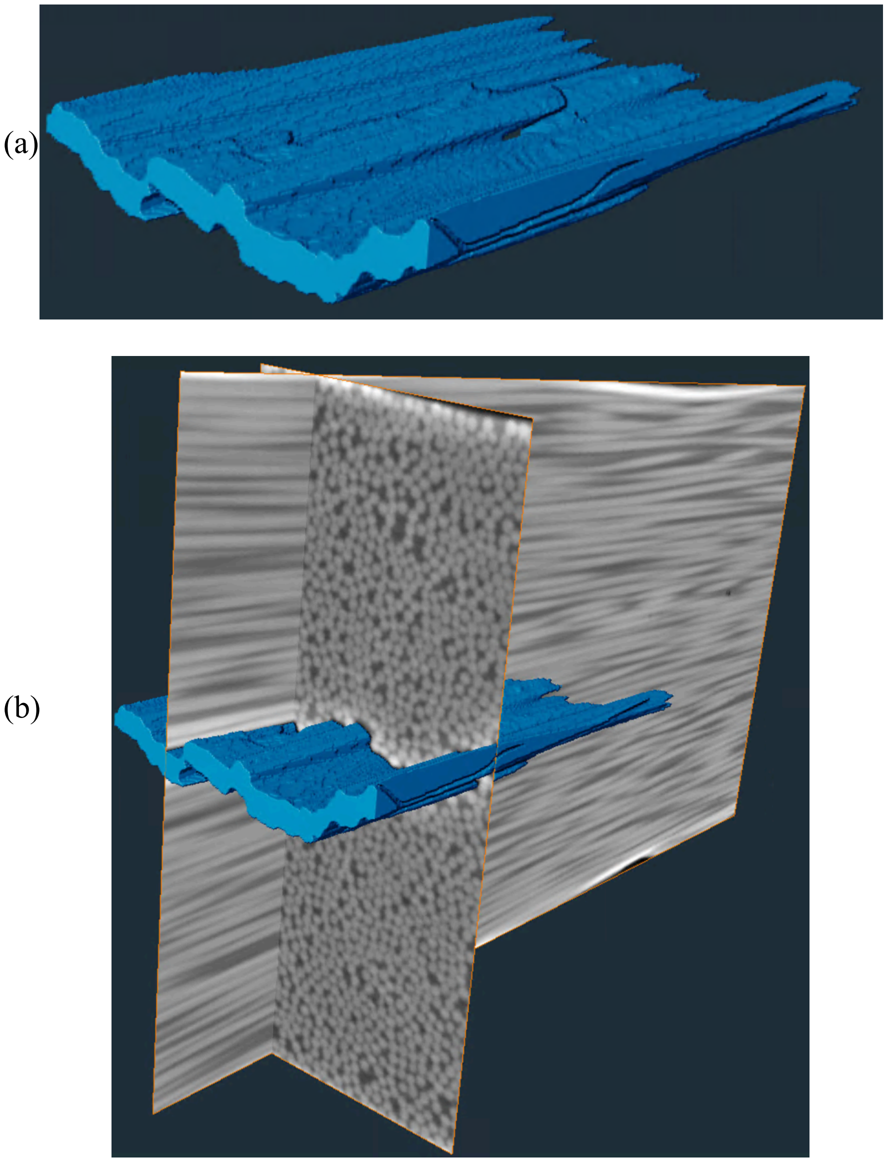

Figure 4.45. (a) Segmentation of crack **(b)** with the reference of tomographic ortho slices in PMMA_Line_15000 laminate

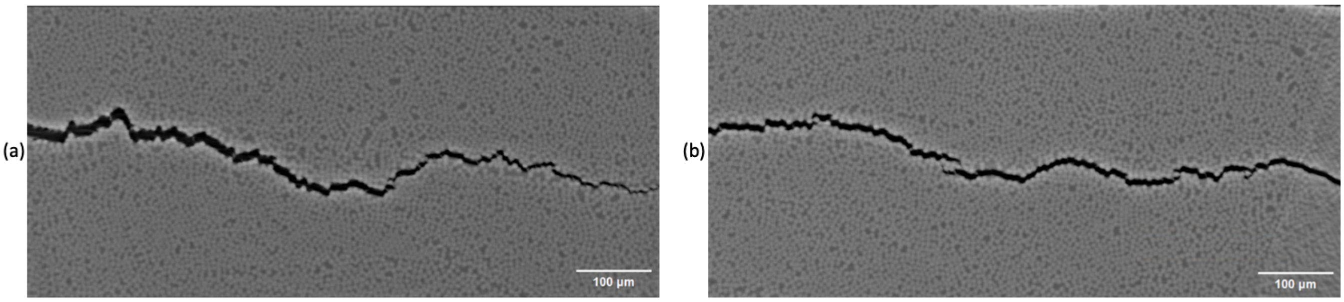

Figure 4.46. Comparisons of YZ cross-section of **(a)** PMMA_Hex_15000, **(b)** NP_0

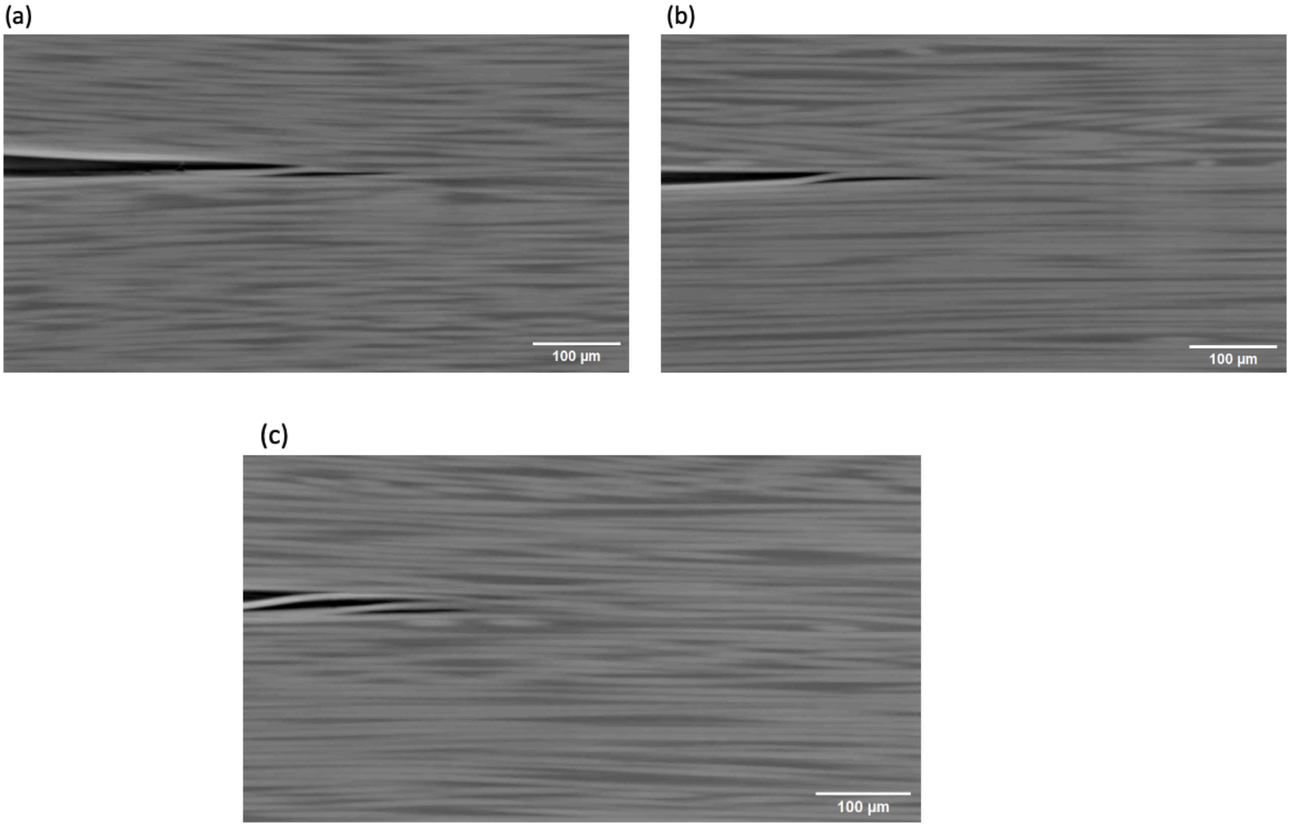

Figure 4.47. XY Cross-section of XCT for **(a)** PMMA_Line_15000, **(b)** PEG_Line_400 and **(c)** NP_2 laminates respectively

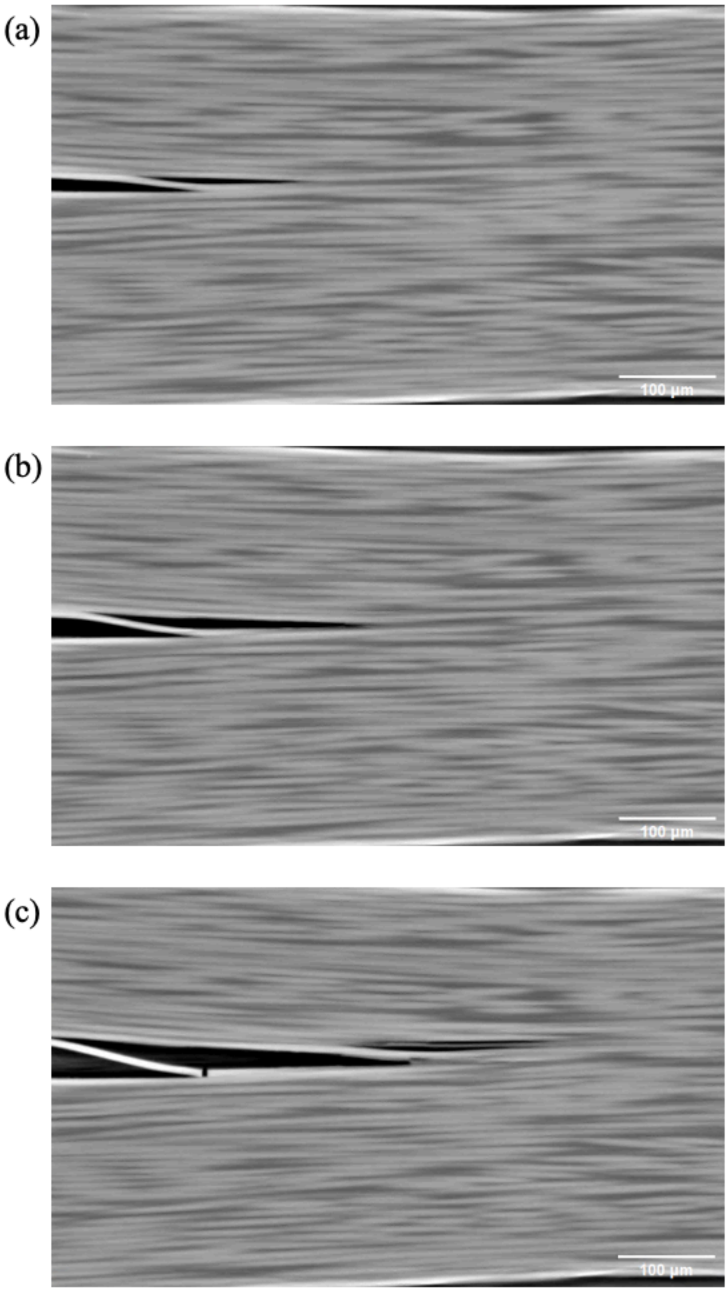

Figure 4.48. From **(a) – (c)** Damage development in PMMA_Line_15000 laminate showing the bridging development, failure and second fibre bridging formation

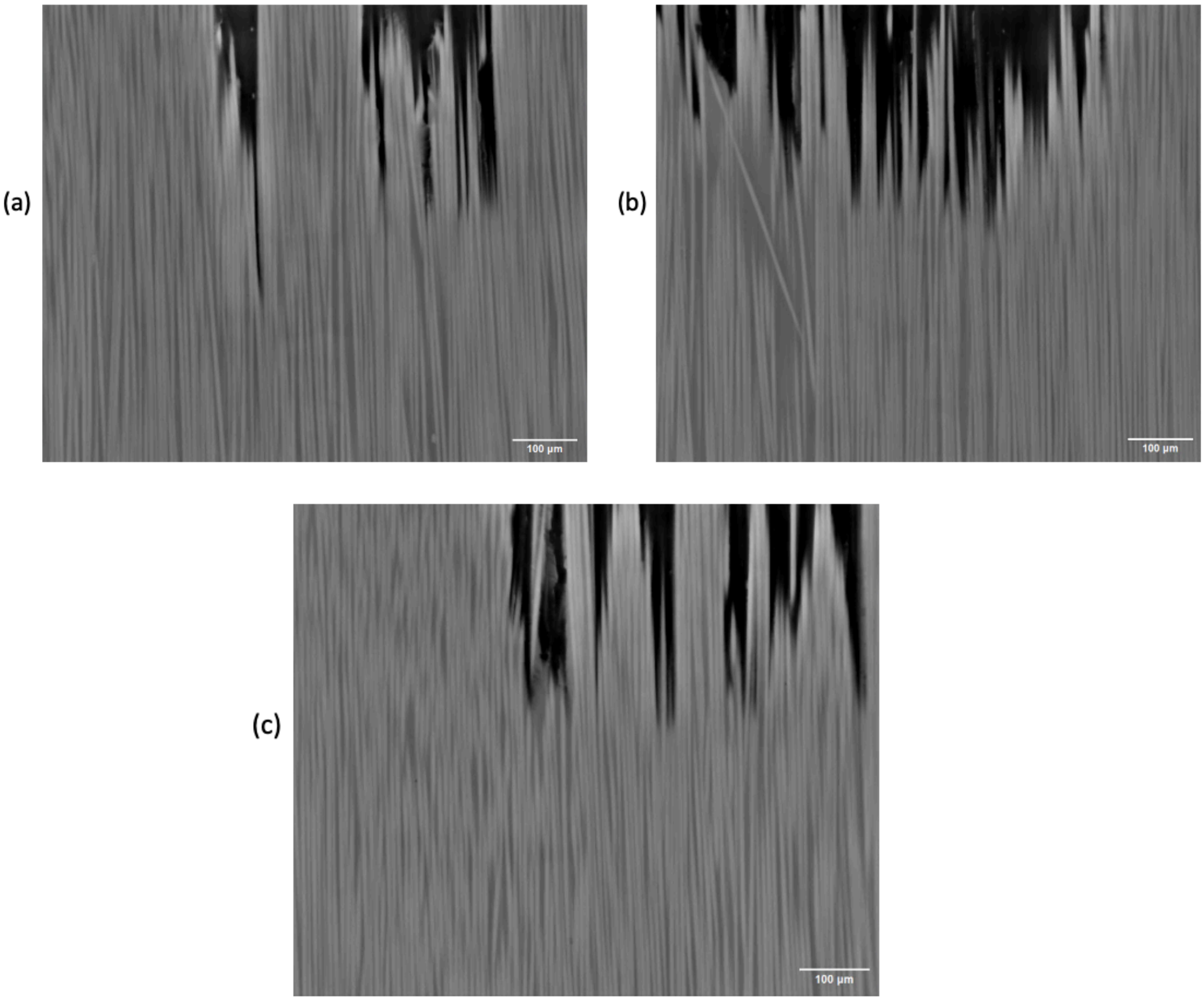

Figure 4.49. XZ Cross-section of XCT for **(a)** PMMA_Line_15000, **(b)** PEG_Line_400 and **(c)** NP_2 laminates respectively

The 3D volume was then processed using DVC in Lavision DaVis 8.4.0 software. As illustrated in Figure 4.49, the non-straight crack tip indicated asynchronous damage propagation, resulting in significant variations in the displacement field along the width direction. This caused DVC to struggle to perform reliable correlations when processing images with the whole Z-slices. To address this challenge, the raw image was cropped to dimensions of 2112 x 1272 x 576 pixels, which corresponded to a physical size of 697 x 420 x 190 µm for mapping of the displacement field.

The Fast Fourier Transform (FFT) DVC algorithm in DaVis was applied to the reference and loaded stages. Following a similar procedure to that used for I12-JEEP in the previous section, multiple steps were preformed, initiating with a subset size of 160 voxels, then progressively reduced to 128 and 96 voxels, with 1, 2 and 3 passes executed at each step respectively. 75% subset overlap was applied between adjacent volumes, achieving a resolution of 7.92 µm. Gaussian-shape (round) was employed as the interrogation volumes, and rigid body movement was removed from the vector result. Voxels with correlation value below 40% were considered as invalid and excluded. Outliers were eliminated using a threshold of 2, and missing vectors were filled by averaging values from the 7 x 7 neighbours. A typical example of displacement field in the Y-direction is shown in Figure 4.50, where a clear mode I opening has be observed. To assess the error in displacement correlation, the above calculation was repeated on the same unstrained region between two loaded steps, where the standard deviation of displacement was taken as the measurement error. As summarized in Table 4.5, largest displacement error was observed in U_x, attributed to the lack of unique features along the fibre direction. Nevertheless, even the largest error was still less than 1x pixel size, demonstrating the confidence of the calculations.

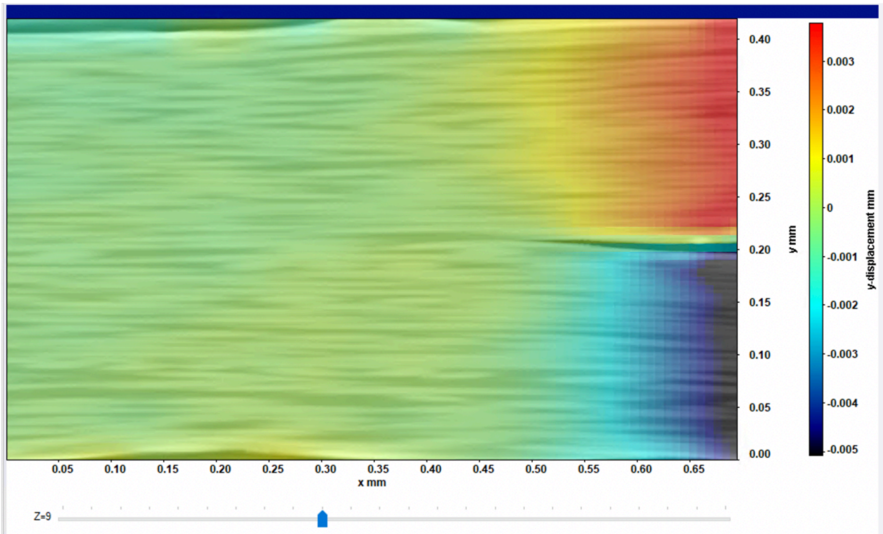

Figure 4.50. Example of DVC result slice in Uy displacement field

Table 4.5. Summary of displacement error in the three directions

Displacement error	**Value / µm**
ΔU_x	0.309
ΔU_y	0.087
ΔU_z	0.035

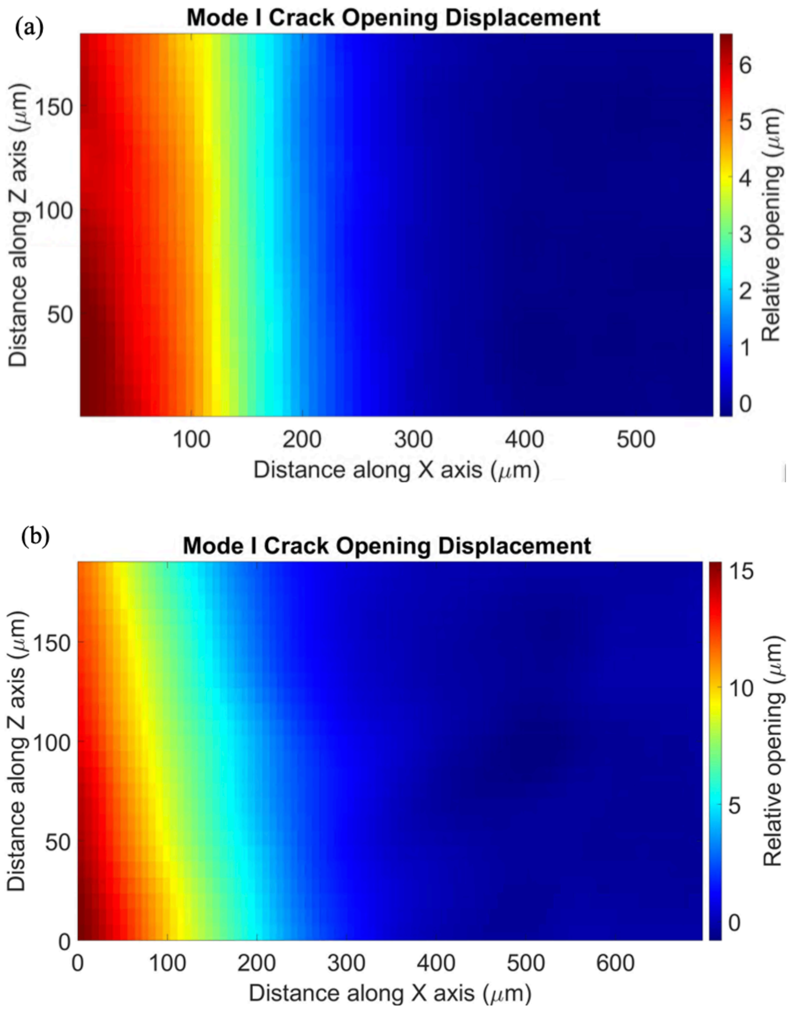

(c)

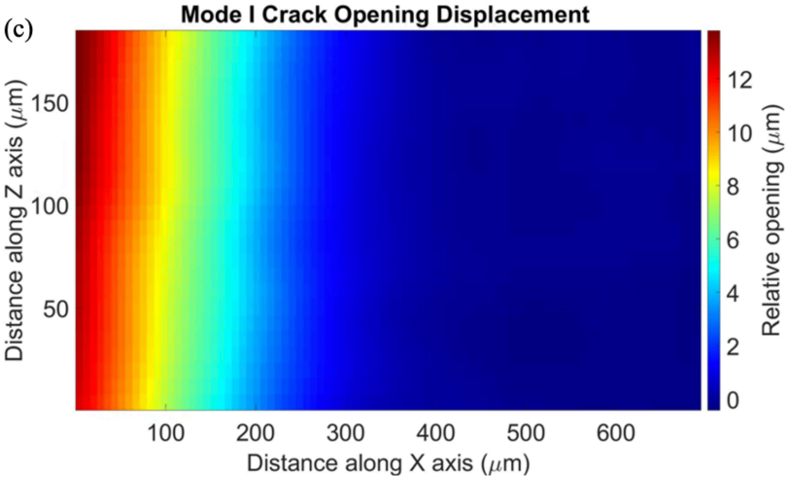

Figure 4.51. Mode I opening displacement field of **(a)** NP_2 **(b)** PMMA_Line_15000 and **(c)** PEG_Line_400; a slant crack front was observed in PMMA_Line_15000 laminate

Following the same analysis in I12-JEEP, the Mode I displacement along the crack development direction was evaluated. Because the high level of crack front variation along the Z-axis, only the middle line (in Z-axis) was selected to measure the relative opening, where the result is shown in Figure 4.52. Both printed laminates possess a larger COD, while PEG_Line_400 sample shows the highest opening at the same distance ahead of crack tip. This agreed with the result of DCB mechanical test in Chapter 3, where PEG_Line_400 displays the largest toughening effect.

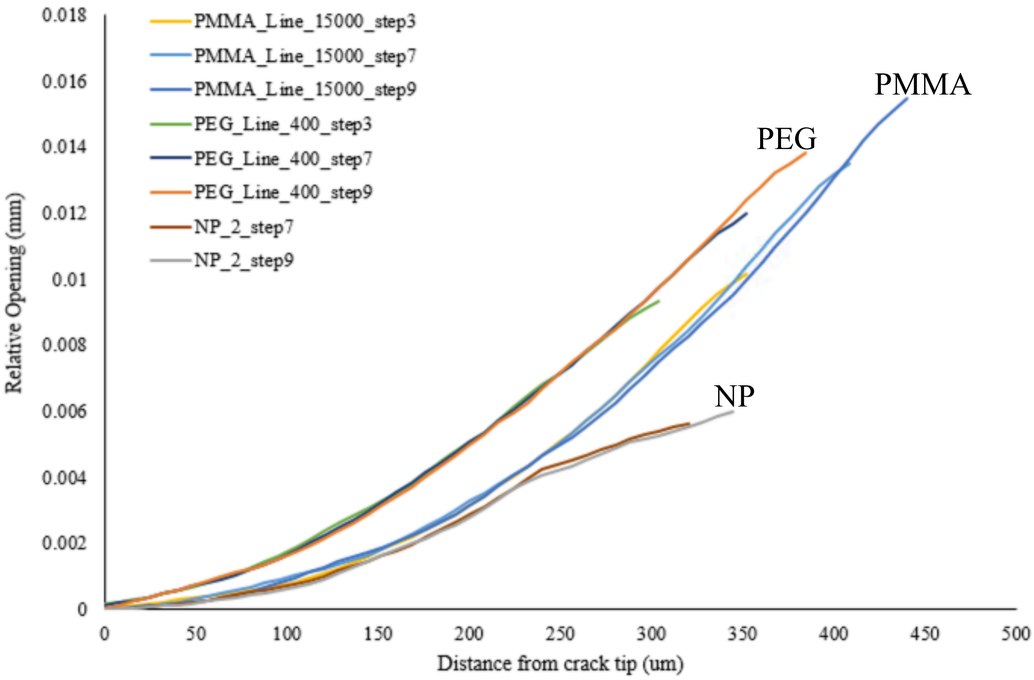

Figure 4.52. Comparison of Mode I COD between PMMA_Line_15000, PEG_Line_400 and NP_2 laminates

Phase congruency analysis was then applied on the full-field displacement data to track the movement of crack tip, using the same process and setting parameter as in the I12-JEEP. A fourth-degree polynomial function was fitted to the tortuous crack tip to a smooth curve front, as detailed in section 4.2.1.3. The evolution of crack front during damage development in PMMA_Line_15000 and PEG_Line_400 are shown as Figure 4.53. The wedge was incrementally moved by 30 µm per step, resulting in a downward movement of 60 µm between odd-number steps. In the PMMA_Line_15000 laminate, the crack front movement initially propagated by approximately 60 µm, synchronized with the motion of wedge, which then decreased and stabilized at ~ 25 – 35 µm between each odd step. This suggested that the steel wedge was not perfectly aligned with the sample pre-crack, preventing pure Mode I opening.

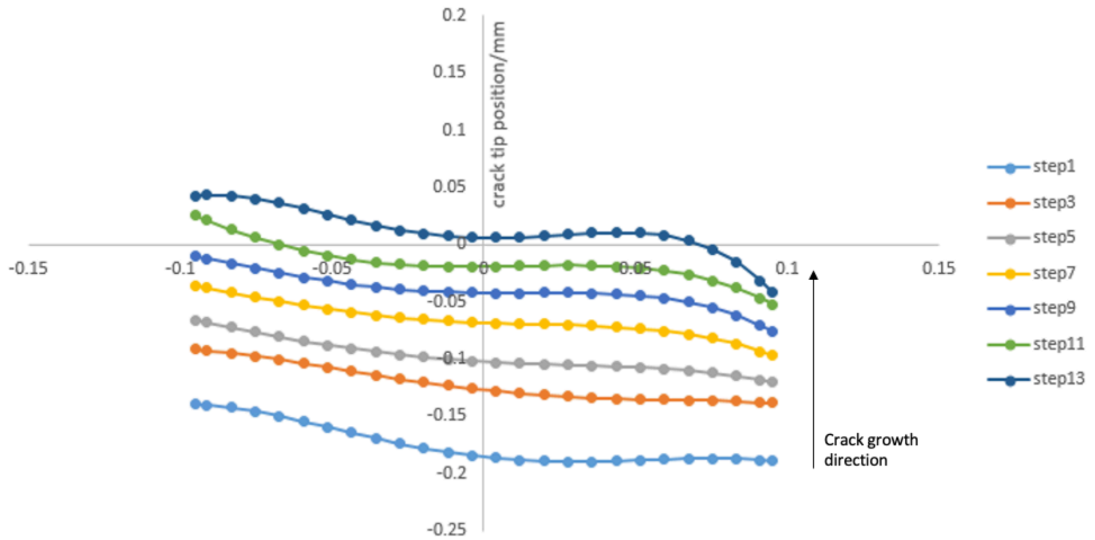

Figure 4.53. Tracking the evolution of crack front movement in PMMA_Line_15000; the wedge motion between each odd-number step is 0.06 mm

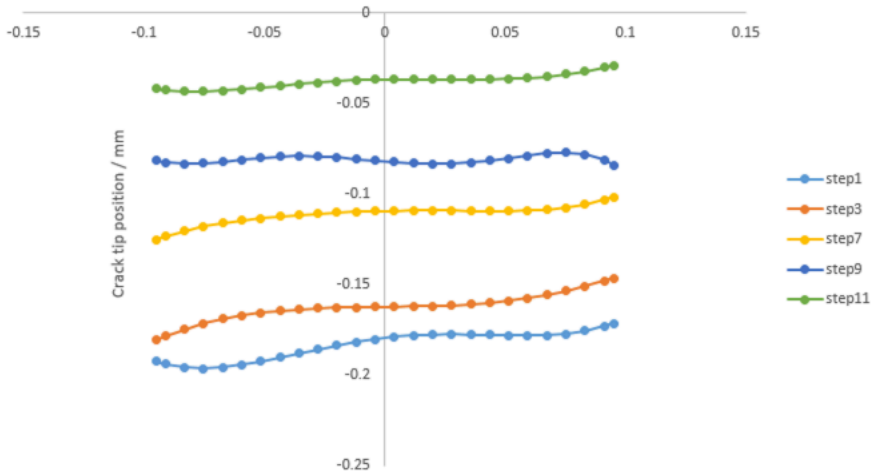

Figure 4.54. Tracking the evolution of crack front movement in PEG_Line_400

Following the methodology detailed in section 4.2.1, the full-field displacement was processed using the Shoemake code [24] in MATLAB to remove the rigid body rotation (Figure 4.55). The processed displacement data was then imported as boundary condition in the finite element analysis to evaluate the variation of critical strain energy. The FE model had the same dimension as the cropped 3D volume (697 x 420 x 190 μm), and the constitutive relationship follows the same used in I12-JEEP analysis shown in Table 4.3. The second contour was selected as the representative result, where the calculation convergency was achieved, while distortions due to the non-straight crack front have not yet occurred (Figure 4.56). A typical distribution of J-integral along the Z-axis (width direction) for a single step of NP_2 sample is displayed in Figure 4.57: gradual variation was observed due to the crack tip located at different positions along the fibre direction. The average value among the Z-axis provided the representative value for each step.

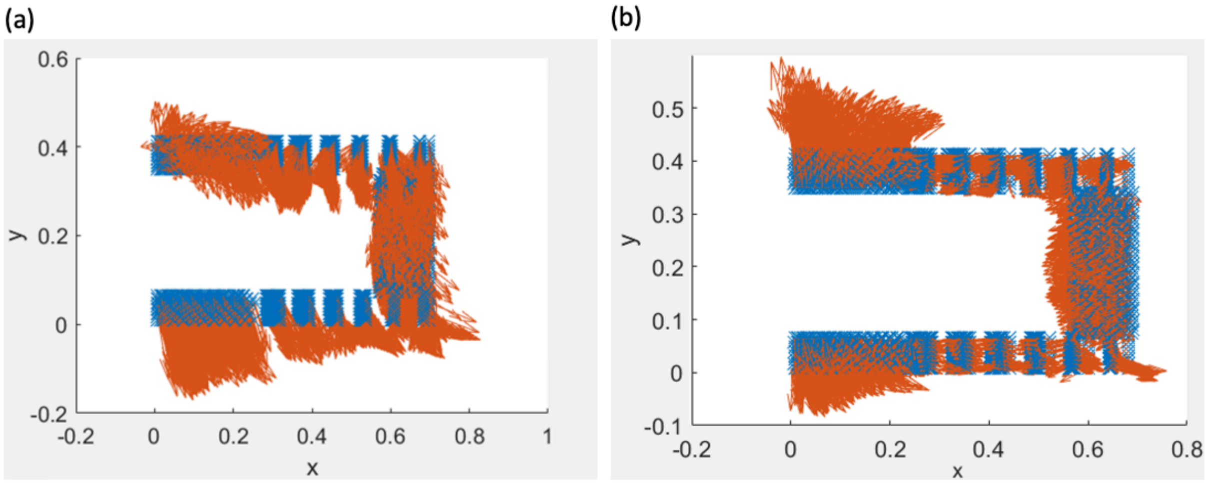

Figure 4.55. The displacement field put as boundary condition in FE model **(a)** before and **(b)** after removing rigid body motion

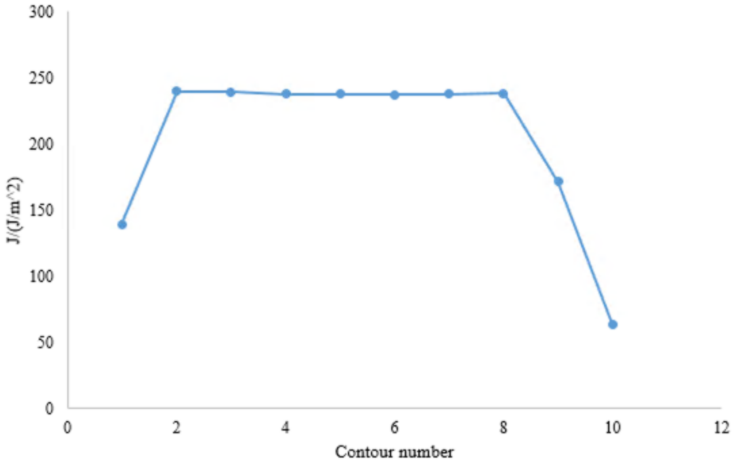

Figure 4.56. Example of J-integral variation with different contour in PMMA_Line_15000; where the calculation converged from the 2nd contour

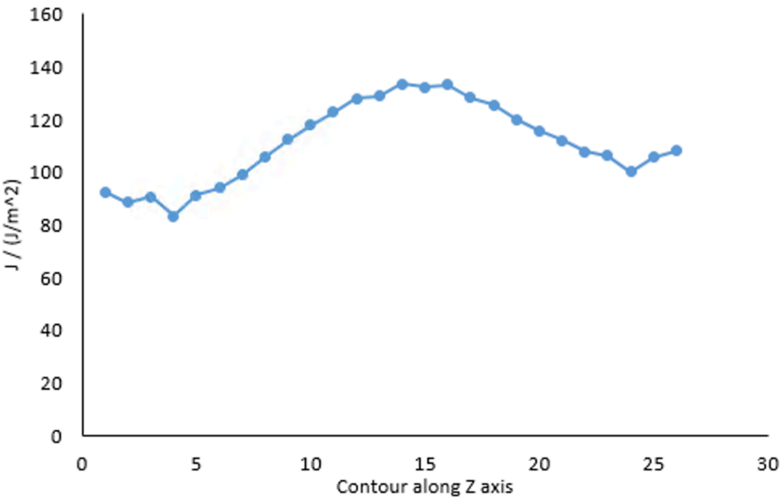

Figure 4.57. Variation of J-integral along the width direction in NP_2

The evolution of J-integral, along with the segregated Mode I, II and III stress intensity factors at different loading stage during wedge insertion are shown in Figure 4.58-59. Here, crack propagation was primarily dominated by Mode I, while less significant Mode II & III have also been observed. The averaged J-integral for the three samples are 96 ± 22 J/m^2 (NP_2), 108 ± 13 J/m^2 (PEG_Line_400) and 155 ± 11 J/m^2 (PMMA_Line_15000), which demonstrated more energy is required to propagate the damage in CFRP after printing. In each step, the standard deviation which represented the variations of J-integral in PMMA_Line_15000 laminate at different Z position was significantly higher than the other two groups. This is due to a more slanted crack front that occurred in the PMMA_Line_15000 specimen. By comparing Figure 4.53 and Figure 4.54, the variation of crack tip position in PMMA_Line_15000 was average at ~ 0.05 mm within a single step, while this value was much reduced in PEG_Line_400. Also shown in Figure 4.51, in the NP_2 and PEG_Line_400 samples, the crack propagated uniformly along the Z-axis, with the crack front remaining parallel to the line printing pattern. While the crack tip position in PMMA_Line_15000 varied along the Z direction, corresponding to different printing locations. This indicated averaging along the Z axis in PMMA_Line_15000 to define J-integral at each wedge insertion position was not representative, which could also explain the differences between result of DCB and COD analysis. Moreover, the above observation suggested that the printing dots might work locally to enhance the fracture energy. Additionally, the variation of crack edge within the cropped volume was ~ 50 µm, which was significantly smaller than the diameter of original printing droplets. This implied that the droplets might separate into smaller feature to influence the fracture toughness, where such features have been observed through fractography under SEM, as will be discussed in Chapter 5.

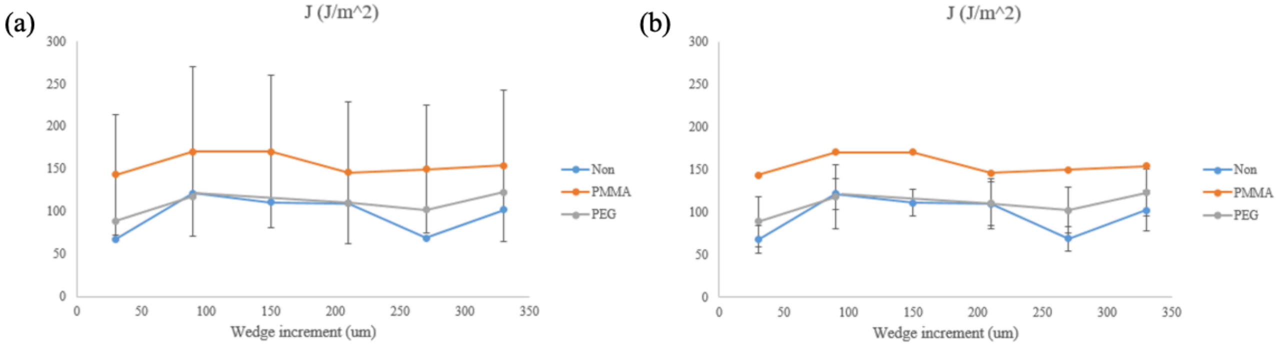

Figure 4.58. Summary of evolution of J-integral for the three samples showing fluctuation of **(a)** PMMA_Line_15000 and **(b)** NP_2 and PEG_Line_400

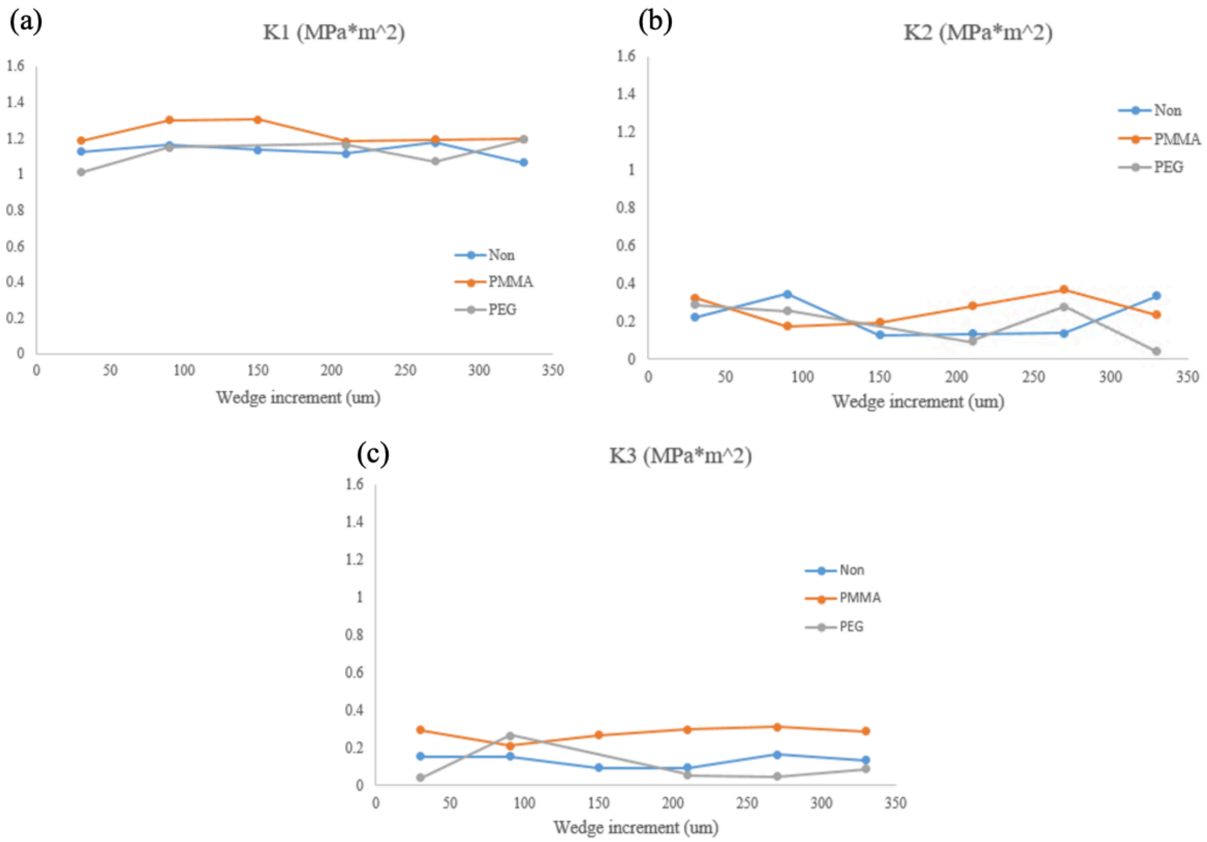

Figure 4.59. Summary of evolution of Stress intensity factors in **(a)** Mode I, **(b)** Mode II and **(c)** Mode III among the three samples

Table 4.6 compares the Mode I critical stress intensity factor measured from the two in-situ s-XCT. In both cases, the PMMA-printed samples demonstrated a stronger resistance to crack extension. The values of K_{1C} measured from TOMCAT beamline, however, were consistently lower than that of I12-JEEP. This was mainly due to the degradation of prepreg during storage. As detailed in Chapter 3, the prepregs of PMMA_Line_15000 (characterized in TOMCAT) have been stored for over 4 years before printing and curing, while PMMA_Hex_15000 (analysed in I12) was made by fresh prepregs. It has been reported by Yi that overtime storage of prepregs in the fridge would lead to a decline of composite fracture toughness [27]. Moreover, using the different beamline would also cause the measurement deviation. Additionally, the enhancement of fracture toughness introduced by PMMA droplets in I12 was also higher than in TOMCAT, which was attributed to the

PMMA solution. 10 wt.% was applied in PMMA_Hex_15000 (I12), while for PMMA_Line_15000 (TOMCAT), the solution density was at 5wt.%. The former laminate had been demonstrated to exhibit better toughening effect [27], which agreed with the FE calculation in this work.

Table 4.6. Comparison of Mode I stress intensity factor measured from the two s-XCT experiments

	I12 (K_{1C}/MPa*$m^{0.5}$)	**TOMCAT (K_{1C}/MPa*$m^{0.5}$)**
PMMA-Printed	2.38 ± 0.44	1.23 ± 0.05
Non-printed	1.76 ± 0.26	1.12 ± 0.04

4.3 Conclusion

This chapter presents a series of in-situ characterizations aimed at studying the Mode I crack opening behaviour, using synchrotron X-ray techniques. Dual X ray imaging and diffraction observation was performed, where the crack front was clearly resolved by processing the radiograph with DIC; the lattice strain however failed to be captured due to the low strain in the partial crystalized carbon fibre, which resulted in a diffused diffraction signal, as well as the limited measurement precision resulting from that only partial Debye ring was captured on detector during the experiments. In-situ XCT was employed to track the evolution of 3D volumes as damage propagation, which enabled the visualization and segmentation of crack and bulk component. The displacement field was resolved using DVC, where the resulting data informed a finite element model to calculate the J-integral and stress intensity factor. The results indicated that the printed laminates exhibited a higher critical strain energy rate and crack opening displacement.

4.4 References

[1.] Korsunsky AM, Wells KE, Withers PJ. Mapping two-dimensional state of strain using synchroton X-ray diffraction. Scripta Materialia. 1998;39(12):1705-12.

[2.] Meng Q, Li H, Wang K, Guo S, Wei F, Qi J, et al. In Situ Synchrotron X-ray Diffraction Investigations of the Nonlinear Deformation Behavior of a Low Modulus β-Type Ti36Nb5Zr Alloy. Metals. 2020;10(12):1619.

[3.] Srisuriyachot J, McNair SAM, Chen Y, Barthelay T, Gray R, Bénézech J, et al. Carbon fibre lattice strain mapping via microfocus synchrotron X-ray diffraction of a reinforced composite. Carbon. 2022;200:347-60.

[4.] Czapski P, Srisuriyachot J, Kaźmierczyk F, Waś T, Jakubczak P, Dolbnya IP, et al. Synchrotron X-ray diffraction and radiography - Lattice strain characterization in thin-walled carbon fibre channel structures subjected to buckling. Carbon. 2023;215:118429.

[5.] Reinhard C, Drakopoulos M, Ahmed S, Deyhle H, James A, Charlesworth C, et al. Beamline K11 DIAD: a new instrument for dual imaging and diffraction at Diamond Light Source. Journal of Synchrotron Radiation. 2021;28.

[6.] Zhang Y. In situ 3D observation of delamination crack propagation in carbon-fibre/epoxy composites: University of Oxford; 2018.

[7.] Lim Y. In-Situ 3D observation of damage development and healing in a carbon-fibre/epoxy composite: University of Oxford; 2019.

[8.] University of California San Fracisco CfALM. How to acquire flat-field correction images [Available from: https://calm.ucsf.edu/how-acquire-flat-field-correction-images#:~:text=Mathematically%2C%20our%20measured%20image%20(I,meas%20–%20Dark)%20%2F%20Flat.

[9.] GmbH L. Product-Manual for DaVis 8.4. 2017.

[10.] Filik J, Ashton A, Chang P, Chater P, Day S, Drakopoulos M, et al. Processing two-dimensional X-ray diffraction and small-angle scattering data in DAWN 2. Journal of Applied Crystallography. 2017;50.

[11.] Basham M, Filik J, Wharmby M, Chang P, El Kassaby B, Gerring M, et al. Data Analysis WorkbeNch (DAWN). Journal of Synchrotron Radiation. 2015;22.

[12.] Mani D, Kupsch A, Müller BR, Bruno G. Diffraction Enhanced Imaging Analysis with Pseudo-Voigt Fit Function. J Imaging. 2022;8(8).

[13.] Thompson P, Cox D, Hastings J. Rietveld refinement of Debye–Scherrer synchrotron X-ray data from Al2O3. Journal of Applied Crystallography. 1987;20(2):79-83.

[14.] Miyagawa H, Mase T, Sato C, Drown E, Drzal LT, Ikegami K. Comparison of experimental and theoretical transverse elastic modulus of carbon fibers. Carbon. 2006;44(10):2002-8.

[15.] Shobhana E, editor X-Ray Diffraction and UV-Visible Studies of PMMA Thin Films2012.

[16.] Buzug TM. Computed tomography. Springer handbook of medical technology: Springer; 2011. p. 311-42.

[17.] Hanke R, Fuchs T, Salamon M, Zabler S. X-ray microtomography for materials characterization. Materials characterization using Nondestructive Evaluation (NDE) methods: Elsevier; 2016. p. 45-79.

[18.] Spanne P, Raven C, Snigireva I, Snigirev A. In-line holography and phase-contrast microtomography with high energy x-rays. Physics in Medicine & Biology. 1999;44(3):741.

[19.] Henke BL, Gullikson EM, Davis JC. X-ray interactions: photoabsorption, scattering, transmission, and reflection at E= 50-30,000 eV, Z= 1-92. Atomic data and nuclear data tables. 1993;54(2):181-342.

[20.] Paganin D, Mayo SC, Gureyev TE, Miller PR, Wilkins SW. Simultaneous phase and amplitude extraction from a single defocused image of a homogeneous object. Journal of microscopy. 2002;206(1):33-40.

[21.] Garcea SC, Wang Y, Withers PJ. X-ray computed tomography of polymer composites. Composites Science and Technology. 2018;156:305-19.

[22.] Drakopoulos M, Connolley, T., Reinhard, C., Atwood, R., Magdysyuk, O., Vo, N., Hart, M., Connor, L., Humphreys, B., Howell, G., Davies, S., Hill, T., Wilkin, G., Pedersen, U., Foster, A., De Maio, N., Basham, M., Yuan, F. & Wanelik, K. I12: the Joint Engineering, Environment and Processing (JEEP) beamline at Diamond Light Source. Journal of Synchrotron Radiation. 2015.

[23.] Westerweel J, Scarano F. Universal outlier detection for PIV data. Experiments in Fluids. 2005;39:1096-100.

[24.] Shoemake K. Animating rotation with quaternion curves. SIGGRAPH Comput Graph. 1985;19(3):245–54.

[25.] Cinar AF. Image-Based Fracture Mechanics with Digital Image Correlation and Digital Volume Correlation: University of Sheffield; 2019.

[26.] Lopez-Crespo P, Shterenlikht A, Patterson EA, Yates JR, Withers PJ. The stress intensity of mixed mode cracks determined by digital image correlation. The Journal of Strain Analysis for Engineering Design. 2008;43(8):769-80.

[27.] Zhang Y. The effect of inkjet printed polymer on the mechanical properties of carbon fibre reinforced plastic: University of Sheffield; 2015.

[28.] Meng M, Le HR, Rizvi MJ, Grove SM. 3D FEA modelling of laminated composites in bending and their failure mechanisms. Composite Structures. 2015;119:693-708.

[29.] Barhli SM, Saucedo-Mora L, Jordan MSL, Cinar AF, Reinhard C, Mostafavi M, Marrow TJ. Synchrotron X-ray characterization of crack strain fields in polygranular graphite. Carbon. 2017;124:357-71.

[30.] Jin X, Wade-Zhu J, Chen Y, Mummery PM, Fan X, Marrow TJ. Assessment of the fracture toughness of neutron-irradiated nuclear graphite by 3D analysis of the crack displacement field. Carbon. 2021;171:882-93.

[31.] F. Maronea MS. Regridding reconstruction algorithm for real-time tomographic imaging. Journal of Synchrotron Radiation. 2012.

[32.] Dowd BA, Campbell GH, Marr RB, Nagarkar VV, Tipnis SV, Axe L, Siddons DP, editors. Developments in synchrotron x-ray computed microtomography at the National Synchrotron Light Source. Developments in X-ray Tomography II; 1999: SPIE.

[33.] Strotton MC, Bodey AJ, Wanelik K, Darrow MC, Medina E, Hobbs C, et al. Optimising complementary soft tissue synchrotron X-ray microtomography for reversibly-stained central nervous system samples. Scientific Reports. 2018;8(1):12017.

Chapter 5

5. Ex-situ characterization and analysis

Following the in-situ characterizations described in Chapter 4, which enabled the 3D observation of crack propagation as well as quantification of fracture toughness, this chapter delves into ex-situ analyses to further explore the impact of inkjet printing. To this end, the fracture surfaces were examined using focus variation microscopy to precisely measure the surface roughness; scanning electron microscopy was applied for fractography and cross-section scanning to identify features not resolved or detected by XCT; X-ray photoelectron spectroscopy was utilized to investigate the fracture surface chemistry associated with the printing droplets; and an attempt was made to resolve the printing dots, with ink containing fluorescein, under fluorescence microscopy.

5.1 Focus variation microscopy

The study of fracture surface roughness plays a pivotal role in investigation of materials toughness, as a rougher crack plane signifies an increase in surface area generated with crack propagation. This enlargement of surface area leads to greater energy dissipation, thereby contributing to enhancement of fracture toughness in brittle materials. Surface roughness measurements derived from in-situ observations with tomographic data, as discussed in the previous chapter, are representative as they derive from the instantaneous fracture surface. Using focus variation (optical) microscopy, a measurement precision on the fracture surface could be achieved with ~3 μm spatial resolution and a height resolution of 300 nm [1].

5.1.1 Working principle and experimental details

Following the fracture toughness assessment using DCB test in chapter 2, the fracture surfaces of specimens were examined for surface roughness, using a focus variation microscope (Alicona InfiniteFocus).

The working principle of Alicona is illustrated in Figure 5.1: A light beam is projected on a small targeted area of surface, and the light that reflects back is captured by a photoelectric detector within the optical system. The microscope continuously captures the images at different heights along the z axis, with each capture process identifying the focus and recording the height axis. These data points were then amalgamated to reconstruct 3D images of surface morphology. By stitching together multiple scans, large FOV with high resolution could be achieved.

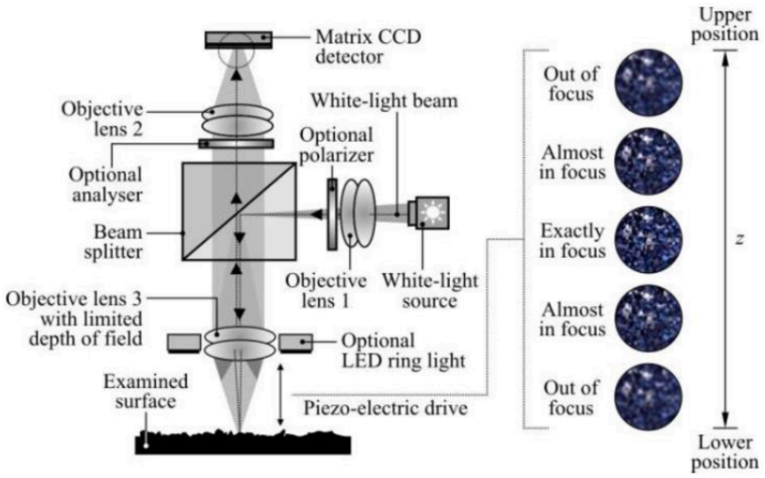

Figure 5.1. Working principle of focus variation microscope [2]

In the experiment, the 10x objective was selected, providing vertical and lateral resolutions of 300 nm and 3.38 μm respectively. This offers sufficient resolution for analysis of CFRP, considering the diameter of carbon fibre is ~7 μm. The scanning images were stitched to generate a larger FOV, as shown in Figure 5.2.

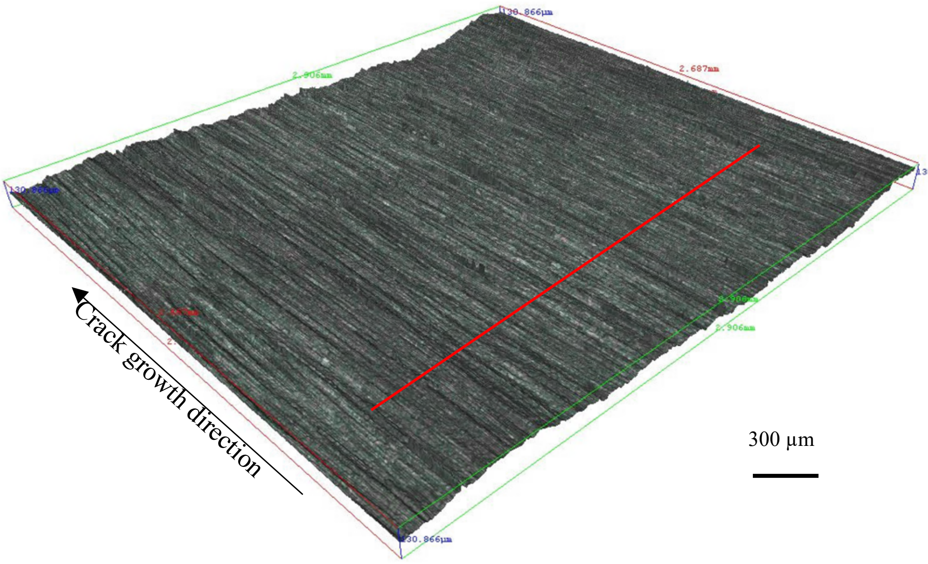

Figure 5.2. Stitched 3D surface image of fracture plane in PEG specimen ~ 5mm away from the printing boundary, with the red line showing the profile filtered into *Ra* and *Wa* factors, whose length is the profile length

The measured surface was then subjected to the Alicona built-in filters. Specifically, the roughness filter eliminates low frequency components from profile and acts as a high-pass filter, while the waviness filter eliminates high frequency components and acts like a low-pass filter [1]. Typical roughness (*Ra*) and waviness (*Wa*) profile obtained by applying the corresponding filters are present in Figure 5.3.

As shown in Figure 5.2, vertical lines normal to fibres are taken to evaluate the *Ra* and *Wa* values. Following ISO 4287, Alicona defines *Ra* as the arithmetic mean of the surface textures, which inverts the valley of roughness profile to get the positive value and calculated by degerming the average deviation of peaks and valleys as $Ra = \frac{1}{l}\int_0^l |Z(x)|dx$, where l is the sampling length and Z is the ordinate value [3]. The average deviation of all points from the waviness plane gives the waviness value. As shown in Figure 5.4, roughness describes fine-scale irregularities that occur over short wavelengths, while waviness refers to the surface unevenness at longer wavelengths. [1]

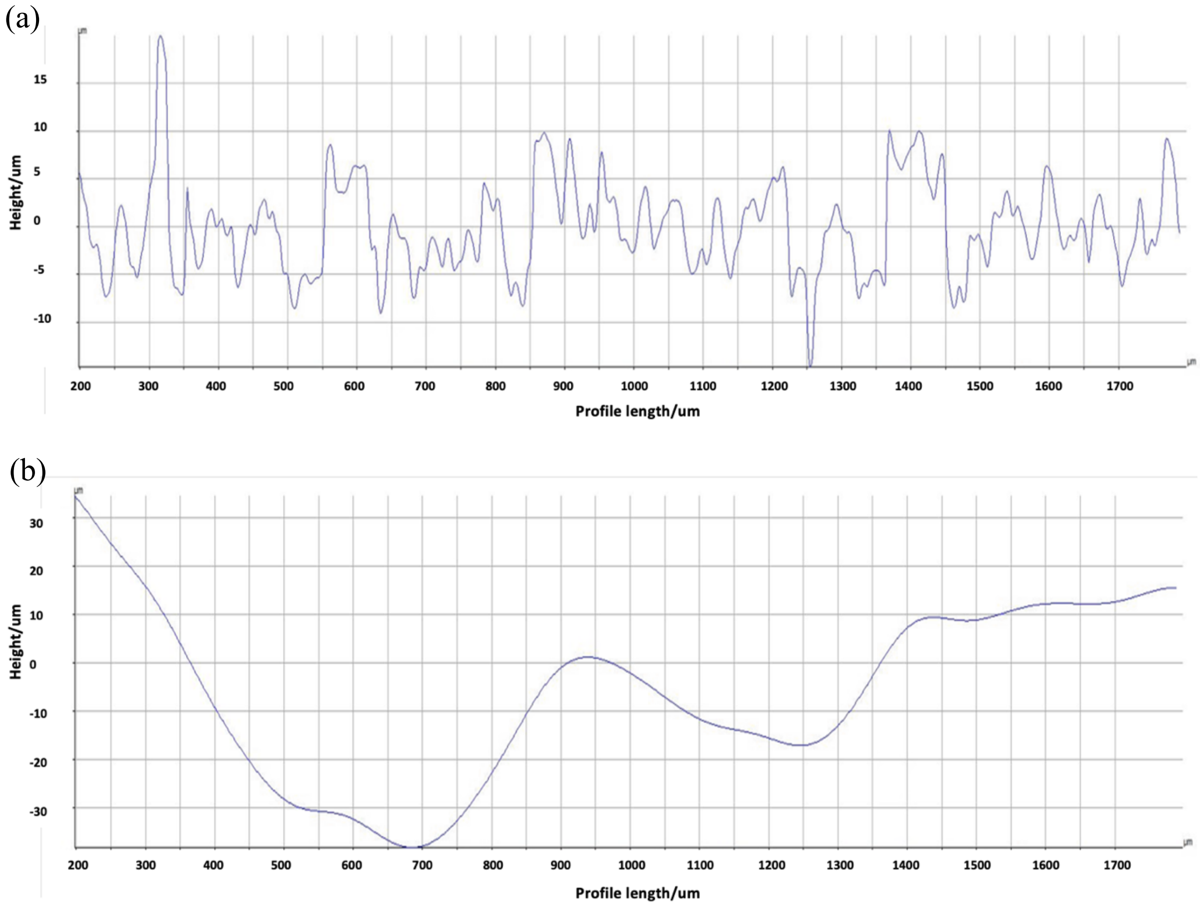

Figure 5.3. Typical example results of **(a)** roughness profile and **(b)** waviness profile obtained after applying the corresponding filters

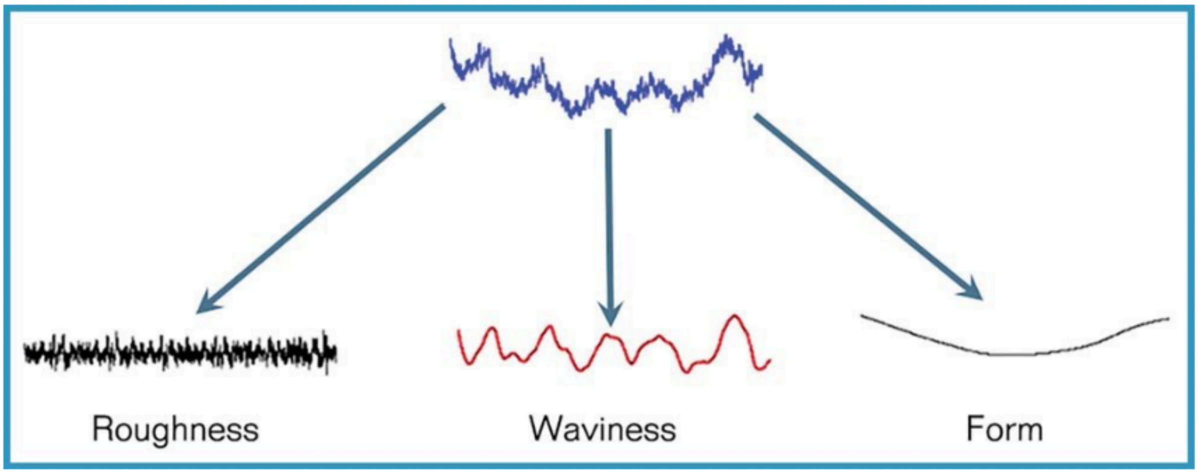

Figure 5.4. Surface unevenness in roughness and waviness [4]

5.1.2 Results and discussion

Height maps of example specimens are displayed in Figure 5.5, showing the topology of fracture surface. Changes of height were more obvious in the direction perpendicular to the fibres (~ ± 20 μm) compared to parallel to the fibres (< 5 μm). The highly directional roughness results from the ease with which cracks propagate through the matrix between fibres, whereas along the fibre direction, crack propagation is more constrained. The roughness and waviness factor measurement are therefore measured along lines perpendicular to the fibres. From characterization in XCT, the thickness of epoxy film where two prepregs are bonded is ~ 10 μm. The observed height variations exceed the 7 μm fibre diameter plus the thickness of resin rich region where the two prepregs be bonded, indicating crack propagated around fibres. No localized patterns of height variation correlating to the printing pattern were identified at this resolution, and qualitatively the differences between the height maps of the specimens were not significant.

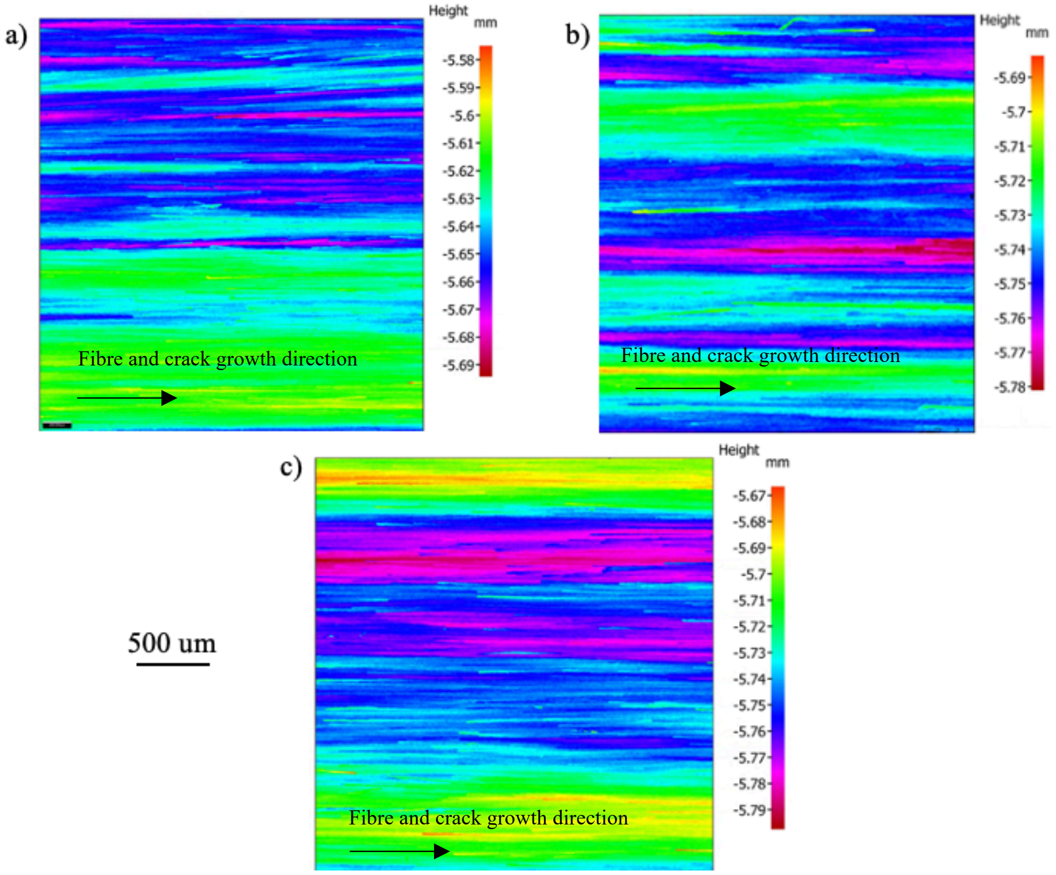

Figure 5.5. Height map of **(a)** NP_2, **(b)** PMMA_Line_15000 and **(c)** PEG_Line_400 specimens

To compare the roughness (*Ra*) and waviness (*Wa*) factors, 31 line-profiles with distance between each other at 50 perpendicular to fibres in the middle of the stitched image (Figure 5.2) were analysed, covering a region of 1500 μm width and the arithmetic averages were taken as the corresponding values. The results are summarized in Table 5.1: The specimens measured in this project are identified with the name codes described in chapter 2. A kernel density estimation (KDE) and cumulative distribution function (CDF) was conducted to analyse the data distribution. As shown in Figure 5.6, the distribution plot indicating a good match with the averaged value, and a significant increase of *Wa* was observed in the printed specimens.

Student's t-test, which is a statistical test to examine whether the difference between two data group is statistically significant (p value smaller than the significant level) or not, was conducted. The result is shown in Table 5.2 and Table 5.3, which demonstrated the printed specimens showed significantly higher waviness than NP_2 specimen, while the non-printed specimen have greater roughness factor than printed laminates.

For comparative analysis, data from a previous research work are included in the table, obtained using the same instrument and characterization settings, and the prepregs were printed with PMMA M_w~15000 in HP (hexagon pattern) PP (parallelogram pattern) and SP (square pattern) respectively [5]. As discussed in Chapter 2, the specimens from the previous study were made from fresh prepregs whereas the specimens used in this work has been stored for some time. In the specimens manufactured with fresh prepreg, both roughness and waviness were significantly higher in the printed specimens compared to the non-printed laminates, with the difference in the waviness highly significant. To sum up, both measurements demonstrate that printing leads to a more significant variation of sample large scale unevenness (*Wa*), while the impact on finer-scale roughness factor is less pronounced.

Table 5.1. Summary of roughness and waviness factor (n=31)

	Roughness (*Ra*) / µm	**Waviness (*Wa*) / µm**
NP_ 2	5.1 ± 0.3	6.9 ± 0.8
PMMA_Line_15000	4.0 ± 0.2	9.9 ± 0.5
PEG_Line_400	4.1 ± 0.2	15.8 ± 0.5
From previous [5]		
Nonprinted	3.6 ± 0.2	9.1 ± 1.0
PMMA (HP)	4.1 ± 0.3	16.6 ± 1.3
PMMA (PP)	4.8 ± 0.7	16.7 ± 2.9
PMMA (SP)	4.5 ± 0.4	15.9 ± 1.2

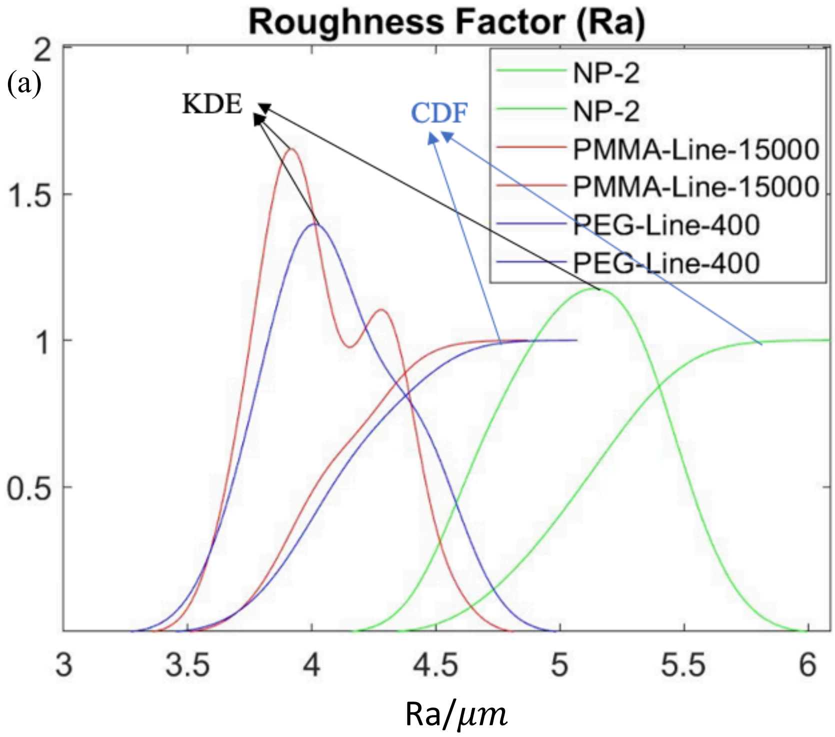

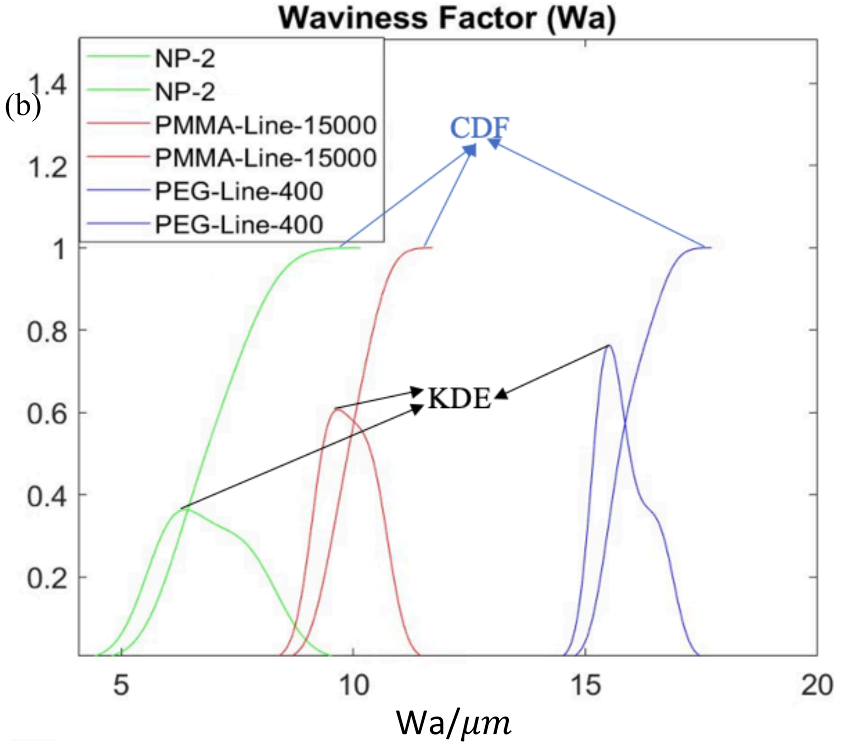

Figure 5.6. Kernel density estimation (KDE) and Cumulative distribution function (CDF) plot of **(a)** Ra and **(b)** Wa among the 31 profile measurements in each specimen (n=31)

Table 5.2. T-test for roughness factor, significant level at p = 0.05

Samples compared		P value	Result
NP_ 2	PMMA_Line_15000	0.00	Different
NP_ 2	PEG_Line_400	0.00	Different
PMMA_Line_15000	PEG_Line_400	0.57	Not Different

Table 5.3. T-test for waviness factor, significant level at p = 0.05

Samples compared		P value	Result
NP_ 2	PMMA_Line_15000	0.00	Different
NP_ 2	PEG_Line_400	0.00	Different
PMMA_Line_15000	PEG_Line_400	0.00	Different

As shown in Figure 5.7, the printed specimens consistently show a significantly higher *Wa*, while the trend in roughness is less clear. Figure 5.8 (a) illustrates the variation in Wa correlates with the fracture toughness (measured from DCB test in Chapter 3), confirming a higher global fracture surface unevenness (*Wa*) corresponds to greater work of fracture (G_{IC}). While the relationship between roughness factor (Ra) and fracture toughness is random.

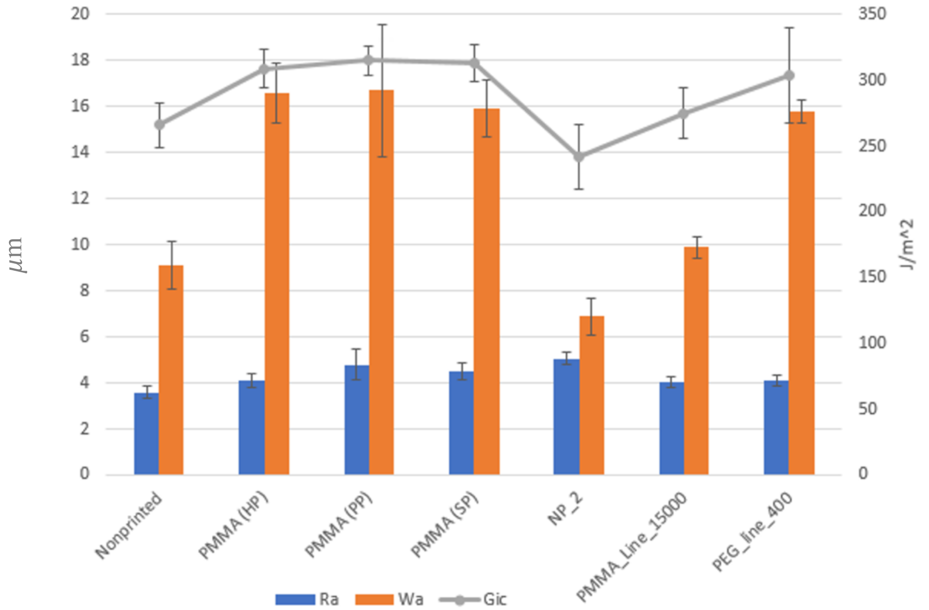

Figure 5.7. Summary of roughness and waviness factor together with fracture toughness for trend observation

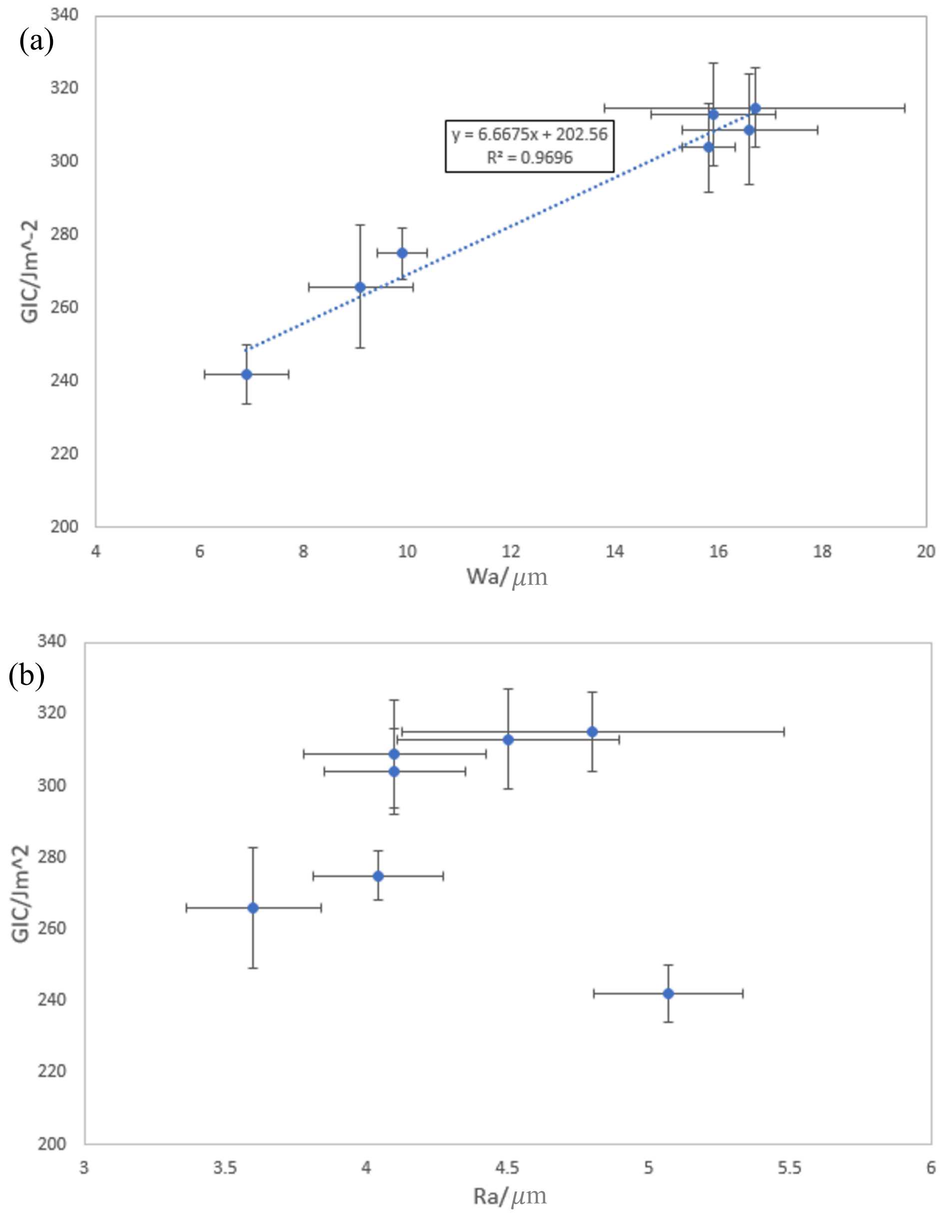

Figure 5.8. Relationship between **(a)** Wa and G_{IC} and **(b)** Ra and G_{IC}; a linear correlation was fit between Wa and G_{IC}. The data was collected from the seven samples shown in Table 5.1

5.2 Scanning electron microscopy

The fracture surfaces of CFRP specimens were examined using a Zeiss Merlin Scanning electron microscope (SEM) for surface morphology observations. Secondary electron imaging (5 keV) was used, which provides superior topographical images. After sample preparation, by cutting with low-speed diamond saw, deionised water was used as the cleaning agent. Acetone and ethanol were avoided as these organic solvents can dissolve the polymer components such as the epoxy matrix. Prior to characterization, a 4 nm-thick Platinum film was coated on each test sample to ensure sufficient electrical conductivity and eliminate the charge effect.

5.2.1 Fractography

The fractography of both virgin and PEG printed specimens are presented in Figure 5.9 & 10. Feather-like patterns, indicative of crack forking caused by the excess of energy associated with relatively fast growth of crack, were apparent on the fracture surface [6].

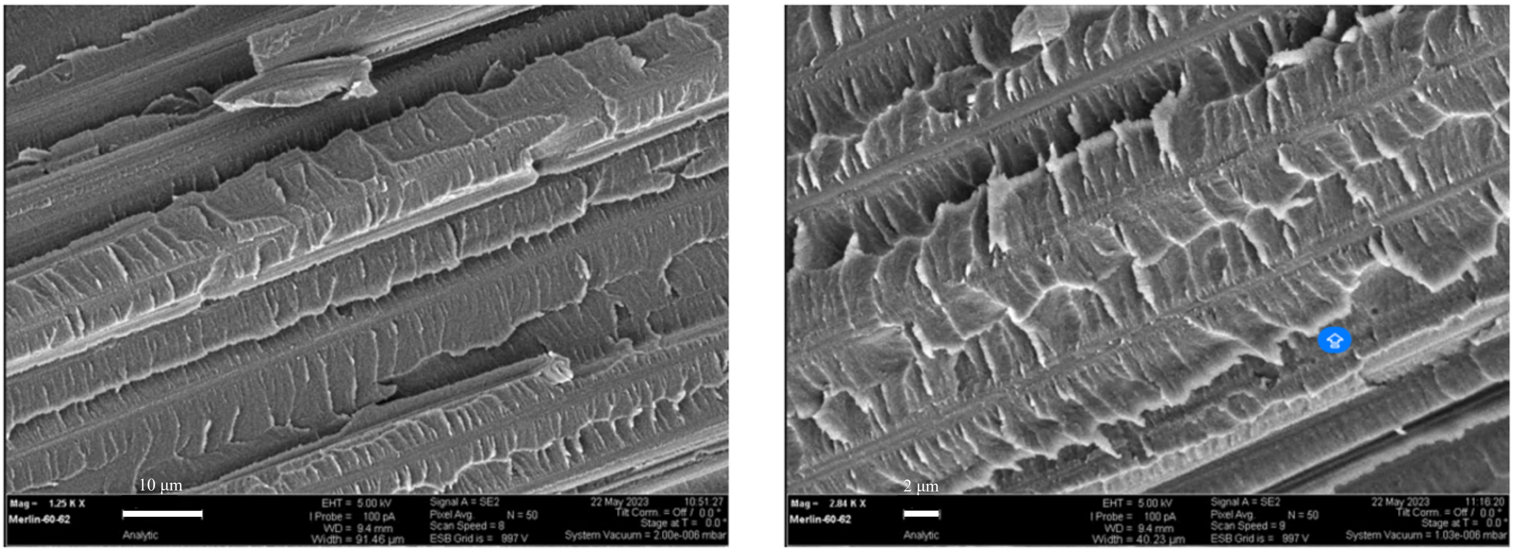

Figure 5.9. SEM fractography scan of virgin specimen

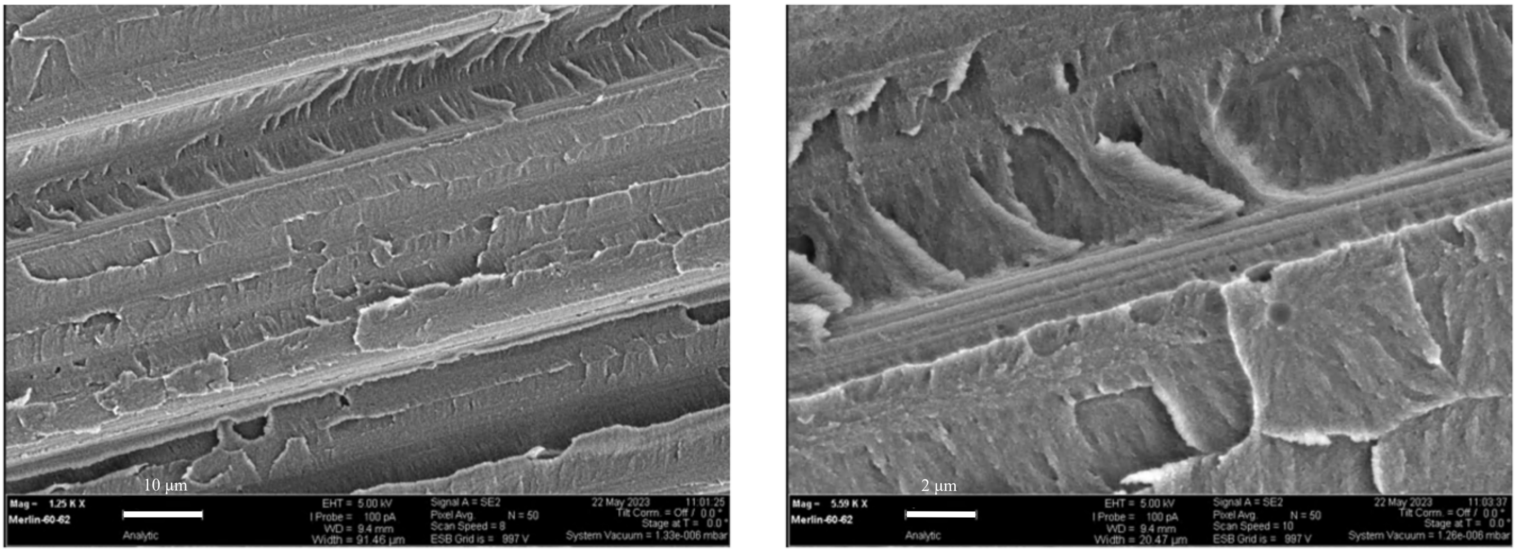

Figure 5.10. SEM fractography scan of PEG_Line_400 laminate

Fractography results are displayed in Figure 5.11 for the PMMA_Line_15000 specimens. Here, some isolated circles with ~7 µm diameter were observed that were not seen in either the non-printed or PEG-printed specimens. Given that the fibre diameter is 7 µm, this raises the possibility that these features might be the cross section of fractured fibres. In XCT observation however, no misoriented broken fibres were observed. Besides, similar feature was reported by Yi, where circles with diameter of ~10 µm appeared only on the fracture surface of PMMA-printed laminate (Figure 2.17, Chapter 2) [7]. According to Yi's optical microscope observation, as shown in Figure 5.12 and 13, the PMMA would separate into various size of particles in the matrix post curing [8], which explaining the random observation of particles in SEM images of PMMA_Line_15000.

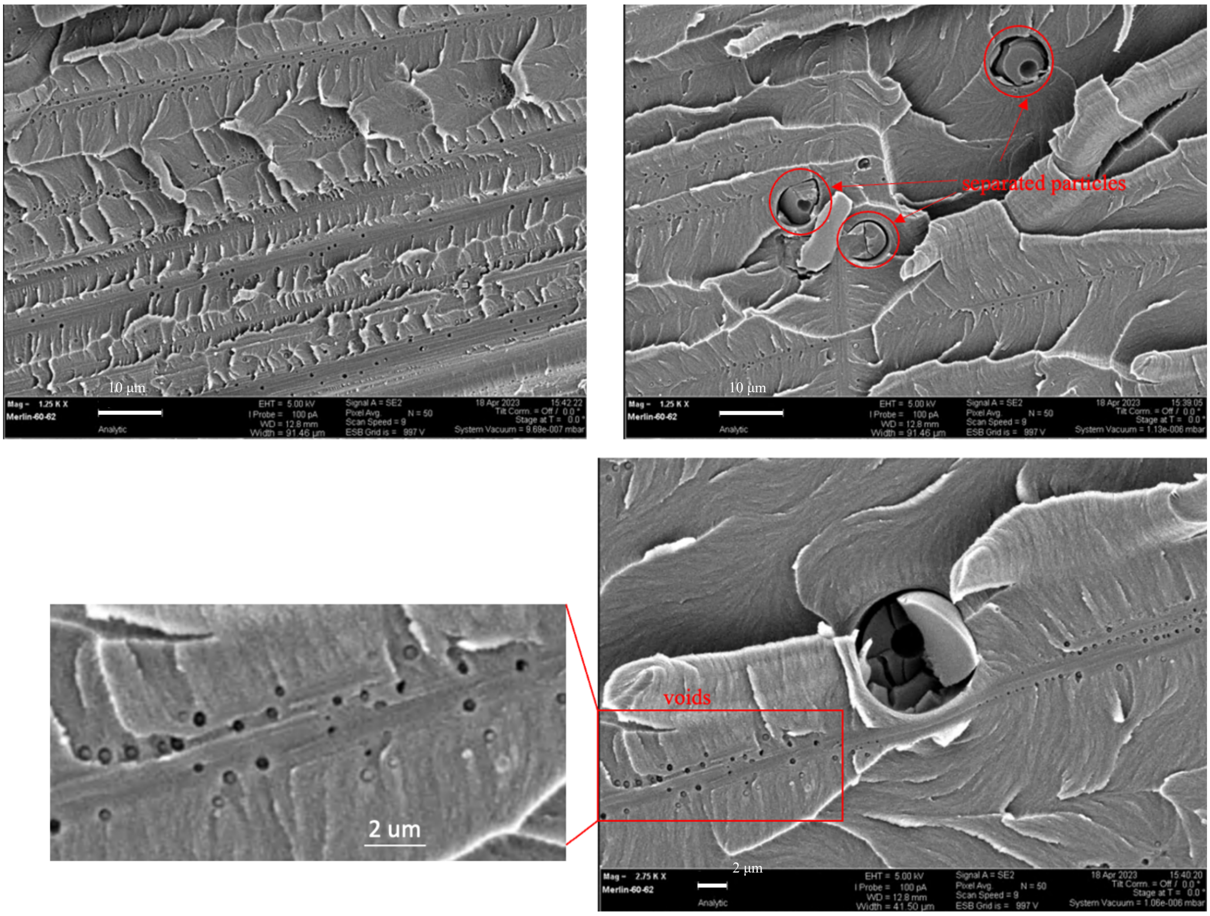

Figure 5.11. Fractographies of PMMA_Line_15000 laminate showing discrete particles and voids

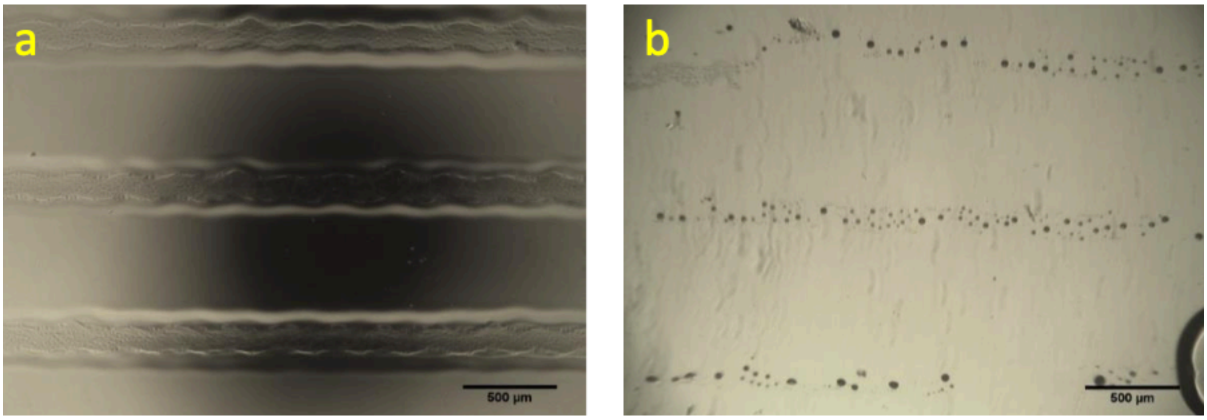

Figure 5.12. Optical image of epoxy coated glass with PMMA printing in line pattern before **(a)** and after **(b)** heating [8]

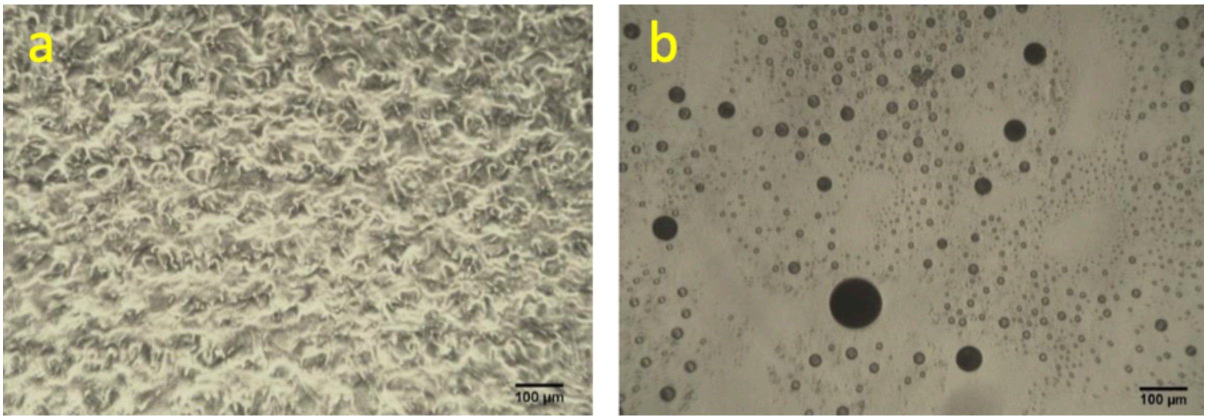

Figure 5.13. Optical image of epoxy coated glass with printing of PMMA thin film before **(a)** and after **(b)** heating [8]

Therefore, it's been inferred that it is more likely that those features are the cross-section of fractured or decohered particles and the differences of particles size between observation from Yi and this work originated from the change of ink concentration. It has been reported that PMMA is not miscible with the hardened epoxy and would form spherical particles post curing [9], giving more confidence that the observed particles originate from the PMMA printing dots. These separated particles were not observed from in-situ tomographic observation in Chapter 4, but as the PMMA and epoxy resin share similar density and chemical composition, attenuation contrast cannot distinguish the two phases. The inability to observe particles of the intact region under phase contrast image in the TOMCAT XCT is due to similar refractive index between PMMA and epoxy in X ray [10, 11].

The observed thermoplastic particles could contribute intrinsically to toughening with the following mechanisms:

(1) The particles might interact with the cracks to absorb energy. As shown in Figure 5.14, the particles could change the cracking direction by crack pinning. Crack deflection is less likely to appear, as the particle size is a lot smaller than crack opening displacement. The particles might also bridge the cracks and deform, and these could be demonstrated as fractured and deformed particles were observed in the scan images [12]. PMMA is a

thermoplastic, with a glass-transition temperature of 105°C, and wouldn't be affected by the hardened epoxy since they are immiscible [8, 13]. The experiments were performed at ~20°C, so significant plastic behaviour of PMMA is not expected, which discounts this mechanism.

(2) As the particles tends to debond from the matrix, extra energy is required that enhance the fracture toughness. Such debonding is observed, but the quantity of particles on the fracture surface is not high, which suggests they might not be the main mechanism contributes to the fracture toughness.

In the PMMA printed specimens, it is noteworthy that there was a large amount of micropores dispersed within the fractured plane that associated with the interface between the fibre and matrix. These voids, with ~ 0.2 μm diameter, could be observed in every scan. Taking a closer look at these pores, some voids have small particles inside them, which might be PMMA. Similar features (Figure 5.15) are widely reported in core-shell rubber (CSR) particle modified CFRP and this cavitation behaviour is generally accepted as a primary toughening mechanism of this category of materials [14-17]. In CSR toughened CFRP, under mechanical stress, cavitation occurs, forming small cavities in the epoxy matrix that absorb energy [16]. These cavitation are considered would blunt the crack tip, leading to extensive plastic zone development in the adjacent of crack front that enhance the toughness [18]. The formation of voids also promotes shear yielding in the matrix that increase the fracture energy [19]. This inspires thoughts on the role of micropores and a toughening hypothesis is proposed: Due to the immiscibility between PMMA and toughened epoxy, the PMMA droplets remained separated with matrix post-curing. During crack propagation, voids nucleation initiated from the dots, which was followed by interfacial decohesion between the glassy PMMA and ductile epoxy. This process required energy to create the extra surface and enhance the work of fracture through inducing of plastic mechanism. Moreover, once after the voids formation, they may then affect the failure of interface between fibres and matrix, which will then affect the way that crack propagates. As the delamination expand, the micropores might bridge the crack front movement and aid the matrix ligaments formation, where the bridging tractions would further increase the work of fracture. [20] And as the size of pores is ~ 0.2 µm, micro-XCT cannot capture these features due to the lack of resolution. Several scans along the fibre direction are performed and a stitched image covering a ~ 600 µm-length region is shown in Given the distance between the printing lines is 250 µm, this stitched region is expected to encompass two to three printed lines. However, the particles and voids did not show any pattern that can be related to such printing line. The voids were observed to be distributed all along the fibre direction, while the separated particles are randomly embedded in the epoxy matrix.

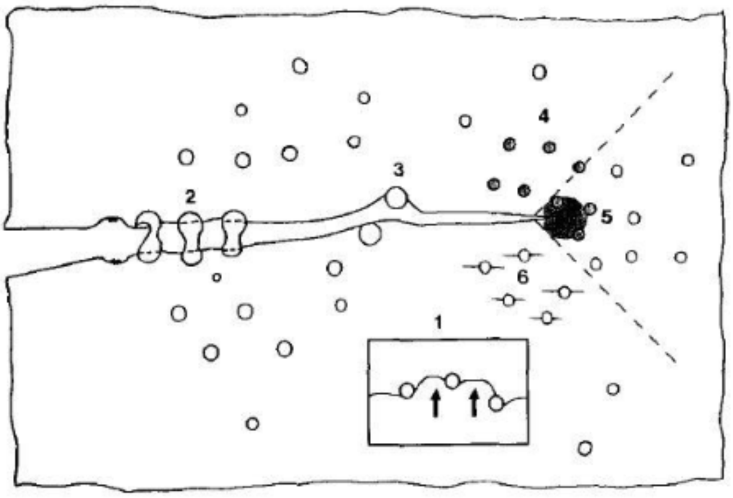

Figure 5.14. Toughening mechanisms proposed in thermoplastic modified epoxy [12]

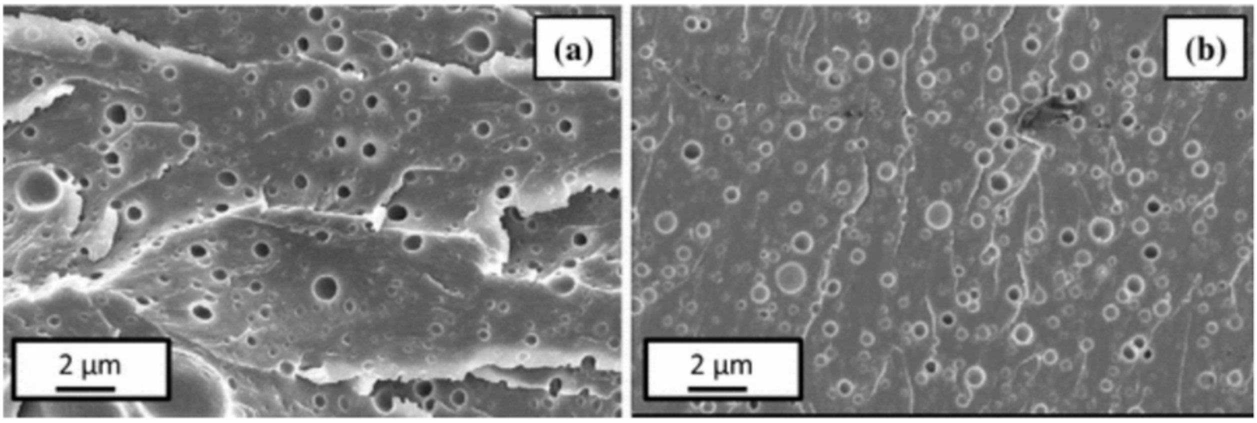

Figure 5.15. Presence of voids in CSRs toughened epoxy [17]

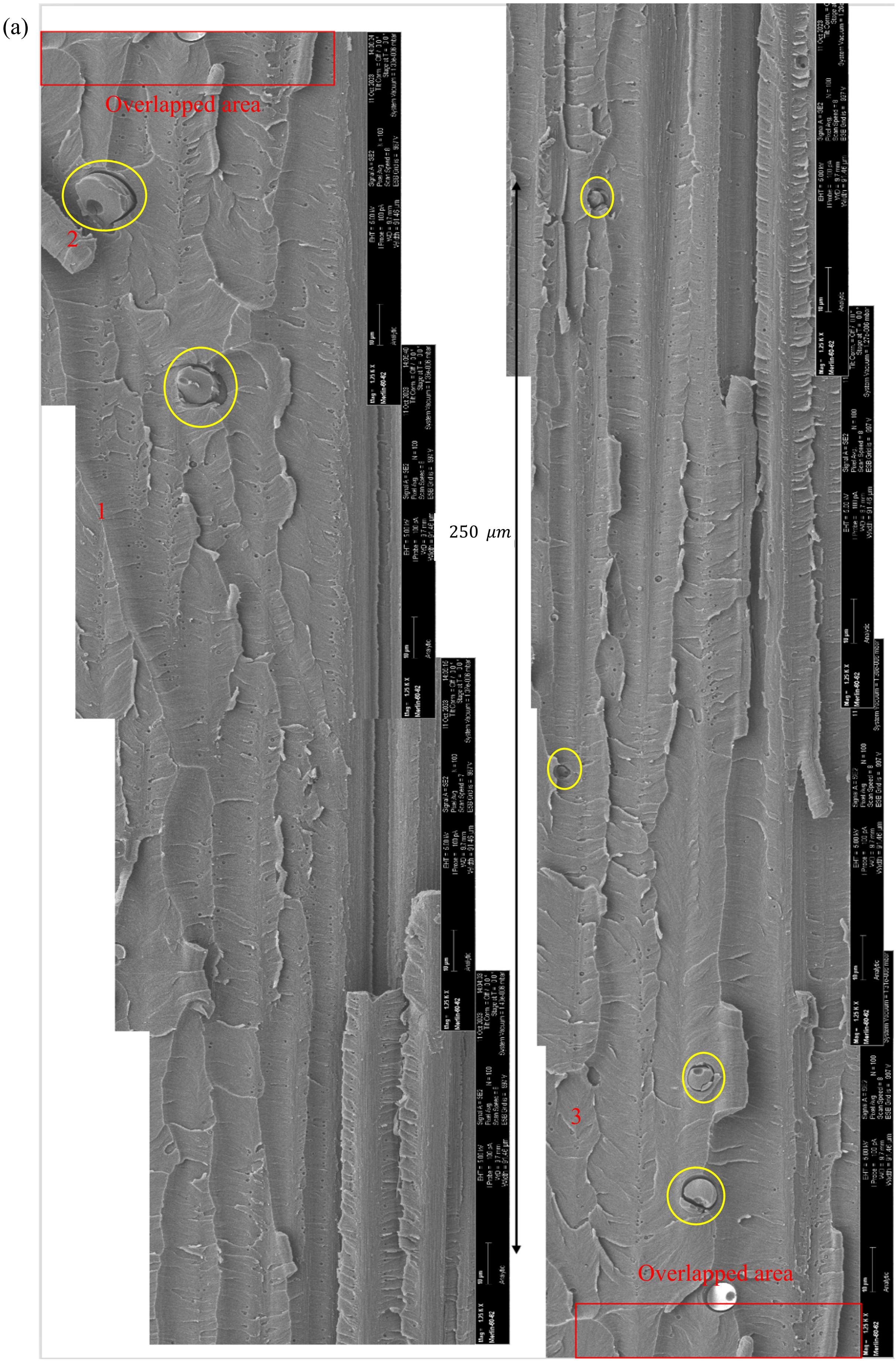
(a)
Overlapped area
2
1
250 μm
3
Overlapped area

(b)

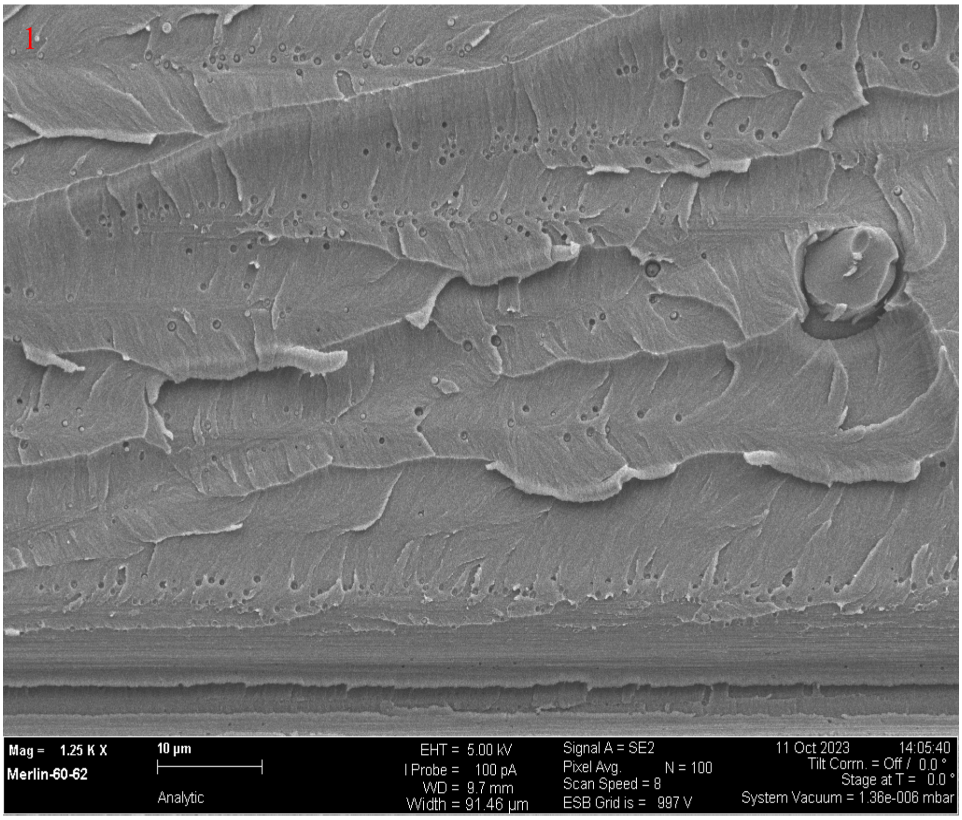
1
Mag = 1.25 K X
Merlin-60-62
10 µm
Analytic
EHT = 5.00 kV
I Probe = 100 pA
WD = 9.7 mm
Width = 91.46 µm
Signal A = SE2
Pixel Avg. N = 100
Scan Speed = 8
ESB Grid is = 997 V
11 Oct 2023 14:05:40
Tilt Corrn. = Off / 0.0 °
Stage at T = 0.0 °
System Vacuum = 1.36e-006 mbar

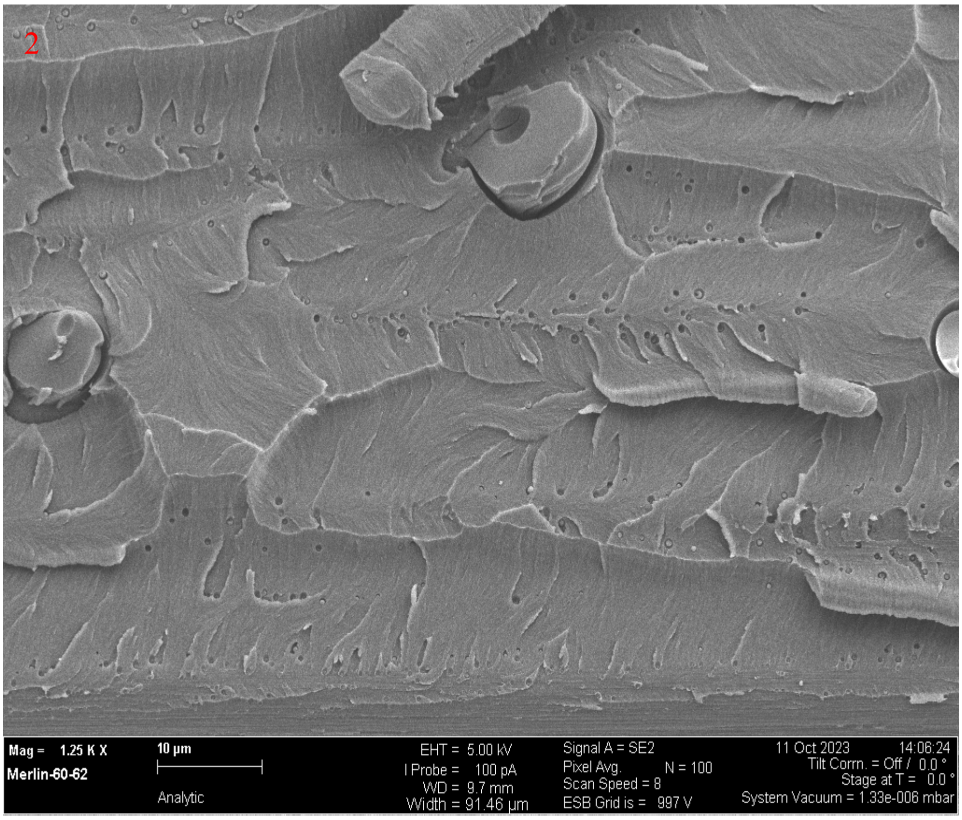
2
Mag = 1.25 K X
Merlin-60-62
10 µm
Analytic
EHT = 5.00 kV
I Probe = 100 pA
WD = 9.7 mm
Width = 91.46 µm
Signal A = SE2
Pixel Avg. N = 100
Scan Speed = 8
ESB Grid is = 997 V
11 Oct 2023 14:06:24
Tilt Corrn. = Off / 0.0 °
Stage at T = 0.0 °
System Vacuum = 1.33e-006 mbar

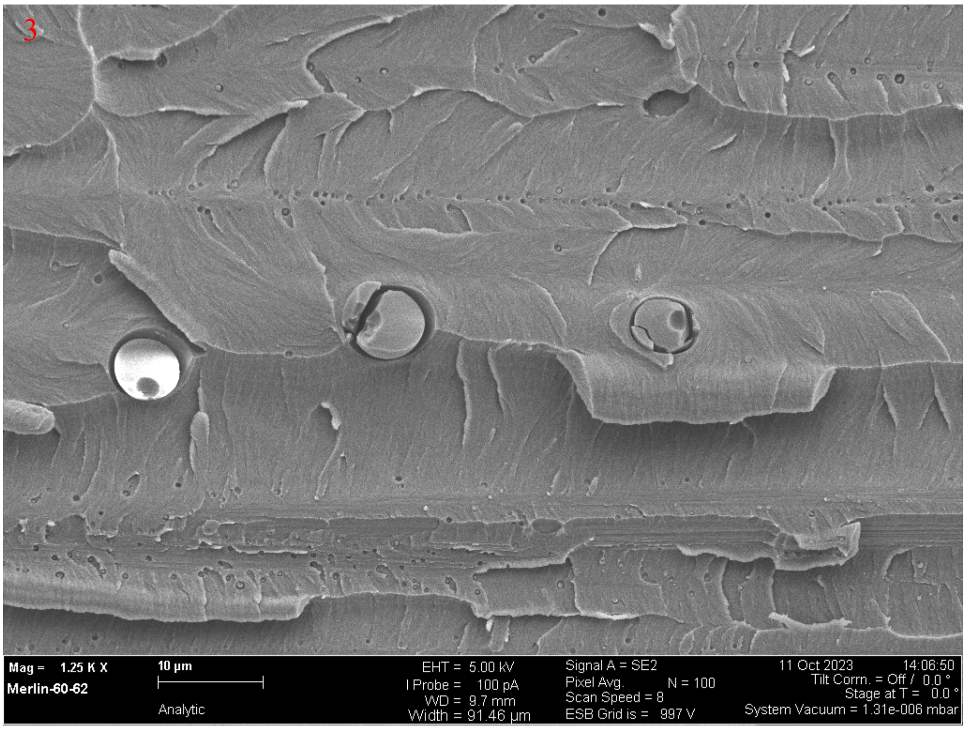

Figure 5.16. (a) Montage of SEM scans for PMMA_Line_15000 specimens along the fibre direction, with the red rectangular represent the overlap area between the two stitched images, yellow circles highlight examples of the separated particles and the full images of the corresponding 3 areas providing more details

5.2.2 Cross-sectional observation

To investigate whether the void and particle features only exist at the fracture surface of the laminates or throughout the component, cross-sectional SEM was conducted on the edges of specimen parallel and perpendicular to the fibre direction. The undamaged laminates were first cut by low-speed diamond saw. As the glass transition temperature of epoxy is relatively low and high temperature could damage the microstructure of the sample surface, a hot mounting method such as using Bakelite is not suitable for CFRP. Here, the specimens were embedded in cold mounting resin [21], curing at room temperature for at least 8 hours before subsequent grinding and polishing (Figure 5.17). The mounted laminates were firstly ground using silicon carbide paper with grit size 320, 600,1200 and 2500 µm and cleaned with deionised water. Polishing was then conducted using a rotating polisher at a speed of 150 rpm and 5 N pressure, starting with a 3-micron diamond suspension for 10 minutes followed by a 1-micron suspension for another 15 minutes. This step is crucial to remove the deformations and scratches from grinding. After fine polishing, the samples were washed with deionized water, dried to ensure a clean surface. A Polyvar Reichert-Jung optical microscope was used to inspect the sample surface during preparation. Optical images of final polished specimen surface are shown in Figure 5.18. The mounted samples were placed in a vacum desiccator for 48 hours to get rid of the outgassing issue before loading in the SEM.

The cross-sectional SEM scans were conducted on PMMA_Line_15000 specimens using Zeiss Merlin at the same scanning condition of fractography, perpendicular and parallel to fibre direction on the edge are presented in Figure 5.19. Stitching of scans in the plane perpendicular to fibre direction was done to increase the field of view at high resolution. As illustrated in Figure 5.19, there was some damage to the carbon fibre during sample preparation. In both high-resolution optical microscope and SEM images, neither the voids nor particle dots were observed across the sample thickness. This could be due to several possible reasons: (1) grinding and polishing might have eliminated the pores and particles; (2) similar to cavitation toughening in rubber modified CFRP, the voids form due to strain, making it impossible to detect them in the intact laminates; (3) the resolution might not be sufficient enough to pick up the micro voids.

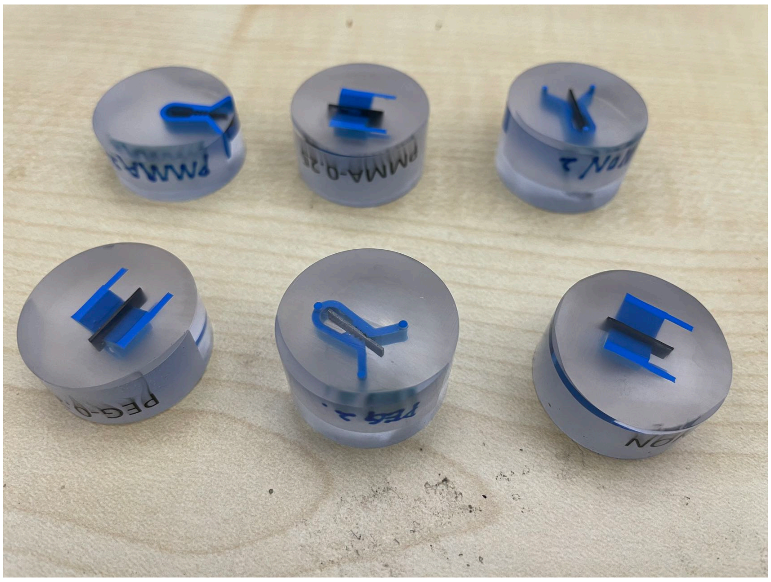

Figure 5.17. Final stubs for cross-sectional SEM

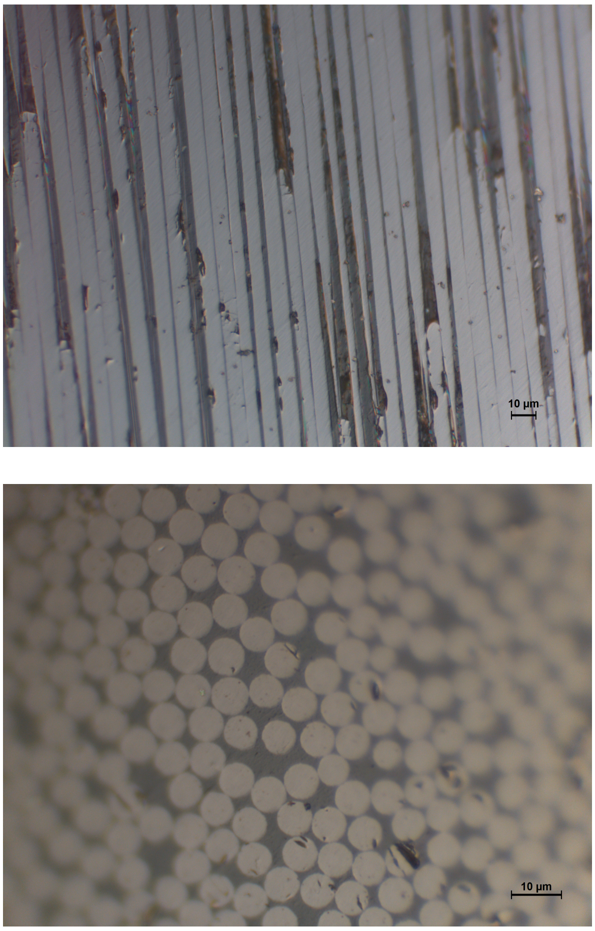

Figure 5.18. Final sample surface of PMMA_Line_15000 specimen under optical microscope

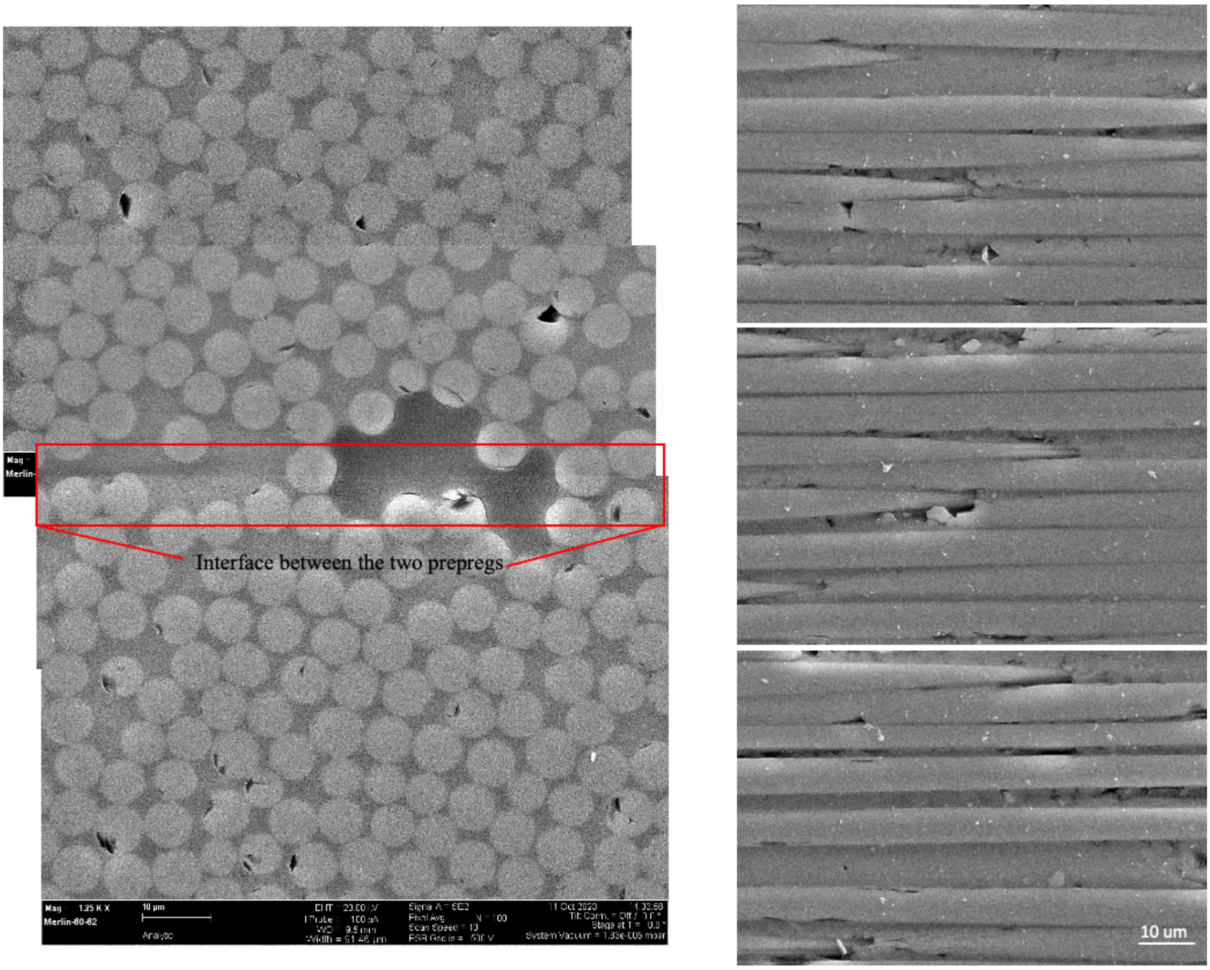

Figure 5.19. SEM scan of PMMA_Line_15000 specimens, with the red rectangular showing the layer where the two plies have joined that appears as resin rich region

5.3 X-ray photoelectron spectroscopy

In chemical adhesion theory, it is established that joint strength could be significantly improved with the higher activity chemical bonding [22]. Thus, it is crucial to investigate the effect of printing deposits on the chemical states of laminates. Moreover, detecting of printing droplets immigration post curing might be possible by mapping chemical status on the fracture plane.

X-ray photoelectron spectroscopy (XPS) is a widely employed spectroscopic technique for analysing chemical composition, state and electronic structure based on photoelectric effect. The schematic working principle of XPS is shown in Figure 5.20. When X-rays penetrate the sample surface, electrons in the inner shells absorb energy and are ejected to form photoelectrons. These ejected electrons are collected and analysed, where the energy of photoelectrons directs to the atomic number and chemical environment and the intensity represents the relative number. The energy of emitted electrons, measured as $\mathrm{E}_{\mathrm{kinetic}}$, and the incident beam energy, which is relative to the X-ray wavelength known from the equipment, allowing calculation of binding energy: $\mathrm{E}_{\mathrm{binding}} = \mathrm{E}_{\mathrm{photon}} - \mathrm{E}_{\mathrm{kinetic}}$, which gauges the chemical potential of the specimen [23]. In this work, K-Alpha X-ray Photoelectron Spectrometer System equipped with monochromatic Al X-ray source was used for the characterization [24].

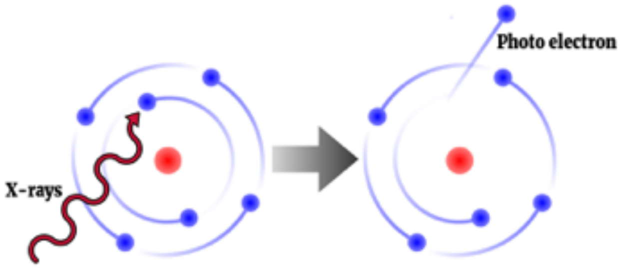

Figure 5.20. Working principle of XPS [25]

To study the effect of printing on the element and chemical bonds, XPS was conducted on the fracture surface of the 4 specimens: NP_1, PEG_Hex_20000, PMMA_Line_15000 and PEG_Line_400 (see Table 3.4, Chapter 3). It is worth noticing that NP_1 and PEG_Hex_20000 were made with fresh prepreg while the prepregs of the other two have been stored in low temperature for two years before printing and curing. As shown in Figure 5.21, a 400-µm size point, the largest available from K-Alpha XPS, was used for these scans, capturing the maximum representable area. The C1s and O1s peaks appear in every sample, indicating they all contain oxygen groups. The raw data underwent a baseline correction and fitting, a comparison of the deconvoluted bands of the C1s binding energy peak for all the specimens is presented in Figure 5.22. Four characteristic peaks can be observed among these specimens, with binding energy at 284.8, 286.0, 287.8 and 289.0 eV, corresponding to C-C, C-OH, C-COOH and C=O bonds respectively. The virgin sample predominantly showed C-C bonds, with significant C-OH and minor C=O presence. The PEG_Hex_20000 specimen had a reduced proportion of low-activity C-C bonds and a dominance of C-OH groups. These have higher chemical bonding activity which could enhance the joint strength between adhesive layers. Li has reported a similar phenomenon in CFRP. In that work a laser treatment was applied on laminate interface that bonded adjacent plies, this enhanced the adhesive strength and bonding force with greater surface roughness, which was accompanied by greater amount of active functional groups [26]. In the PMMA_Line_15000 and PEG_Line_400 specimens, the differences in functional groups were less pronounced; however, there was still a clear increase in the proportion of active groups (C-OH and C=O) in these printed specimens, indicating enhanced bonding activity. It has been reported that cured resin exposed for years would be oxidized and a slight increase of active groups were observed [27], the effect however is much less in uncured prepreg under low temperature, therefore, the change of functional groups and chemical environment should mainly result from printing of the thermoplastic deposits.

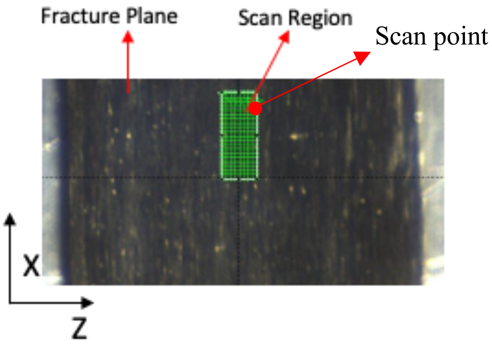

Figure 5.21. Schematic of XPS scan on the laminate fracture surface, with read circle represents the scan point and green rectangular shows the scan region

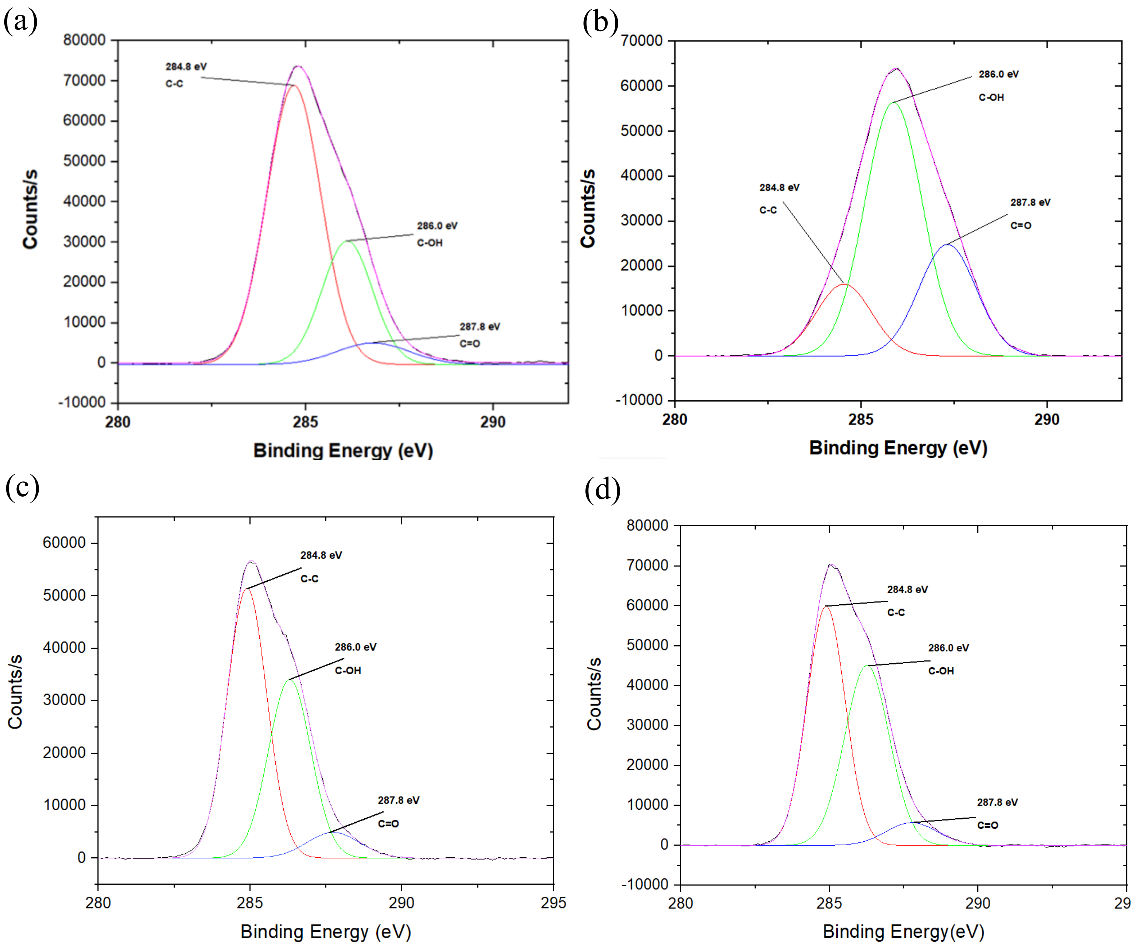

Figure 5.22. Deconvolution bands of C1s peak for **(a)** NP_1, **(b)** PEG_Hex_20000 **(c)** PMMA_Line_15000 and **(d)** PEG_Line_400 specimens

Region scans with a 50-µm spot size were then conducted at the same regions of the specimens to determine if there is a pattern of binding energy values that might be related to the printing pattern. For each scan, the spectrograms from every individual 50-µm spot were exported, and the binding energy (BE) value of the peak point was recorded as the BE of that specific spot. As peak fitting might induce some error, deconvolution is not applied here for mapping comparison. The resulting BE maps for all the tested specimens are displayed in Figure 5.23. The analysis of these maps revealed random variations in binding energy across the samples, indicating the absence of any consistent detectable pattern. The arithmetic mean of mapping points was calculated as the mapping BE of the respective specimen, and a comparison between 400 µm spot measurement and mapping BE among the four specimens are summarized in Table 5.4. The BE measured from averaging of 50 µm mapping are slightly higher than the 400 µm single spot scan. Overall, the two measurements are similar, where PEG_Line_20000 specimen shows the highest BE resulting from significant of C-OH and C=O groups (Figure 5.22) and NP_1 demonstrates the lowest BE value.

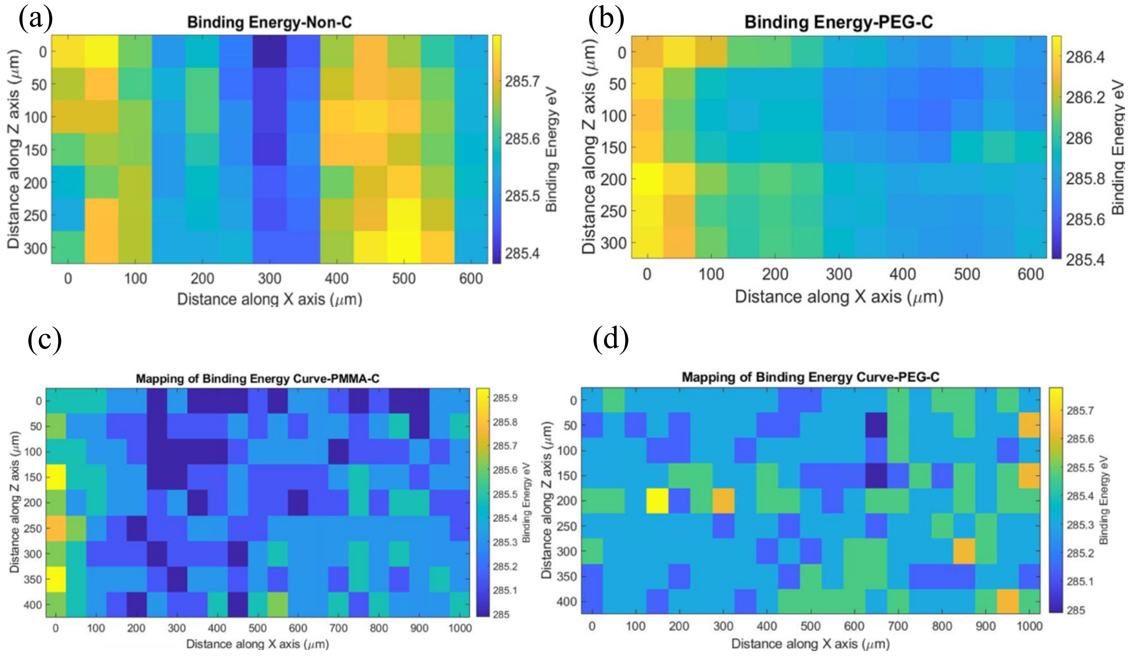

Figure 5.23. Binding energy map on the fracture plane of **(a)** NP_1, **(b)** PEG_Hex_20000 **(c)** PMMA_Line_15000 and **(d)** PEG_Line_400 specimens

Table 5.4. Comparison of C1s Binding Energy (unit: eV) measured from 400 µm large spot scan and 50 µm step size mapping among the four specimens

	NP_1	**PEG_Hex_20000**	**PMMA_Line_15000**	**PEG_Line_400**
400 µm spot	284.98	285.88	285.08	285.08
Mapping	285.60 ± 0.10	285.94 ± 0.21	285.25 ± 0.18	285.31 ± 0.12

The same measurements were performed on the edge of laminates, aiming to assess if the printing deposits could be located at the interface between the prepregs in the laminate. Samples were cut using a clean blade along the fibre direction to expose fresh surfaces of edge. The spot scans were processed on the edge of the intact region of laminates, while two mapping scans were conducted in each sample, one at the location containing the crack and another in an undamaged area. An optical microscope was used to capture images of the scanned surfaces, assisting in correlating edge morphology with binding energy. As shown in Figure 5.24, the deconvolution bands of C1s peak display similar results across all samples, predominantly showing low-activity C-C bonds. This similarity in the chemical environment at the edges of both printed and virgin samples suggests that the printing deposits likely did not penetrate beyond the printed plane post-curing. The similarity of spectrum might also be due to the lack of resolution, as the thickness of resin rich region in between two plies measured from tomography is ~10 μm, the XPS spot size is well above the interface thickness that the result contains large amount of signal from the bulk therefore might not be precise enough to represent the chemical status of printing layer.

A comparison of the C1s deconvolution measured from 400 μm spot scan on the fracture surface and edge of intact laminate is presented in Figure 5.25 and 24. In the PMMA_Line_15000 specimen, the ratios between the amount of C-C and C-O are similar, while a significant amount of C=O was only observed in fracture plane. Whereas in the PEG_Line_400 laminate, significant amount of both active groups appeared on the fracture surface. Additionally, the binding energy (BE) mapping graphs did not reveal any discernible patterns (Figure 5.27-27). It is deduced that the increased amount of oxidized carbon results from the oxidation of epoxy during fracture. This has been observed in other epoxy matrix composites such as glass fibre reinforced plastic (GFRP) [28].

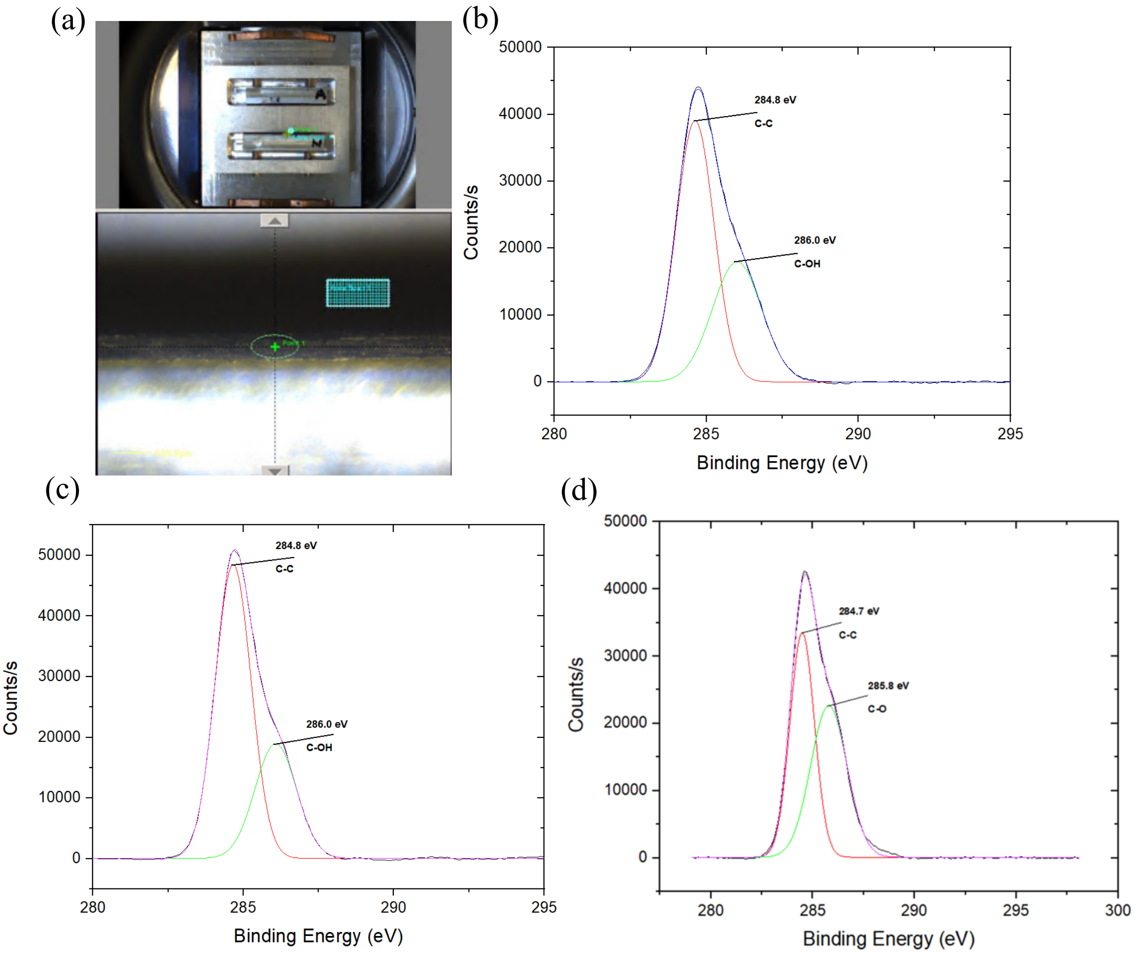

Figure 5.24. (a) measuring set up for edge scan with green cross showing the snap point position and the devolution bands of C1s result for **(b)** NP_2, **(c)** PEG_Line_400 and **(d)** PMMA_Line_15000 specimens

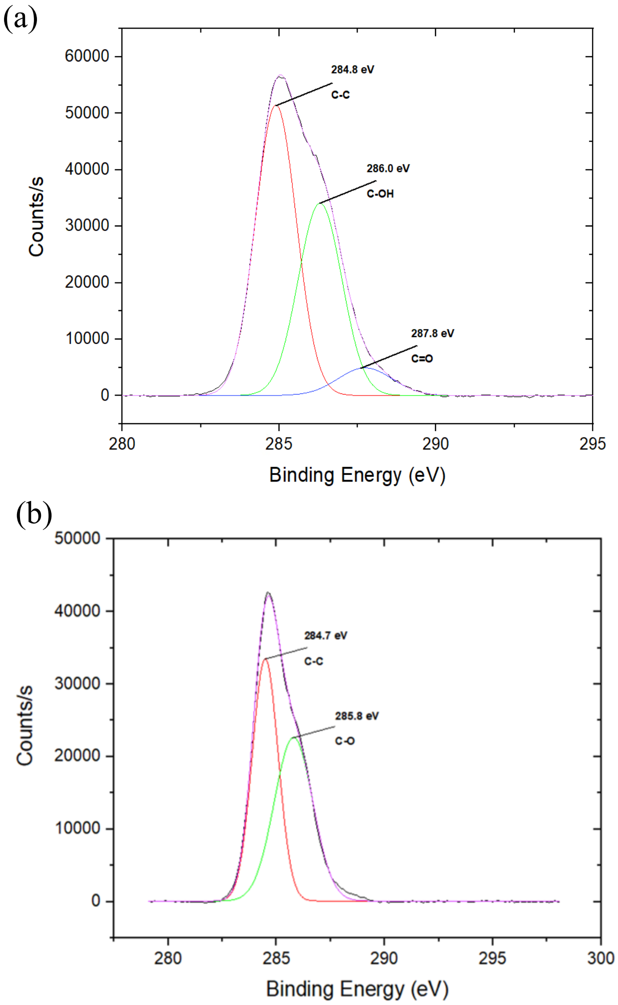

Figure 5.25. Direct comparison of C1s deconvolution in PMMA_Line_15000 laminate from **(a)** fracture plane and **(b)** sample edge

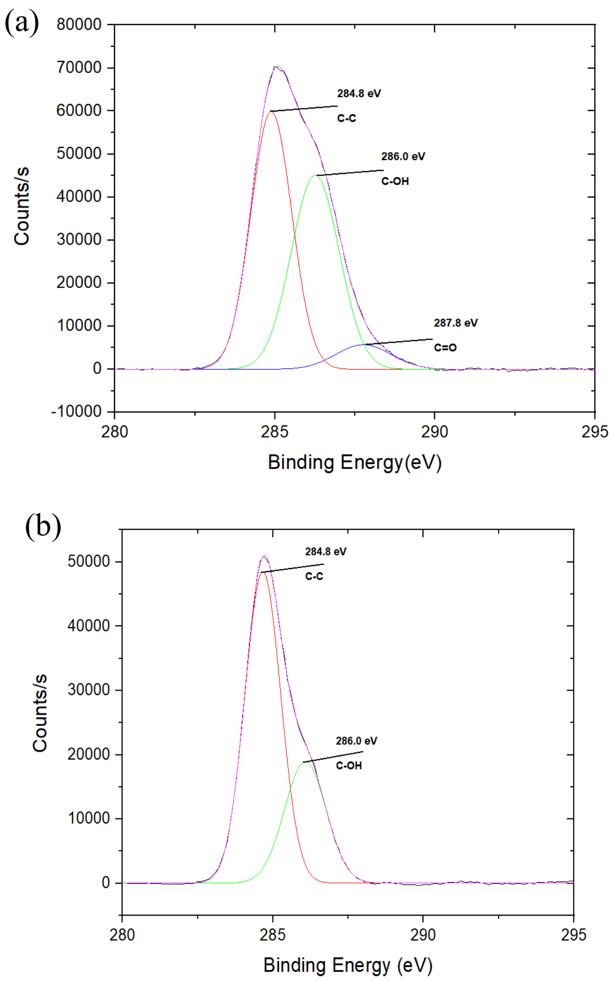

Figure 5.26. Direct comparison of C1s deconvolution in PEG_Line_400 laminate from **(a)** fracture plane and **(b)** sample edge

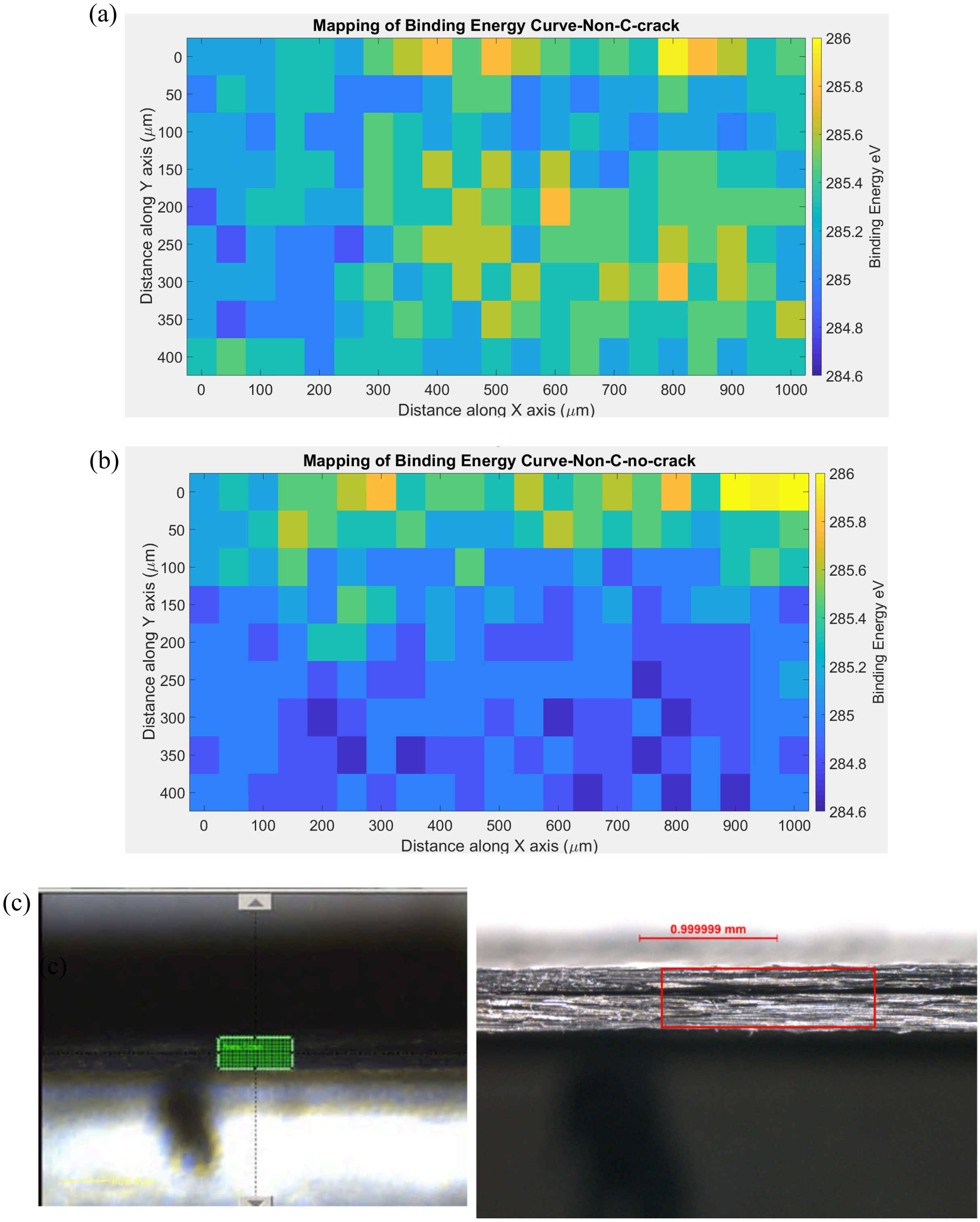

Figure 5.27. Binding energy map on the edge of NP_2 laminate in the region **(a)** containing crack and **(b)** ahead of crack with **(c)** optical microscope showing the morphology of measured surface in (a)

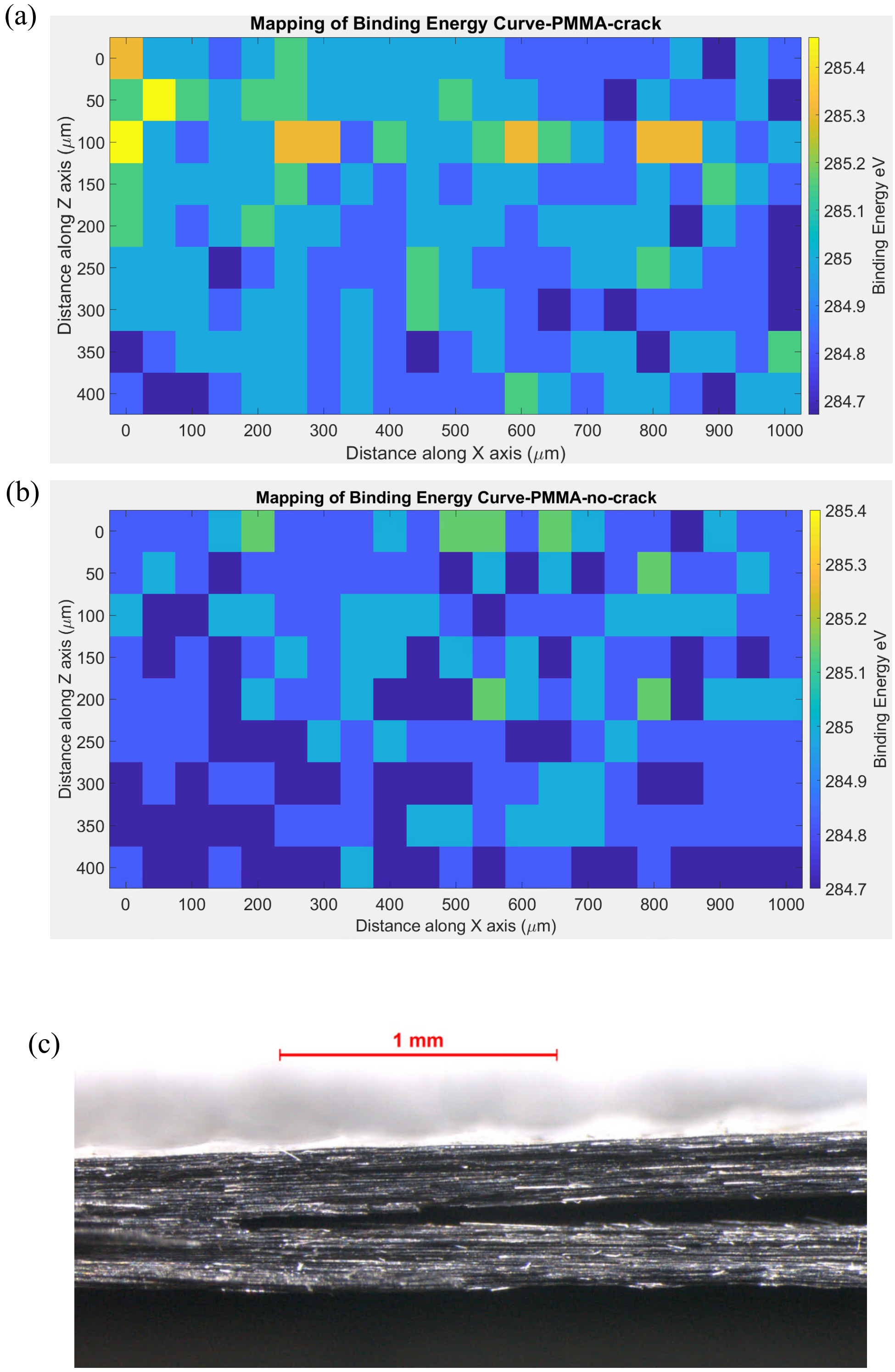

Figure 5.28. Binding energy map on the edge of PMMA_Line_15000 laminate in the region **(a)** containing crack and **(b)** ahead of crack with **(c)** optical microscope showing the morphology of measured surface in (a)

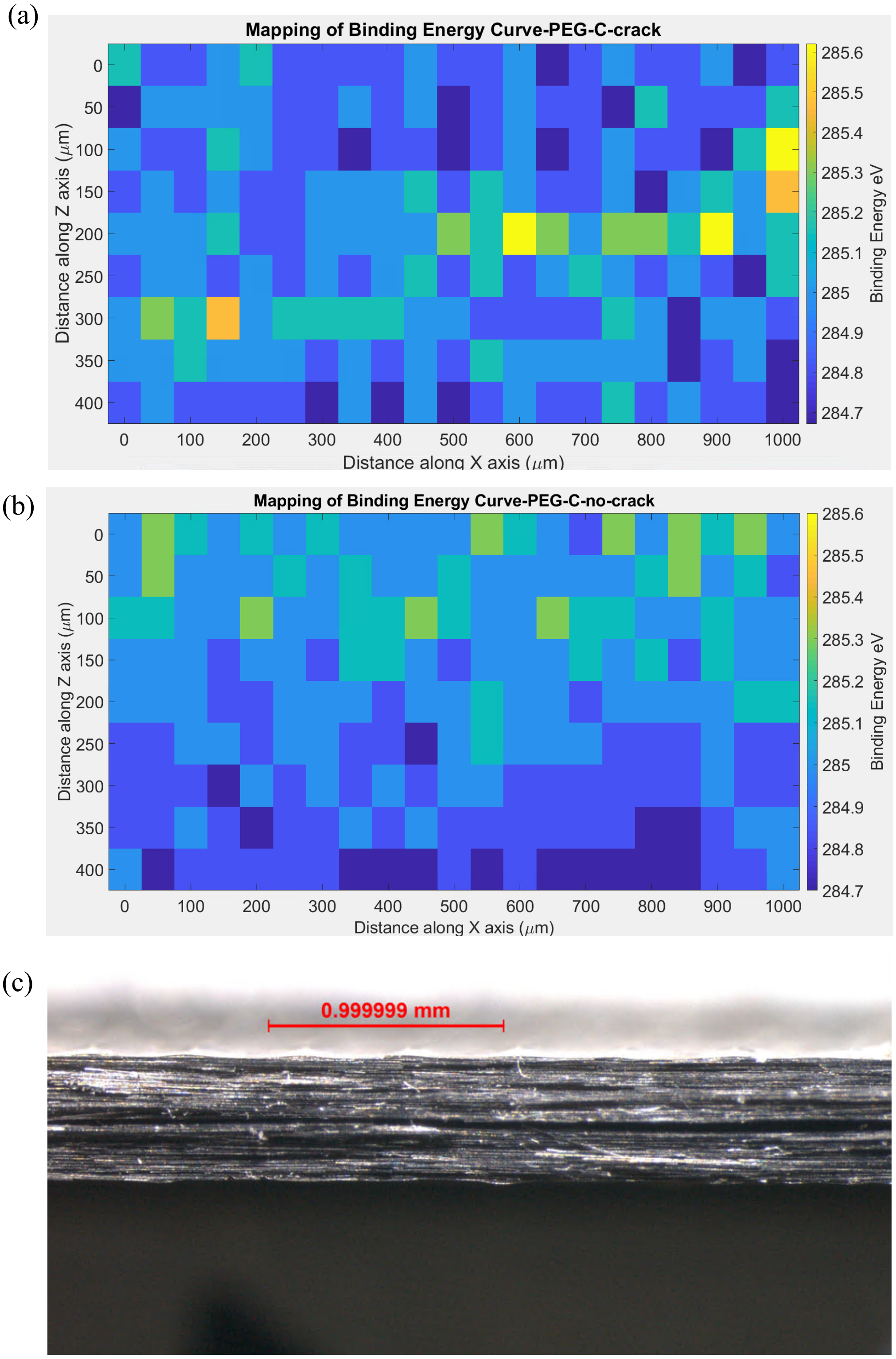

Figure 5.29. Binding energy map on the edge of PEG_Line_400 laminate in the region **(a)** containing crack and **(b)** ahead of crack with **(c)** optical microscope showing the morphology of measured surface in (a)

5.4 Confocal (Fluorescence) Microscopy

A study [8] by the partners at University of Sheffield had previously incorporated fluorescein into PMMA inks, allowing them to capture images of printed deposits on the prepreg before curing, as depicted in Figure 5.30. To study the deposits on the laminates, cured specimens of PMMA_Flu and PEG_Flu specimens were prepared, as detailed in Chapter 3. The fracture surfaces of these fluorescein-contained laminates were examined using a ZEISS LSM 980 confocal microscope. A continuous-wave 488 nm laser was employed to activate the fluorescein dye. A multidirectional Z-stack (in Y direction) acquisition was conducted over a thickness region of 96 μm. As shown in Figure 5.31, post curing, the printing pattern had disappeared, and dye signals were dispersed throughout the specimen along the fibre direction, which is in line with Figure 5.30 (a) that fluorescein tends to spread along the fibre direction. Figure 5.31 (c) demonstrates the section perpendicular to fibre direction, where the width of signal (Z direction) was in line with the fibre diameter while the length (Y direction) was at least 5 times larger than the that. These linear features suggests that post curing, the fluorescein has penetrated into the laminate.

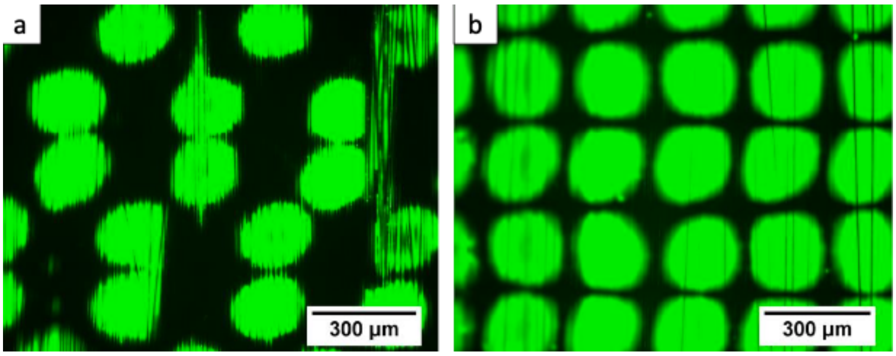

Figure 5.30. Deposits with fluorescein on prepreg before curing in **(a)** hexagonal and **(b)** square pattern [8]

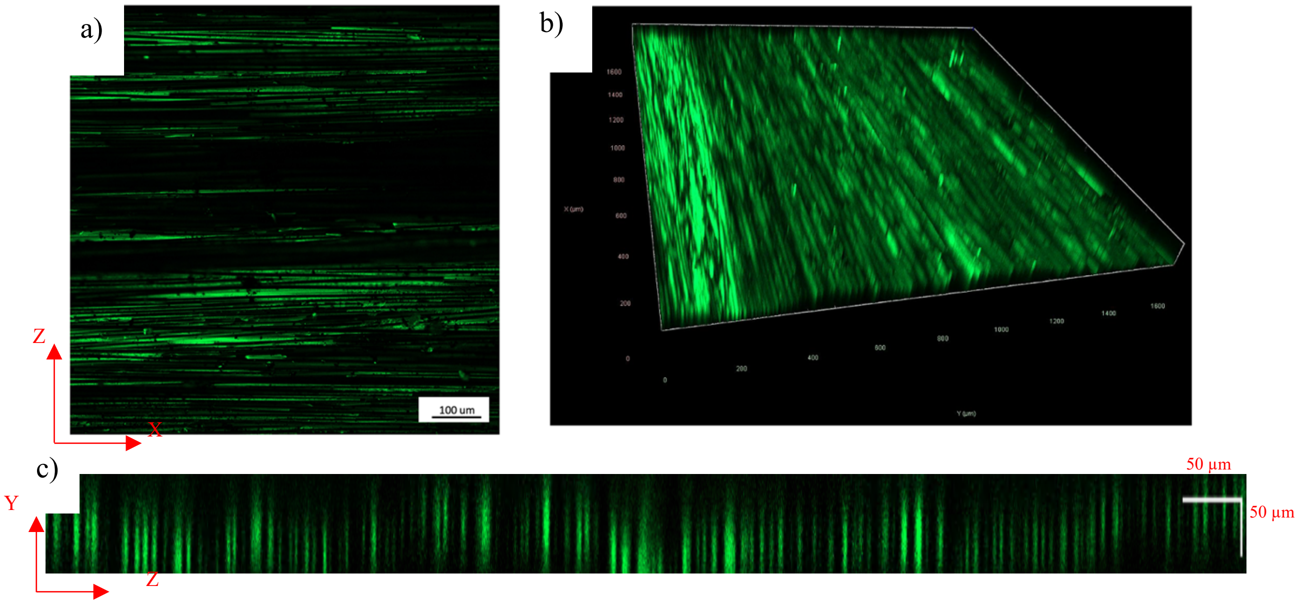

Figure 5.31. Fluorescein microscope showing the ***(a)*** fracture plane and ***(c)*** Y-Z section of laminate printed with fluorescein mixed PMMA

To determine whether this redistribution of fluorescein was due to dot migration during high-temperature curing or the dye separating from the deposits and moving freely, the same characterization was performed on the epoxy-coated glass slides, representing the matrix environment of CFRP, printed with fluorescein-mixed thermoplastic inks, manufacturing as detailed in Chapter 3. The results are depicted in Figure 5.32: Prior to curing, a square printing pattern was evident in both PMMA and PEG printed specimens. In PMMA prints, spherical particles with a diameter of approximately 180 µm formed due to incompatibility between PMMA and hardened epoxy. Satellites were observed in this specimen (indicating the printing settings are not optimal), and there are some dots not aligned to the intended pattern due to the unevenness of epoxy surface. The PEG deposits had a slightly larger diameter of approximately 200 µm, and consisted of smaller spherical particles, suggesting that PEG, with smaller molecular size, didn't mix with the dye. A scan of a pure epoxy-coated slide without printing, as seen in Figure 5.32 (c), revealed no detectable signal, indicating all fluorescence came from the printing deposits.

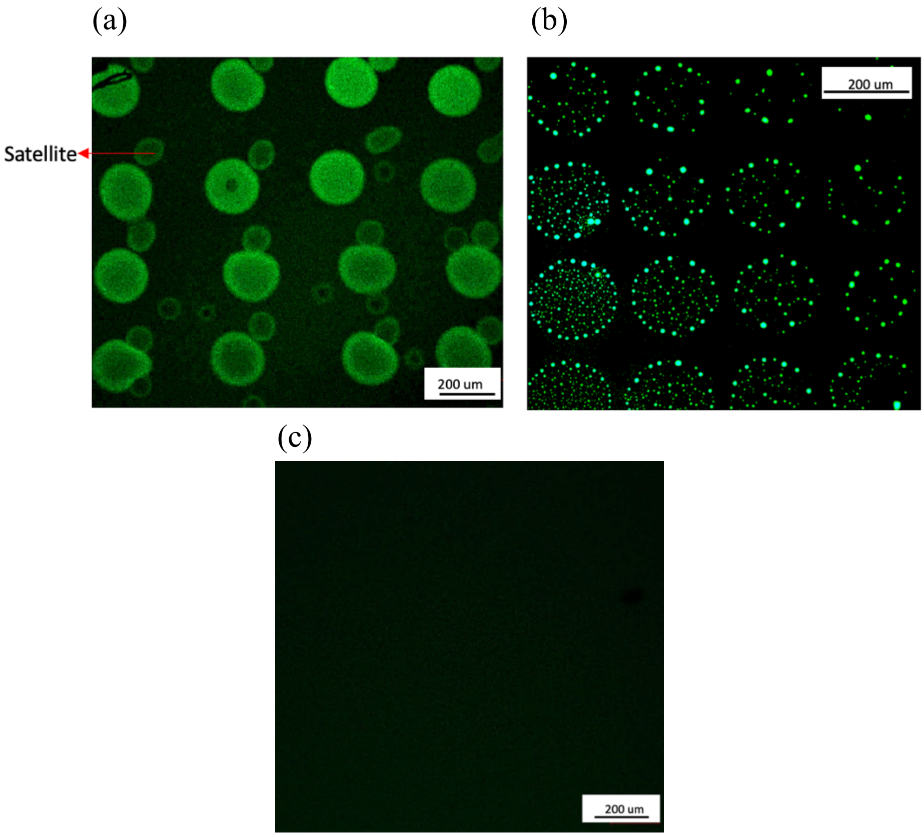

Figure 5.32. Fluorescein microscope showing the printing dots in dye included **(a)** PMMA and **(b)** PEG printed epoxy coated slides, with **(c)** scan on pure epoxy coated slide without printing

To mimic the heat cycle during the curing process, the printed slices were heated to 177 ℃ in a vacuum chamber and for 180 mins, then cooled down to ambient temperature. The heated slides post heating were re-examined under the microscope. As shown in Figure 5.33, the fluorescein signal was found to be dispersed throughout the field of view, indicating the dye spread throughout the epoxy under high temperature. An inspection of specimens with brightfield contrast from transmitted light revealed that in the PMMA-printed slides, the dots remained separate, though the square pattern was not retained, and the dot size decreased, indicating that some droplets had broken down into randomly distributed particles. While in the PEG-printed sample, the deposits appeared to merge with the epoxy post curing.

In summary, fluorescein migrates from the deposits, diffusing throughout the specimen, suggesting that tracking dots in CFRP with fluorescent dye is unreliable. Post-heating, PMMA particles remained separated from the matrix, although the original pattern was lost. Whereas, in PEG-printed epoxy, the deposits likely dissolved into the matrix during curing.

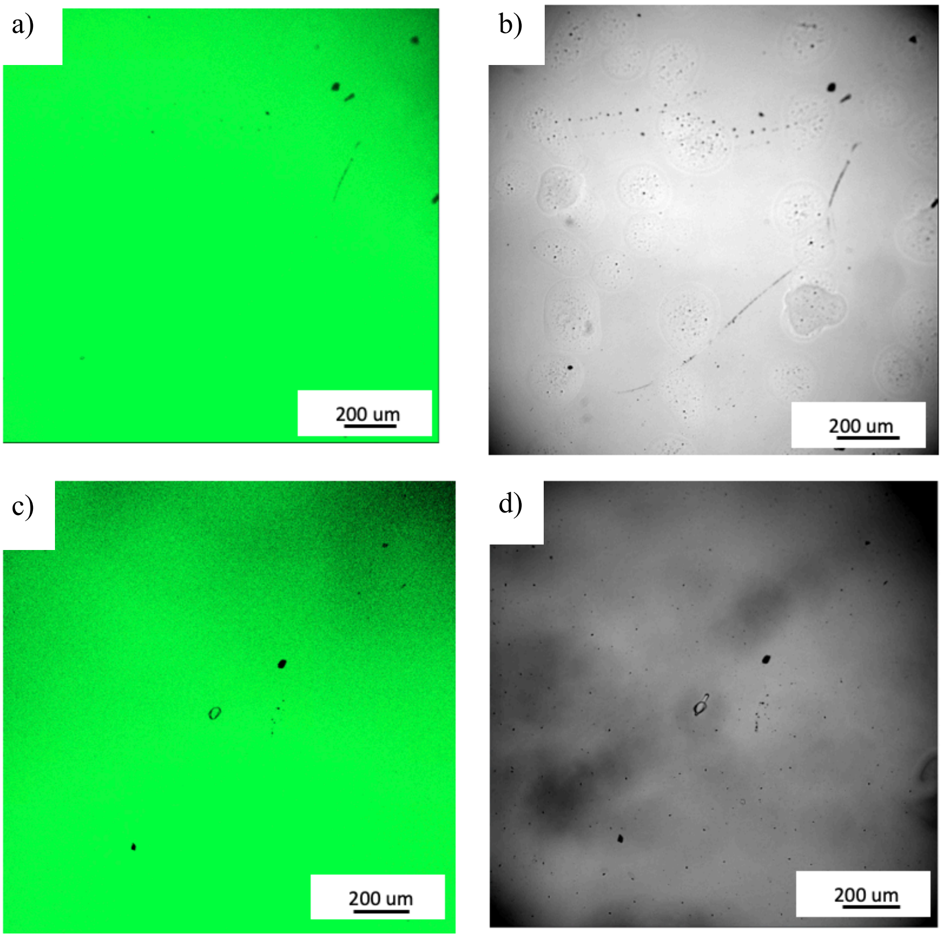

Figure 5.33. Fluorescein signal of **(a)** PMMA printed and **(c)** PEG printed specimens post curing, with **(b)** PMMA- and **(d)** PEG- printed epoxy examined under the transmitted light at the same position

5.5 Conclusion

This chapter presents a series of ex-situ characterizations aimed at examining the changes in laminate materials following the inkjet printing of thermoplastic droplets.

The fracture surface roughness in terms of large-scale waviness has a linear correlation with fracture toughness, The increase of crack surface unevenness in the printed specimen indicating a higher degree of crack deflection contributes to enhancement of the work of fracture.

Under SEM, voids and spherical particles were only observed in the fractography of PMMA_Line_15000 laminate, which might contribute to the toughening by extending the plastic zone, aiding the formation of matrix bridging (voids) and interacting with crack (particles).

Chemical state of the composites was analysed using XPS, which reveals the printed specimens contained a greater number of active functional groups in the fracture plane, thereby enhancing bonding between adjacent layers. However, no pattern related to the printing geometry was observed among the above characterizations.

The examination under a confocal microscope revealed that while PMMA deposits remained separate from matrix, while PEG merged with the epoxy resin.

5.6 References

[1.] Auner-Straße. Alicona IF measurme Suite Version 5.1. 2013.

[2.] Kapłonek W, Nadolny K, Krolczyk G. The Use of Focus-Variation Microscopy for the Assessment of Active Surfaces of a New Generation of Coated Abrasive Tools. Measurement Science Review. 2016;16:42-53.

[3.] ISO 4287:1997 Geometrical product specifications (GPS) – Surface texture: Profile method – Terms, definition and surface texture parameters. 1997.

[4.] Mark Malburg MZ. Surface Roughness Is More than a Number [Available from: https://www.powertransmission.com/articles/9279-surface-roughness-is-more-than-a-number.

[5.] Lim Y. In-Situ 3D observation of damage development and healing in a carbon-fibre/epoxy composite: University of Oxford; 2019.

[6.] Andrews EH. Fracture in polymers. (No Title). 1968.

[7.] Zhang Y, Stringer J, Hodzic A, Smith PJ. Toughening mechanism of carbon fibre-reinforced polymer laminates containing inkjet-printed poly(methyl methacrylate) microphases. Journal of Composite Materials. 2017;52(11):1567-76.

[8.] Zhang Y. The effect of inkjet printed polymer on the mechanical properties of carbon fibre reinforced plastic: University of Sheffield; 2015.

[9.] Ritzenthaler S, Girard-Reydet E, Pascault JP. Influence of epoxy hardener on miscibility of blends of poly(methyl methacrylate) and epoxy networks. Polymer. 2000;41:6375-86.

[10.] Thi Hong P, Nguyen HQ, Nghiem HTM. Complex refractive index measurements of poly(methyl methacrylate) (PMMA) over the UV-VIS-NIR region. Opt Continuum. 2023;2(11):2280-9.

[11.] Su W-F, Fu Y-C, Pan W-P. Thermal properties of high refractive index epoxy resin system. Thermochimica Acta. 2002;392-393:385-9.

[12.] Pearson RA, Yee AF. Toughening mechanisms in thermoplastic-modified epoxies: 1. Modification using poly(phenylene oxide). Polymer. 1993;34(17):3658-70.

[13.] Gomez CM, Bucknall CB. Blends of poly(methyl methacrylate) with epoxy resin and an aliphatic amine hardener. Polymer. 1993;34(10):2111-7.

[14.] Chen J, Kinloch AJ, Sprenger S, Taylor AC. The mechanical properties and toughening mechanisms of an epoxy polymer modified with polysiloxane-based core-shell particles. Polymer. 2013;54(16):4276-89.

[15.] Thirunavukkarasu N, Bhuvaneswari Gunasekaran H, Peng S, Laroui A, Wu L, Weng Z. Study on the interface toughening of particle/fibre reinforced epoxy composites with molecularly designed core–shell particles and various interface 3D models. Materials & Design. 2023;225:111510.

[16.] Quan D, Ivankovic A. Effect of core–shell rubber (CSR) nano-particles on mechanical properties and fracture toughness of an epoxy polymer. Polymer. 2015;66:16-28.

[17.] Carolan D, Ivankovic A, Kinloch AJ, Sprenger S, Taylor AC. Toughened carbon fibre-reinforced polymer composites with nanoparticle-modified epoxy matrices. Journal of Materials Science. 2017;52(3):1767-88.

[18.] Wong W-Y. Toughening of epoxy carbon fibre composites using dissolvable phenoxy fibres: Queen Mary University of London; 2013.

[19.] Bagheri R, Pearson RA. Role of particle cavitation in rubber-toughened epoxies: 1. Microvoid toughening. Polymer. 1996;37(20):4529-38.

[20.] Sørensen BF. 11 - Delamination fractures in composite materials. In: Talreja R, Varna J, editors. Modeling Damage, Fatigue and Failure of Composite Materials: Woodhead Publishing; 2016. p. 213-40.

[21.] Srinivasa V, Shivakumar V, Nayaka V, Jagadeeshaiaih S, Seetharam M, Shenoy R, Nafidi A. Fracture morphology of carbon fiber reinforced plastic composite laminates. Materials Research. 2010;13:417-24.

[22.] Baldan A. Adhesion phenomena in bonded joints. International Journal of Adhesion and Adhesives. 2012;38:95-116.

[23.] Greczynski G, Hultman L. X-ray photoelectron spectroscopy: Towards reliable binding energy referencing. Progress in Materials Science. 2020;107:100591.

[24.] Scientific TF. K-Alpha X-ray Photoelectron Spectrometer System [Available from: https://www.thermofisher.com/uk/en/home/electron-microscopy/products/xps-instruments/k-alpha.html#features.

[25.] How XPS works: Diamond light source; [Available from: https://www.diamond.ac.uk/industry/Techniques-Available/Spectroscopy/X-ray-Photoelectron-Spectroscopy-XPS/How-XPS-works.html.

[26.] Li S, Sun T, Liu C, Yang W, Tang Q. A study of laser surface treatment in bonded repair of composite aircraft structures. Royal Society Open Science. 2018;5(3):171272.

[27.] Zhang T, Zhang T, He Y, Zhang S, Ma B, Gao Z. Long-Term Atmospheric Aging and Corrosion of Epoxy Primer-Coated Aluminum Alloy in Coastal Environments. Coatings. 2021;11(2):237.

[28.] Gao Y, Liang X, Bao W, Wu C, Li S. Degradation characteristics of epoxy resin of GFRP rod in the decay-like fracture of composite insulator. IEEE Transactions on Dielectrics and Electrical Insulation. 2019;26(1):107-14.

Chapter 6

6. Finite element microstructure meshfree model (FEMME) of inkjet printing modified CFRP

6.1 Introduction to the FEMME model

In mechanics of materials, computational modelling serves as a powerful tool to simulate experiments and predict materials performance. While physical experiments can be limited by imperfections, high costs, and the impracticality of repetition, numerical models offer viable solutions to these challenges, allowing for simulation of mechanical testing under conditions that are free from practical limitations. [1]

Discretization of the model is a crucial factor that decides the calculation fidelity and resolution. In finite element (FE) analysis, for instance, an adequate level of discretization, such as the appropriate mesh or element size is always required to address the microstructure and integrate the damage propagation [2]. An element that is too coarse results in inaccurate calculation, and in scenarios like cohesive modelling may even disable the calculation of the fracture process [3]. Coarse meshes in inelastic quasi-brittle materials often lead to a significant overestimation of strain energy release in fracture propagation [4]. Reducing the mesh size, however, will dramatically increase the computational cost. A mesh sensitivity analysis therefore would normally be performed in conventional FE for an optimum discretization that balance the calculation's computational accuracy and cost. For fracture propagation studies, the Extended Finite Element Method (XFEM) provides an efficient solution to resolve the crack evolution in quasi-static conditions by adopting local enrichments of nodes for mesh refinement, however, a pre-definition of crack path is required in this method [5].

As an alternative, multiscale models such as CAFE that combine cellular automata (CA) and finite element (FE) techniques provide a high efficiency, flexible approach to model quasi-brittle fracture development. In a CAFE model, the CA layer represents the material's microstructure while the FE layer describes the macroscale properties and strains, with local enrichment activated only in region near the fracture events, which subsequently reduces the total computational cost. [6, 7] To simulate composite microstructures with a higher precision and complexity, Saucedo-Mora proposed the Finite Element Microstructure Meshfree (FEMME) model that includes the adaption of microstructure-based Meshfree model to link the FE and CA layers. In a FEMME model, the microstructure activation is localized to regions meeting the damage criteria, enhancing the computational efficiency without necessitating a predefined crack path. As the microstructure could be well defined and modelled in the subsequent layers, this enables a coarse mesh in the FE model without loss of accuracy. [4]

The schematic structure of a FEMME model is displayed in Figure 6.1. There are three layers contained in FEMME: (1) finite element (FE), (2) microstructure adapted meshfree (MAM) and (3) Cellular Automata (CA), where these different length scale models are interactively connected via energy homogenization.

The FE layer captures the geometry of the component and is implemented in a solver such as Abaqus. A tetrahedral mesh is applied to increase the versatility of model. As shown in Figure 6.2, the subdivision is achieved through an interactive algorithm where the largest tetrahedron face is divided into 4 similar sized tetrahedron cells defined by midpoints of the edge [8]. This process is iterated until the average volume is sufficient to represent the microstructure. With sufficient subdivision, the calculation becomes insensitive to the FE mesh size. Boundary conditions are applied in this layer, and the FE layer represents the bulk mechanical response from the microstructure. The mechanical properties in the FE layer are determined by the damage that been simulated within the microstructure layer.

The microstructure layer comprises a mesh free model and a cellular automata model. The matrix operations of both layers are achieved through NumPy in Python. The subdivision of the FE tetrahedron generate cells in the microstructure layer. Heterogeneities such as particles, pores or other phases are then defined mathematically by their geometry, where the size of the cells determines the resolution of the subsequent damage description. In the FE layer, microstructures within the regions that reach a defined criterion (e.g. critical stress or strain) will be active, and the nodal solutions from FE mesh are input to the mesh free layer for displacement calculation. In the mesh free layer, a series of ellipsoids are defined as particle domains (PD), which represent pores and particles. This is followed by Delaunay triangulation to define the inter particle domains (IPD) representing the bulk material between these. To calculate the fracture behaviour, the nodes in FE layer must sit in either a particle domain or an inter particle domain. The next microstructure layer is the cellular automata (CA) layer, where the nodal solution in the mesh free layer is shared for the strain calculation. If any cell in the CA layer reaches the pre-defined critical criteria, the cell erodes and releases fracture energy. This allows simulation of the damage behaviour. By introducing the CA layer, a pre-definition of the crack path is not required. All the model layers are linked through energy homogenization by the Hill-Mandel method [9], where the sum of released fracture energy from the CA cells is used to recalculate the materials constitutive relationship in the host domains of the mesh free layer, which subsequently affects the mesh in FE model where the degradation of stiffness in FE is proportional to the sum of decrease in domain strain energy (in the mesh free layer) within the mesh. Through this approach, FEMME is capable to simulate the macroscale mechanical response that considers the microstructure fracture propagation. The algorithm of FEMME method was originally developed by Saucedo-Mora, and full details of the method can be found in [4]. The FEMME method has been applied in this project to simulate delamination behaviour of CFRP and to examine the potential role of microstructure features such as bridging fibres and printed droplets.

As summarized in Figure 6.1, the process of setting up a FEMME model includes six steps: (1) defining the macrostructure geometry of the FE based on the real sample geometry and applying the boundary conditions, which informed the calculation in FE layer; (2) the nodal solutions of the mesh elements that been activated were imposed to domains within those regions in the microstructure mesh free layer; (3) domains that reach the defined critical value are activated, and the displacement solutions are mapped in the CA model to calculate the strains in the cells; (4) cells with stress or strains that are higher than the defined failure value are eroded, with the fracture energy released from the system. The displacement field is updated, and these interactive steps repeat until no cell reaches the failure criteria; (5) the constitutive relationships in the mesh free model are updated based on the released fracture energy of the cells; (6) the strain energy of meshfree model informs the FE model to update the mechanical properties of the elements and compute the macrostructure response of the bulk component.

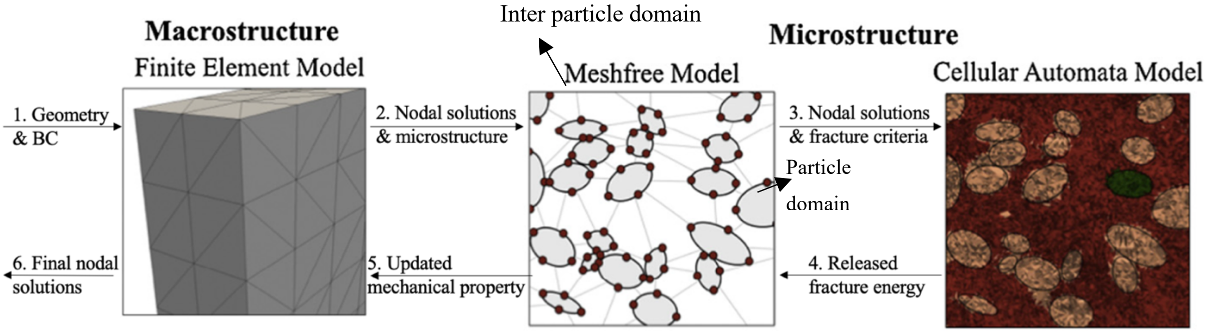

Figure 6.1. Structure of a FEMME model showing interaction between layers [4]

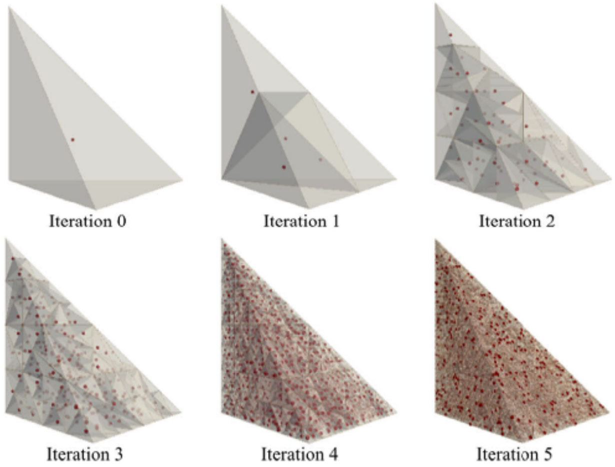

Figure 6.2. Integration subdivision of tetrahedral, with a red dot marks each cell centre [8]

6.2 Structure of inkjet printing modified CFRP laminate FEMME

Here, the FEMME framework was applied to CFRP composites for the first time, with the objective of model validation using the experimental data from the double cantilever beam tests. This extended the application of FEMME and simulated the damage development of Mode I fracture propagation behaviour in CFRP laminates. This work has been done in collaboration with Saucedo-Mora. The author was responsible for preparing materials, microstructure and experimental data, while Saucedo-Mora provided the model framework; collaboration work was conducted to design the model that applies the FEMME framework to CFRP.

The geometry of the FE layer was decided according to the dimensions of the 2-ply laminate in the double cantilever beam (DCB) tests as outlined in Chapter 3. As shown in Figure 6.3, the whole component was represented by a single layer finite element mesh, sizing at 50 x 3 x 0.5 mm (in X, Y and Z directions respectively). The use of a single layer was because the crack needs to grow within the finite element model, that said, the interface between two plies should be embedded into a finite element layer. Due to the height of the sample, if multiple layers were introduced in the FE model, the mesh would become too distorted. Here, an optimized size of FE layer needed to be defined that should be big enough to contain a representative volume of microstructure, and small enough to capture the elastic property of the interface. The single FE layer well satisfied the above requirement and was thus applied here. Four-node tetrahedral elements (C3D4) were applied and subsequently divided into sub-tetrahedral which enables efficient and versatile geometry modelling. A notch (29.65 mm length) was incorporated in the component to represent a pre-crack. In this layer, there was no geometrical differentiation between the notch and the rest of the beam, the only difference was in the mechanical properties, where the stiffness of the notched beam was much lower than the rest. Numerically, the notch was treated as broken element. Here, the stiffness of notch was defined as 0.01% of the bulk materials (instead of 0) to avoid numerical instabilities. The displacement (blue arrow in Figure 6.3) was imposed on the nodes of the border, and beam theory was applied to calculate the forces applied to the 2 plies.

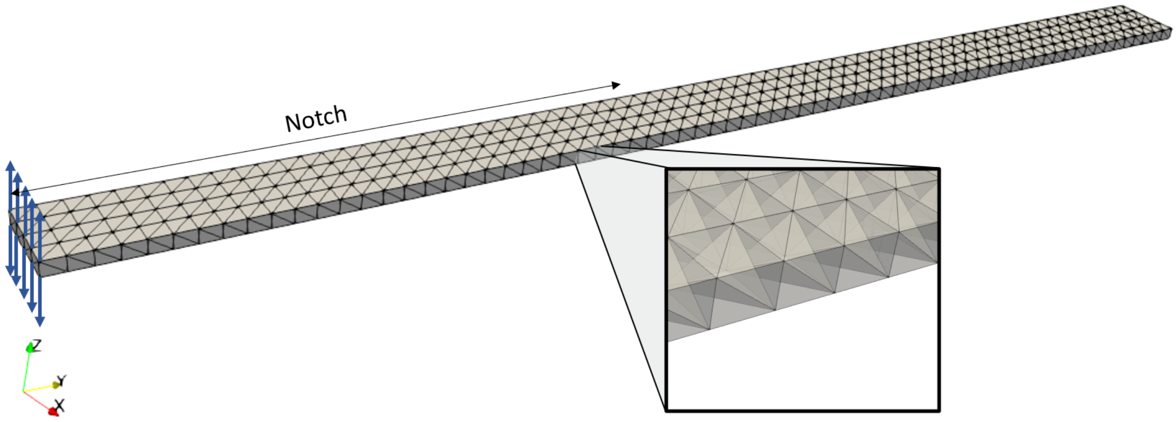

Figure 6.3. Overview of the laminates model at FE layer

In order to transfer from the FE layer to mesh free layer, an activation criterion needed to be defined. A preliminary test demonstrated that within a reasonable region (below 100% of bulk strength), the actual code would not influence the result but only the computational cost. Here, we defined the mesh free layer to be activated when the stress in an FE element reached a critical value of 70% of the bulk tensile strength. The printed deposits in the mesh free layer were simulated by inducing dots that had the same Young's modulus as PMMA at 3000 MPa [10], with 0.1 mm diameter in hexagon pattern so that the distance between centre of each dot was 0.2 mm (dx) and 0.6 mm (dy) respectively. The dots were within particle domains located in the middle plane of the components. They were explicitly inserted to enhance the discretization of the model at the microstructure layer to make the discretization finer with smaller cells.

As shown in Figure 6.4 and Figure 6.5, fibres were embedded in a separated layer to study the effect of bridging on the FEMME model. During the in-situ XCT observation, significant amount of fibre and matrix bridging had been observed. While the current model was not capable to simulate the actual carbon fibre peeling and ligament bridging, it was still meaningful to introduce the bridging in the FEMME delamination model and study the effect. That said, the model with the fibre was not intended to replicate and simulate experiment, it was instead a tool to introduce and study the bridging mechanism. Straight fibres were inserted across the edges of the FE elements, as shown in Figure 6.4. The diameter of the fibres was 10 μm, and the length was defined to across the top to bottom of the FE mesh, which ensured crack crosses the fibre with independence of the path. The fibres had a fitted failure strain of 0.01, and since the mechanical performance was given by the strain, the length of the fibre is not affecting the calculation. The fibre distribution in the model is shown in Figure 6.5, where the quantity of which was simplified as the bridging carbon fibre density (40 fibres/mm^2 in the damage area) measured from synchrotron XCT in I12-JEEP. Those fibres were randomly distributed at the central axis; and all the fibres were stochastically oriented at angles between 0 to 45° to the central axis, which represented the observed fibres in various angles. The paired crossing point at the borders of tetrahedra element was used to define the fibre path. And by assuming a perfect bond between fibre and matrix, the strain of the FE element was determined in the fibre direction to define the strain along the fibre, after that, the stress and subsequently the reaction force of the fibre could then be generated following elasto-plastic truss rule. This force served as the Neumann boundary condition [11] to then re-evaluate the displacement of nodes. This process was iterated until the strain of fibre converges.

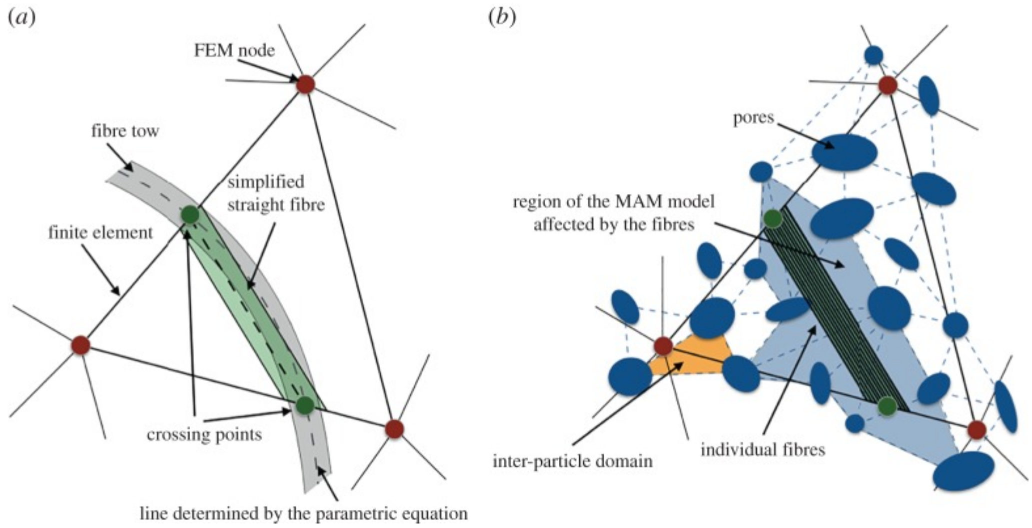

Figure 6.4. Schmatic relationship between fibre and FE element in **(a)** FE layer and **(b)** meshfree layer [12]

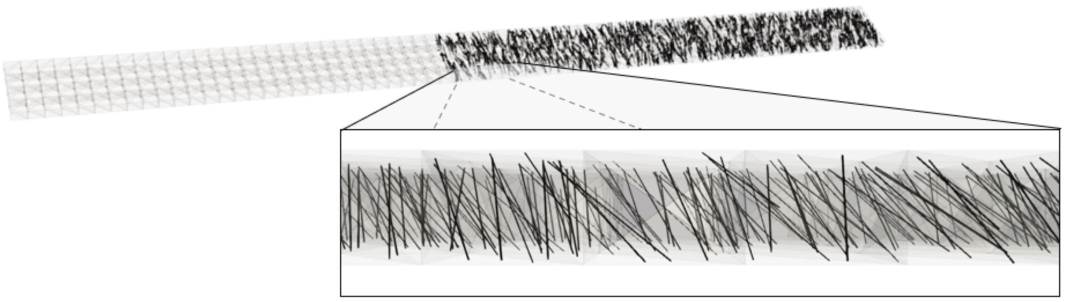

Figure 6.5. Fibre insertion within the composite beam model

Activation in the CA layer occurs within domains where stress surpasses 50% of the tensile strength, with domains subdivided into tetrahedra cells. The cell was eroded upon reaching the predefined tensile strength, which subsequently released the fracture energy from the system. The fracture energy (G_{IC}) of cells is as measured in Chapter 3, where in this case for all the specimens were approximated at 332 J/m^2. This then in return informed the mesh free and FE layer to redefine the modulus and recalculate the mechanical response.

The properties of components used in this model are summarised in Table 6.1. For calculation of each fitted parameter, step by step tests have been processed through the load displacement curves. This is because different parameters have a higher importance at different stages of the load-displacement curve. Specifically, the matrix modulus would affect the slope of the linear part of the curve and can be adjusted with this. Then, the fibre effect become more prominent once damage initiated, which was controlled by the bulk tensile strength and had a significant influence on the peak load at the transition point between the linear and nonlinear parts. Close to the peak load, if the fibre modulus was very high, the sample would have a spurious over-stiffening, which was not observed experimentally and that determined the region where this parameter could be fitted with a higher fidelity. Finally, the fibre failure strain had an influence on the slope of the post peak curve.

It is worth noticing that the fitted modulus and strength are significantly lower than the real value. This is because the current model does not aim to simulate the real mechanical behaviour, as simplification of longitudinal fibres would not restrict the damage in the pre-crack plane. Instead, the fitting parameters were applied to replicate the stress-strain curve which would then be utilised to study the effect of general fibre bridging and interfacial strength on fracture propagation.

Table 6.1. Summary of material parameters in the model

Parameter	**Value**	**Source**
Matrix modulus	20.5 MPa	Fitted
Bulk tensile strength (matrix + dots)	0.18 MPa	Fitted
Bulk fracture energy	332 J/m^2	Experiment
Fibre modulus	28.3 GPa	Fitted
Fibre failure strain	0.01	Fitted

To simulate the Mode I fracture propagation in double cantilever beam (DCB) geometry, displacement boundary condition was inserted at the top and bottom surface of the component to apply a 5 mm COD through 700 steps. Damage was assessed in the CA layers, and the released fracture energy was accounted to recalculate the modulus in meshfree and FE layer. Details of the energy homogenization were as follows:

$$\mathrm{U}_{\mathrm{cell(eroded)}} = 0 \quad (6.1)$$

$$\mathrm{U}_{\mathrm{IPD\ or\ PD}} = \sum_{\mathrm{i=0}}^{\mathrm{i=n}} \mathrm{U}_{\mathrm{cell_n}} = (\mathrm{Vol} \cdot ([\mathrm{D}]_{\mathrm{new}} \cdot \bar{\varepsilon}) \cdot \bar{\varepsilon})_{\mathrm{IPD\ or\ PD}} \quad (6.2)$$

$$\mathrm{U}_{\mathrm{FE}} = \sum_{\mathrm{i=0}}^{\mathrm{i=m}} \mathrm{U}_{\mathrm{IPD_m}} + \sum_{\mathrm{i=0}}^{\mathrm{i=l}} \mathrm{U}_{\mathrm{PD_l}} = (\mathrm{Vol} \cdot ([\mathrm{D}]_{\mathrm{new}} \cdot \bar{\varepsilon}) \cdot \bar{\varepsilon})_{\mathrm{FE}} \quad (6.3)$$

the energy of eroded cells was removed (equation 6.1), which then informed the recalculation of $[\mathrm{D}]_{\mathrm{new}}$ and subsequently Youngs modulus (*E*), following linear elasticity (Hooke’s law):

$$[\mathrm{D}] = \begin{bmatrix} 1-v & v & v & 0 & 0 & 0 \\ v & 1-v & v & 0 & 0 & 0 \\ v & v & 1-v & 0 & 0 & 0 \\ 0 & 0 & 0 & \frac{1-2v}{2} & 0 & 0 \\ 0 & 0 & 0 & 0 & \frac{1-2v}{2} & 0 \\ 0 & 0 & 0 & 0 & 0 & \frac{1-2v}{2} \end{bmatrix} \cdot \frac{E}{(1+v)(1-2v)} \quad (6.4)$$

with these, the damage progression considering the effect of fracture could be efficiently modelled, and the mechanical response of the bulk to the displacement boundary condition was extracted.

6.3 Results and discussion

The FEMME framework was applied to successfully simulate Mode I fracture propagation in a two-layer CFRP laminate. As shown in Figure 6.6, the fracture in the laminate could be evaluated, and tensile strain in the damage zone was tracked, where the strain gradually decreased from the end of the laminate (on notch side) to reach zero ahead of the crack tip. The grey elements in Figure 6.6 (a) are those with damage development, and the black elements are fully damaged (broken). Figure 6.6 (b) & (d) show more details of the crack development region: Within the inter particle domains (transparency tetrahedrons), the black cells represented the ones that were broken, where high strain was observed and were surrounded by domains unloaded by the crack with lower strain. Figure 6.6 (c) & (e) display the crack (red layer) inside the interparticle domain, at the stages of the peak load and stable crack growth respectively, corresponding to Figure 6.6 (b) & (d). It is worth noticing the large values of strain displayed belong to broken regions of the material, thus, these strains are not real mechanical strain of the material, and only denote the opening of the crack within this area.

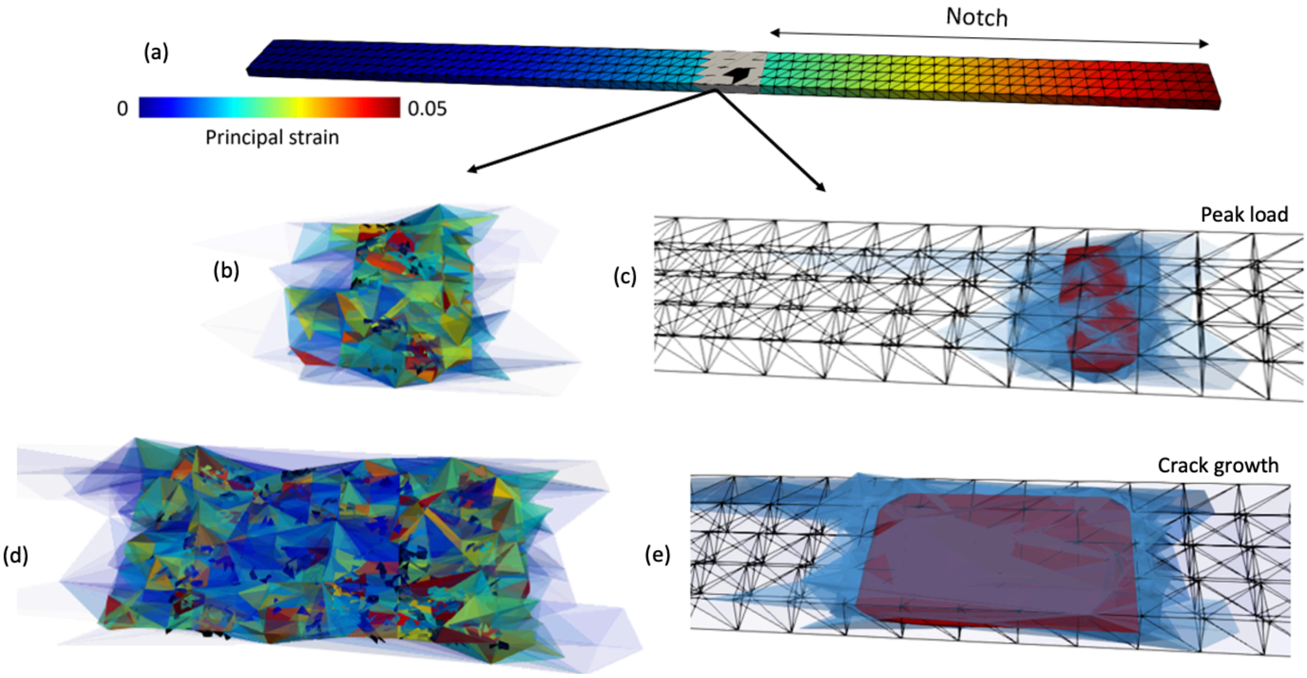

Figure 6.6. (a) strain field of the opened laminate where the grey region represents the damage development area, with details of damaged layer and cells in **(b-c)** at peak load and **(d-e)** at crack propagation stage

Figure 6.7 displays the variation of force across the specimen at different loading stages, with the corresponding strain field within the damaged region on the right. The fracture process zone (FPZ) was characterized as the region between points of onset of stable force growth and maximum load. With the insertion of fibres, fracture process zone enlarged, as fibres were tracking the top and bottom plies. Moreover, with the further development of crack propagation, the length of FPZ grew and stabilized at ~ 5 mm for CFRP in the model with fibres.

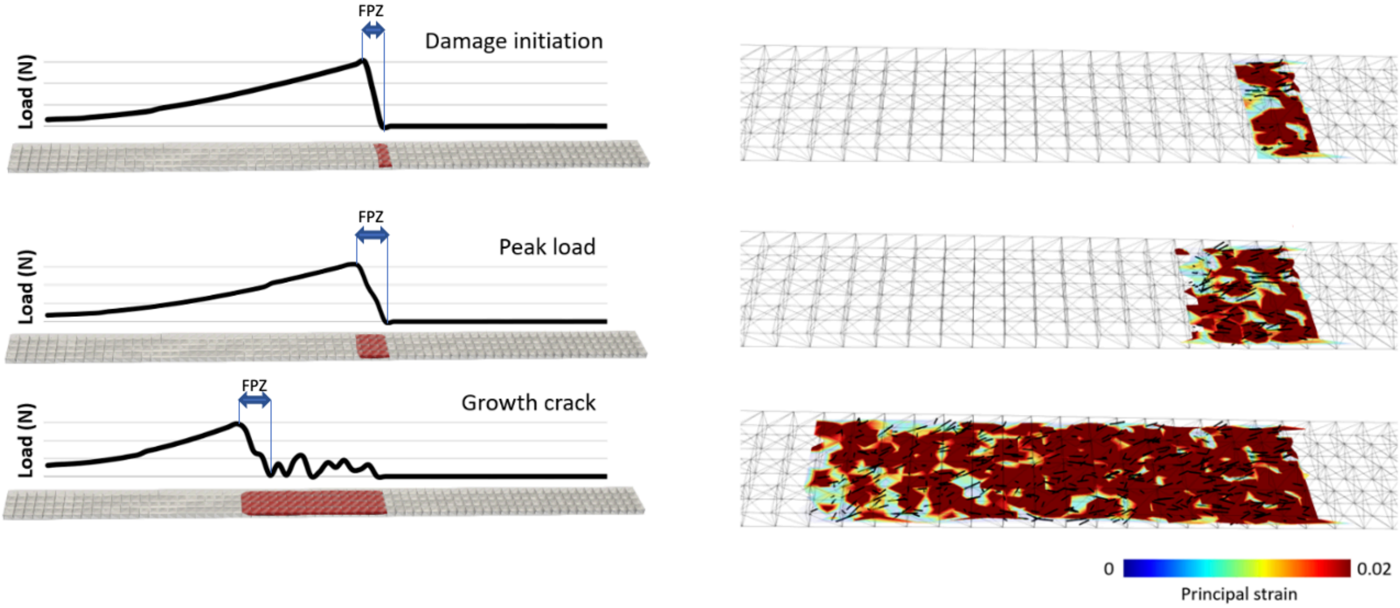

Figure 6.7. Tracking of interaction force of the nodes along the fibre direction at different steps, where fracture process zone (FPZ) marked in blue is characterized as the region between onset of stable load increment and peak load; with the corresponding strain field on the right. Fibres are inserted in the model.

The printing dots were cantered at particle domains. However, during fracture propagation, the crack was not restricted to the interface plane, it was instead allowed to move freely within the FE mesh (Figure 6.8 (a)), which meant the particles did not stop the damage development in this framework. This is because the model of interfacial layer was not physically generated in the model. Therefore, mechanically in the FEMME model the dots are not doing anything, where the resolution is not enough to mimic the interaction between crack and dots. The dots, as shown in green of Figure 6.8, were therefore only applied for an enrichment of the discretization in the model. They were part of the interparticle domains but not affecting directly to the mechanical performance of the sample. The model relies on two conditions that affect the insertion of the dots: First, a coarse FE mesh is needed to host a representative volume of microstructure, so the dots cannot be explicitly modelled within the FE layer. For this reason, the dots needed to be introduced in the microstructural layer and be part of the IPDs of the meshfree model. Secondly, in the FEMME model, the crack needed to grow within the FE elements and cannot be restricted to the FE element faces. In this case, the freedom given by the FEMME model makes the crack capable of deflection from the interface. For those reasons, the role of the dots in the model is solely to enhance the microstructural discretization. The effect of printing, instead, must then be indirectly inserted through an increment of the tensile strength of the matrix, which would reproduce the toughening of the interface between plies. This will be detailed in the later part.

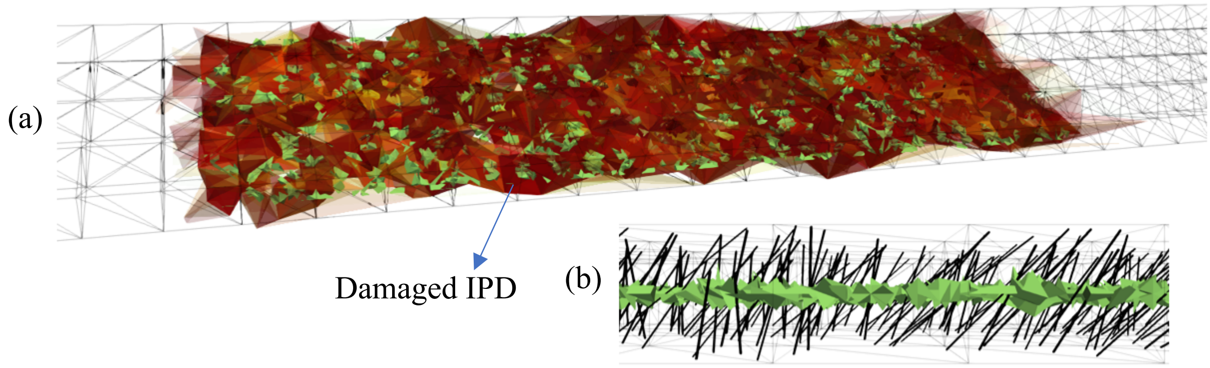

Figure 6.8. Result viewing of the model showing **(a)** crack (represent as the red) could escape the printing deposits (green dots) and moves up and down from the plane; with **(b)** the details of inserted fibres and dot plane

The model was well fitted to the load-displacement curve of experimental where insight of how crack propagation was affected by bridging could be obtained: as shown in Figure 6.9, during the elastic loading, models with and without fibre possess the same Youngs modulus. While the fibres could enhance the fracture resistance at the early stage, which extended the elastic region that the damage influence took longer to appear on the global behaviour. Once the crack initiated, the fibres became more important where a higher interfacial load was observed in the model. However, with further crack propagation, the work of fracture in the two models become identical, meaning the toughness of the bulk CFRP was mainly provided by the matrix. Because there was more energy released in the model with fibres (black line) during the onset of crack propagation, in the later stage model without fibres (red line) displayed a higher force with a larger amount of energy release that the total amount of fracture energy remains similar. With the bridging mechanism included, the model fitted better with the experimental data, therefore, the rest of laminate in the model were all embedded with fibres. Moreover, it is worth noticing that the curves from real tests experienced a sharp drop of load at the end of elastic stage. This originated from the stress concentration of the notch, where the current static model was unable to capture.

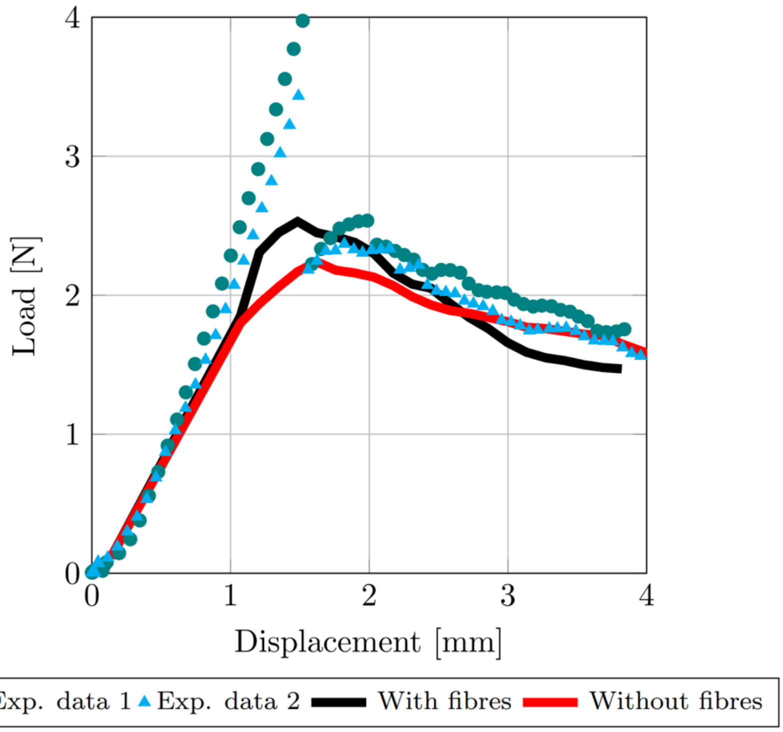

Figure 6.9. Load-displacement curves from FEMME model with and without fibre in PMMA-printed sample, with the comparison of DCB experiment results of PMMA_Line_15000 sample

As shown in Figure 6.10, simulation with fibre fitted well with the load-displacement result from experiment for the three specimens, where the interfacial strength were at 0.2 MPa, 0.22 MPa and 0.24 MPa for Non-, PMMA- and PEG- printed specimens respectively. As the three laminates share similar modulus, a higher interfacial critical stress meant a larger critical strain. This agreed with the observation from in-situ XCT, where PEG_Line_400 displayed the largest COD, followed by PMMA_Line_15000, and NP_2 possess the lowest.

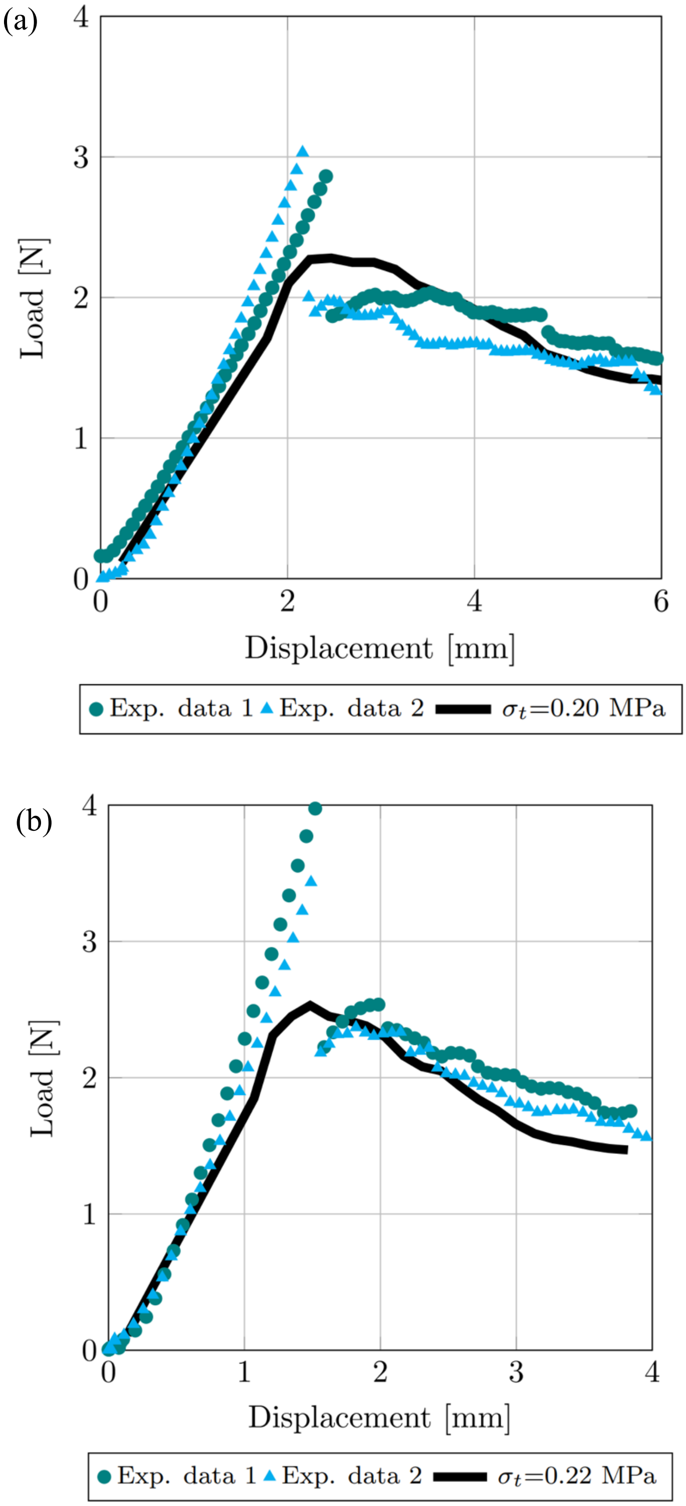

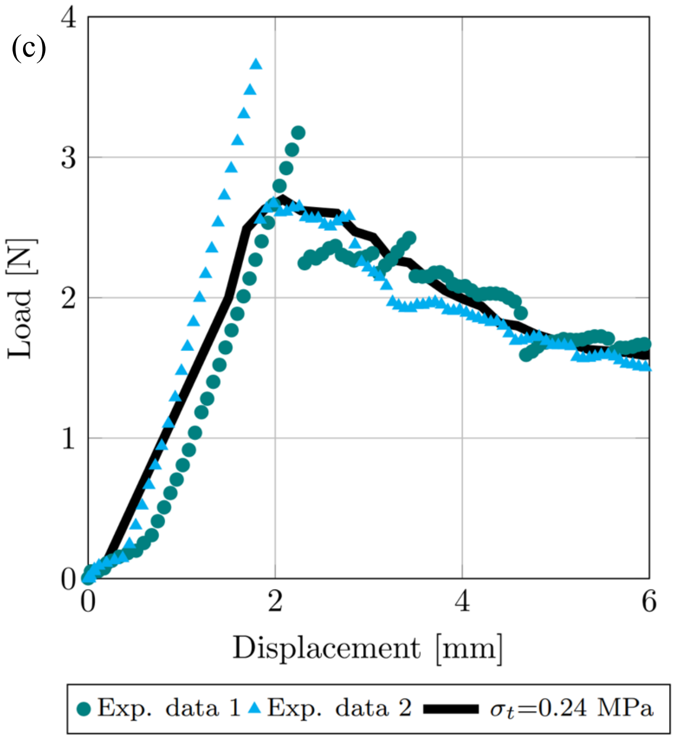

Figure 6.10. Comparison of Load displacement curves in **(a)** Non-, **(b)** PMMA- and **(c)** PEG- printed specimens; where dash lines represent the experimental data from DCB test (from NP_2, PMMA_Line_15000 and PEG_Line_400 respectively in Chapter 3, and black continuous line shows the fitted model result with fibre insertion

6.4 Conclusion and future work

In conclusion, this work successfully extended the application of Finite element microstructure meshfree model (FEMME) to carbon fibre composite, where the Model I fracture propagation had been mimicked. Due to the limitation of framework, it failed to capture the interaction between crack and printing dots, where the insertion of dots was only for enhancement of discretization. The DCB experiments (Chapter 3) had been replicated with the tuning of critical stresses, where an increasing of interfacial strength appeared in printed laminates, indicating a higher opening displacement that agreed with the observation from in-situ XCT.

To improve the model, future work could be conducted by introducing: 1. Longitudinal fibres in the bulk to simulate the unidirectional CFRP. This would restrict the crack in the pre-crack plane (interface of the two plies) [12], which could enlarge the effect of printing dots and potentially be able to capture the interaction between crack and dots. By restricting the damage in the interface, the actual damage propagation between the fibre and matrix interface could also possibly be resolved, which would better describe the real mechanical behaviours. 2. A finer FE discretization: this will allow a better reproduction of stresses around the notch as well as a better constrain of the crack within the predefined crack plane. The drawback of which is a much higher computational cost (a few orders of magnitude more operations). 3. The dynamic approach: In the real experimental (dash line in Figure 6.10), during crack initiation, the load reached up to 4 N then suddenly dropped, which was caused by the stress concentration of notch. Currently the framework failed to monitor this process, this is because the model is static, which could be modified by inclusion of dynamic model [13].

6.5 References

[1.] Rappaz M, Bellet M, Deville M. Numerical Modeling in Materials Science and Engineering 2010.

[2.] Talreja R. Multi-scale modeling in damage mechanics of composite materials. Journal of Materials Science. 2006;41:6800-12.

[3.] Carpinteri A, Colombo G. Numerical analysis of catastrophic softening behaviour (snap-back instability). Computers & Structures. 1989;31(4):607-36.

[4.] Saucedo-Mora L, Marrow TJ. FEMME: A multi-scale Finite Element Microstructure MEshfree fracture model for quasi-brittle materials with complex microstructures. Engineering Fracture Mechanics. 2015;147:355-72.

[5.] Oliver J, Huespe AE, Sánchez PJ. A comparative study on finite elements for capturing strong discontinuities: E-FEM vs X-FEM. Computer Methods in Applied Mechanics and Engineering. 2006;195(37):4732-52.

[6.] Shterenlikht A, Howard I. The CAFE model of fracture—application to a TMCR steel. Fatigue & Fracture of Engineering Materials & Structures. 2006;29:770-87.

[7.] Saucedo Mora L, Mostafavi M, Khoshkhou D, Reinhard C, Atwood R, Zhao S, et al. 3D cellular automata finite element (CAFE) modelling and experimental observation of damage in quasi-brittle nuclear materials: Indentation of a SiC-SiC fibre ceramic matrix composite2013.

[8.] Saucedo Mora L, Marrow T. Method for the explicit insertion of microstructure in Cellular Automata Finite Element (CAFE) models based on an irregular tetrahedral Finite Element mesh: Application in a multi-scale Finite Element Microstructure MEshfree framework (FEMME). Finite Elements in Analysis and Design. 2015;105.

[9.] Hill R. On the micro-to-macro transition in constitutive analyses of elastoplastic response at finite strain. Mathematical Proceedings of the Cambridge Philosophical Society. 1985;98(3):579-90.

[10.] 6.777J/2.751J Material Property Database, Materials: PMMA. In: Technology MIo, editor.

[11.] Venkateshan SP, Swaminathan P. Chapter 13 - Laplace and Poisson Equations. In: Venkateshan SP, Swaminathan P, editors. Computational Methods in Engineering. Boston: Academic Press; 2014. p. 529-73.

[12.] Saucedo-Mora L, Marrow TJ. Multi-scale damage modelling in a ceramic matrix composite using a finite-element microstructure meshfree methodology. Philos Trans A Math Phys Eng Sci. 2016;374(2071):20150276.

[13.] Rosa AL, Yu RC, Ruiz G, Saucedo L, Sousa JLAO. A loading rate dependent cohesive model for concrete fracture. Engineering Fracture Mechanics. 2012;82:195-208.

Chapter 7

7. Discussion, conclusion and future work

7.1 Discussion

7.1.1 Toughening from Inkjet Printing

The enhancement of fracture resistance through depositing of PMMA or PEG droplets via inkjet printing in the scale-down laminate has been consistently demonstrated by both DCB tests, and in-situ XCT observations. Through the DCB experiments, the fracture energy was quantified, where the printed specimens exhibit greater G_{1c} with statistical significance. The tomographic analysis further confirms the toughening mechanism: printed samples displayed greater Mode I crack opening displacements derived from DVC, as well as higher J-integral values obtained from full-field informed finite element analyses. Together, these results substantiate that the toughening effect on the scale-down specimen, which implies investigating the toughening mechanism in two-layer thin specimens could represent bulk composites.

The sample dimension in DCB was smaller than the suggested in ASTM 5582 standard, which is due to the size constrains of Deben tube for tomographic characterization. To ensure comparability, the laminate geometries were kept consistent across specimens. The 3D tomography revealed that the crack front exhibited fluctuations during propagation, leading to a varied surface area creation. In thin laminates, such variations were not averaged out, thereby contributing to the observed fluctuations in G_{1c}.

With respect to the printing materials, small molecular weight PEG demonstrates better toughening capacity, where PEG_Line_400 series achieving the greatest improvement – an increase in fracture energy improvement of 24%.

Compared with other toughening methods such as interleaving or stitching, which often yield the increase in work of fracture exceeding 50%, the inkjet printing approach offers a more modest effect. Nevertheless, its unique advantages such as little weight penalty and negligible sacrifice on other mechanical properties such as fatigue resistance underscore its engineering value. Rather than serving as a bulk toughening strategy, inkjet printing would be a better suit for local reinforcement in regions requiring elevated fracture resistance, such as areas designated for drilling in the subsequent manufacturing steps.

7.1.2 Mechanism behind fracture energy increment

From measurement of focus variation microscopy, it has been observed that the fracture plane of laminates with printing dots always associated with higher global surface unevenness (*Wa*). Moreover, as illustrated in Figure 7.1, there is a linear correlation between work of fracture (G_{IC}) and waviness (*Wa*). This indicates the inkjet printing deposits promote greater surface generation as crack propagation, thereby requiring additional energy input and leading to the enhanced fracture toughness.

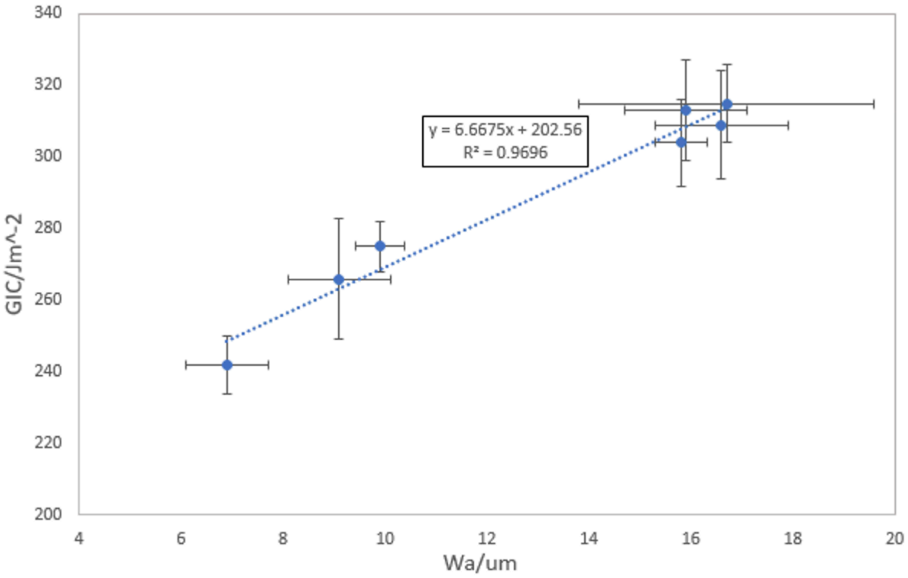

Figure 7.1. A linear correlation appeared between *Wa* and G_{IC}

The exact toughening mechanisms, however, differ between PMMA- and PEG- printed laminates. Micro voids and separated particles were found on the fracture surface of the composite printed with PMMA droplets under SEM fractography (Figure 7.2). These pores were likely been formed via cavitation process: Due to the immiscibility between PMMA and epoxy matrix, the PMMA deposit remained separated. Under the mechanical stress, voids formation initiated from PMMA dots that consumed energy, while interfacial decohesion creating extra surface further increased the work of fracture. Besides, as delamination further propagated, the voids could facilitate matrix bridging traction that further enhanced the damage resistance. Debonding of separated PMMA particles from the matrix had also been observed, where extra energy was consumed that contributed to the fracture toughness.

Attempt to visualize these particles and voids using low energy phase contrast s-XCT were unsuccessful, due to the similarity of X-ray attenuation coefficient of printing dots and epoxy and the limited XCT resolution.

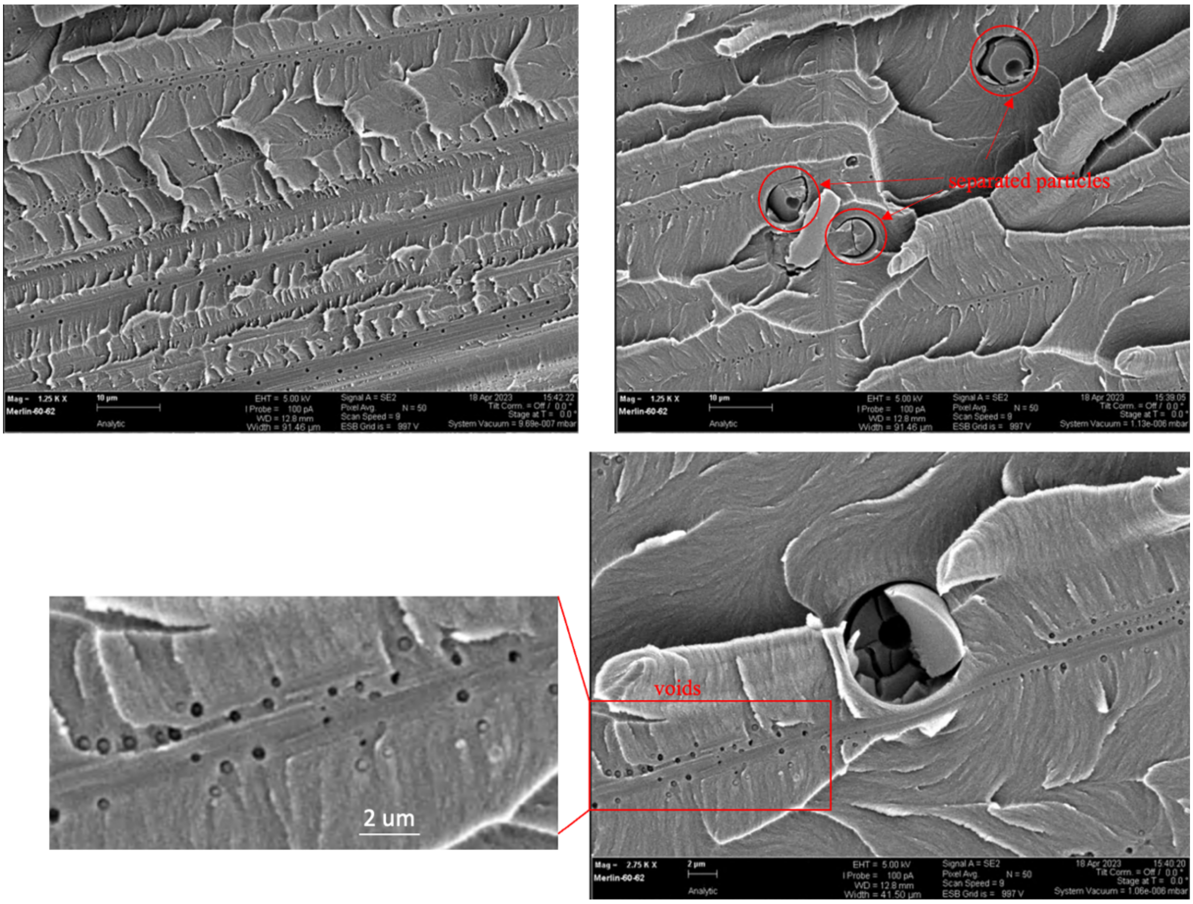

Figure 7.2. Micro voids and separated particles were observed on the fracture surface of PMMA-printed laminates

For the PEG modified laminates, characterization under confocal microscopy indicated that the dots might have dissolved into the matrix during curing. XPS spot analysis confirms this: A dominance of C-OH as well as a significant higher portion of C=O present in PEG-printed laminate. The pronounced level of high-activity bond enhances the joint strength between adhesive layers. Therefore, it is indicated that the PEG affected the matrix properties to improve the critical strain energy.

Finite element micromechanical modelling demonstrated that matrix bridging plays a important role in fracture resistance by extending the elastic regime and delaying damage initiation. In-situ XCT observation confirmed the occurrence of both fibre and matrix bridging during crack growth. However, the bridge counts turn out to be similar between different laminates, indicating the printing deposits do not directly affect the extend of bridging.

7.1.3 Printing pattern

The line-printed pattern was designed to examine whether the printing deposits influence crack propagation in a global or local manner, and whether the printing pattern affects the toughening response. Optical microscope observations after curing revealed that PEG deposits dissolved into the epoxy, whereas PMMA remain discrete while the original pattern lost. Moreover, on the fracture surface of PMMA-printed laminates, pronounced micropores and particles were evident; however, fractographic montages did not reveal any special distribution corresponding to the initial line printing pattern. Synchrotron XRD analysis detected crystalized PMMA peaks, yet their spatial appearance was random rather than aligned with the original pattern. Similarly, full-field displacement-informed finite element analysis enabled the tracking of J-integral and Mode I stress intensity factor during crack propagation, where a fluctuation in fracture resistance was anticipated as crack traversed region with and without printing deposits. However, no such periodic response was observed. Collectively, these findings indicate that the printing deposits undergo migration during curing, result in random alignment of dots within the composite. Consequently, the original line-printing pattern exerts minor influence on the toughening efficiency.

7.2 Conclusion

The work conducted in this thesis was a study of the effects of inkjet printing PMMA or PEG on delamination toughness of CFRP uni-directional composite. Multi-scale observations, both in-situ and ex-situ, were employed to study the damage propagation behaviour and laminate properties, comparing printed and non-printed specimens. A 3D finite-element microstructure meshfree (FEMME) framework was applied, which successfully replicated the DCB mechanical experiment. Based on the characterizations and modelling, possible toughening mechanisms were proposed that lead to a more comprehensive understanding of inkjet printing modified CFRP.

PMMA and PEG droplets were deposited on the interface of prepregs to make the two-ply inkjet printing modified laminates. The enhancement of fracture toughness in these scale-down samples with printing was proven through double cantilever beam (DCB) mechanical test of the fracture propagation resistance. A linear correlation was identified between fracture energy of laminate and its global fracture surface unevenness. Additionally, the printed laminates exhibited a greater amount of active functional group on the fracture plane, suggesting the droplets enhanced the adhesive strength and bonding force between fibre and matrix, which resulted in the increase of damage surface roughness. The exact mechanisms of PMMA and PEG dots on CFRP appeared to be different: Micro pores and particles were observed on the fracture surface of the laminate printed with PMMA droplets. The formation of voids would consume extra energy, while as delamination further propagated, they could facilitate matrix bridging traction that further enhanced the damage resistance. The particles could also contribute to fracture toughness improvement via debonding from the epoxy matrix. For the PEG-printed laminates, the droplets might have dissolved into the matrix post curing which benefit the adhesion to improve the fracture energy. Despite the above findings, the pattern that correlating to the printing was not observed, indicating the droplets might have diffused post curing.

In-situ observations by X-ray computed tomography were conducted to study the Mode I delamination in printed- and non-printed laminates. Under synchrotron-XCT, the evolution of damage in the 3D volume has been resolved, where the torturous crack path was observed, with a similar amount of fibre bridging and peeling across all the specimens. Due to the lack of contrast, the thermoplastic printing dots failed to be observed. By applying DVC to the

3D images, the displacement fields were evaluated, where a larger critical crack opening displacement was measured in the printed laminates that reflected the toughening effect. The full field displacement then informed a finite element model to calculate the evolution of J-integral from which the stress intensity factor in modes I, II and III were obtained. The laminates with inkjet printing were consistently associated with higher J-integral, which demonstrated the toughing effect. Separating the stress intensity factor illustrated the crack propagation occurred with a Mode I stress intensity factor, where K_{1C} was higher in laminate with printing; associated with less significant Mode II and negligible Mode III, which aligning with the COD observation. A dual X-ray diffraction and imaging methodology was developed with the aim of tracking the elastic strain at the crack tip. Tracking of crack front was achieved by employing DIC to analyse the radiographs, while the lattice strain was measured from the shift of q value in carbon fibre (002) plane. PMMA peaks were observed under XRD, where the random appearance indicates the droplets might have diffused after curing.

Finally, a finite element microstructure meshfree fracture model (FEMME) was applied to CFRP fracture propagation, simulating the Mode I damage behaviour. The DCB test was successfully replicated, where the load-displacement curve was fitted with the experiment data by tuning the interfacial strength. The printed laminates were fitted with a larger interfacial strength, to achieve this, a larger opening displacement was required that increase the strain and stress at the crack tip, which agreed with the COD analysis from in-situ XCT observation.

7.3 Potential future work

- The mechanical behaviour of polymers can be significantly influenced by the strain rate [1], leading to variations in fracture toughness under different loading conditions.

In real world applications, the CFRP composite may encounter diverse environments. To advance the engineering application of inkjet printing composites, it is valuable to perform the DCB test (detailed in Chapter 2) across a range of loading rates. Such test would help determine the reproducibility of toughening effect and identify the rate at which maximum toughening occurs.

- To investigate the toughening mechanism, this study simplified the specimens by using two-ply laminates. In practical application, unidirectional CFRP always contains multiple layers. Conducting similar in-situ XCT observations on specimens with more layers, such as 16-ply laminates [2] would be insightful. This approach may reveal whether the crack only propagate along the plane where it initiated, i.e. the middle plane where pre-crack was inserted, providing valuable insights into crack propagation behaviours. Such comprehension could guide the manufacturing design by clarifying whether it is necessary to deposit the printing droplets in every layer or interval printing could achieve similar toughening effects, thereby reducing the manufacturing cost.
- It has been previously reported that intrinsic self-healing behaviour was observed in the laminates with PMMA droplets [3]. In Chapter 4, a full field displacement informed finite element model was developed to track the variations of J-integral as well as the stress intensity factor. This methodology could also be applied to study the healing effect.
- The extension of FEMME framework on CFRP has been successfully achieved. However, certain limitations remain that could be addressed to further improve the model's ability to simulate the real mechanical behaviour. Firstly, longitudinal carbon fibres could be embedded across the bulk of the component. By doing that, the crack development would be restricted to the pre-crack plane [4], which amplify

the effect of dots as the interaction between crack and droplets could be better captured. Secondly, the current framework could not adequately describe the stress concentration during the onset of damage. This could be addressed by introducing a dynamic model at the end of elastic loading stage [5]. Thirdly, a finer model discretization would also benefit the reproduction of delamination propagation process, though it would come at the cost of increased computational demands.

7.4 References

[1.] Lee W, Yoo T, Baek K, Cho M, Chung H, Shin H, Seog Lee Y. Strain rate effects on fracture toughness of polymer nanocomposites: A multiscale study. Engineering Fracture Mechanics. 2024;298:109924.

[2.] Zhang Y. The effect of inkjet printed polymer on the mechanical properties of carbon fibre reinforced plastic: University of Sheffield; 2015.

[3.] Zhang Y, Stringer J, Hodzic A, Smith PJ. Toughening mechanism of carbon fibre-reinforced polymer laminates containing inkjet-printed poly(methyl methacrylate) microphases. Journal of Composite Materials. 2017;52(11):1567-76.

[4.] Saucedo-Mora L, Marrow TJ. Multi-scale damage modelling in a ceramic matrix composite using a finite-element microstructure meshfree methodology. Philos Trans A Math Phys Eng Sci. 2016;374(2071):20150276.

[5.] Rosa AL, Yu RC, Ruiz G, Saucedo L, Sousa JLAO. A loading rate dependent cohesive model for concrete fracture. Engineering Fracture Mechanics. 2012;82:195-208.